



Xinxin Yu

# CONTACT MODELLING IN MULTIBODY APPLICATIONS



Xinxin Yu

## **CONTACT MODELLING IN MULTIBODY APPLICATIONS**

Dissertation for the degree of Doctor of Science (Technology) to be presented with due permission for public examination and criticism in the Auditorium 1316 at Lappeenranta-Lahti University of Technology LUT, Lappeenranta, Finland on the 8<sup>th</sup> of October 2021, at noon.

Acta Universitatis  
Lappeenrantaensis 976

- Supervisors Professor Aki Mikkola  
LUT School of Energy Systems  
Lappeenranta-Lahti University of Technology LUT  
Finland
- Academy Researcher Fellow Marko Matikainen  
LUT School of Energy Systems  
Lappeenranta-Lahti University of Technology LUT  
Finland
- Reviewers Professor Qiang Tian  
School of Aerospace Engineering  
Beijing Institute of Technology  
China
- Professor Dan Negrut  
Department of Mechanical Engineering  
University of Wisconsin-Madison  
USA
- Opponents Professor Dan Negrut  
Department of Mechanical Engineering  
University of Wisconsin-Madison  
USA
- Professor Jorge A.C. Ambrósio  
Department of Mechanical Engineering  
Instituto Superior Técnico  
Portugal

ISBN ISBN 978-952-335-702-0  
ISBN ISBN 978-952-335-703-7 (PDF)  
ISSN-L 1456-4491  
ISSN 1456-4491

Lappeenranta-Lahti University of Technology LUT  
LUT University Press 2021

---

## Abstract

**Xinxin Yu**

**Contact modelling in multibody applications**

Lappeenranta 2021

71 pages

Acta Universitatis Lappeenrantaensis 976

Diss. Lappeenranta–Lahti University of Technology LUT

ISBN 978-952-335-702-0, ISBN 978-952-335-703-7 (PDF), ISSN-L 1456-4491, ISSN 1456-4491

Multibody system dynamics (MSD) offers a reliable and easy-to-use tool to analyze the dynamics of complex systems. This approach allows for the description of equations of motion for a dynamic system that consist of interconnected components which may be rigid or deformable. Even though there are a number of applications in multibody dynamics, formulating the contact descriptions still remains challenging.

Approaches such as the penalty method, the complementarity method, and constraint-based methods have been proposed for contact modeling. Contact examples for such applications include rigid granular contact, flexible beam contact, and wheel-rail contact.

This dissertation contributes to contact modelling in multibody systems to develop the methods and gain insight into the contact problem. The kinematics and dynamic equations for rigid and flexible bodies are discussed as well as the kinematics of wheel-rail contact. Beam elements based on the absolute nodal coordinate formulation (ANCF) are implemented to describe large deformations in flexible multibody applications. In addition, the cone complementarity method (CCP) and penalty method are developed for the simulation of rigid and flexible multibody systems. Finally, for the application of wheel-rail contact simulation, two constraint-based formulations are compared and analyzed.

Keywords: Multibody dynamics, Contact modelling, Railroad dynamics, Complementarity problem, Absolute nodal coordinate formulation

---

---

## Acknowledgements

This study was carried out in the Laboratory of Computational Dynamics at LUT University, Finland, between 2017 and 2021.

First and foremost, I would like to thank my supervisor Aki Mikkola for providing me with the opportunity to join his excellent research group. Your brilliant plans of the research, professional guidance and awesome networks greatly contributes to my research. You developed me and changed my life. My appreciation also goes to second supervisor Marko K. Matikainen for his guidance during my studies and dissertation. The work presented here would not be completed without their help.

I express my heartfelt appreciation to Professor José L. Escalona from University of Seville (Spain) for accepting me into his distinguished research team and offering generous and continuous help and guidance. A large part of the research of my PhD was done with your help. You have extensive knowledge, and highly accomplished skills in teaching and guiding. You make me strong and confident.

I would like to express my kindest thanks to Professor Qiang Tian and Professor Dan Negrut for their efforts in reviewing this dissertation and for their kind and useful comments and advice. Their comments has led to the much more appealing work. I would like to extend my thanks to Prof. Dan Negrut and Professor Jorge A.C. Ambrósio for their participation as the opponents.

I would like to thank all my colleagues for their effort and help during my studies. Above all, I would like to recognize the close research cooperation with Mr. Babak Bozorgmehri, Dr. Javier Anceituno and Dr. Oleg Dmitrochenko.

Also I appreciate Dr. Scott Semken and Ms. Elizabeth Waweru for your guiding with English language.

Last, I would like to thank my parents, Ms. Cuihua Wang and Mr. Jijiang Yu for all their generous and merciful supports.

Xinxin Yu  
October 2021  
Lappeenranta, Finland

---

Abstract

Acknowledgements

Contents

List of publications	9
Author's contributions	11
Symbols and abbreviations	13
<b>1 Introduction</b>	<b>19</b>
1.1 Multibody system dynamics . . . . .	19
1.2 Contact methods in multibody dynamics . . . . .	20
1.3 Multibody applications of contact formulations . . . . .	22
1.4 Objective and scope of the dissertation . . . . .	24
1.5 Scientific contributions . . . . .	25
<b>2 Equations of motion for multibody systems</b>	<b>27</b>
2.1 Kinematics of rigid and flexible bodies . . . . .	27
2.2 Kinematics of the wheel-rail contact . . . . .	29
2.3 Dynamics of rigid and flexible bodies . . . . .	36
<b>3 Contact simulation of multibody dynamics</b>	<b>39</b>
3.1 Contact force model . . . . .	39
3.2 Penalty method . . . . .	46
3.3 Cone complementarity approach . . . . .	48
3.4 Constraint-based methods for wheel-rail contact . . . . .	50
<b>4 Summary of findings</b>	<b>57</b>
4.1 Cone complementarity method versus penalty method . . . . .	57
4.2 Two constraint-based contact methods for wheel-rail contact simulation . . . . .	60

---

<b>5</b>	<b>Conclusions</b>	<b>65</b>
	<b>References</b>	<b>67</b>
	<b>Publications</b>	

This dissertation includes a comprehensive introduction and the following publications.

*Publication I*

Yu, X., Dmitrochenko, O., Matikainen, M.K., Orzechowski, G., and Mikkola, A. (2019) Cone complementarity approach for dynamic analysis of multiple pendulums. *Advances in Mechanical Engineering*, Vol. 11, p. 1687814019856748.

*Publication II*

Yu, X., Matikainen, M.K., Harish, A.B., and Mikkola, A. (2020) Procedure for non-smooth contact for planar flexible beams with cone complementarity problem. *Proceedings of the Institution of Mechanical Engineers, Part K: Journal of Multi-body Dynamics*, Vol. 235, pp. 179-196.

*Publication III*

Bozorgmehri, B., Yu, X., Matikainen, M.K., Harish, A.B., and Mikkola, A. (2021) A study of contact methods in the application of large deformation dynamics in self-contact beam. *Nonlinear Dynamics*, Vol. 103, pp. 581-616.

*Publication IV*

Escalona, J.L., Yu, X., and Aceituno, J.F. (2020) Wheel–rail contact simulation with lookup tables and KEC profiles: a comparative study. *Multibody System Dynamics*, pp. 1-37.



This section presents the contribution of the author in the writing of the following articles. The articles were written under the supervision of Professor Aki Mikkola from LUT University, Professor José L. Escalona from University of Seville (Spain), and Academy Researcher Fellow Marko Matikainen from LUT University. This dissertation was written under the supervision of Professor Aki Mikkola, Professor José L. Escalona as the external supervisor, and Academy Researcher Fellow Marko Matikainen.

*Publication I*

Xinxin Yu was the main author and investigator for this publication. The CCP contact model was firstly developed by the Oleg Dmitrochenko. Later, the author continued the work with Oleg, implemented the CCP and penalty method for granular chain applications and was responsible for most of the writing. The other co-authors provided guidance and assistance, and wrote the work together.

*Publication II*

Xinxin Yu was the main author, and investigator, who developed the contact model based on the CCP approach and penalty method in the context of beam-to-rigid contact. The author was responsible for developing the model, analyzing the results and was responsible for most of the writing. Marko Matikainen provided the assistance of implementation of ANCF. The other co-authors provided guidance and assistance, and the authors wrote the work together.

*Publication III*

Xinxin Yu was the second author, and investigator for this publication. Xinxin Yu firstly developed the point-wise contact formulations based on the CCP approach and multibody penalty method in the context of beam-to-beam contact. Later, Babak Bozorgmehri continued the work, developed the oriented bounding boxes (OBBs) contact detection model, the point-wise and line-to-line formulations for the finite element (FE) penalty method. Babak Bozorgmehri and Marko Matikainen provided the assistance with self-contact implementation. The other co-authors provided guidance and assistance, and wrote the work together.

*Publication IV*

The research related to *Publication IV* started during the author's three month visit in 2019 to the Department of Mechanical and Manufacturing Engineering at Universidad de Sevilla. This research has been carried out under the supervision of Professor José L. Escalona, and the support of the SmartTram-LUT project with reference 6292/31/201.

Xinxin Yu was the second author, and investigator for this publication. The two constraint-based contact formulations for wheel/rail contact were developed by José L. Escalona. Xinxin Yu implemented bogie vehicle with two contact formulations. Javier F. Aceituno was responsible for the interpolation of the lookup table and compared the wheelset kinematics using contact lookup tables and KEC-method. The authors analyzed the numerical results and wrote the work together.

## ALPHABETICAL SYMBOLS

$\mathbf{a}^T$	Transpose of vector or matrix $\mathbf{a}$
$(\mathbf{a}^B)^T$	Transpose of vector or matrix $\mathbf{a}^B$
$(\mathbf{a}_C^B)^T$	Transpose of vector or matrix $\mathbf{a}_C^B$
$\mathbf{A}$	Rotation matrix of body frame with respect to global frame
$\mathbf{A}^A, \mathbf{A}^B$	Rotation matrices of body frame with respect to global frame for body $A$ and $B$
$\mathbf{A}^{t,lrp}, \mathbf{A}^{t,rrp}$	Rotation matrices of the left and right railhead frames with respect to the track frame
$\mathbf{A}^{bti}$	Rotation matrix of the body-track frame with respect to the global frame
$\mathbf{A}^{bti,i}$	Rotation matrix of body frame with respect to the body-track frame
$\mathbf{A}^{wti}$	Rotation matrix of the wheelset track frame with respect to the global frame
$\mathbf{A}^{wti,wi}$	Rotation matrix of the wheelset body frame with respect to the wheelset track frame
$\mathbf{A}^{wti,wIi}$	Rotation matrix of the wheelset intermediate frame with respect to the wheelset track frame
$\mathbf{A}^{wIi,wi}$	Rotation matrix of the wheelset body frame with respect to the wheelset intermediate frame
$\mathbf{A}_P^i$	Rotation matrix of contact frame with respect to global frame to the contact surface at point $P$
$c_N$	Normal penalty parameter
$c_r$	Coefficient of restitution
$C_{damp}$	Hysteresis damping factor
$\mathbf{C}^{clt}$	Jacobian matrix of all wheel-rail contact constraints modelled with lookup tables
$\mathbf{C}^{clu}$	Vector of lookup table constraints
$\mathbf{C}^{KEC}$	Vector of KEC constraints
$\mathbf{D}$	Incidence matrix which can define the location and direction of the contact force in global frame
$E$	Young's modulus
$\mathbf{E}$	Green-Lagrange strain tensor
$f_{i,n}$	Normal contact force for $i$ -th contact
$f_{i,t}$	Tangential contact force for $i$ -th contact
$f_{fla}^{nor,wi}$	Flange normal contact force at the wheelset

---

$\mathbf{f}_i$	Vector of multipliers which consists of the magnitude of tangential contact force $f_{i,t}$ and normal contact force $f_{i,n}$
$\mathbf{F}$	Deformation gradient
$\mathbf{F}_P^i$	Vector of contact forces acting at the contact point $P$ for $i$ -th contact
$g_{i,n}$	Normal relative penetration between the bodies in contact
$\dot{g}_{i,n}$	Normal relative velocity between the bodies in contact
$\dot{g}_{i,n}^{(-)}$	Normal relative velocity before contact
$\dot{g}_{i,n}^{(+)}$	Normal relative velocity after contact
$g^{wi}$	Wheel-rail normal relative penetration at the flange contact
$\dot{g}^{wi}$	Normal relative velocity between wheel flange and rail head
$h^{lw}$ and $h^{rw}$	Functions that defines the left and right wheel profile
$\mathbf{I}$	Identity matrix
$K_{hertz}$	Hertzian contact stiffness constant
$L_w$	Wheel profile positioning with respect to the track centreline
$L_r$	Rail profile positioning with respect to the track centreline
$\mathbf{M}$	System mass matrix
$\mathbf{M}^{fb}$	Mass matrix of ANCF beam
$\mathbf{M}^{rb}$	Mass matrix of rigid body
$\mathbf{n}_P^i$	Unit-normal vector at the contact point $P$ with respect to global frame for $i$ -th contact
$\bar{\mathbf{n}}_c^{rp}$	Normal vector to the rail surface at the contact point
$\mathbf{N}$	Matrix which represents the direction of the reaction forces for KEC method
$\mathbf{N}_m$	Matrix of shape function
$\mathbf{N}_{m,P}^A$	Matrix of shape function at contact point $P$ of element $A$
$\mathbf{N}_{m,Q}^B$	Matrix of shape function at contact point $Q$ of element $B$
$\mathbf{q}^{fb}$	Vector of the nodal coordinates for ANCF beam element
$\mathbf{q}^{fb,A}, \mathbf{q}^{fb,B}$	Vector of the nodal coordinates for beam elements $A$ and $B$
$\dot{\mathbf{q}}^{fb,B}$	Time derivative of the nodal coordinates for beam element $B$
$\mathbf{q}^{rb}$	Vector of generalized coordinates for rigid body
$\mathbf{Q}^c$	Vector of system generalized contact forces
$\mathbf{Q}^{c,i}$	Vector of system generalized contact forces for $i$ -th contact
$\mathbf{Q}^{c,rb}$	Vector of generalized contact forces of rigid body
$\mathbf{Q}^{c,fb}$	Vector of generalized contact forces of ANCF beam
$\mathbf{Q}^{elast,fb}$	Vector of generalized elastic forces of ANCF beam
$\mathbf{Q}^{exter}$	Vector of system generalized external forces
$\mathbf{Q}^{exter,rb}$	Vector of generalized external forces of rigid body
$\mathbf{Q}^{exter,fb}$	Vector of generalized external forces of ANCF beam
$\mathbf{Q}_{fla}^{nor}$	Vector of generalized wheel-rail normal flange forces

---

$\mathbf{Q}^{tang}$	Vector of generalized tangential tread and flange forces
$r_0$	Rolling radius of the wheel when centered in the track
$\bar{r}_y^i$ and $\bar{r}_z^i$	Position components of the body frame with respect to the body-track frame
$\mathbf{r}_{P,0}^{fb}$	Initial position vector of the arbitrary particle $P$ of the undeformed ANCF beam element with respect to global frame
$\mathbf{r}_P^{fb}$	Current position vector of the arbitrary particle $P$ of the ANCF beam element with respect to global frame
$\mathbf{r}_P^{rb}$	Position vector of the arbitrary particle $P$ of the rigid body with respect to global frame
$\mathbf{r}_P^A$	Position vector of the contact point $P$ of the body $A$ with respect to global frame
$\mathbf{r}_Q^B$	Position vector of the contact point $Q$ of the body $B$ with respect to global frame
$\mathbf{r}^{(1)}, \mathbf{r}^{(2)}, \mathbf{r}^{(3)}$	Position vector of nodal points for beam element with respect to global frame
$\mathbf{r}_{,y}^{(1)}, \mathbf{r}_{,y}^{(2)}, \mathbf{r}_{,y}^{(3)}$	Slope vectors which can be computed as $\mathbf{r}_{,y} = \frac{\partial \mathbf{r}}{\partial y}$
$\bar{\mathbf{r}}^i$	Position vector of body frame with respect to the body-track frame
$\bar{\mathbf{r}}^{wi}$	Position vector of the wheelset body frame with respect to the wheelset track frame
$\bar{\mathbf{r}}_c^{rp}$	Position vector of the contact point with respect to the rail profile frame
$\bar{\mathbf{r}}^{lir}, \bar{\mathbf{r}}^{rir}$	Position vectors of left and right rail irregularities
$\mathbf{R}$	Position vector of the body frame with respect to the global frame
$\mathbf{R}^A, \mathbf{R}^B$	Position vectors of the body frame with respect to the global frame for body $A$ and $B$
$\dot{\mathbf{R}}^A, \dot{\mathbf{R}}^B$	Time derivatives of position vectors $\mathbf{R}^A$ and $\mathbf{R}^B$
$\mathbf{R}^t$	Position vector of an arbitrary point on the ideal track centreline with respect to a global frame
$\mathbf{R}^{bti}$	Position vector of the body-track frame with respect to the global frame
$\mathbf{R}^{wti}$	Position vector of the wheelset track frame with respect to the global frame
$\mathbf{R}_P^i$	Position vector of point $P$ of body $i$ with respect to global frame
$\mathbf{R}_P^{wi}$	Position vector of an arbitrary point $P$ on the surface of the left or right wheel profile
$R_x^t, R_y^t, R_z^t$	Position components of an arbitrary point on the ideal track centreline with respect to global frame

---

$s$	Arc-length associated with the track centreline
$s_1^w$	Transverse wheel surface parameter
$s_2^w$	Angular wheel surface parameter
$s_1^r$	Longitudinal rail surface parameter
$s_2^r$	Transverse rail surface parameter
$\mathbf{S}$	Second Piola–Kirchhoff stress tensor
$\bar{\mathbf{t}}_c^{wi}$	Unit-tangent vector to the wheel surface at the contact point
$\mathbf{t}_P^i$	Unit-tangent vector at the contact point $P$ with respect to global frame
$U$	Strain energy
$\bar{\mathbf{u}}_P$	Position vector of the arbitrary point $P$ with with respect to body frame
$\bar{\mathbf{u}}_P^A$	Position vector of the contact point $P$ with with respect to body frame of body $A$
$\bar{\mathbf{u}}_Q^B$	Position vector of the contact point $Q$ with with respect to body frame of body $B$
$\hat{\mathbf{u}}_Q^{lrp}, \hat{\mathbf{u}}_P^{rrp}$	Position vectors of points $P$ and $Q$ with respect to rail profile frames
$\hat{\mathbf{u}}_P^i$	Position vector of point $P$ with respect to body frame for body $i$
$\hat{\mathbf{u}}_P^{wi}$	Position vector of point $P$ with respect to wheelset intermediate frame
$\hat{\mathbf{u}}_{fla}^{wiI}$	Position vector of flange contact point with respect to wheelset intermediate frame
$V$	Volumn
$\mathbf{V}$	Quadratic term matrix in the cone complementarity problem approach
$v_\epsilon$	Velocity tolerance
$\mathbf{v}_t$	Tangential relative velocity at the contact point
$W^{exter,fb}$	Work done by externally applied forces
$W^{c,i}$	Work done by contact forces for $i$ -contact
$y^{lir}, y^{rir}$	Position components of left and right rail irregularity in lateral direction
$z^{lir}, z^{rir}$	Position components of left and right rail irregularity in vertical direction

## GREEK SYMBOLS

$\beta$	Orientation angle of the rail profiles
$\delta$	Linearized rotation angle due to the irregularity

---

$\Delta t$	Time step
$F_i$	Complementarity condition for CCP approach
$l_x, l_y$	The length and width of the beam element in the local physical coordinate system $\{x, y\}$
$\gamma_i$	Contact impulse for $i$ -th contact
$\gamma_{i,n} = f_{i,n}\Delta t$	Normal contact impulse for $i$ -th contact
$\gamma_{i,t} = f_{i,t}\Delta t$	Tangential contact impulse for $i$ -th contact
$\lambda$	Vecor of Lagrange multipliers
$\mu$	Coefficient of friction
$\nu$	Poisson's ratio
$\Omega$	Discretized flexible body
$\Omega_e$	One element of the discretized flexible body
$\rho$	Density
$\Phi$	Gap function
$\varphi$	Rotation angle of the body
$\varphi^A, \varphi^B$	Rotation angles of the body $A$ and $B$
$\dot{\varphi}^A, \dot{\varphi}^B$	Time derivative of rotation angles of $\varphi^A$ and $\varphi^B$
$\bar{\varphi}, \bar{\theta}$ and $\bar{\psi}$	Euler angles of body frame with respect to body-track frame
$\varphi^t, \theta^t$ and $\psi^t$	Euler angles of track frame with respect to the global frame
$\xi$	Vector of local bi-normalized coordinates
$\xi$	Abscissa beam parameter in the local bi-normalized coordinate system
$\eta$	Ordinate beam parameter along the width of an element in the local bi-normalized coordinate system
$\xi_a$	Alignment of the railhead centrelines' irregularities
$\xi_c$	Cross level of the railhead centrelines' irregularities
$\xi_g$	Gauge variation of the railhead centrelines' irregularities
$\xi_v$	Vertical profile of the railhead centrelines' irregularities

## ABBREVIATIONS

2D	Two-dimensional
3D	Three-dimensional
ANCF	Absolute nodal coordinate formulation
CCP	Cone complementarity problem
CP	Complementarity problem
DAE	Differential-algebraic equations
FEM	Finite element method
KEC	Knife-edge equivalent contact
KKT	Karush-Kuhn-Tucker
LCP	Linear complementarity problem

MSD	Multibody system dynamics
NCP	Nonlinear complementarity problem
OBB	Oriented bounding boxes
ODE	Ordinary differential equations
PSD	Power spectral density

## REFERENCE FRAMES

$\langle O; X, Y, Z \rangle$	Global frame
$\langle O^t; X^t, Y^t, Z^t \rangle$	Track frame
$\langle O^i; X^i, Y^i, Z^i \rangle$	Body frame
$\langle O^{lrp}; X^{lrp}, Y^{lrp}, Z^{lrp} \rangle$	Left rail profile frame
$\langle O^{rrp}; X^{rrp}, Y^{rrp}, Z^{rrp} \rangle$	Right rail profile frame
$\langle O^{bti}; X^{bti}, Y^{bti}, Z^{bti} \rangle$	Body-track frame for body $i$
$\langle O^{wi}; X^{wi}, Y^{wi}, Z^{wi} \rangle$	Wheelset frame
$\langle O^{wIi}; X^{wIi}, Y^{wIi}, Z^{wIi} \rangle$	Wheelset intermediate frame

## Introduction

Predicting of contact phenomena in the dynamics of a rigid and/or flexible multibody system is important. Contact modelling in multibody dynamics is challenging due to several factors that must be considered, such as the geometry and material properties of contacting bodies, and the description of frictional contact phenomenon. In addition, the contact phenomena may lead to a short duration, large velocity change, rapid energy dissipation, and dynamic instability. Hence, the development of contact models in terms of accuracy and efficiency, is of great interest to the research community.

### 1.1 Multibody system dynamics

The Multibody System Dynamics (MSD) approach allows for the straightforward description of the equations of motion for a dynamic system. This approach can be applied to a wide variety of applications that consist of interconnected bodies, which can be assumed to be rigid or deformable depending on the application. The interconnection between bodies can be described by joints (via kinematic constraints) and/or forces. As shown in Fig. 1.1, a multibody system can be described using a number of rigid and/or flexible bodies interconnected by kinematic joints and force elements.

In general, the configuration of a system can be described using a set of generalized global coordinates, which can directly determine the position and orientation of the body. In addition, joints are accounted for by employing constraint equations that couple the generalized global coordinates. This way, the movement of one body influences the movement of other bodies based on the joint interconnection types [44].

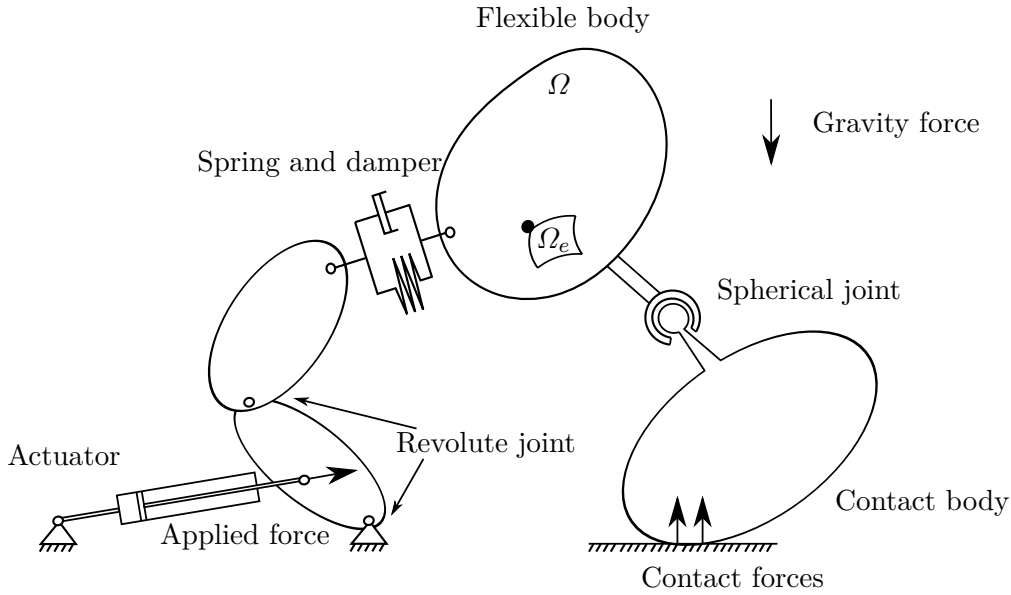


**Figure 1.1.** The abstract drawing of a multibody system with bodies, joints and forces elements,  $\Omega$  represents the discretized flexible body and  $\Omega_e$  represents one element of the discretized flexible body.

## 1.2 Contact methods in multibody dynamics

The penalty, complementarity, and constraint-based methods are often used to describe contact in multibody dynamics applications. In this chapter, the pros and cons of the penalty, complementarity-based, and constraint-based methods are explained.

### Penalty method

Due to its simplicity and robustness, the penalty method is widely used to describe contact in MSD simulation. Using this method, interpenetration is allowed between contact surfaces, and the contact force is expressed as a continuous function of the penetration between two surfaces [21, 16, 30]. Therefore, the penalty method is also referred to as the continuous [26], compliant, or elastic method [16]. However, the stiffness constant in this approach depends non-linearly on material properties and surface geometries. In addition, small stiffness constant may lead to large penetration. Alternatively, high values might lead to a stiff system of ordinary differential equations that will result in increased computational cost for the simulation.

Alternatively, the penalty method can be used to enforce the contact constraint that is usually used in the finite element method (FEM). In such a case, the variation of contact energy is computed based on the selected penalty parameter to solve the minimization problem [29, 54]. For this reason, the interpenetration between the two bodies in contact is ensured to be minimal. Since the positive definiteness of the system matrix must be preserved to ensure algorithm efficiency and stability, a carefully chosen penalty parameter is necessary for this method.

The similarities between the FE penalty method and MSD methods are as follows:

1. Contact force is calculated as a continuous function of penetration between two surfaces, and
2. The dynamic equations of motion do not need an additional variable, and
3. The selection of the stiffness constant or penalty parameter is fundamental for the contact simulation.

The differences are:

1. With the MSD penalty method, the elastic component (the spring) and the energy dissipation component (the damper) are used to prevent penetration between contacting bodies, but
2. FE penalty method is a constraint method. The contact forces are treated as constraint reactions, which is estimated as penalty term based on penalty parameter. The iteration procedure [6] is used to fulfill the criteria for minimal penetration.

### Complementarity method

An alternative approach to solving the contact problem is to employ one of the non-smooth methods. In these methods, local contact deformation is neglected. In the complementarity method, the contact constraints are included in the differential algebraic equations in terms of the complementarity conditions to prevent penetration between the contact surfaces [2]. The idea of the complementarity condition is that when the normal gap function is zero, the normal contact force is above zero and vice versa. This leads to a complementarity problem and contact forces can be solved using a convex quadratic optimization method. Therefore, the complementarity approach is one type of constraint-based approach.

### Constraint-based method

The constraint-based method is based on the geometry constraint of the contacting surface, where penetration or separation are not allowed [45, 49, 10]. Contact between two bodies is computed by solving a set of nonlinear constraint equations that establish that the contacting surfaces coincide at one or more singular contact points for bodies with non-conformal surfaces. The contact constraint equations should be fulfilled at position, velocity, and acceleration levels. Furthermore, the normal contact forces are described through the Lagrange multipliers, which are associated with the contact constraints at each contact point.

The similarities between the complementarity method and the constraint-based method are as follows:

1. In rigid body contact, the local contact deformation is neglected,
2. The contact impulses in complementarity method and contact forces in constraint-based method are introduced as additional variables into dynamic equations of motion, and
3. The contact constraints are included in the differential algebraic equations.

The differences are:

1. In complementarity method, the contact constraints are introduced in terms of the complementarity conditions to prevent penetration. The complementarity conditions can be treated as unilateral constraints and
2. In the constraint-based method, the contact constraint equations are expressed as the bilateral constraints and should be fulfilled.

### 1.3 Multibody applications of contact formulations

Computational contact mechanics is a topic of significant industrial and research interest due to its numerous applications. The contact description plays an important role in a wide variety of applications that comprise interconnected bodies, which may be rigid or deformable. Simple applications, which rigid granular contact or flexible beam contact, to more complex engineering applications, with wheel-rail contact, demonstrate the need for accurate contact modeling within the multibody dynamics framework.

### Contact between granular bodies

Multiple pendulum studies can be found in the literature [7, 34] with different practical applications in the analysis of walking [35] or bearings absorbing earthquake shocks [9]. In a multibody system analysis, thousands or millions of contacts between particles or bodies can be modeled. Individual solid bodies in a bulk of granular material [22] can move freely until contact is made with other bodies or solid walls. In such cases, the contact impulses will affect the response of the bodies. An accurate multiple-impact numerical model is needed to simulate granular chains. Multibody dynamics and impulse dynamics can be simultaneously applied to describe the behavior of granular chains.

To solve a convex quadratic program based on a fixed time step, Tasora et al. [53] proposed cone complementarity problem (CCP) to simulate non-smooth rigid multibody dynamics with collision, contact, and friction. Later, they [51] implemented C++ into the nonlinear complementarity problem (NCP) solver to solve multiple unilateral contacts with friction for more than 100,000 colliding rigid bodies. Compared to other algorithms, this model demonstrated remarkable performance. In addition, Anitescu proposed a time integration formulation method and a fixed-point iteration algorithm in CCP approach to handle large scale contacts and granular flow problem [1]. Furthermore, in the work of Tasora et al. [53], it is found that simulation time increases linearly with respect to the number of bodies in the CCP approach.

### Flexible beam contact

Contact between highly flexible bodies or self-contact of a flexible body are important in many applications including contact between a belt and pulley or crash-worthiness analysis in aerospace and automotive engineering. From three-dimensional (3D) [19] to beam-to-beam contact [55], several works have been presented to simulate quasi-static scenarios. In general, a node-to-node contact strategy between beams is commonly used [5, 27]. The orthogonality conditions for arbitrary contact between two beams are proposed by Wriggers and Zavarise [55]. In their work, the minimal distance criterion is used to find the closest points on the center lines of contacting beams. Extending the ideas advanced in [29, 27], a surface-to-surface approach for beam-to-beam contact is presented in [28]. Based on the mortar method, Puso and Laursen [40, 41] proposed a segment-to-segment contact method to prevent over-constraints that caused by the node-on-segment contact approach in the event of large frictionless and frictional sliding. In addition, Fischer and Wriggers [15] compared two mortar contact methods, and concluded that the Lagrange multiplier method needs element-wise contact detection, whereas the point-wise detection is required in the

penalty method. Puso et al. [42] extended the mortar contact method for higher order element formulations to simulate large deformation frictional contact.

### Wheel-rail contact

In a multibody dynamics simulation of railway vehicles, the modelling of wheel-rail contact plays a fundamental role throughout the literature. Among these works, two well-known approaches are commonly used to simulate wheel/rail contact in multibody railway simulations: the elastic approach and the constraint approach.

One main feature of the elastic and the constraint approaches is the determination of the location of the contact points. In this sense, two methodologies can be used for this contact search. This search can be addressed using the *online* method [39, 31]. In this approach, the location of the contact points is determined at each time step of the dynamic simulation by solving a set of algebraic nonlinear equations that evaluate the contact points as a function of the wheelset-track's relative position. Pombo and Ambrósio developed a 3D online contact detection approach to analyse the lead/lag flange contact scenarios [39], small radius track simulation [37], and the simulations with including track irregularities [38]. In addition, according to the evaluation of contact between each wheel strip and rail, Marques et al. [31] proposed an approach to determine contact points in the conformal zone between wheel tread and flange to avoid the inaccuracies of the minimum distance method.

Alternatively, the search for the contact points can be done using the so-called *offline* method. In this approach, the contact solution is solved in a pre-processing stage as a function of the wheelset relative position with respect to the track. It is then stored in a lookup table that is later used during the dynamic simulations through interpolation in the stored data [47, 48, 10]. In [47], a *hybrid* method, which is a combination of a constraint contact lookup table for the tread contact and an elastic online approach for the flange is proposed for contact search. As an extension in [48], the combination of nodal and non-conformal contact detection is used to solve significant jumps of contact points in turnouts. Furthermore in [10], a constraint contact lookup table approach that accounts for track irregularities with two entries, the lateral displacement and the track gauge variation, is proposed and compared with the online solution of the contact constraints.

## 1.4 Objective and scope of the dissertation

The objective of this work is to gain insights into the computational contact mechanics for rigid and flexible multibody systems and apply them to different applications in multibody dynamics. With this goal, the objectives and the scope of the thesis are as follows:

- Previously, the complementarity approach has been used to describe contacts between rigid bodies [51, 52]. In addition, penalty method and the differential variational inequality (DVI) method are used in [25, 24] to solve the frictional contact/impact problem based on the ANCF and discrete element method. In their method, a spherical decomposition approach is used for beam to beam contact detection. As the extension, *Publication I-III* described and compared the use and limitations of the CCP approach and penalty method for rigid and flexible contact simulations in the planar case. The master slave detection algorithm is used to detect the contact events and identify the potential contact point candidates.
- *Publication IV* supports and focuses on the use of the constraint approach in the applications of wheel-rail contact. Clearly, the elastic approach is better suited for a more detailed contact analysis. That is due to the consideration of actual wheel/rail surface areas in contact are allowed. However, when the wheel-rail profiles geometry is not well-known, or for better computational efficiency, the use of the constraint approach is superior. That is why *Publication IV* focuses on two constraint-based method for wheel-rail simulation.

## 1.5 Scientific contributions

The penalty method, the complementarity method, and constraint-based approaches are studied in this dissertation. Rigid granular pendulum contacts, flexible beam contacts, and wheel-rail contacts for railway simulation are introduced as the applications for verification of the proposed methods. Accordingly, the scientific contributions of the study can be summarized in two main categories.

Firstly, applications of two contact descriptions, (1) the complementarity approach and (2) the penalty method, are studied and compared. To make the comparison, different contact cases, covered in *Publications I-III*, are analyzed as follows.

- *Publication I* applies both contact approaches to solve a practical problem of rigid granular chains in a planar case. The penalty method is based on dissipative contact force models, combining a linear spring with a linear damper. The kinematic results are very close between both approaches with specified contact stiffness and damping coefficients.
- *Publication II* extends the scientific knowledge of *Publication I* by introducing contact descriptions of both approaches in the framework of flexible multibody dynamics. To make the comparison of the two approaches, the damping component is included in the penalty method using the continuous

contact model introduced by Hunt and Crossley [20]. Beam-like structures that undergo large displacements and deformations are implemented based on the nonlinear finite element approach and the absolute nodal coordinate formulation (ANCF). A master-slave detection algorithm is implemented for both contact models. The kinematic results indicate that a good kinematic agreement between both approaches can be obtained when the coefficient of restitution is zero.

- As the extension of *Publication II*, *Publication III* introduces the contact mechanics to analyze beams undergoing large overall motion with large deformations and in self-contact situations. An internal iteration scheme based on the Newton solver to fulfill the criteria for minimal penetration is used in the penalty method. The intersection of the oriented bounding boxes (OBBs) approach is used for the contact detection. The ANCF is used as an underlying finite element method for modelling beam-like structures. The study demonstrates the applicability of both approaches in a situation where a variety of flexible-to-flexible contact types occur.

Secondly, the use and limitations of two constraint-based formulations for the wheel-rail contact simulation, (1) contact lookup tables and (2) the Knife-edge Equivalent Contact constraint method (KEC-method) are discussed in *Publication IV*. To deal with the 2-point contact scenario, the lookup table method is combined with the hybrid method as a penetration-based elastic contact model for the flange and constraint method in the tread. Alternatively, a regularization of the tread-flange transition which allows for the use of the constraint approach in the tread and flange simultaneously are used in the KEC-method. Both methods are studied and compared with the special emphasis in the calculation of contact forces. Although results show a good agreement between both approaches, the use of the KEC-method is more extensive. That is due to only the KEC method is capable of reproducing the wheel-climbing scenario.

---

## Equations of motion for multibody systems

---

This chapter introduces the kinematic description of a planar rigid body and a planar ANCF beam, and the equation of motion for a system that describes the contact of a flexible beam and rigid body.

### 2.1 Kinematics of rigid and flexible bodies

Generalized coordinates for a planar rigid body can be written as

$$\mathbf{q}^{rb} = [\mathbf{R}^T \quad \varphi]^T, \quad (2.1)$$

where  $\mathbf{R}$  is the position vector of the body frame with respect to global frame,  $\varphi$  is the rotation angle of the body [44] and  $\mathbf{a}^T$  represents the transpose of vector or matrix  $\mathbf{a}$ .

The position vector of a arbitrary particle  $P$  of the rigid body can be defined as

$$\mathbf{r}_P^{rb} = \mathbf{R} + \mathbf{A}\bar{\mathbf{u}}_P \quad (2.2)$$

where  $\bar{\mathbf{u}}_P$  is the position vector of the arbitrary point  $P$  with respect to body frame, and the matrix  $\mathbf{A}$  is the rotation matrix of body frame with respect to global frame, which can be written as

$$\mathbf{A} = \begin{bmatrix} \cos \varphi & -\sin \varphi \\ \sin \varphi & \cos \varphi \end{bmatrix}. \quad (2.3)$$

The ANCF is a finite element based approach that can predict the dynamic responses of structures such as beams, plates and shell-like bodies subjected to

large deformations [43, 12] in multibody applications. The absolute position vectors and slope coordinates define the global position and orientations of the element [4, 43]. This leads to a constant and symmetric mass matrix and identically zero centrifugal and Coriolis forces, which can provide some advantages during analysis of dynamic conditions [4]. As shown in Fig. 2.1, three nodes that are located at the end points and at the midpoint of the longitudinal axis of the beam [32] is used per ANCF beam element.

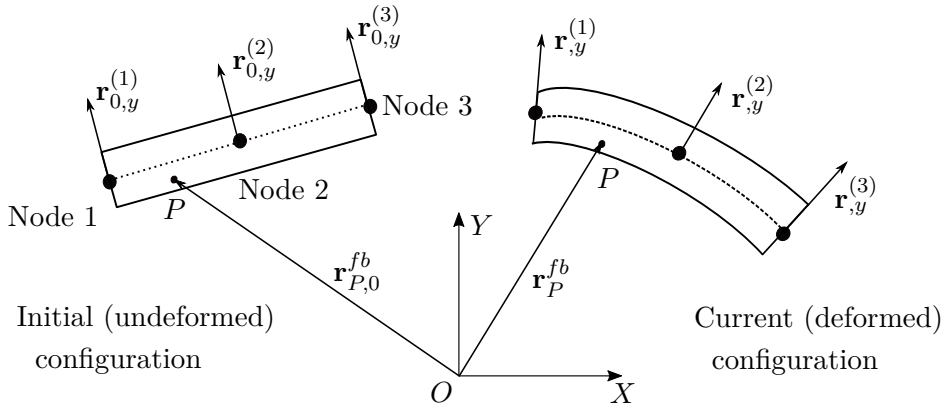


**Figure 2.1.** Beam element kinematics defined in reference and deformed configuration,  $\mathbf{r}_{P,0}^{fb}$  defines the initial position vector of particle  $P$  and  $\mathbf{r}_P^{fb}$  defines its current position vector,  $\mathbf{r}_{,y}^{(1)}$ ,  $\mathbf{r}_{,y}^{(2)}$ ,  $\mathbf{r}_{,y}^{(3)}$  are displacement gradients at the nodal points.

The position vectors in the global frame of one position vector and one slope vector are used as the nodal coordinates at each nodal location. The position vector is denoted by  $\mathbf{r}$  and the slope vector can be defined as the partial derivative of position vector with respect to local element coordinate  $y$ , such as  $\mathbf{r}_{,y} = \frac{\partial \mathbf{r}}{\partial y}$ . Accordingly, the vector of the nodal coordinates  $\mathbf{q}^{fb}$  for one element, as shown in Fig. 2.1, is given by:

$$\mathbf{q}^{fb} = \left[ \mathbf{r}^{(1)T} \quad \mathbf{r}_{,y}^{(1)T} \quad \mathbf{r}^{(2)T} \quad \mathbf{r}_{,y}^{(2)T} \quad \mathbf{r}^{(3)T} \quad \mathbf{r}_{,y}^{(3)T} \right]^T. \quad (2.4)$$

where  $\mathbf{r}^{(1)}$ ,  $\mathbf{r}^{(2)}$  and  $\mathbf{r}^{(3)}$  are position vectors at nodal points.

Since four degrees of freedom are specified at each node, a three-node beam element has a total of 12 degrees of freedom. Due to practical reasons with numerical integration over volume, the shape functions are defined in the local bi-normalized coordinate system  $\{\xi, \eta\}$  of the element as:

$$\begin{aligned}
N_1(\xi, \eta) &= \frac{(\xi + 1)^2}{2} - \frac{3\xi}{2} - \frac{1}{2}, \\
N_2(\xi, \eta) &= \frac{\ell_y \eta}{2} + \frac{\ell_y \eta (\xi + 1)^2}{4} - \frac{3\ell_y \eta (\xi + 1)}{4}, \\
N_3(\xi, \eta) &= 2\xi - (\xi + 1)^2 + 2, \\
N_4(\xi, \eta) &= \ell_y \eta (\xi + 1) - \frac{\ell_y \eta (\xi + 1)^2}{2}, \\
N_5(\xi, \eta) &= \frac{(\xi + 1)^2}{2} - \frac{\xi}{2} - \frac{1}{2}, \\
N_6(\xi, \eta) &= \frac{\ell_y \eta (\xi + 1)^2}{4} - \frac{\ell_y \eta (\xi + 1)}{4},
\end{aligned} \tag{2.5}$$

where the abscissa beam parameter  $\xi$  and the ordinate beam parameter along the width of an element  $\eta$  in the local bi-normalized coordinate system are defined as:

$$\xi = \frac{2x}{\ell_x} - 1; \quad \eta = \frac{2y}{\ell_y} - 1, \tag{2.6}$$

where  $\ell_x$  is the length and  $\ell_y$  is the width of the beam element in the local physical coordinate system  $\{x, y\}$  in the undeformed (or reference configuration). The shape function matrix for the beam element can be written in the following way,

$$\mathbf{N}_m = \begin{bmatrix} N_1 \mathbf{I}_2 & N_2 \mathbf{I}_2 & N_3 \mathbf{I}_2 & N_4 \mathbf{I}_2 & N_5 \mathbf{I}_2 & N_6 \mathbf{I}_2 \end{bmatrix} \tag{2.7}$$

where  $\mathbf{I}_2$  is an identity matrix with the size of two by two.

In the ANCF, the global position vector of an arbitrary point on the element can be defined using the shape function from Eq. (2.7), and the vector of the nodal coordinates from Eq. (2.4) as

$$\mathbf{r}_P^{fb} = \mathbf{N}_m \mathbf{q}^{fb}. \tag{2.8}$$

where  $\mathbf{r}_P^{fb}$  is the current position vector of the arbitrary particle  $P$  of the element.

## 2.2 Kinematics of the wheel-rail contact

This section introduces details of the multibody modelling of railway vehicles. To this end, track kinematics, vehicle kinematics, wheelset kinematics and wheel-rail contact constraints will be discussed.

### Track kinematics

Track geometry is the superposition of the ideal geometry and the irregularities. Fig. 2.2 shows the track frame  $\langle O^t; X^t, Y^t, Z^t \rangle$  associated with the track centreline at each value of arc-length  $s$ . The components of the position vector of an arbitrary point on the ideal track centreline with respect to a global frame is given by,

$$\mathbf{R}^t(s) = \begin{bmatrix} R_x^t(s) \\ R_y^t(s) \\ R_z^t(s) \end{bmatrix} \quad (2.9)$$

where  $R_x^t$ ,  $R_y^t$ , and  $R_z^t$  are position components with respect to global frame  $\langle O; X, Y, Z \rangle$ . They are measured with respect to the global frame as a function of the arc-length  $s$ .

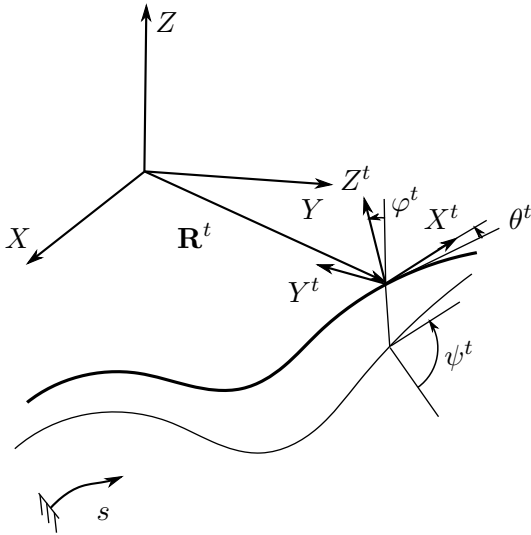


**Figure 2.2.** *Publication IV:* Ideal track centreline,  $\mathbf{R}^t$  is the position vector of an arbitrary point on the ideal track centreline with respect to a global frame,  $\varphi^t$ ,  $\theta^t$  and  $\psi^t$  are Euler angles of track frame with respect global frame.

The rotation matrix from the track frame to the global frame is given by:

$$\mathbf{A}^t(s) = \begin{bmatrix} \cos \theta^t \cos \psi^t & \sin \varphi^t \sin \theta^t \cos \psi^t - \cos \varphi^t \sin \psi^t & \sin \varphi^t \sin \psi^t + \cos \varphi^t \sin \theta^t \cos \psi^t \\ \cos \theta^t \sin \psi^t & \cos \varphi^t \cos \psi^t + \sin \varphi^t \sin \theta^t \sin \psi^t & \cos \varphi^t \sin \theta^t \sin \psi^t - \sin \varphi^t \cos \psi^t \\ -\sin \theta^t & \sin \varphi^t \cos \theta^t & \cos \varphi^t \cos \theta^t \end{bmatrix}, \quad (2.10)$$

where the Euler angles  $\psi^t$  is the *azimut* or *heading* angle,  $\theta^t$  is the vertical slope, and  $\varphi^t$  is the *cant* or *superelevation* angle, all the angles above are given as a function of  $s$  and depicted in Fig. 2.2.

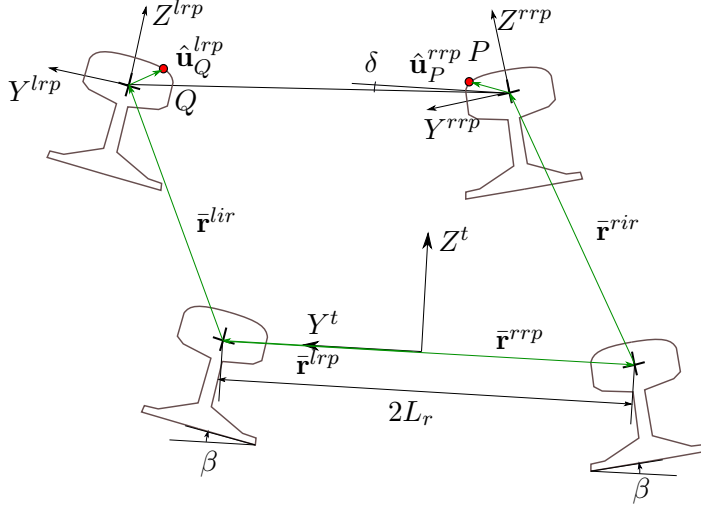


**Figure 2.3.** Track irregularity.  $\bar{\mathbf{r}}^{lir}$  and  $\bar{\mathbf{r}}^{rir}$  are irregular vectors of left and right rail heads,  $\hat{\mathbf{u}}_Q^{lrp}$  and  $\hat{\mathbf{u}}_P^{rrp}$  are position vectors of points  $P$  and  $Q$  with respect to rail profile frames,  $\beta$  is the orientation angle of the rail profiles,  $\delta$  is the linearized rotation angle due to the irregularity and  $L_r$  is the rail profile positioning with respect to the track centreline.

The displacement of the railheads due to irregularity in a cross-section of the track ( $Y^t - Z^t$  plane) is depicted in Fig. 2.3. Two frames  $\langle O^{lrp}; X^{lrp}, Y^{lrp}, Z^{lrp} \rangle$  and  $\langle O^{rrp}; X^{rrp}, Y^{rrp}, Z^{rrp} \rangle$  are defined at each railhead ( $lrp$  represents *left rail profile* frame, and  $rrp$  represents *right rail profile* frame). As shown in Fig. 2.3, the irregularity vectors  $\bar{\mathbf{r}}^{lir}$  ( $lir$  represents *left rail irregularity*) and  $\bar{\mathbf{r}}^{rir}$  ( $rir$  represents *right rail irregularity*) describe the displacement of the real rail centrelines with respect to ideal ones. The  $Y$  and  $Z$  components of the irregularity vectors in the track frame can be expressed as the functions of  $s$ , given by,

$$\bar{\mathbf{r}}^{lir}(s) = \begin{bmatrix} 0 \\ y^{lir} \\ z^{lir} \end{bmatrix}, \quad \bar{\mathbf{r}}^{rir}(s) = \begin{bmatrix} 0 \\ y^{rir} \\ z^{rir} \end{bmatrix}. \quad (2.11)$$

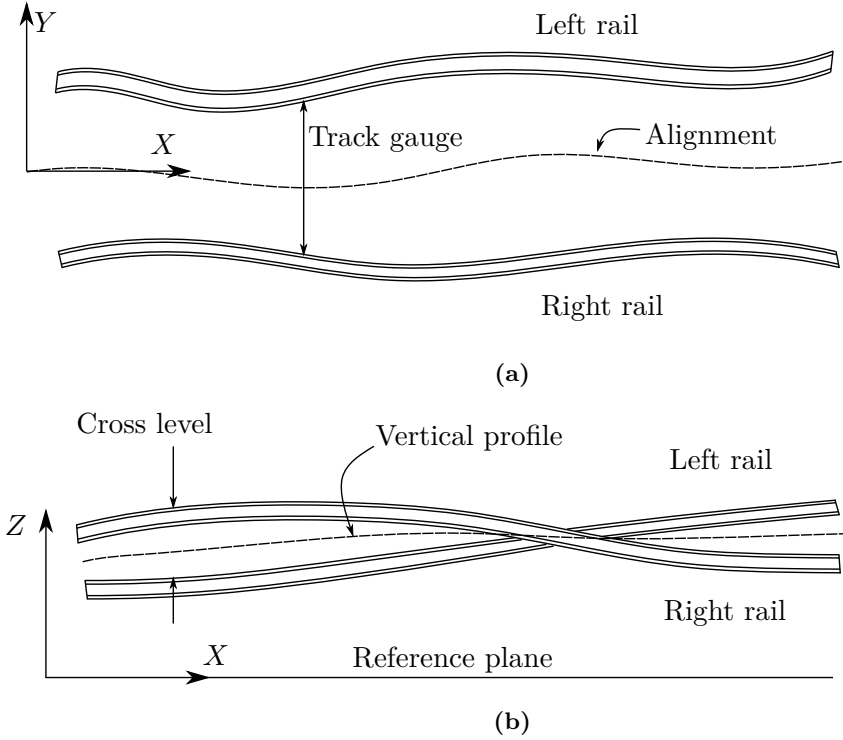


**Figure 2.4.** Representation of four combinations of the railhead centrelines' irregularities.

In the railway industry, the following four combinations of the railhead centrelines' irregularities shown in Fig. 2.4 are measured:

- Alignment ( $\xi_a$ ):  $\xi_a(s) = (y^{lir} + y^{rir})/2$
- Vertical profile ( $\xi_v$ ):  $\xi_v(s) = (z^{lir} + z^{rir})/2$
- Gauge variation ( $\xi_g$ ):  $\xi_g(s) = y^{lir} - y^{rir}$
- Cross level ( $\xi_c$ ):  $\xi_c(s) = z^{lir} - z^{rir}$

### Vehicle kinematics

For the modelling of a railway vehicle, a set of relative body-track frame coordinates, as shown in Fig. 2.5, is selected in this work. In this formulation [11],

each modelled body belonging to the railway vehicle is followed by a track-frame, which is called *body-track frame*  $\langle O^{bti}; X^{bti}, Y^{bti}, Z^{bti} \rangle$ , along the track centreline.

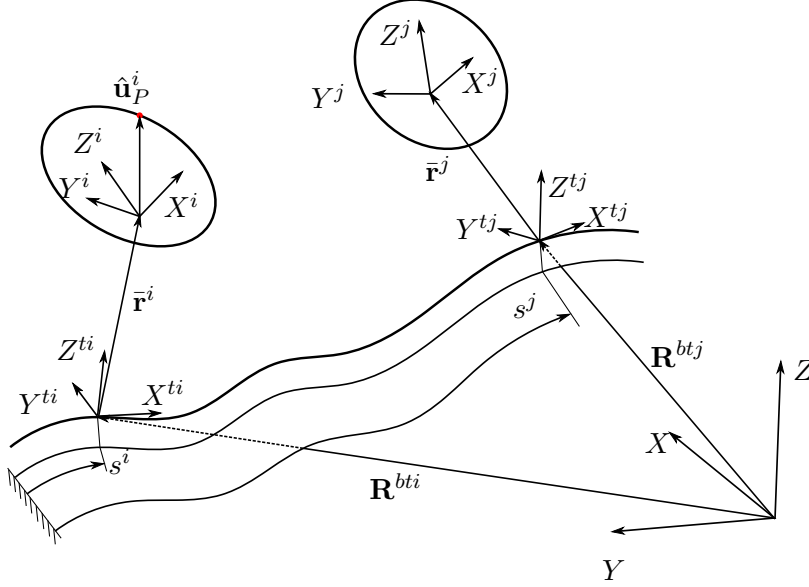


**Figure 2.5.** Kinematics of the bodies of a railway vehicle with relative body-track frame coordinates, vectors  $\mathbf{R}^{bti}$  and  $\mathbf{R}^{btj}$  are the position vectors of body track frame with respect to global frames,  $\bar{\mathbf{r}}^i$  and  $\bar{\mathbf{r}}^j$  are position vectors of body  $i$  and  $j$  with their track frames,  $\hat{\mathbf{u}}_P^i$  is the position vector of the point  $P$  with respect to the body frame.

The body-track frame is defined in the way that the  $X$ -component of the relative position vector  $\bar{\mathbf{r}}^i = [0 \quad \bar{r}_y^i \quad \bar{r}_z^i]^T$  of the body frame with respect to the body-track frame is zero. Therefore, for each body  $i$ , the following set of coordinates is defined as

$$\mathbf{q}^i = [s^i \quad \bar{r}_y^i \quad \bar{r}_z^i \quad (\bar{\Phi}^i)^T]^T = [s^i \quad \bar{r}_y^i \quad \bar{r}_z^i \quad \bar{\varphi}^i \quad \bar{\theta}^i \quad \bar{\psi}^i]^T, \quad (2.12)$$

where  $s^i$  is the arc-length coordinate for body  $i$ ,  $\bar{r}_y^i$  and  $\bar{r}_z^i$  are position components in  $Y^{bti}$  and  $Z^{bti}$  direction,  $\bar{\varphi}^i$ ,  $\bar{\theta}^i$  and  $\bar{\psi}^i$  are Euler angles of body frame with respect to body-track frame.

The absolute position vector of point  $P$  that belongs to body  $i$  in Fig. 2.5 is given by

$$\mathbf{R}_P^i = \mathbf{R}^{bti} + \mathbf{A}^{bti}(\bar{\mathbf{r}}^i + \mathbf{A}^{bti,i}\hat{\mathbf{u}}_P^i). \quad (2.13)$$

Here,  $\mathbf{R}^{bti}$  and  $\mathbf{A}^{bti}$  are the position vector and rotation matrix of the body-track frame with respect to the global frame,  $\bar{\mathbf{r}}^i$  and  $\mathbf{A}^{bti,i}$  are the position vector and rotation matrix of body frame with respect to the body-track frame,  $\hat{\mathbf{u}}_P^i$  is the position vector of point  $P$  with respect to body frame, which is constant.

### Wheelset kinematics

The track-relative coordinates of a rigid wheelset  $i$  (superscript  $wi$ ) are:

$$\mathbf{q}^{wi} = [s^{wi} \quad \bar{r}_y^{wi} \quad \bar{r}_z^{wi} \quad \bar{\varphi}^{wi} \quad \bar{\theta}^{wi} \quad \bar{\psi}^{wi}]^T. \quad (2.14)$$

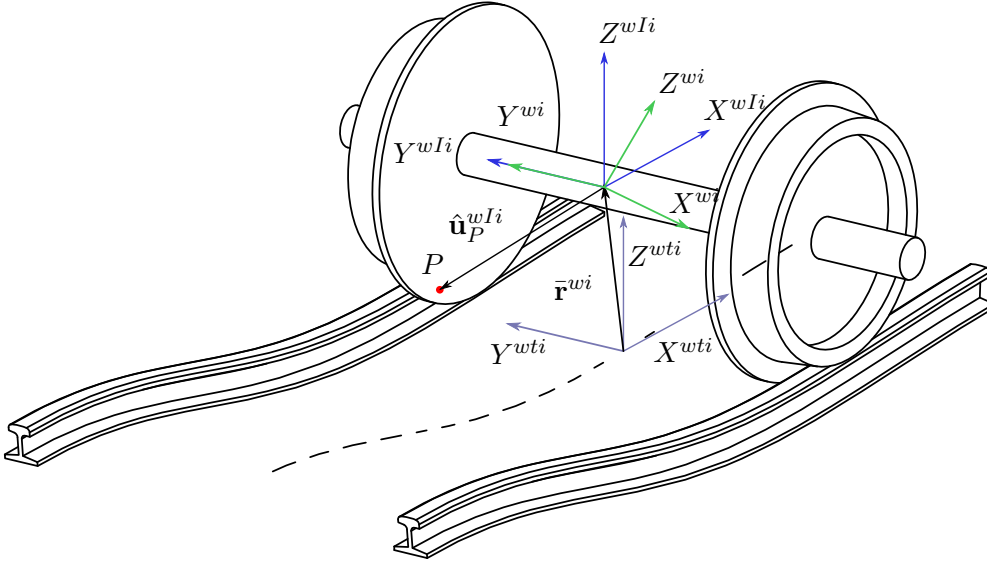


**Figure 2.6.** Frames for rigid wheelset kinematics.  $\bar{\mathbf{r}}^{wi}$  is the position vector of wheelset frame with respect to the wheelset-track frame in the wheelset-track frame,  $\hat{\mathbf{u}}_P^{wIi}$  is the position vector of the point  $P$  at left wheel with respect to the wheelset intermediate frame.

For each rigid wheelset, an additional frame that rotates with the wheelset with the exception of the rolling angle  $\bar{\theta}^{wi}$  is defined as the *wheelset intermediate frame*,  $\langle O^{wIi}; X^{wIi}, Y^{wIi}, Z^{wIi} \rangle$ , (see Fig. 2.6). The rotation matrix of the wheelset body frame with respect to the wheelset track frame  $wti$  is given by the following equation:

$$\mathbf{A}^{wti,wi} = \mathbf{A}^{wti,wIi}(\bar{\psi}^{wi}, \bar{\varphi}^{wi}) \mathbf{A}^{wIi,wi}(\bar{\theta}^{wi}), \quad (2.15)$$

where  $\mathbf{A}^{wti,wIi}$  is the rotation matrix of wheelset intermediate frame with respect to the wheelset track frame,  $\mathbf{A}^{wIi,wi}$  is the rotation matrix of wheelset frame with respect to the wheelset intermediate frame, and the brackets show the functional dependency of the rotation matrices.

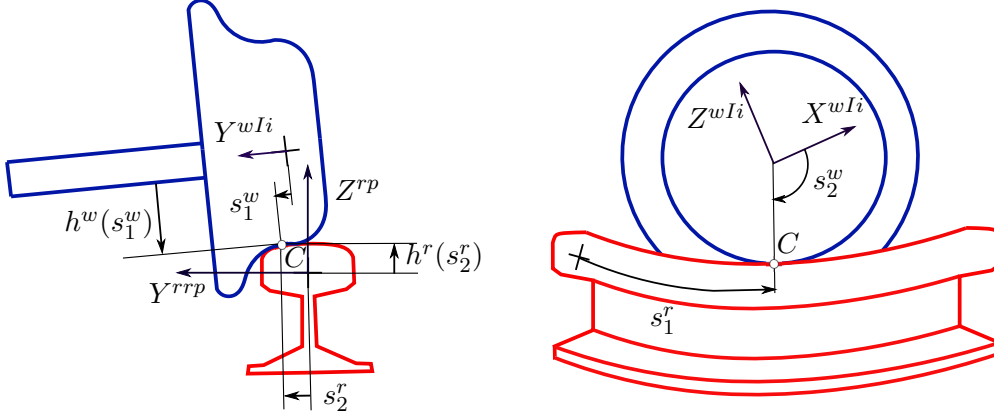


**Figure 2.7.** Wheel profile and rail profile geometry.  $s_1^w$  is the transverse wheel surface parameter,  $s_2^w$  is the angular wheel surface parameter,  $s_1^r$  is the longitudinal rail surface parameter and  $s_2^r$  is the transverse rail surface parameter.

The position vector of an arbitrary point  $P$  on the surface of the left or right wheel profile can be obtained as

$$\mathbf{R}_P^{wi} = \mathbf{R}^{wti} + \mathbf{A}^{wti}(\bar{\mathbf{r}}^{wi} + \mathbf{A}^{wti,wIi}\hat{\mathbf{u}}_P^{wIi}), \quad (2.16)$$

where  $\hat{\mathbf{u}}_P^{wIi}$  may take the following forms for the left ( $P = L$ ) or right wheels ( $P = R$ ):

$$\hat{\mathbf{u}}_R^{wIi} = \begin{bmatrix} h^{rw}(s_1^{rw}) \cos s_2^{rw} \\ -L_w + s_1^{rw} \\ -h^{rw}(s_1^{rw}) \sin s_2^{rw} \end{bmatrix}, \quad \hat{\mathbf{u}}_L^{wIi} = \begin{bmatrix} h^{lw}(s_1^{lw}) \cos s_2^{lw} \\ L_w + s_1^{lw} \\ -h^{lw}(s_1^{lw}) \sin s_2^{lw} \end{bmatrix}. \quad (2.17)$$

Here,  $lw$  and  $rw$  stand for *left wheel* and *right wheel*,  $s_1^{lw}$ ,  $s_2^{lw}$ ,  $s_1^{rw}$ , and  $s_2^{rw}$  are the parameters needed to define the points on the wheel surface,  $h^{lw}$  and  $h^{rw}$  are the functions that define the left and right wheel profile, as shown in Fig. 2.7.  $L_w$  is the wheel profile positioning with respect to the track centreline.

### Wheel-rail contact constraints

According to the wheel-rail non-conformal contact constraints, the absolute position vector of the contact point on the wheel is equal to the absolute position

vector of the contact point on the rail. Furthermore, the tangent plane to the wheel at the contact point is parallel to the tangent plane to the rail at the contact point. While neglecting the influence of the wheelset yaw angle in the contact geometry, the 3D surface-to-surface contact constraints can be approximated into 2D curve-to-curve contact constraints. The 2D curve-to-curve contact constraints can be written as a set of three constraint equations per wheel-rail pair as follows:

$$\begin{aligned}\bar{r}_{x,c}^{wi}(\mathbf{q}^{wi}, s_1^w) - \bar{r}_{x,c}^{rp}(s_2^r) &= 0, \\ \bar{r}_{y,c}^{wi}(\mathbf{q}^{wi}, s_1^w) - \bar{r}_{y,c}^{rp}(s_2^r) &= 0, \\ \left[\bar{\mathbf{t}}_{1,c}^{wi}(\mathbf{q}^{wi}, s_1^w)\right]^T \bar{\mathbf{n}}_c^{rp}(s_2^r) &= 0,\end{aligned}\tag{2.18}$$

where  $c$  can be  $lc$  (left contact) or  $rc$  (right contact),  $w$  can be  $lw$  (left wheel) or  $rw$  (right wheel),  $rp$  can be  $lrp$  (left rail profile) or  $rrp$  (right rail profile).  $s_1^w$  is the transverse wheel surface parameter, and  $s_2^r$  is the transverse rail surface parameter.  $\bar{\mathbf{r}}_c^{wi}$  and  $\bar{\mathbf{r}}_c^{rp}$  are position vectors,  $\bar{r}_{x,c}^{wi}$  and  $\bar{r}_{y,c}^{wi}$  are the  $X$  and  $Y$  components of vector  $\bar{\mathbf{r}}_c^{wi}$ ,  $\bar{r}_{x,c}^{rp}$  and  $\bar{r}_{y,c}^{rp}$  are the  $X$  and  $Y$  components of vector  $\bar{\mathbf{r}}_c^{rp}$ ,  $\bar{\mathbf{t}}_{1,c}^{wi}$  is the unit-tangent vector to the wheel surface at the contact point, and  $\bar{\mathbf{n}}_c^{rp}$  is the normal vector to the rail surface at the contact point. All of the above vectors are defined in the wheelset track frame.

### 2.3 Dynamics of rigid and flexible bodies

According to the principle of virtual work, the virtual work of all forces and torques including the applied and inertia forces equals to zero:

$$(\delta \mathbf{q}^{rb})^T (\mathbf{M}^{rb} \ddot{\mathbf{q}}^{rb} - \mathbf{Q}^{exter,rb} - \mathbf{Q}^{c,rb}) = 0,\tag{2.19}$$

where  $\mathbf{M}^{rb}$  is the mass matrix of rigid body,  $\mathbf{Q}^{exter,rb}$  is the vector of generalized external forces and  $\mathbf{Q}^{c,rb}$  is the vector of generalized contact forces. In this work, the body reference coordinate system is assumed to be located at the center of the mass and thus, the quadratic velocity for inertia forces is not shown in the equation, this is valid in two-dimensional (2D) only. It is important to note here, that the forces related to the contact is absent when the gap function is zero or positive but only considered in the presence of interpenetration. The constraint forces associated with mechanical joints are not considered in Eq. (2.19).

Taking into account that the variation vector  $\delta \mathbf{q}^{rb}$  is independent, the resulting differential equation for the rigid body system from Eq. (2.19) yields

$$\mathbf{M}^{rb} \ddot{\mathbf{q}}^{rb} - \mathbf{Q}^{exter,rb} - \mathbf{Q}^{c,rb} = \mathbf{0}. \quad (2.20)$$

In ANCF, the equation of motion can be derived using the concept of the virtual work as follows:

$$(\delta \mathbf{q}^{fb})^T (\mathbf{M}^{fb} \ddot{\mathbf{q}}^{fb} + \mathbf{Q}^{elast,fb} - \mathbf{Q}^{exter,fb} - \mathbf{Q}^{c,fb}) = \mathbf{0}, \quad (2.21)$$

where  $\mathbf{M}^{fb}$  is the mass matrix of ANCF,  $\mathbf{Q}^{exter,fb}$  is the vector of generalized external forces and  $\mathbf{Q}^{c,fb}$  is the vector of generalized contact forces of ANCF,  $\mathbf{Q}^{elast,fb}$  is the vector of generalized elastic forces of ANCF. Again, the constraint forces associated with mechanical joints are not considered in Eq. (2.21).

The mass matrix  $\mathbf{M}^{fb}$  is a constant and symmetric matrix, which can be defined as:

$$\mathbf{M}^{fb} = \int_V \rho \mathbf{N}_m^T \mathbf{N}_m dV \quad (2.22)$$

where  $\rho$  is the density and  $V$  denotes the volume.

For the structural mechanics based ANCF beam element [32], the vector of generalised elastic forces can be derived with using the variation of strain energy:

$$\delta U = \int_V \mathbf{S} : \delta \mathbf{E} dV = \int_V \mathbf{S} : \frac{\partial \mathbf{E}}{\partial \mathbf{q}^{fb}} dV \delta \mathbf{q}^{fb} = (\mathbf{Q}^{elast,fb})^T \delta \mathbf{q}^{fb} \quad (2.23)$$

where  $\mathbf{S}$  is the second Piola–Kirchhoff stress tensor, and  $\mathbf{E}$  is the Green–Lagrange strain tensor, which can be expressed as:

$$\mathbf{E} = \frac{1}{2} (\mathbf{F}^T \mathbf{F} - \mathbf{I}) \quad (2.24)$$

where  $\mathbf{F}$  is the deformation gradient and  $\mathbf{I}$  is the identity matrix.

The deformation gradient  $\mathbf{F}$  is given by:

$$\mathbf{F} = \frac{\partial \mathbf{r}^{fb}}{\partial \mathbf{r}_0^{fb}} = \frac{\partial \mathbf{r}^{fb}}{\partial \boldsymbol{\xi}} \left( \frac{\partial \mathbf{r}_0^{fb}}{\partial \boldsymbol{\xi}} \right)^{-1} \quad (2.25)$$

where  $\boldsymbol{\xi} = [\xi, \eta]$  is the vector of local bi-normalized coordinates,  $\mathbf{r}_0^{fb}$  is the initial position vector and  $\mathbf{r}^{fb}$  is the current position vector, both vectors are shown in Fig. 2.1.

The vector of generalized external force  $\mathbf{Q}^{exter,fb}$  can be obtained using virtual work, as

$$\delta W^{exter,fb} = (\mathbf{Q}^{exter,fb})^T \delta \mathbf{q}^{fb} \quad (2.26)$$

The virtual work from Eq. (2.21) must hold for any variation  $\delta \mathbf{q}^{fb}$ , the equation of motion for ANCF can be written as

$$\mathbf{M}^{fb} \ddot{\mathbf{q}}^{fb} + \mathbf{Q}^{elast,fb} - \mathbf{Q}^{exter,fb} - \mathbf{Q}^{c,fb} = \mathbf{0}, \quad (2.27)$$

The generalized coordinate array  $\mathbf{q}$  consists of the rigid body coordinate  $\mathbf{q}^{rb}$  and nodal position coordinate  $\mathbf{q}^{fb}$ :

$$\mathbf{q} = \begin{bmatrix} \mathbf{q}^{rb} \\ \mathbf{q}^{fb} \end{bmatrix}. \quad (2.28)$$

Rearranging the equation of motion for the rigid body and ANCF beam (see Eq. (2.20), Eq. (2.27)), the equation of motion in the form of DAE (differential-algebraic equations) can be written for a system of rigid and flexible bodies as follows:

$$\mathbf{M}\ddot{\mathbf{q}} - \mathbf{Q}^{exter} + \mathbf{Q}^c = \mathbf{0}, \quad (2.29)$$

where  $\mathbf{M}$  is the system mass matrix,  $\mathbf{Q}^{exter}$  is the system generalized external force vector and  $\mathbf{Q}^c$  is the system generalized contact force vector, they are written as:

$$\mathbf{M} = \begin{bmatrix} \mathbf{M}^{rb} & \\ & \mathbf{M}^{fb} \end{bmatrix}, \quad \mathbf{Q}^{exter} = \begin{bmatrix} \mathbf{Q}^{exter,rb} \\ \mathbf{Q}^{exter,fb} - \mathbf{Q}^{elast,fb} \end{bmatrix}, \quad \mathbf{Q}^c = \begin{bmatrix} \mathbf{Q}^{c,rb} \\ \mathbf{Q}^{c,fb} \end{bmatrix}. \quad (2.30)$$

The equation of motion in DAE form of Eq. (2.29) is solved by the semi-implicit Euler method as follows:

$$\begin{aligned} \dot{\mathbf{q}}^{(l+1)} &= \dot{\mathbf{q}}^{(l)} + \ddot{\mathbf{q}}^{(l)} \Delta t, \\ \mathbf{q}^{(l+1)} &= \mathbf{q}^{(l)} + \dot{\mathbf{q}}^{(l+1)} \Delta t, \end{aligned} \quad (2.31)$$

where  $\Delta t$  is time step and  $(l)$  and  $(l+1)$  represent the previous and current steps respectively.

---

## Contact simulation of multibody dynamics

---

This chapter starts with a brief description of three different contact models namely, rigid-to-rigid, rigid-to-flexible and flexible-to-flexible. Furthermore, the penalty method and the method based on complementary conditions are introduced to simulate contact phenomenon. Two constraint-based formulations for the wheel-rail contact simulation in multibody dynamics are also presented.

### 3.1 Contact force model

#### Rigid-to-rigid contact

As shown in Fig. 3.1, assume that body  $A$  and body  $B$  are in contact. For  $i$ -th contact event, a collision detection process produces a pair of contact points  $P$  and  $Q$ , and a set of two orthonormal vectors  $\mathbf{n}_P^i$  and  $\mathbf{t}_P^i$  at the contact point  $P$ , which can form a contact plane (which is called contact frame). The vector  $\mathbf{n}_P^i$  is normal with respect to the surface at contact point  $P$ , which directs from the body  $A$  to the body  $B$ , and vector  $\mathbf{t}_P^i$  is tangential to the surface at contact point  $P$ .

If the contact is active, then  $\Phi_i = 0$ . So, at the contact point, the contact force acting at the contact point is

$$\mathbf{F}_P^i = \begin{bmatrix} \mathbf{t}_P^i & \mathbf{n}_P^i \end{bmatrix} \begin{bmatrix} f_{i,t} \\ f_{i,n} \end{bmatrix} = \mathbf{A}_P^i \mathbf{f}_i, \quad (3.1)$$

where  $\mathbf{A}_P^i = \begin{bmatrix} \mathbf{t}_P^i & \mathbf{n}_P^i \end{bmatrix}$ , is the rotation matrix of contact frame with respect to global frame to the contact surface at point  $P$ .  $\mathbf{f}_i$  is the vector which consists of the magnitude of contact forces by means of multipliers  $f_{i,t}$  and  $f_{i,n}$ .

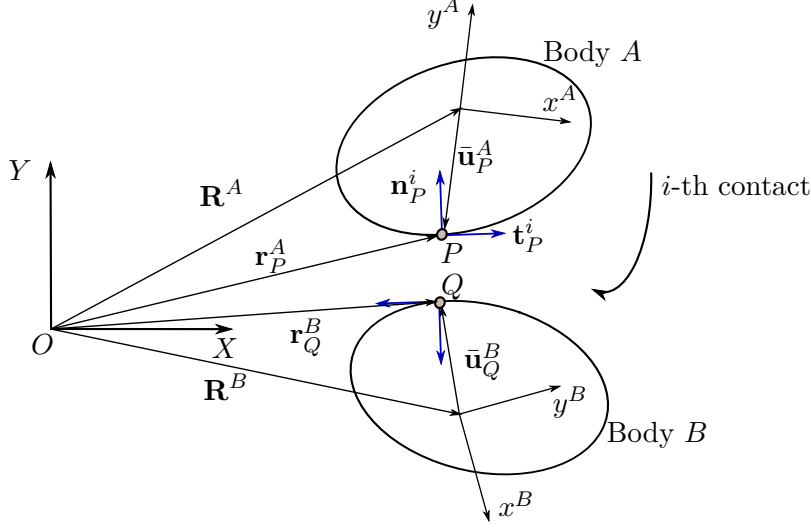


**Figure 3.1.** Illustration of rigid bodies  $A$  and  $B$  in contact. A pair of arbitrary contact points are located via position vectors  $\mathbf{r}_P^A$  and  $\mathbf{r}_Q^B$ . A set of two orthonormal vectors  $\mathbf{n}_P^i$  and  $\mathbf{t}_P^i$  are generated at the contact point  $P$ ,  $\mathbf{R}^A$  and  $\mathbf{R}^B$  are the position vectors of the origin of the body frames with respect to the origin of the global frame,  $\bar{\mathbf{u}}_P^A$  and  $\bar{\mathbf{u}}_Q^B$  are position vectors of contact points with respect to their body frames.

The virtual work associated with the contact force  $\mathbf{F}_P^i$  from Eq. (3.1) can now be expressed as:

$$\begin{aligned} \delta W^c &= \delta W^{c,A} + \delta W^{c,B} \\ &= \left( \delta(\mathbf{R}^A)^T + \delta(\varphi^A)^T \tilde{\bar{\mathbf{u}}_P^A} (\mathbf{A}^A)^T - \delta(\mathbf{R}^B)^T - \delta(\varphi^B)^T \tilde{\bar{\mathbf{u}}_Q^B} (\mathbf{A}^B)^T \right) \mathbf{A}_P^i \mathbf{f}_i \quad (3.2) \\ &= \delta \mathbf{q}^T \mathbf{Q}^{c,i} \end{aligned}$$

where  $\mathbf{R}^A$  and  $\mathbf{R}^B$  are the position vectors of the origin of the body frames with respect to the origin of the global frame,  $\mathbf{A}_A$  and  $\mathbf{A}_B$  are rotation matrices,  $\bar{\mathbf{u}}_P^A$  and  $\bar{\mathbf{u}}_Q^B$  are the local position vectors of contact points  $P$  and  $Q$  with respect to the body frames, and  $\varphi^A$  and  $\varphi^B$  are rotation angles of body  $A$  and  $B$ , respectively.  $(\mathbf{a}^B)^T$  represents the transpose of vector or matrix  $\mathbf{a}^B$ .  $\tilde{\cdot}$  is the tilde operator, which can be explained as follows:

$$\mathbf{a} = [x \ y]^T, \quad \tilde{\mathbf{a}} = [-y \ x]^T. \quad (3.3)$$

The vectors  $\delta \mathbf{q}$  and  $\mathbf{Q}^{c,i}$  appearing in Eq. (3.2) can be expressed as:

$$\delta \mathbf{q} = \begin{bmatrix} \delta \mathbf{R}^A \\ \delta \varphi^A \\ \delta \mathbf{R}^B \\ \delta \varphi^B \end{bmatrix}, \quad \mathbf{Q}^{c,i} = \mathbf{D}_i \mathbf{f}_i, \quad \mathbf{D}_i = \begin{bmatrix} \mathbf{A}_P^i \\ \tilde{\mathbf{u}}_P^A (\mathbf{A}^A)^T \mathbf{A}_P^i \\ -\mathbf{A}_P^i \\ -\tilde{\mathbf{u}}_Q^B (\mathbf{A}^B)^T \mathbf{A}_P^i \end{bmatrix} \quad (3.4)$$

where the matrix  $\mathbf{D}_i$  is an incidence matrix which can define the location and direction of the contact force in the global reference frame.

### Rigid-to-flexible contact

The modified form of node-to-node contact strategy between the beam and the rigid body is implemented in this work. As shown in Fig. 3.2, predefined slave points, are distributed equally along the beam surface. An orthogonality condition [5, 27] is used to help each slave points on the ANCF beam to find their corresponding master points (potential contact point) on the rigid body [5, 27].

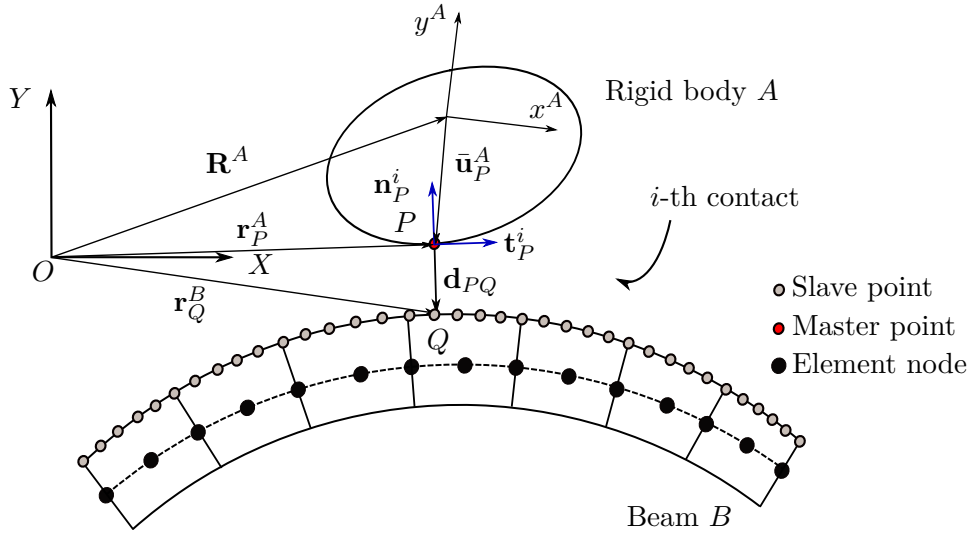


**Figure 3.2.** Beam contact detection with using master slave algorithm

Given the position vector of slave point on the beam, the position vector of the corresponding master point  $\mathbf{r}_Q^B$  on the rigid body are determined with using orthogonality condition:

$$h(x) = (\mathbf{r}_P^A(x) - \mathbf{r}_Q^B)^T \mathbf{t}_P^i(x) = 0, \quad (3.5)$$

where  $\mathbf{r}_P^A$  and  $\mathbf{t}_P^i$  are the position vector and tangential vector of master point on the rigid body, which can be expressed as:

$$\mathbf{r}_P^A = \mathbf{R}^A + \mathbf{A}^A \bar{\mathbf{u}}_P^A(x), \quad \mathbf{t}_P^i = \mathbf{A}^A \bar{\mathbf{t}}_P^i(x) \quad (3.6)$$

where  $\bar{\mathbf{u}}_P^A(x) = [x \ g(x)]^T$  is the position vector of the master point on the rigid body and  $\bar{\mathbf{t}}_P^i(x) = [1 \ \partial g(x)/\partial x]^T$  is tangential vector at master point, both are defined in the body frame as the function of surface parameter  $x$ . Eq. (3.5) leads to a nonlinear equation in one unknown variable  $x$  which can be solved using the Newton-Raphson method. The position vectors of the slave points on the beam are used as the initial values to start the Newton-Raphson iteration.

After having obtained the pairs of potential contact points from contact detection, the contact force is calculated and imposed on the flexible bodies. Consider the case of contact of a beam with a rigid body, as shown in Fig. 3.3.

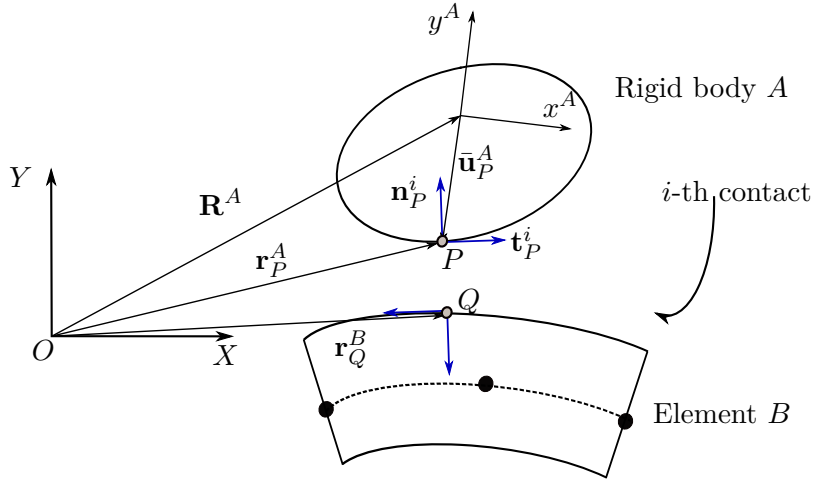


**Figure 3.3.** Illustration of rigid body  $A$  and element  $B$  in contact.

The contact force vector is computed according to Eq. (3.1). The virtual work associated with the contact force in the system can be expressed as:

$$\begin{aligned} \delta W^c &= \delta W^{c,A} + \delta W^{c,B} \\ &= \left( \delta(\mathbf{R}^A)^T + \delta(\varphi^A)^T \bar{\mathbf{u}}_P^A (\mathbf{A}^A)^T - \delta(\mathbf{q}^{fb,B})^T (\mathbf{N}_{m,Q}^B)^T \right) \mathbf{A}_P^i \mathbf{f}_i \\ &= \delta \mathbf{q}^T \mathbf{Q}^{c,i} \end{aligned} \quad (3.7)$$

where  $\mathbf{N}_{m,Q}^B$  is the shape function at contact point  $Q$  of element  $B$ , and  $\mathbf{q}^{fb,B}$  is the vector of nodal coordinates for ANCF beam of element  $B$ .  $(\mathbf{a}_C^B)^T$  represents the transpose of vector or matrix  $\mathbf{a}_C^B$ .

The vectors  $\delta\mathbf{q}$  and  $\mathbf{Q}^{c,i}$  appearing in Eq. (3.7) can be expressed as:

$$\delta\mathbf{q} = \begin{bmatrix} \delta\mathbf{R}^A \\ \delta\varphi^A \\ \delta\mathbf{q}^{fb,B} \end{bmatrix}, \quad \mathbf{Q}^{c,i} = \mathbf{D}_i \mathbf{f}_i, \quad \mathbf{D}_i = \begin{bmatrix} \mathbf{A}_P^i \\ \tilde{\mathbf{u}}_P^A (\mathbf{A}^A)^T \mathbf{A}_P^i \\ -(\mathbf{N}_{m,Q}^B)^T \mathbf{A}_P^i \end{bmatrix}. \quad (3.8)$$

### Flexible-to-flexible contact

In the beam-to-beam contact, the identify of the possible pairs of contact elements is the first task. This definition of a pair of contact elements is addressed based on the position vectors of the middle node  $\mathbf{r}_i^O$  of element  $i$  from beam  $I$  and the middle node  $\mathbf{r}_j^O$  of element  $j$  from beam  $J$  as shown in Fig. 3.4. The pair of the elements  $A$  and  $B$  with minimum distance of  $d_{min}$  is treated as the potential pair of contact elements, and  $d_{min}$  can be expressed as follows:

$$d_{min} = \min(\|\mathbf{r}_i^O - \mathbf{r}_j^O\|), \quad i = 1, 2, \dots, n_I, \quad j = 1, 2, \dots, n_J, \quad (3.9)$$

where  $n_I$  is the number of element of beam  $I$  and  $n_J$  is the number of element of beam  $J$ , and the position vectors of the middle nodes  $\mathbf{r}_i^O$  and  $\mathbf{r}_j^O$  are defined from Eq. (2.8) with local coordinate ( $\xi = 0, \eta = 0$ ).

In the case of self contact shown in Fig. 3.5, the pair of closest elements has to be considered within the beam. It is assumed that the adjacent elements cannot contact with each other, which means element  $i$  cannot interact with element  $i - 1$  and element  $i + 1$ . To prevent the adjacent middle nodes from being detected, the pair of adjacent elements are not included in the calculation of the minimum distance  $d_{min}$ , and the minimum distance  $d_{min}$  is expressed as follows:

$$d_{min} = \min(\|\mathbf{r}_i^O - \mathbf{r}_j^O\|), \quad i = 1, 2, \dots, n_I - 2, \quad j = i + 2, i + 3, \dots, n_I, \quad (3.10)$$

After detecting the pair of closest elements  $A$  and  $B$ , bounding box technique is developed to determine an active contact between the contacting OBBs and the potential contact points on the closest elements  $A$  and  $B$  are determined in the case of point-to-segment contact, point-to-point contact and line-to-line contact. More detailed explanation can be found in *Publication III*.

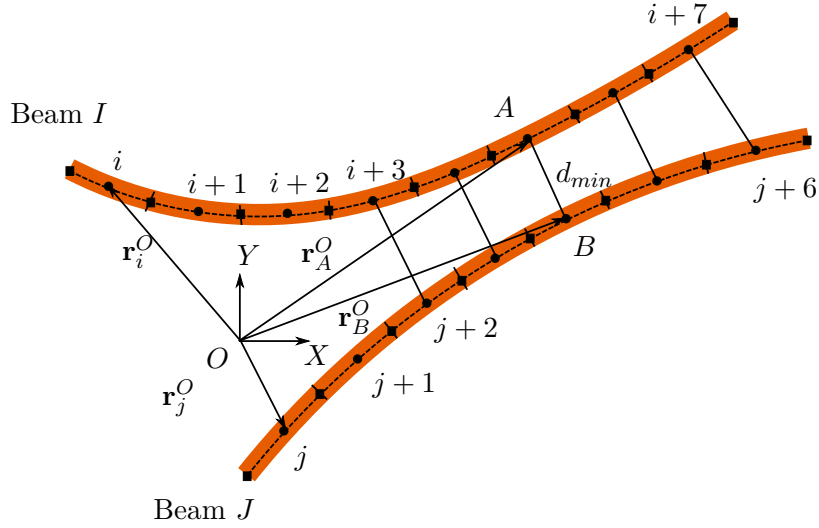


**Figure 3.4.** *Publication III:* Checking the closest potential contact elements  $i$  and  $j$  by comparing the distance between the mid-nodes from each pair of elements between two beams,  $\mathbf{r}_i^O$  and  $\mathbf{r}_j^O$  are the middle nodes from element  $i$  and  $j$ .

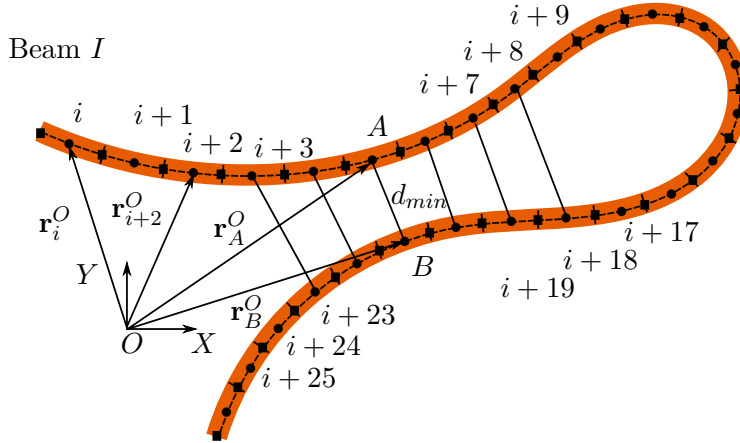


**Figure 3.5.** *Publication III:* Checking the closest potential contact elements  $i$  and  $j$  by comparing the distance between the mid-nodes from each pair of elements in case of self-contact,  $\mathbf{r}_i^O$  and  $\mathbf{r}_j^O$  are the middle nodes from element  $i$  and  $j$ .

Consider the case of contact of a beam with a beam, as shown in Fig. 3.6. The virtual work  $\delta W^c$  related to the contact force associated with the contact force can be expressed as:

$$\begin{aligned}
\delta W^c &= \delta W^{c,A} + \delta W^{c,B} \\
&= \left( \delta(\mathbf{q}^{fb,A})^T (\mathbf{N}_{m,P}^A)^T - \delta(\mathbf{q}^{fb,B})^T (\mathbf{N}_{m,Q}^B)^T \right) \mathbf{A}_P^i \mathbf{f}_i \\
&= \delta \mathbf{q}^T \mathbf{Q}^{c,i}
\end{aligned} \tag{3.11}$$

where  $\mathbf{N}_{m,P}^A$  is the shape function at contact points  $P$  of element  $A$ ,  $\mathbf{q}^{fb,A}$  and  $\mathbf{q}^{fb,B}$  are the vectors of nodal coordinates for ANCF beam element  $A$  and  $B$ .

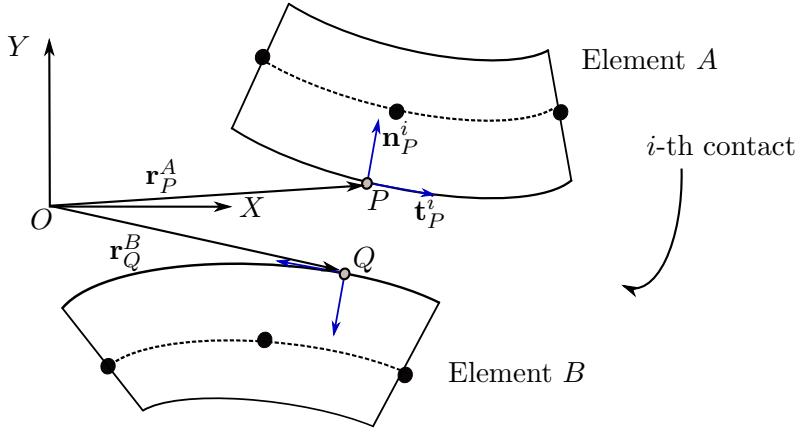


**Figure 3.6.** Illustration of element  $A$  and element  $B$  in contact.

The vectors  $\delta \mathbf{q}$  and  $\mathbf{Q}^{c,i}$  appearing in Eq. (3.11) can be expressed as:

$$\delta \mathbf{q} = \begin{bmatrix} \delta \mathbf{q}^{fb,A} \\ \delta \mathbf{q}^{fb,B} \end{bmatrix}, \quad \mathbf{Q}^{c,i} = \mathbf{D}_i \mathbf{f}_i, \quad \mathbf{D}_i = \begin{bmatrix} (\mathbf{N}_{m,P}^A)^T \mathbf{A}_P^i \\ -(\mathbf{N}_{m,Q}^B)^T \mathbf{A}_P^i \end{bmatrix}. \tag{3.12}$$

The  $\mathbf{D}_i$  matrix from Eqs. (3.4), (3.8) and (3.12) are computed based on the  $i$ -th pair of potential contact points. If there is  $N_k$  presence of contact events happening at the same time step,  $\mathbf{D}$  matrix and vector  $\mathbf{f}$  can be built as:

$$\mathbf{F}_c = \mathbf{D} \mathbf{f}, \quad \mathbf{D} = \underbrace{\begin{bmatrix} \mathbf{D}_1 & \mathbf{D}_2 & \cdots & \mathbf{D}_{N_k} \end{bmatrix}}_{N_{dof} \times 2N_k}, \quad \mathbf{f} = \begin{bmatrix} \mathbf{f}_1 \\ \mathbf{f}_2 \\ \vdots \\ \mathbf{f}_{N_k} \end{bmatrix} \left. \vphantom{\begin{bmatrix} \mathbf{f}_1 \\ \mathbf{f}_2 \\ \vdots \\ \mathbf{f}_{N_k} \end{bmatrix}} \right\} 2N_k \times 1, \tag{3.13}$$

where  $N_{dof}$  is the total number of freedom of the system.

### 3.2 Penalty method

In *Publication I* and *II*, the penalty method introduced in [16] is implemented for rigid-to-rigid and flexible-to-rigid contact to compare against the complementarity method. This method is also known as a continuous contact force model. The normal contact force  $f_{i,n}$  is computed based on the Hertzian model, included in the elastic and dissipative components [20, 26] as:

$$f_{i,n} = K_{hertz} g_{i,n}^{1.5} + C_{damp} g_{i,n}^{1.5} \dot{g}_{i,n}, \quad (3.14)$$

where  $K_{hertz}$  is the Hertzian contact stiffness constant,  $C_{damp}$  is the hysteresis damping factor,  $g_{i,n}$  is the normal relative penetration and  $\dot{g}_{i,n}$  is the normal relative velocity between the bodies in contact.

For rigid-to-rigid contact, the normal relative penetration and velocity in Eq. (3.14) are given by:

$$\begin{aligned} g_{i,n} &= \left( \mathbf{R}^A + \mathbf{A}^A \bar{\mathbf{u}}_P^A - \mathbf{R}^B - \mathbf{A}^B \bar{\mathbf{u}}_Q^B \right)^T \mathbf{n}_P^i, \\ \dot{g}_{i,n} &= \left( \dot{\mathbf{R}}^A - \dot{\varphi}^A \mathbf{A}^A \bar{\mathbf{u}}_P^A - \dot{\mathbf{R}}^B + \dot{\varphi}^B \mathbf{A}^B \bar{\mathbf{u}}_Q^B \right)^T \mathbf{n}_P^i, \end{aligned} \quad (3.15)$$

and for rigid-to-flexible contact, the normal relative penetration and velocity in Eq. (3.14) are given by:

$$\begin{aligned} g_{i,n} &= \left( \mathbf{R}^A + \mathbf{A}^A \bar{\mathbf{u}}_P^A - \mathbf{N}_{m,Q}^B \mathbf{q}^{fb,B} \right)^T \mathbf{n}_P^i, \\ \dot{g}_{i,n} &= \left( \dot{\mathbf{R}}^A - \dot{\varphi}^A \mathbf{A}^A \bar{\mathbf{u}}_P^A - \mathbf{N}_{m,Q}^B \dot{\mathbf{q}}^{fb,B} \right)^T \mathbf{n}_P^i, \end{aligned} \quad (3.16)$$

where  $\dot{\mathbf{R}}^A$ ,  $\dot{\mathbf{R}}^B$ ,  $\dot{\varphi}^A$ ,  $\dot{\varphi}^B$  and  $\dot{\mathbf{q}}^{fb,B}$  are the time derivatives of  $\mathbf{R}^A$ ,  $\mathbf{R}^B$ ,  $\varphi^A$ ,  $\varphi^B$  and  $\mathbf{q}^{fb,B}$  respectively. It is noted that  $\dot{g}_{i,n}$  is not the time derivative of the  $g_{i,n}$ , that is due to the fact that time derivative of normal vector  $\bar{\mathbf{n}}_P^i$  is not considered.

The Hertzian contact stiffness constant  $K_{hertz}$  is based on the radius and material properties of two bodies of the contact points ( $k = i, j$ ) as [17]:

$$K_{hertz} = \frac{4}{3(\sigma_i + \sigma_j)} \left[ \frac{R_i R_j}{R_i + R_j} \right]^{0.5}, \quad \sigma_k = \frac{1 - \nu_k^2}{E_k}, \quad (3.17)$$

where  $\nu_k$  is the Poisson's ratio and  $E_k$  is the Young's modulus of sphere  $k$ .

Damping factor  $C_{damp}$  is given by [20, 18]:

$$C_{damp} = \frac{3K_{hertz}(1 - c_r)}{2\dot{g}_{i,n}^{(-)}}, \quad c_r = -\frac{\dot{g}_{i,n}^{(-)}}{\dot{g}_{i,n}^{(+)}} \quad (3.18)$$

where  $c_r$  is the coefficient of restitution, which is determined experimentally with solid spheres of different materials in [17],  $\dot{g}_{i,n}^{(-)}$  is the velocity before contact, and  $\dot{g}_{i,n}^{(+)}$  is the velocity after contact. Thus,  $c_r$  has values from 0 to 1.

The tangential friction force  $\mathbf{f}_{i,t}$  acts in a direction opposite to the contact velocity with a magnitude of  $\mu_i f_{i,n}$ . Therefore, the slipping friction force  $\mathbf{f}_{i,t}$  can be computed with the help of velocity direction vector such as [18],

$$\mathbf{f}_{i,t} = -\mu_i f_{i,n} \frac{\mathbf{v}_{i,t}}{\|\mathbf{v}_{i,t}\|} \quad (3.19)$$

where  $\mathbf{v}_{i,t}$  is the tangential relative velocity at the contact point.  $\mathbf{v}_{i,t}/\|\mathbf{v}_{i,t}\|$  returns a unit vector along the direction of  $\mathbf{v}_{i,t}$ .

To avoid an infinite number produced by  $\mathbf{v}_{i,t}/\|\mathbf{v}_{i,t}\|$ , the unit vector  $\mathbf{v}_{i,t}/\|\mathbf{v}_{i,t}\|$  is replaced by  $\text{dir}_\epsilon(\mathbf{v}_{i,t}, v_\epsilon)$  [18], which is

$$\text{dir}_\epsilon(\mathbf{v}_{i,t}, v_\epsilon) = \begin{cases} \frac{\mathbf{v}_{i,t}}{\|\mathbf{v}_{i,t}\|} & \|\mathbf{v}_{i,t}\| \geq v_\epsilon \\ \frac{\mathbf{v}_{i,t}}{v_\epsilon} \left( \frac{3}{2} \frac{\|\mathbf{v}_{i,t}\|}{v_\epsilon} - \frac{1}{2} \left( \frac{\|\mathbf{v}_{i,t}\|}{v_\epsilon} \right)^3 \right) & \|\mathbf{v}_{i,t}\| < v_\epsilon \end{cases}, \quad (3.20)$$

where velocity tolerance  $v_\epsilon$  is the small velocity tolerance.

*Publication III* describes the application of the penalty method for enforcing contact constraints in different cases of beam-to-beam contact. According to the penalty method [55, 57, 50], the normal contact force  $f_{i,n}$  is computed as

$$f_{i,n} = c_N g_{i,n}, \quad (3.21)$$

where  $c_N$  is the normal penalty parameter, and the normal relative penetration  $g_{i,n}$  for beam to beam contact can be computed as

$$g_{i,n} = \left( \mathbf{N}_{m,P}^A \mathbf{Q}^{fb,A} - \mathbf{N}_{m,Q}^B \mathbf{Q}^{fb,B} \right)^T \mathbf{n}_P^i. \quad (3.22)$$

An internal iteration scheme [6] based on the Newton solver is used to fulfill the criteria for minimal penetration of Eq. (3.22). More detailed information can be found in *Publication III*.

### 3.3 Cone complementarity approach

In this work, non-smooth events such as the Coulomb friction and the non-penetration condition are described as unilateral constraints and included into the differential algebraic equations from Eq. (2.29). Consequently, the above problem is relaxed to a cone complementarity problem, which can be solved using a convex quadratic optimization method with conic constraints [33, 56].

#### Posing problem

Substituting the contact force from Eq. (3.13) and acceleration (see Eq. (2.29))

$$\ddot{\mathbf{q}}^{(l)} = \mathbf{M}^{-1}(\mathbf{Q}^{exter,(l)} + \mathbf{Q}^{c,(l+1)}), \quad (3.23)$$

into Eq. (2.31), the discretized equation of velocity combined with the complementarity conditions of non-penetration and friction model can be rewritten as:

$$\begin{aligned} \dot{\mathbf{q}}^{(l+1)} &= \dot{\mathbf{q}}^{(l)} + \mathbf{M}^{-1}\mathbf{Q}^{exter,(l)}\Delta t + \mathbf{M}^{-1}\mathbf{D}^{(l)}\mathbf{f}^{(l+1)}\Delta t, \\ \mathbf{q}^{(l+1)} &= \mathbf{q}^{(l)} + \dot{\mathbf{q}}^{(l+1)}\Delta t, \end{aligned} \quad (3.24a)$$

$$\left. \begin{aligned} 0 \leq \gamma_{i,n}^{(l+1)} \perp \Phi_i^{(l+1)} \geq 0 \\ -\gamma_{i,n}^{(l+1)} \leq 0, \quad \gamma_{i,t}^{(l+1)} - \mu\gamma_{i,n}^{(l+1)} \leq 0 \end{aligned} \right\}, \quad \forall i \in \{1, 2, \dots, N_k\}, \quad (3.24b)$$

where  $\perp$  represents perpendicular, as  $a \perp b = ab = 0$ ,  $\gamma_{i,t} = f_{i,t}\Delta t$  and  $\gamma_{i,n} = f_{i,n}\Delta t$  are normal and tangential contact impulses. Gap function  $\Phi_i^{(l+1)}$  can be approximated as

$$\Phi_i^{(l+1)} \approx \Phi_i^{(l)} + \Delta t v_{i,n}^{(l+1)} + \Delta t \mu_i v_{i,t}^{(l+1)}. \quad (3.25)$$

The relaxation of  $\Delta t \mu_i v_{i,t}^{(l+1)}$  is used to pose the problem of non-penetration constraints Eq. (3.24) as a cone complementarity problem (CCP) [3]. In the cone complementary problem, the following definitions of  $\mathbf{d}_i$  and  $\gamma_i^{(l+1)}$  are used:

$$\mathbf{d}_i = \begin{bmatrix} v_{i,t}^{(l+1)} \\ \frac{\Phi_i^{(l)}}{\Delta t} + v_{i,n}^{(l+1)} \end{bmatrix}, \quad \gamma_i^{(l+1)} = \begin{bmatrix} \gamma_{i,t}^{(l+1)} \\ \gamma_{i,n}^{(l+1)} \end{bmatrix}. \quad (3.26)$$

For the  $i$ -th contact, according to Eq. (3.24b),  $\gamma_{i,n}^{(l+1)} > 0$ , and  $\frac{\Phi_i^{(l+1)}}{\Delta t} = \frac{\Phi_i^{(l)}}{\Delta t} + v_{i,n}^{(l+1)} + \mu_i v_{i,t}^{(l+1)} = 0$ . Consequently,

$$\mathbf{d}_i^T \gamma_i^{(l+1)} = v_{i,t}^{(l+1)}(\gamma_{i,t}^{(l+1)} - \mu_i \gamma_{i,n}^{(l+1)}) = 0. \quad (3.27)$$

### Formulating the cone complementarity problem

In what follows, it is necessary to reformulate the optimization problem with equilibrium constraints [53] to account for the above cone complementarity constraints. To this end, the initial term of  $\mathbf{d}_i$  is defined as

$$\mathbf{d}_{i,0} = \begin{bmatrix} 0 \\ \frac{1}{\Delta t} \Phi_i^{(l)} \end{bmatrix}. \quad (3.28)$$

According to Eq. (3.26) and Eq. (3.24), the term of  $\mathbf{d}_i$  can be rewritten as

$$\begin{aligned} \mathbf{d}_i &= \begin{bmatrix} 0 \\ \frac{1}{\Delta t} \Phi_i^{(l)} \end{bmatrix} + \begin{bmatrix} v_{i,t}^{(l+1)} \\ v_{i,n}^{(l+1)} \end{bmatrix} \\ &= \mathbf{p}_i + (\mathbf{D}^{(l)})^T \mathbf{M}^{-1} \mathbf{D}^{(l)} \boldsymbol{\gamma}_i^{(l+1)}, \end{aligned} \quad (3.29)$$

where

$$\mathbf{p}_i = \mathbf{d}_{i,0} + (\mathbf{D}^{(l)})^T (\dot{\mathbf{q}}^{(l)} + \mathbf{M}^{-1} \mathbf{Q}^{exter,(l)} \Delta t). \quad (3.30)$$

The quadratic term matrix  $\mathbf{V} = (\mathbf{D}^{(l)})^T \mathbf{M}^{-1} \mathbf{D}^{(l)}$  is then defined, and Eq. (3.27) can be given as

$$\mathbf{d}_i^T \boldsymbol{\gamma}_i^{(l+1)} = (\mathbf{p}_i + \mathbf{V} \boldsymbol{\gamma}_i^{(l+1)})^T \boldsymbol{\gamma}_i^{(l+1)} = 0. \quad (3.31)$$

Below, the following vector  $\mathbf{p}$  will be used:

$$\mathbf{p} = [\mathbf{p}_1 \quad \mathbf{p}_2 \quad \cdots \quad \mathbf{p}_{N_k}]^T. \quad (3.32)$$

According to Karush-Kuhn-Tucker (KKT) conditions, Eq. (3.31) can be solved as a convex quadratic optimization problem with conic constraints as follows [33]:

$$\begin{aligned} \min \quad f &= \frac{1}{2} (\boldsymbol{\gamma}^{(l+1)})^T \mathbf{V} \boldsymbol{\gamma}^{(l+1)} + \mathbf{p}^T \boldsymbol{\gamma}^{(l+1)}, \\ \text{subject to} \quad & \boldsymbol{\gamma}_i^{(l+1)} \in F_i, \end{aligned} \quad (3.33)$$

whose solution is the contact impulse  $\boldsymbol{\gamma}^{(l+1)}$ . In this work, the root finding of complementarity problem from Eq. (3.33) is solved with using MATLAB in-build function *quadprog*. One can also choose Fischer-Burmeister formulation [14],

which has been widely used for solving nonlinear complementarity problems and variational inequality problems with polyhedral cone constraints.

According to Eq. (3.24), the unilateral constraint is written as:

$$F_i = \begin{cases} -\gamma_{i,n}^{(l+1)} \leq 0 \\ \gamma_{i,t}^{(l+1)} - \mu\gamma_{i,n}^{(l+1)} \leq 0 \end{cases} . \quad (3.34)$$

In the CCP approach, the contact is considered to be inelastic, thus the coefficient of restitution is assumed to be 0 [2, 33].

### 3.4 Constraint-based methods for wheel-rail contact

The multibody contact modelling of railway vehicles is presented as the final application in this thesis. In this section, two constraint-based formulations for the wheel-rail contact simulation in multibody dynamics are presented; (1) the use of contact lookup tables and (2) the KEC-method. A more detailed description of the above two methods can be found in [10, 11].

#### Contact lookup table method

Lookup tables are calculated in a preprocessing stage. For each of the wheelset positions, six simplified contact constraints Eq. (2.18) (3 for left contact and three for right contact) are solved to find the values of six coordinates: the wheelset position and orientation coordinates  $z^{wi}$  and roll angle  $\varphi^{wi}$  and the transverse and angular wheel surface parameters  $s_1^w$  and  $s_2^w$ , and longitudinal and transverse rail surface parameter  $s_1^r$  and  $s_2^r$ , which are needed to locate the contact points on the left and right contact surfaces. Thus a set of discrete numerical values is assigned to the lateral displacement of the wheelset  $y^{wi}$  and track gauge variation  $\xi_g$ , to create a contact lookup table:

$$\begin{aligned} z^{wi} &= z_{clt}(y^{wi}, \xi_g), & \varphi^{wi} &= \varphi_{clt}(y^{wi}, \xi_g) \\ s^{lw} &= s_{clt}^{lw}(y^{wi}, \xi_g), & s^{lr} &= s_{clt}^{lr}(y^{wi}, \xi_g) & s^{rw} &= s_{clt}^{rw}(y^{wi}, \xi_g), & s^{rr} &= s_{clt}^{rr}(y^{wi}, \xi_g) \end{aligned} \quad (3.35)$$

where the subscript *clt* stands for ‘contact lookup table’. Fig. 3.7 shows the example of the lookup table of wheelset vertical displacement coordinate  $z^{wi}$  with respect to the track centreline within a range of track gauge variations  $\xi_g$ . The results comes from the wheel-rail profile combination of S1002 wheel profile and LB-140-Area rail profile

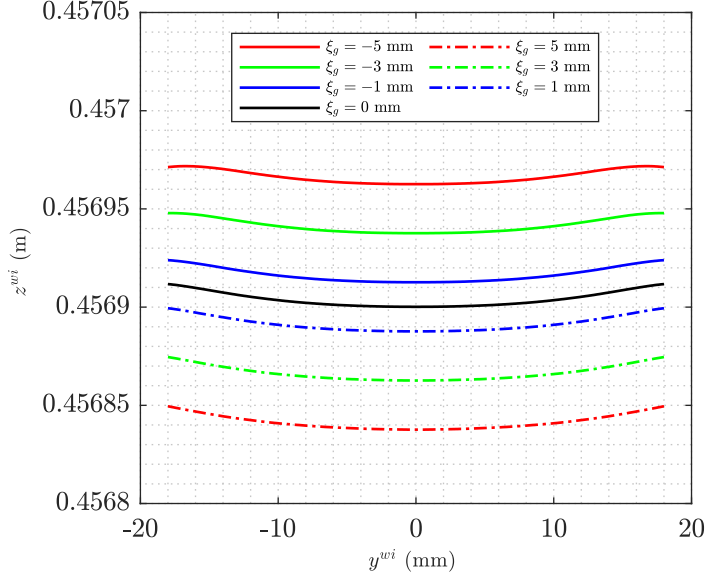


**Figure 3.7.** Wheelset vertical displacement with respect to track centreline for different values of gauge irregularity for the wheel-rail profile combination of S1002 wheel profile and LB-140-Area rail profile.

In a dynamic simulation, given the longitudinal position of the wheelset  $s^{wi}$ , the values of the track irregularities  $\xi_a$ ,  $\xi_v$ ,  $\xi_g$  and  $\xi_c$  can be obtained (see Section 2.2). The lateral displacement that has to be used to enter the lookup table is not  $y^{wi}$  which gives the lateral displacement with respect to the ideal track centreline, but  $\bar{y}^{wi}$  that gives the lateral displacement with respect to the irregular track centreline:

$$\bar{y}^{wi} = y^{wi} - \xi_a \quad (3.36)$$

In turn, the outputs of the lookup table  $\bar{z}^{wi}$  and  $\bar{\varphi}^{wi}$  have to be interpreted differently, being  $\bar{z}^{wi} = z^{wi} + \xi_v$  and  $\bar{\varphi}^{wi} = \varphi^{wi} + \xi_c/2L_r$ . The kinematic constraints associated with wheelset  $wi$  finally yield

$$\mathbf{C}^{cvt,wi} = \begin{bmatrix} z^{wi} - \xi_v - z_{cvt}(\bar{y}^{wi} + \xi_a, \xi_g) \\ \varphi^{wi} - \xi_c/2L_r - \varphi_{cvt}(\bar{y}^{wi} + \xi_a, \xi_g) \end{bmatrix} = \mathbf{0}. \quad (3.37)$$

The position along the track  $s^{wi}$  and pitch angle  $\theta^{wi}$  in this method are assumed to be zero. That is due to these coordinates have no influence on the contact geometry. In addition, since the negligible influence on the contact geometry, the

yaw angle  $\psi^{wi}$  is assumed to be zero. More details in railway multibody simulation using contact lookup tables can be found in [10].

With using lookup table method, normal contact forces in the tread are computed as reaction forces associated with the contact constraints, while normal contact forces at flange are calculated as elastic forces as a function of the wheel-rail penetration. For tread and flange contact, tangential contact forces are computed as applied forces using any established creep contact theory (as Kalker non-linear theory [23] or Polach theory [36]).

The resulting equations of motion of the railway vehicle yield:

$$\begin{aligned} \mathbf{M}\ddot{\mathbf{q}} + (\mathbf{C}_{\mathbf{q}}^{clu})^T \boldsymbol{\lambda} &= \mathbf{Q} + \mathbf{Q}_{fla}^{nor} + \mathbf{Q}^{tang} \\ \mathbf{C}^{clu} &= \mathbf{0} \end{aligned} \quad (3.38)$$

where  $\mathbf{M}$  is the vehicle mass matrix,  $\mathbf{C}_{\mathbf{q}}^{clu}$  is the Jacobian matrix of all wheel-rail contact constraints modelled with lookup tables,  $\boldsymbol{\lambda}$  is the array of Lagrange multipliers,  $\mathbf{Q}_{fla}^{nor}$  is the vector of generalized wheel-rail normal flange forces, and  $\mathbf{Q}^{tang}$  is the vector of generalized tangential tread and flange forces.  $\mathbf{Q}$  includes all other generalized applied forces and generalized quadratic-velocity inertial forces.

The generalized normal forces at the wheel tread are computed using the method of Lagrange multipliers. Therefore, these forces are treated as reaction forces whose value can be computed as

$$\mathbf{Q}_{tread}^{nor} = -(\mathbf{C}_{\mathbf{q}}^{clu})^T \boldsymbol{\lambda}. \quad (3.39)$$

In this research, the flange normal contact force at wheelset  $i$  ( $wi$ ) is computed based on a Hunt-Crossley force model [10, 30, 20], including the elastic and dissipative components:

$$\begin{aligned} \mathbf{Q}_{fla}^{nor,wi} &= \left( \frac{\partial g^{wi}}{\partial \mathbf{q}^{wi}} \right)^T f_{fla}^{nor,wi}, \\ f_{fla}^{nor,wi} &= \begin{cases} K_{hertz}(g^{wi})^{3/2} + C_{damp}\dot{g}^{wi}g^{wi} & \text{if } g^{wi} > 0 \\ \mathbf{0} & \text{if } g^{wi} \leq 0 \end{cases}, \end{aligned} \quad (3.40)$$

where  $\bar{\mathbf{r}}_{fla}^{wi}$  is the position vector of the contact point in the flange,  $\frac{\partial g^{wi}}{\partial \mathbf{q}^{wi}}$  is the partial derivative of penetration  $g^{wi}$  with respect to wheelset coordinates, vector  $f_{fla}^{nor,wi}$  is the elastic normal force in the flange,  $g^{wi}$  is the wheel-rail penetration at

the flange contact,  $\dot{g}^{wi}$  is the relative velocity between wheel flange and rail head. Note that the terms  $\bar{\mathbf{r}}_{fla}^{wi}$ ,  $g^{wi}$  and  $K_{hertz}$  are interpolated from the lookup table. The position vector  $\bar{\mathbf{r}}_{fla}^{wi}$  appearing in Eq. (3.40) is given by:

$$\bar{\mathbf{r}}_{fla}^{wi} = \bar{\mathbf{r}}^{wi} + \mathbf{A}^{wti,wIi} \hat{\mathbf{u}}_{fla}^{wiI}, \quad (3.41)$$

where  $\hat{\mathbf{u}}_{fla}^{wiI}$  is the position vector of flange contact point with respect to wheelset intermediate frame.

### KEC method

In KEC-method, an equivalent wheel profile that contacts a infinitely narrow rail provides the same wheelset kinematics than the real wheel-rail profiles. As shown in Fig. 3.8, the sketch on the upper-left is the real wheel-rail profiles combination while the sketch on the upper-right is the KEC profile. For each real wheel-rail profiles combination, the non-real KEC wheel equivalent profiles can be found, as shown in the lower part of the same figure.

Compared to the approximate contact constraint in Eq. (2.18), the contact constraint equations of a wheelset with KEC profiles have a simpler form. That is due to only the condition of the coincidence of two contact points belonging to the wheel and rail surfaces has to be fulfilled, and the orthogonality condition for the normal and tangential vectors of two contact surfaces is not considered into KEC constraint [11]. Thus, the KEC constraint equations are given by:

$$\mathbf{C}^{KEC,wi}(\mathbf{q}^{wi}, \mathbf{s}^k) = \begin{bmatrix} 0 & r_0 + f^{lk} & 1 & 0 \\ 0 & r_0 + f^{rk} & 0 & 1 \\ 1 & L_w & \varphi^{wi} & 0 \\ 1 & -L_w & 0 & \varphi^{wi} \end{bmatrix} \begin{bmatrix} \bar{z}^{wi} \\ \varphi^{wi} \\ s^{lk} \\ s^{rk} \end{bmatrix} - \begin{bmatrix} y^{wi} - y^{lir} \\ y^{wi} - y^{rir} \\ -f^{lk} - z^{lir} \\ -f^{rk} - z^{rir} \end{bmatrix} \quad (3.42)$$

where  $\mathbf{s}^k = [s^{lk} \quad s^{rk}]^T$  are the lateral positions of the contact point on the left and right KEC profiles,  $f^{lk}$  and  $f^{rk}$  are the value of the equivalent profiles at these locations (see lower part of the Fig. 3.8), and  $r_0$  is the rolling radius of the wheel when centered in the track.

Considering all the developments shown in this chapter, the equations of motion of the railway vehicle by using the KEC method can also be written in the following DAE form:

$$\begin{aligned} \mathbf{M}\ddot{\mathbf{q}} + \mathbf{N}\lambda &= \mathbf{Q} + \mathbf{Q}^{tang} \\ \mathbf{C}^{KEC} &= \mathbf{0} \end{aligned} \quad (3.43)$$

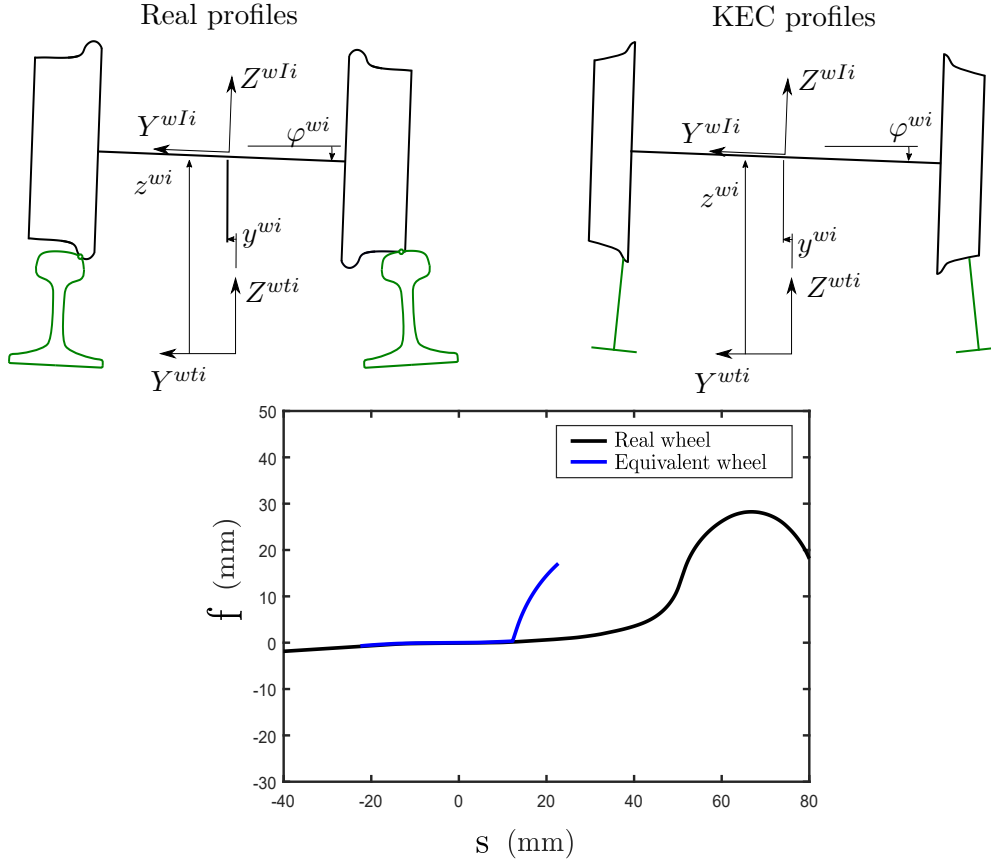


**Figure 3.8.** *Publication IV:* Real profile and KEC wheel profile.

where matrices  $\mathbf{N}$  represents the direction of the reaction forces, which is associated with all the wheelsets in the vehicle,  $\mathbf{C}^{KEC}$  is KEC constraint equations. More detailed information related to the above matrices can be found in [13].

In the classical method of the Lagrange multipliers, the rows of the Jacobian matrix provide the direction of the reaction forces in the space of the generalized coordinates, while the multipliers mean the number that these rows have to be multiplied by to obtain the generalized reaction forces. In the problem at hand, the Jacobian matrix is not needed to find the direction of the reaction forces, because these directions are known in advance: the normal vectors to the real wheel profiles. Therefore, the reaction forces for wheelset  $wi$  can be obtained as:

$$\mathbf{Q}^{nor} = - \begin{bmatrix} \bar{\mathbf{n}}_{lw} & \bar{\mathbf{n}}_{rw} \\ \hat{\mathbf{r}}_{lw} \times \hat{\mathbf{n}}_{lw} & \hat{\mathbf{r}}_{rw} \times \hat{\mathbf{n}}_{rw} \end{bmatrix} \begin{bmatrix} \lambda_{lw}^{wi} \\ \lambda_{rw}^{wi} \end{bmatrix} = -\mathbf{N}^{wi} \boldsymbol{\lambda}^{wi} \quad (3.44)$$

where the vector of Lagrange multipliers  $\lambda^{wi}$  represents the magnitude of the normal contact forces at the left and right wheels.



---

## Summary of findings

Different contact approaches were considered in rigid and flexible multibody dynamics first, followed by studies on the wheel-rail contact in multibody dynamic simulation of railway vehicles. This chapter summarizes the results obtained in *Publication I, II, III*, and *IV*, and has been divided into two main sections.

### 4.1 Cone complementarity method versus penalty method

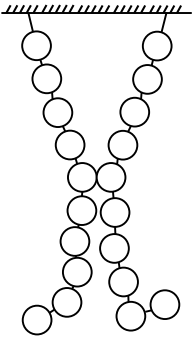
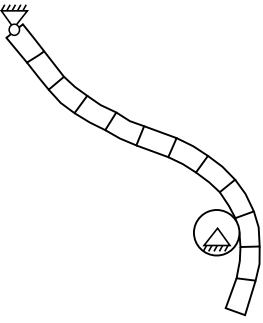
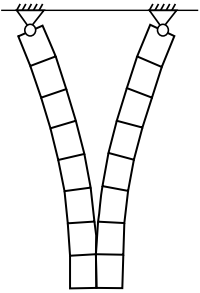
The cone complementarity method (CCP) and penalty method for the simulation of rigid and flexible multibody systems were studied and compared in the first three publications. For this purpose, three different contact types; (1) rigid-to-rigid, (2) rigid-to-flexible and (3) flexible-to-flexible, were constructed to evaluate the proposed methods. The main information of contact studies are listed in Tab. 4.1.

#### Rigid-to-rigid contact

*Publication I* introduces two planar approaches based on the cone complementarity problem (CCP) and penalty method. To this end, two planar approaches based on the CCP and penalty method are employed and applied to a practical problem of granular chains, as shown in the first figure of Tab. 4.1.

A simple case of two pendulums with two balls has been analyzed to compare both approaches. With specified contact stiffness and damping coefficients for penalty method, the results of Y-displacement of the rigid ball can lead to identical results. In addition, the energy changes instantly as shown in Fig. 4.1 (a). That is due to the nonlinear behavior of the CCP approach. However, the energy changes

**Table 4.1.** Notes of contact studies for CCP method versus penalty method

CONTACT CASES	MULTIBODY APPLICATIONS	NOTES
Rigid-to-rigid		<ul style="list-style-type: none"> <li>• Dynamic numerical examples of two-pendulum with two rigid balls and two rigid granular pendulums</li> <li>• For the penalty method, contact stiffness coefficient <math>K_{hertz} = 3.6 \cdot 10^5 \text{ N/m}^{1.5}</math></li> <li>• Implemented in <i>Publication I</i></li> </ul>
Rigid-to-flexible		<ul style="list-style-type: none"> <li>• Dynamic numerical examples of ANCF beam contact with rigid ground, rigid body with an arbitrary shape and pendulum contact</li> <li>• For the penalty method, contact stiffness coefficient <math>K_{hertz} = 3.13 \cdot 10^7 \text{ N/m}^{1.5}</math></li> <li>• Implemented in <i>Publication II</i></li> </ul>
Flexible-to-flexible		<ul style="list-style-type: none"> <li>• Dynamic numerical examples of side-to-side, corner-to-side, corner-to-corner contact, and self-contact</li> <li>• For the penalty method, contact stiffness coefficient <math>K_{hertz} = 4.07 \cdot 10^7 \text{ N/m}^{1.5}</math></li> <li>• Implemented in <i>Publication III</i></li> </ul>

in Fig. 4.1 (b) is a continuous with using the penalty method. In addition, the results of the granular chains demonstrated that CCP is a computationally feasible approach for a planar case with multiple contacts.

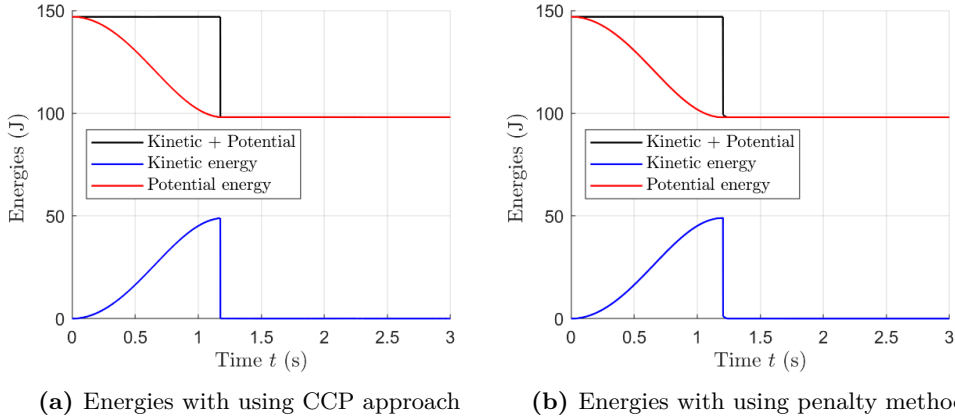


**Figure 4.1.** *Publication I:* Energies of two-pendulum contact with using both approaches.

### Rigid-to-flexible contact

The contact problems can be solved with reasonably acceptable accuracy when using the complementarity approach. However, this approach is often limited to rigid body contacts [1, 51, 52]. For this reason, the continuation of *Publication I*, *Publication II* extends the CCP approach to flexible bodies in the planar contact case, as shown in the second figure of Tab. 4.1. Beam elements based on the absolute nodal coordinate formulation (ANCF), are implemented to consider the large deformations. To make a comparison of the penalty method and the CCP approach under the same coefficient of restitution, the damping component is introduced in the penalty method with using the continuous contact model [20].

In the CCP approach, the contact is considered to be inelastic, thus the coefficient of restitution is assumed to be 0 [2, 33]. To obtain the identical Y displacement of the beam from both approaches, the stiffness constant for continuous contact force model (Eq. (3.14)) needs to be regularized by the factor  $\alpha$  as:

$$K_{reg} = \alpha K_{hertz} \quad (4.1)$$

To this end, the results of Y-displacement and velocity of the beam using the penalty method with  $c_r = 0$  and cone complementarity approach, lead to identical results with the corrector factor  $\alpha = 3.8$  in Eq. (4.1). Comparing the normal penetration for both methods, the unphysical interpenetration is observed during

the contact event by using the penalty method only. This is due to the nonlinear minimization problem being solved in CCP approach. The total energy of the system is minimized by considering the potential, kinetic and strain energy associated with the contact constraint. Furthermore in CCP approach, the non-penetration constraints prevent the ANCF beam from penetrating into the ground and the beam exerting pressure on the ground due to the contact force. For this reason, the normal contact force from CCP approach is 25 times bigger than penalty method. In addition, the computational efficiency results show that there were no significant differences between the two approaches.

### Flexible-to-flexible contact

As the extension of *Publication II*, *Publication III* aims to propose a contact procedure for the beam to beam contact (see the last figure Tab. 4.1). The method is applied with linear complementarity condition (LCP) and the penalty to enforce the contact constraint. In addition, a novel contact detection algorithm, which is based on the oriented bounding box (OBB) approach is developed. Different contact cases, as side-to-side (segment-to-segment), corner-to-side (point-to-segment), and corner-to-corner (point-to-point) contact scenarios, are presented in *Publication III*.

The numerical results of normal penetration indicate that the evaluation of gap function with the LCP and penalty methods is in close agreement with their values. Meanwhile, the trajectory comparison results show that solutions for the beam with the LCP and penalty method are in close agreement. The computational efficiency between both methods was compared in Tab. 4.2. The results show that the optimization based approach in evaluating the contact force components in LCP method is more efficient than the classic Newton iterative solver used with the penalty method. That is due to the fact that the whole motion differential equation in penalty method is iteratively evaluated per contact event within a time integration step and the re-evaluation in each Newton iteration slows down the computational efficiency.

In the last example, a highly flexible beam undergoing multiple self-contact events is studied. The example parameters were adapted from "flying spaghetti" in [46] As shown in Fig. 4.2, the self contact events including sliding and non-frictional contacts occur several times during the simulation from  $t = 2.84$  s.

## 4.2 Two constraint-based contact methods for wheel-rail contact simulation

In multibody dynamic simulation of railway vehicles, the modelling of wheel-rail contact plays a fundamental role through the literature. Hence, *Publication IV*

## 4.2 Two constraint-based contact methods for wheel-rail contact simulation61

**Table 4.2.** *Publication III:* CPU and the elapsed time with the evaluation of the functions associated with the Newton and Lemke’s solvers when the penalty and LCP methods are respectively used for simulation of the corner-to-side contact problem. Eight beams discretization is used with the simulation.

Elapsed time	LCP (s)	Penalty (s)
Total simulation until the end of 1 <sup>st</sup> contact event	13.947	53.9697
Function evaluation during the 1 <sup>st</sup> contact event	Lemke’s algorithm: 0.012	Newton solver: 39.76

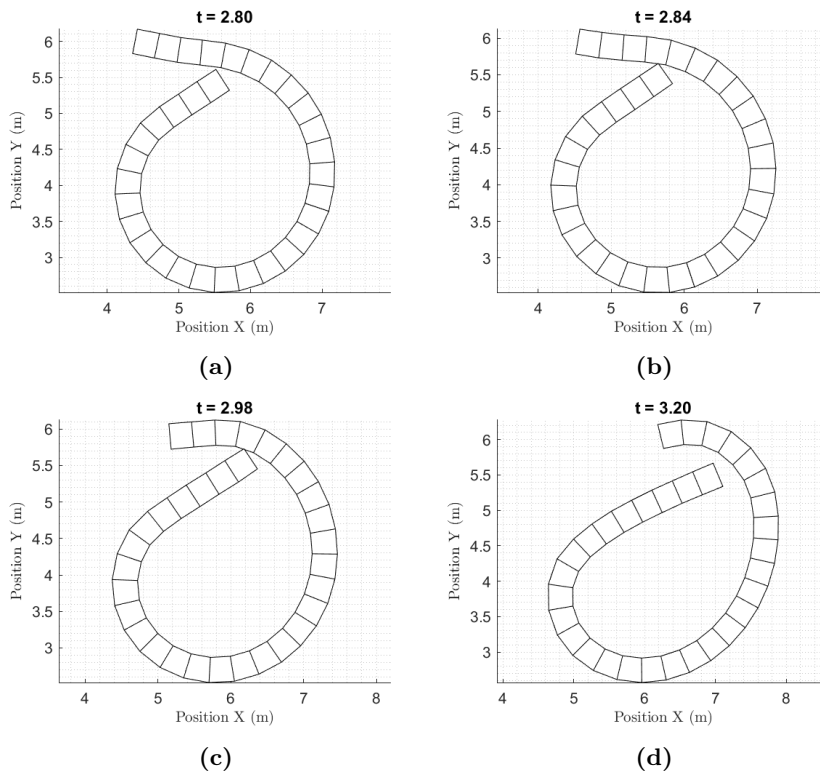


**Figure 4.2.** *Publication III:* Snapshots of the self-contact events in the flying spaghetti problem in the simulation when using the penalty methods. The number of meshes in beam is 32.

analyzed the differences between two constraint-based contact models, the lookup table, and the KEC-method. For this purpose, a numerical comparison of three different case studies is presented: (1) simulation in irregular track with a wheel-rail profile combination that does not show 2-point contact, (2) simulation in irregular

track with a wheel-rail profile combination that shows 2-point contact, and (3) a wheelset climbing and derailment scenario with a wheel-rail profile combination that shows 2-point contact. A three-body suspended vehicle consists two wheelsets and a bogie frame is studied in all cases. Analytical expressions of the power spectral density functions (PSD) [8] is used to generate track irregularities.

The proposed first case study considers a wheel-rail profile combination that does not show 2-point contacts, which is used by the metropolitan train of the city of Seville (see Fig. 4.3). The comparison results of kinematics and normal contact forces for the wheelsets show that, the results of both approaches are almost identical with 1-point contact case. In this example, normal contact forces of both approaches are treated as reaction forces using Eq. (3.39), that is due to there is always a unique contact point per wheel-rail pair. Furthermore, the right wheel for both wheelsets experiences a higher normal contact force than the left one, When the vehicle negotiates the left curve.

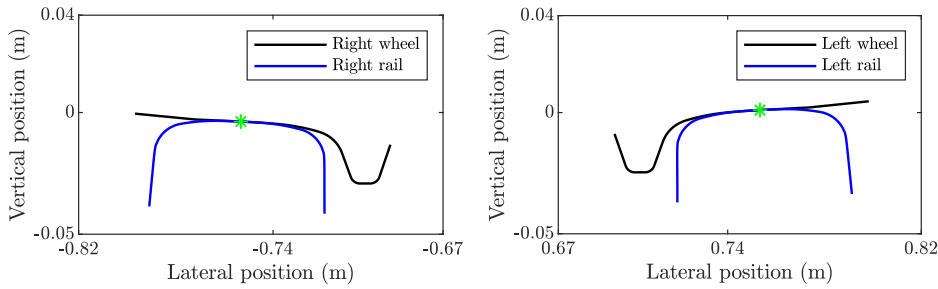


**Figure 4.3.** *Publication IV:* Wheel-rail profile combination which does not show two point contacts (used by the metropolitan train of the city of Seville).

The second case study is the same bogie vehicle whose wheelsets use a wheel-rail profile combination that shows two-point contacts (S1002 wheel profile and LB-140-Area rail profile), as shown in Fig. 4.4. The flange contact stiffness parameter plays an important role to control the simulations with using the lookup table method and hybrid contact approach, when two-point wheel-rail contact scenarios occur. According to the wheel-rail profile combination shown in Fig. 4.4, the Hertzian stiffness at the flange contact point can be calculated with using the Hertz contact theory as  $K_{hertz} = 7.7075 \cdot 10^{13} \text{ N/m}^{1.5}$ . However, the numerical results show that the Hertzian stiffness that is close to  $7.075 \cdot 10^{13} \text{ N/m}^{1.5}$  may lead the time integrators to stall during the simulation. A low value for the stiffness such as  $K_{hertz} = 1 \cdot 10^9 \text{ N/m}^{1.5}$ , will lead to relatively smooth even with multiple flange contacts and good computation efficiency. But the results of flange to rail-head indentations may be large that can be considered as being physically inadmissible.

## 4.2 Two constraint-based contact methods for wheel-rail contact simulation63

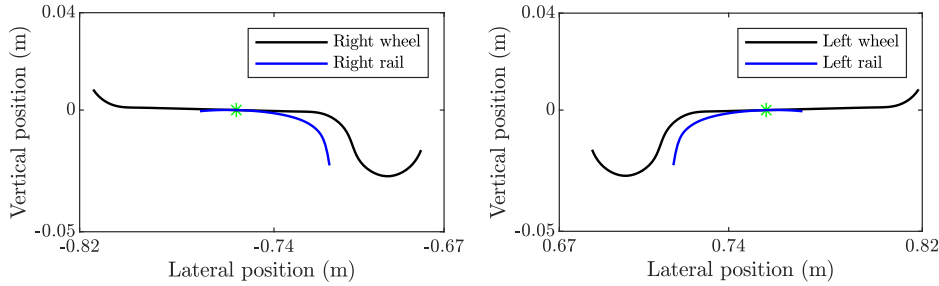


**Figure 4.4.** *Publication IV:* Wheel-rail profile combination which shows two point contact (S1002 wheel profile and LB-140-Area rail profile).

To obtain physically admissible indentations and improve computation efficiency of the vehicle simulation, the Hertzian parameters for the flange contact are chosen as constant values of  $K_{hertz} = 1 \cdot 10^{10} \text{ N/m}^{1.5}$  and  $C_{damp} = 1 \cdot 10^8 \text{ N} \cdot \text{s/m}^2$ , for the lookup table approach.

With 2-point contact case, the resulting lateral displacements are quite similar using both approaches with slight differences observable in the yaw angles. Since different contact approaches (constrained in the KEC-method, elastic in the lookup table method) used in the wheel flange area, the comparison of normal contact forces shows that the normal contact forces at the right tread and flange differ when the wheelset is negotiating the curve.

Wheel climbing and derailment phenomenon may occur, when the vehicle is running at a high forward velocity or on a small radius curve. That is due to the large angle of attack is generated by the friction force. The derailment studies using both approaches are presented as the last case study. The wheelset climbing scenario during the simulation is depicted in Fig. 4.5. Accordingly, the configurations of the rear left wheel in the contact point section is shown in the same figure with different wheelset lateral displacements. It can be observed that the wheel is completely moved up to the top of the rail when the lateral displacement increases, which agrees with the results proposed in [48].

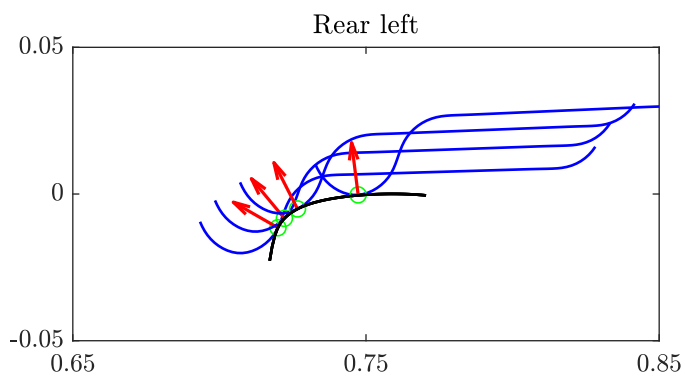


**Figure 4.5.** *Publication IV:* Wheel/rail contact in point section with different wheelset lateral displacement during the simulation.

---

## Conclusions

This dissertation discussed the contact applications associated with the dynamic simulation of rigid and flexible multibody systems. Contact examples for such applications include rigid granular contact, flexible beam contact, and wheel-rail contact. The pros and cons of the penalty, complementarity, and constraint-based methods are compared and analyzed. It was found that the complementarity approach and penalty method can achieve good agreement of kinematics with the applications of rigid and/or flexible multibody bodies. Meanwhile, two constraint-based methods for wheel-rail contact simulation provide close dynamic behavior and normal contact forces.

Different contact applications involving rigid and flexible multibody dynamics are analyzed from *Publications I-III* to compare the complementarity approach and penalty method. *Publication I* applies both approaches to a practical problem of granular chains. The results indicate that both methods can achieve good convergence for vertical position, when the contact stiffness and damping coefficients are specified. In addition, the results of granular pendulum demonstrated that CCP is a computationally feasible approach for a planar case with multiple contacts.

In general, the CCP approach is often limited to rigid body contacts because of high computational cost. *Publication II* and *III* extends the scientific knowledge of both approaches in the framework of flexible multibody dynamics. In *Publication II*, the CCP approach was compared against the penalty method with respect to kinematics, contact penetrations and contact forces. The Hertzian stiffness parameter in penalty method is regularized by a correction factor. Both approaches can achieve the same kinematic results in the case of flexible-to-rigid contact. In the penalty method, the structural deformation of the beam is ignored by allowing a penetration in the contact process. However, in the CCP approach, the penetration is prevented with using the nonlinear minimization problem. In addition, two

approaches have similar computation efficiency in the numerical results. To avoid penetration when using the penalty method, *Publication III* makes use of an internal iteration scheme based on Newton's iteration method to fulfill the criteria for minimal penetration. The results show that penetration based on the penalty method and the complementarity approach are in acceptable agreement (both are under 0.5 mm) in the case of flexible-to-flexible contact. However, the optimization based complementarity problem approach is computationally more economical than Newton's iteration method used with the penalty method.

Contact lookup tables and KEC-method for the wheel-rail contact simulation are introduced and compared in *Publication IV*. As displayed in the numerical results, both approaches provide similar dynamic behavior and normal contact forces for 1-point contact and 2-point contact wheel-rail profile combination in the presence of track irregularities. However, the KEC-method is able to predict derailment while the lookup-hybrid method only predicts a permanent and stable flange contact. Therefore, the KEC-method can be considered as being superior compare to lookup table method, when doing safety analysis.

### **Suggestions for future work**

There are several research topics where the work presented in this dissertation can be extended.

The CCP method for the flexible body simulation presented in *Publication II* and *III* could be extended to include 3D contact. A 3D ANCF beam with deformable cross sections could be used to analyze large deformations in multibody applications, such as cloth simulations, and rope knotting.

Similarly, the KEC method proposed in *Publication IV* can be extended with one more dimension. The result could be used to analyze lead-lag contact phenomena. Moreover, the KEC method could be also used for wheel wear analysis, safety analysis, and the analysis of comfort.

---

## REFERENCES

---

- [1] ANITESCU, M. Optimization-based simulation of nonsmooth rigid multibody dynamics. *Mathematical Programming* 105, 1 (2006), 113–143.
- [2] ANITESCU, M., POTRA, F. A., AND STEWART, D. E. Time-stepping for three-dimensional rigid body dynamics. *Computer Methods in Applied Mechanics and Engineering* 177, 3–4 (1999), 183–197.
- [3] ANITESCU, M., AND TASORA, A. An iterative approach for cone complementarity problems for nonsmooth dynamics. *Computational Optimization and Applications* 47, 2 (2010), 207–235.
- [4] BERZERI, M., CAMPANELLI, M., AND SHABANA, A. A. Definition of the elastic forces in the finite element absolute nodal coordinate formulation and the floating frame of reference formulation. *Multibody System Dynamics* 5, 1 (2001), 21–54.
- [5] BOSO, D., LITEWKA, P., SCHREFLER, B., AND WRIGGERS, P. A 3D beam-to-beam contact finite element for coupled electric-mechanical fields. *International Journal for Numerical Methods in Engineering* 64, 13 (2005), 1800–1815.
- [6] BOZORGMEHRI, B., YU, X., MATIKAINEN, M. K., HARISH, A. B., AND MIKKOLA, A. A study of contact methods in the application of large deformation dynamics in self-contact beam. *Nonlinear Dynamics* 103, 1 (2021), 581–616.
- [7] BRAUN, M. On some properties of the multiple pendulum. *Archive of Applied Mechanics* 72, 11-12 (2003), 899–910.
- [8] CLAUS, H., AND SCHIEHLEN, W. Modeling and simulation of railway bogie structural vibrations. *Vehicle System Dynamics* 29, S1 (1998), 538–552.
- [9] DAO, N. D., RYAN, K. L., SATO, E., AND SASAKI, T. Predicting the displacement of triple pendulum<sup>TM</sup> bearings in a full-scale shaking experiment

- using a three-dimensional element. *Earthquake Engineering & Structural Dynamics*, 42, 11 (2013), 1677–1695.
- [10] ESCALONA, J. L., AND ACEITUNO, J. F. Multibody simulation of railway vehicles with contact lookup tables. *International Journal of Mechanical Science* 155 (2019), 571–582.
- [11] ESCALONA, J. L., ACEITUNO, J. F., URDA, P., AND BALLING, O. Railway multibody simulation with the knife-edge-equivalent wheel–rail constraint equations. *Multibody System Dynamics* 48, 4 (2020), 373–402.
- [12] ESCALONA, J. L., HUSSIEN, H. A., AND SHABANA, A. A. Application of the absolute nodal co-ordinate formulation to multibody system dynamics. *Journal of Sound and Vibration* 214, 5 (1998), 833–851.
- [13] ESCALONA, J. L., YU, X., AND ACEITUNO, J. F. Wheel-rail contact simulation with lookup tables and KEC profiles: A comparative study. *Multibody System Dynamics* (2020), 1–37.
- [14] FISCHER, A. A special newton-type optimization method. *Optimization* 24, 3-4 (1992), 269–284.
- [15] FISCHER, K. A., AND WRIGGERS, P. Frictionless 2D contact formulations for finite deformations based on the mortar method. *Computational Mechanics* 36, 3 (2005), 226–244.
- [16] FLORES, P., MACHADO, M., SILVA, M., AND MARTINS, J. On the continuous contact force models for soft materials in multibody dynamics. *Multibody System Dynamics* 25, 3 (2011), 357–375.
- [17] GOLDSMITH, W., AND FRASIER, J. T. *Impact: The theory and physical behaviour of colliding solids*. Edward Arnold Ltd., London, England, 1960.
- [18] GONTHIER, Y., MCPHEE, J., LANGE, C., AND PIEDBAUF, J. C. A regularized contact model with asymmetric damping and dwell-time dependent friction. *Multibody System Dynamics* 11, 2 (2004), 209–233.
- [19] HARISH, A. B., AND WRIGGERS, P. Modeling of two-body abrasive wear of filled elastomers as a contact-induced fracture process. *Tribology International* 138 (2019), 16–31.
- [20] HUNT, K. H., AND CROSSLEY, F. R. E. Coefficient of restitution interpreted as damping in vibroimpact. *Journal of Applied Mechanics* 42, 2 (1975), 440–445.
- [21] HUNĚK, I. On a penalty formulation for contact-impact problems. *Computers & structures* 48, 2 (1993), 193–203.

- [22] JAEGER, H. M., NAGEL, S. R., AND BEHRINGER, R. P. Granular solids, liquids, and gases. *Reviews of Modern Physics* 68, 4 (1996), 1259–1273.
- [23] KALKER, J. *Three dimensional elastic bodies in rolling contact*. Kluwer Academic Publishers, Dordrecht/Boston/London, 1990.
- [24] KHUDE, N., STANCIULESCU, I., MELANZ, D., AND NEGRUT, D. Efficient parallel simulation of large flexible body systems with multiple contacts. *Journal of Computational and Nonlinear Dynamics* 8, 4 (2013), 041003.
- [25] KHUDE, N. N. *Efficient simulation of flexible body systems with frictional contact/impact*. PhD thesis, The University of Wisconsin-Madison, 2015.
- [26] LANKARANI, H. M., AND NIKRAVESH, P. E. A contact force model with hysteresis damping for impact analysis of multibody systems. *Journal of Mechanical Design* 112, 3 (1990), 369–376.
- [27] ŁITEWKA, P. Hermite polynomial smoothing in beam-to-beam frictional contact. *Computational Mechanics* 40, 5 (2007), 815–826.
- [28] ŁITEWKA, P. Enhanced multiple-point beam-to-beam frictionless contact finite element. *Computational Mechanics* 52, 6 (2013), 1365–1380.
- [29] ŁITEWKA, P., AND WRIGGERS, P. Frictional contact between 3D beams. *Computational Mechanics* 28, 1 (2002), 26–39.
- [30] MACHADO, M., MOREIRA, P., FLORES, P., AND LANKARANI, H. M. Compliant contact force models in multibody dynamics: Evolution of the hertz contact theory. *Mechanism and Machine Theory* 53 (2012), 99–121.
- [31] MARQUES, F., MAGALHÃES, H., POMBO, J., AMBRÓSIO, J., AND FLORES, P. A three-dimensional approach for contact detection between realistic wheel and rail surfaces for improved railway dynamic analysis. *Mechanism and Machine Theory* 149 (2020), /103825.
- [32] NACHBAGAUER, K., PECHSTEIN, A. S., IRSCHIK, H., AND GERSTMAYR, J. A new locking-free formulation for planar, shear deformable, linear and quadratic beam finite elements based on the absolute nodal coordinate formulation. *Multibody System Dynamics* 26, 3 (2011), 245–263.
- [33] NEGRUT, D., SERBAN, R., AND TASORA, A. Posing multibody dynamics with friction and contact as a differential complementarity problem. *Journal of Computational and Nonlinear Dynamics* 13, 1 (2018), 014503.
- [34] NIGMATULLIN, R. R., OSOKIN, S. I., AWREJCEWICZ, J., WASILEWSKI, G., AND KUDRA, G. The fluctuation spectroscopy based on the scaling

- properties of beta-distribution: analysis of triple pendulum data. *Mechanical Systems and Signal Process* 52–53 (2015), 278–292.
- [35] PLAUT, R. H., AND VIRGIN, L. N. Pendulum models of ponytail motion during walking and running. *Journal of Sound and Vibration* 332, 16 (2013), 3768–3780.
- [36] POLACH, O. Creep forces in simulations of traction vehicles running on adhesion limit. *Wear* 258, 7-8 (2005), 992–1000.
- [37] POMBO, J., AND AMBRÓSIO, J. Application of a wheel–rail contact model to railway dynamics in small radius curved tracks. *Multibody System Dynamics* 19, 1 (2008), 91–114.
- [38] POMBO, J., AND AMBRÓSIO, J. An alternative method to include track irregularities in railway vehicle dynamic analyses. *Nonlinear Dynamics* 68, 1 (2012), 161–176.
- [39] POMBO, J., AMBRÓSIO, J., AND SILVA, M. A new wheel–rail contact model for railway dynamics. *Vehicle System Dynamics* 45, 2 (2007), 165–189.
- [40] PUSO, M. A., AND LAURSEN, T. A. A mortar segment-to-segment contact method for large deformation solid mechanics. *Computer Methods in Applied Mechanics and Engineering* 193, 6-8 (2004), 601–629.
- [41] PUSO, M. A., AND LAURSEN, T. A. A mortar segment-to-segment frictional contact method for large deformations. *Computer Methods in Applied Mechanics and Engineering* 193, 45-47 (2004), 4891–4913.
- [42] PUSO, M. A., LAURSEN, T. A., AND SOLBERG, J. A segment-to-segment mortar contact method for quadratic elements and large deformations. *Computer Methods in Applied Mechanics and Engineering* 197, 6-8 (2008), 555–566.
- [43] SHABANA, A. A. Definition of the slopes and the finite element absolute nodal coordinate formulation. *Multibody System Dynamics* 1, 3 (1997), 339–348.
- [44] SHABANA, A. A. *Computational dynamics*. John Wiley & Sons, Inc, 2009.
- [45] SHABANA, A. A., ZAAZAA, K. E., AND SUGIYAMA, H. *Railroad vehicle dynamics: a computational approach*. CRC press, 2007.
- [46] SIMO, J. A finite strain beam formulation, the three-dimensional dynamic problem. Part I. *Computer Methods in Applied Mechanics and Engineering* 49, 1 (1985), 55–70.

- [47] SUGIYAMA, H., ARAKI, K., AND SUDA, Y. On-line and off-line wheel/rail contact algorithm in the analysis of multibody railroad vehicle systems. *Journal of Mechanical Science and Technology* 23, 4 (2009), 991–996.
- [48] SUGIYAMA, H., SEKIGUCHI, T., MATSUMURA, R., YAMASHITA, S., AND SUDA, Y. Wheel/rail contact dynamics in turnout negotiations with combined nodal and non-conformal contact approach. *Multibody System Dynamics* 27, 1 (2012), 55–74.
- [49] SUGIYAMA, H., AND SUDA, Y. On the contact search algorithms for wheel/rail contact problems. *Journal of Computational and Nonlinear Dynamics* 4, 4 (2009), /041001.
- [50] SUN, D., LIU, C., AND HU, H. Dynamic computation of 2D segment-to-segment frictional contact for a flexible multibody system subject to large deformations. *Mechanism and Machine Theory* 158 (2021), /104197.
- [51] TASORA, A., AND ANITESCU, M. A fast NCP solver for large rigid-body problems with contacts, friction, and joints. *Multibody dynamics. Springer, Dordrecht* (2009), 45–55.
- [52] TASORA, A., AND ANITESCU, M. A matrix-free cone complementarity approach for solving large-scale, nonsmooth, rigid body dynamics. *Computer Methods in Applied Mechanics and Engineering* 200, 5-8 (2011), 439–453.
- [53] TASORA, A., NEGRUT, D., AND ANITESCU, M. Large-scale parallel multibody dynamics with frictional contact on the graphical processing unit. *Proceedings of the Institution of Mechanical Engineers, Part K: Journal of Multi-body Dynamics* 222, 4 (2008), 315–326.
- [54] WRIGGERS, P. *Computational Contact Mechanics*, 2 ed. Springer-Verlag, Berlin, Heidelberg, 2006.
- [55] WRIGGERS, P., AND ZAVARISE, G. On contact between three-dimensional beams undergoing large deflections. *Communications in Numerical Methods in Engineerings* 13, 6 (1997), 429–438.
- [56] YU, X., DMITROCHENKO, O., MATIKAINEN, M. K., ORZECOWSKI, G., AND MIKKOLA, A. Cone complementarity approach for dynamic analysis of multiple pendulums. *Advances in Mechanical Engineering* 11, 6 (2019), 1–15.
- [57] ZAVARISE, G., AND WRIGGERS, P. Contact with friction between beams in 3-D space. *International Journal for Numerical Methods in Engineering* 49, 8 (2000), 977–1006.



## **Publication I**

Yu, X., Dmitrochenko, O., Matikainen, M. K., Orzechowski, G., and Mikkola, A.  
**Cone complementarity approach for dynamic analysis of multiple  
pendulums**

Reprinted with permission from  
*Advances in Mechanical Engineering*  
11(6) (2019) 1687814019856748.  
© 2019, SAGE.



# Cone complementarity approach for dynamic analysis of multiple pendulums

Xinxin Yu , Oleg Dmitrochenko, Marko K Matikainen ,  
Grzegorz Orzechowski and Aki Mikkola

## Abstract

The multibody system dynamics approach allows describing equations of motion for a dynamic system in a straightforward manner. This approach can be applied to a wide variety of applications that consist of interconnected components which may be rigid or deformable. Even though there are a number of applications in multibody dynamics, the contact description within multibody dynamics still remains challenging. A user of the multibody approach may face the problem of thousands or millions of contacts between particles and bodies. The objective of this article is to demonstrate a computationally straightforward approach for a planar case with multiple contacts. To this end, this article introduces a planar approach based on the cone complementarity problem and applies it to a practical problem of granular chains.

## Keywords

Multibody dynamics, contact analysis, semi-implicit Euler method, Coulomb friction

Date received: 7 March 2018; accepted: 17 May 2019

Handling Editor: James Baldwin

## Introduction

A multibody system consists of a number of bodies which can interact via constraints or forces. The forces can be described conditionally if, for example, there is physical contact between the bodies. Accordingly, a number of individual solid bodies in a bulk of granular material<sup>1</sup> can move freely until they establish contact with other bodies or solid walls during which the contact (collision) forces (impulses) alter the response of the bodies.

Granular chains<sup>2</sup> are shown to be proper models for polymers driven far from equilibrium.<sup>3</sup> In the application of granular chains, it is important to obtain an accurate multiple impact models with a numerical method. Models which are governed by Newton's and Poisson's restitution law are widely used in describing the contact laws. Coulomb's unilateral contact law with dry friction can be used to model the interaction between multiple particles.<sup>4</sup> Multibody dynamics and

collision dynamics can be simultaneously applied to describing the behavior of granular chains. Individual multiple pendulums have been studied in the literature solely as a physics problem<sup>5,6</sup> with different practical applications in the analysis of walking<sup>7–9</sup> or bearings absorbing earthquake shocks.<sup>10</sup>

Regardless of the applications, the problem of interacting pendulums is theoretically challenging and fascinating. Techniques of multibody dynamics can be combined with the collision dynamics of colliding pairs to obtain the mutual interactions of pendulums in time. Obviously, the time integrals of interactions are dependent on a number of geometric and physical

---

Mechanical Engineering, LUT University, Lappeenranta, Finland

### Corresponding author:

Xinxin Yu, Mechanical Engineering, LUT University, Yliopistonkatu 34,  
53850 Lappeenranta, Finland.  
Email: xinxin.yu@lut.fi



Creative Commons CC BY: This article is distributed under the terms of the Creative Commons Attribution 4.0 License (<http://www.creativecommons.org/licenses/by/4.0/>) which permits any use, reproduction and distribution of the work without further permission provided the original work is attributed as specified on the SAGE and Open Access pages (<https://us.sagepub.com/en-us/nam/open-access-at-sage>).

parameters in the system under investigation. If one wants to simulate the granular with many contacts successfully, small time steps which can achieve numerical stability may be needed. Therefore, these issues motivate researchers to investigate the innovative time integration method to deal with the multiple contacts. In this field, Pang<sup>11</sup> has investigated in-depth time integration methods for calculating multiple frictional contacts with local compliance.

Using unilateral constraints, complementarity formulas can compute contact impulses to avoid penetration between rigid bodies. Simulations of multiple contacts can be performed with linear complementarity problem (LCP) and nonlinear complementarity problem (NCP) methods. When solving the time integration problem, LCP can unify linear and quadratic programmer solvers.<sup>12</sup> The methods of Gauss–Seidel and Jacobi are widely used to solve LCP. For the numerical solution of a large-scale symmetric positive-definite LCP, Kocvara and Zowe<sup>13</sup> have proposed an algorithm. Yao et al.<sup>14</sup> have established a linear complementary model to describe the non-holonomic system with friction by LCP. However, while the friction is nonzero or minor, the time integration interpretation will be lost, which makes the LCP solver imprecise.<sup>15</sup> Therefore, a more complex NCP which can be seen as an extension of LCP was proposed. DE Stewart and Trinkle<sup>16</sup> have proposed an implicit time-stepping method for simulating rigid body contact with Coulomb friction and inelastic impacts. The method is based on the NCP, which calculates the generalized position at the end of each time step. In this article, a semi-implicit time-stepping method is utilized with the complementarity principle to calculate the generalized position at the end of the time step. Tasora and Anitescu<sup>17</sup> have implemented C++ into the NCP solver to solve multiple unilateral contacts with friction with more than 100,000 colliding rigid bodies, which shows remarkable performance compared with other algorithms. However, when dealing with a large number of contacts and polyhedral approximation in friction, LCP and NCP solvers remain limited.<sup>18</sup>

An alternative approach for solving contact problems is the so-called penalty method (i.e. continuous method contact force model<sup>19</sup> or complaint contact force model),<sup>20</sup> which can be used to analyze contact forces as a continuous function of indentation and compliance of the contact surface.<sup>21</sup> This method typically needs small time step in the time integration scheme because of the stability limitations.<sup>16</sup> It is also noteworthy that choosing parameters requires little effort, because the selection of parameters depends on the contact case. Moreover, the selection of parameters' value may lead to high stiffness of the ordinary differential equation (ODE), which can make time differentiation slower due to small time step requirements.

Therefore, the selection has to be done with care keeping in mind that the system does not lead to unnecessary high eigenfrequencies.

In the two-dimensional Coulomb case, this article introduces an optimization-based method of the cone complementarity problem (CCP) for the simulation of interacting multiple pendulums. This method is used for the simulation of non-smooth rigid multibody dynamics with collision, contact, and friction, solving a convex quadratic program based on a fixed time step.<sup>22</sup> Tasora et al. have chosen to use the interior point method with a CCP, which turned out to be more accurate than the Gauss-Jacobi.<sup>21</sup> M Anitescu and colleagues<sup>23,24</sup> have proposed a time integration formulation method and a fixed-point iteration algorithm to solve a large CCP with low calculation which can handle large-scale contacts and large granular flow problems. Alessandro Tasora et al. have found that the fixed-point iteration algorithm displays linear complexity when solving a large CCP. In other words, the simulation time could increase linearly when the number of bodies increases in the model.<sup>21</sup> The complementarity condition to build a Coulomb dry friction model combined with a non-penetration condition in a spatial case is introduced in Negrut et al.<sup>18</sup>

This article provides an important opportunity to advance the understanding of multibody contact in planar cases. The differential complementarity approach is utilized to analyze the contact dynamics of the two flexible quadruple pendulums. Comparing with the three-dimensional (3D) Coulomb friction model,<sup>18,23,24</sup> the explicit two-dimensional (2D) expressions in this article are much simpler. The changes of kinetic energy and potential energy have been explained by comparing the introduced approach with penalty method.

This article reviews and analyzes basic methods and formulations used in contact dynamics with the CCP. The overall structure of the study is as follows. Section “Methods and formulations” begins by laying out the theoretical methods and formulations of the research, including the friction model, motion, and CCP. The application of multibody contacts is studied through the contact description of multiple pendulums in section “Dynamic simulation of multiple pendulum interactions.” The contact dynamics is separated into three parts: contact with the ground, contact with each other, and the rope inextensibility constraint with the explanation of force transformation matrices and gap functions. Section “Performance investigation” displays the numerical results of contacts two pendulum. The paper gives some conclusions of the method for solving the CCP and a short discussion of the future direction of the study in the final section.

## Methods and formulations

This article uses a complementarity approach to express the Coulomb friction model. The approach employs a non-penetration condition, and it is based on a set of differential equations and algebraic inequalities, which characterize the dynamics of multibody systems with friction and contact. The resulting problem is expressed in the form of a CCP.

### System state

In the planar multibody case, the position of a particle of a body with respect to the global coordinate system can be described with the help of a body reference coordinate system. Therefore, a set of generalized coordinates for a multibody system can be written as

$$\mathbf{q} = \left[ \mathbf{R}_1^T \quad \varphi_1 \quad \cdots \quad \mathbf{R}_{n_b}^T \quad \varphi_{n_b} \right]^T \quad (1)$$

where  $\mathbf{R}$  describes the translation of a body reference coordinate system with respect to the global coordinate system and  $\varphi$  is the rotation angle of the body reference system and  $n_b$  is the number of bodies. Accordingly, generalized velocities can be written as

$$\dot{\mathbf{q}} = \left[ \dot{\mathbf{R}}_1^T \quad \omega_1 \quad \cdots \quad \dot{\mathbf{R}}_{n_b}^T \quad \omega_{n_b} \right]^T \quad (2)$$

where  $\dot{\mathbf{R}}$  describes the velocity of a body reference coordinate system with respect to the global coordinate system and  $\omega$  is the angular velocity of the body reference system.

### Non-penetration contact constraints

If two rigid bodies come into contact, they should not penetrate. This means that any two bodies that are closer than a prescribed distance are considered to produce an active contact event. Accordingly, it is assumed that gap function  $\Phi_i$  exists and can be used to describe the non-penetration constraint as follows

$$\begin{aligned} \Phi_i > 0 & \text{ if two bodies share no point} \\ \Phi_i = 0 & \text{ if two bodies share one point} \\ \Phi_i < 0 & \text{ if two bodies are in penetration} \end{aligned} \quad (3)$$

where  $i$  represents the  $i$ th contact.

Modern collision detection algorithms can be utilized to define the contact points of the bodies with arbitrary shapes. Different methods of contact detection for several shape descriptors in a 2D and 3D case are proposed in Hogue,<sup>25</sup> such as polygons, ellipses, and discrete function representations. It is important to note that the description of contact points for bodies with arbitrary shapes is often a challenging task. For example, there may be multiple contact points or the shape of the body may be concave, making it impossible to define the gap function between contact points.

In this study, circular bodies are considered for the sake of simplicity, whose gap function description is shown in Figure 1. Accordingly, the non-penetration constraint becomes  $\Phi_i \geq 0$ .

### Coulomb friction model

The frictional contact model used in this article is based on the Coulomb dry friction model. For a contact event  $i$ , when the contact is active between bodies, that is  $\Phi_i = 0$ , normal contact force  $f_2^{(i)}$  and tangential force  $f_1^{(i)}$  may exist at the contact point. Both normal contact forces and tangential contact forces can be described by set-valued force laws. It is for this reason that for any contact event  $i$ , the friction force can assume any value between 0 and  $\mu f_2^{(i)}$ . Therefore, the contact forces follow two conditions

$$f_2^{(i)} > 0 \quad (4a)$$

$$f_1^{(i)} \leq \mu f_2^{(i)} \quad (4b)$$

As for the normal contact force, if there is no contact ( $\Phi_i > 0$ ) at the contact point, the normal contact force must be zero ( $f_2^{(i)} = 0$ ). On the other hand, if contact exists ( $\Phi_i = 0$ ), the normal contact force ( $f_2^{(i)} > 0$ ) exists as well.

The frictional force at the contact point changes instantaneously from sticking to sliding. If the contact model is sliding<sup>26,27</sup>—that is, the relative tangential velocity  $v_T$  at the contact point is not zero—the frictional contact force and normal contact force fulfill the relationship  $f_1^{(i)} = \mu f_2^{(i)}$ . While the stick happens at the contact point, relative tangential velocity  $v_T$  is zero; the friction model follows  $f_1^{(i)} < \mu f_2^{(i)}$ . As soon as the

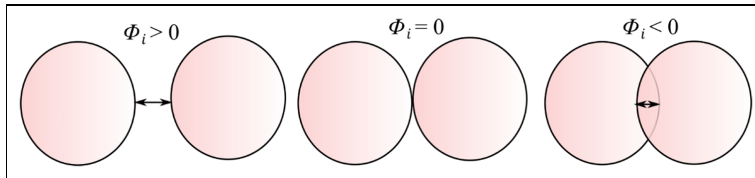


Figure 1. Gap function descriptions between two circular bodies.

normal contact force  $f_2^{(i)}$  happens at the contact point, which is  $f_2^{(i)} \geq 0$ , the contact forces can be expressed as a Coulomb friction law.

For a contact event  $i$ , when assuming  $\mathbf{n}_i$  to be the normal vector at the contact point which points toward the exterior of the body,  $\boldsymbol{\tau}_i$  is the tangential vectors at the contact point. Accordingly,  $\mathbf{n}_i$ ,  $\boldsymbol{\tau}_i$  are unit orthogonal vectors. The reaction force on the contact point can be expressed by means of multipliers  $\hat{\gamma}_{i,n} \geq 0$ , whereas  $\hat{\gamma}_{i,u}$  and  $\hat{\gamma}_{i,w}$  can have an arbitrary value.

Here,  $\mathbf{f}_1^{(i)} = \boldsymbol{\tau}_i \hat{\gamma}_{i,\tau}$ ,  $\mathbf{f}_2^{(i)} = \mathbf{n}_i \hat{\gamma}_{i,n}$ . So, for each contact  $i$ , both situations can be displayed by two equalities and one complementarity condition<sup>28</sup>

$$\hat{\gamma}_{i,n} \geq 0, \Phi_i \geq 0 \quad (5a)$$

$$\Phi_i \hat{\gamma}_{i,n} = 0 \quad (5b)$$

$$\mu \hat{\gamma}_{i,n} - \hat{\gamma}_{i,\tau} \geq 0, |v_T| \geq 0 \quad (5c)$$

$$|v_T|(\mu \hat{\gamma}_{i,n} - \hat{\gamma}_{i,\tau}) = 0 \quad (5d)$$

the body of high index  $B$ , and vector  $\boldsymbol{\tau}_i$  is tangential with respect to the contact point.

If the contact is active, then  $\Phi_i = 0$ . So, at the contact point, the force acting on body  $A$  at point  $P$  is as follows

$$\mathbf{F}_{i,A} = \boldsymbol{\tau}_i \hat{\gamma}_{i,\tau} + \mathbf{n}_i \hat{\gamma}_{i,n} = [\boldsymbol{\tau}_i \quad \mathbf{n}_i] \begin{bmatrix} \hat{\gamma}_{i,\tau} \\ \hat{\gamma}_{i,n} \end{bmatrix} = \mathbf{A}_i \hat{\boldsymbol{\gamma}}_i \quad (6)$$

where  $\mathbf{A}_i = [\boldsymbol{\tau}_i \quad \mathbf{n}_i]$  is the orthogonal rotation matrix consisting of unit orthogonal tangential and normal vectors at the  $i$ th contact point. The reaction force is imposed on the system by means of multipliers  $\hat{\gamma}_{i,n}$  and  $\hat{\gamma}_{i,\tau}$ ; that is, the normal component of the force is  $\mathbf{f}_2 = \mathbf{n}_i \hat{\gamma}_{i,n}$  and the tangential component of the force is  $\mathbf{f}_1 = \boldsymbol{\tau}_i \hat{\gamma}_{i,\tau}$ . Here

$$\hat{\boldsymbol{\gamma}}_i = \begin{bmatrix} \hat{\gamma}_{i,\tau} \\ \hat{\gamma}_{i,n} \end{bmatrix}$$

is the multiplier vector and is not known at time ( $t$ ).

The position of the contact point  $P$  on body  $A$  can be written as

$$\mathbf{r}_A^P = \mathbf{R}_A + \mathbf{A}_A \bar{\mathbf{s}}_{i,A} \quad (7)$$

where  $\bar{\mathbf{s}}_{i,A}$  is the position vector of contact point  $P$  with respect to the body reference coordinate system of body  $A$ .  $\mathbf{A}_A$  is the orientation matrix of body  $A$  and can be written as

$$\mathbf{A}_A = \begin{bmatrix} \cos \varphi_A & -\sin \varphi_A \\ \sin \varphi_A & \cos \varphi_A \end{bmatrix} \quad (8)$$

The virtual displacement of the contact point is

### Notation problem setup

In each configuration at time ( $t$ ), the collection of  $N_K$  contacts is denoted by  $\mathcal{A}(\mathbf{q}(t), \Phi_i)$ . Here,  $N_K$  describes the total contact frequency of the bodies. As shown in Figure 2, it can be assumed that two bodies of index  $A$  and  $B$  are in contact in  $n_b$  bodies. So, for contact event  $i$ , a collision detection process produces the point of contact  $P$ , a signed distance function  $\Phi_i$ , and a set of two orthonormal vectors  $\mathbf{n}_i$  and  $\boldsymbol{\tau}_i$  at the contact plane. The vector  $\mathbf{n}_i$  is normal with respect to the contact point, which leads from the body of lower index  $A$  to

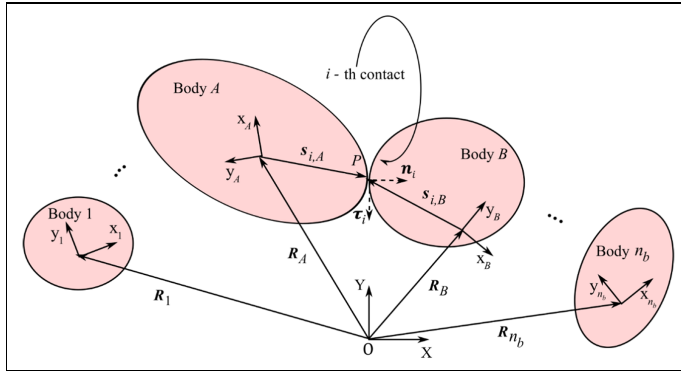


**Figure 2.** Illustration of rigid body A and B in contact. An arbitrary contact point is located via local constant vectors  $\mathbf{s}_{i,A}$  and  $\mathbf{s}_{i,B}$ . A set of two orthonormal vectors  $\mathbf{n}_i$  and  $\boldsymbol{\tau}_i$  is generated at the contact point.

$$\delta r_A^p = \delta(\mathbf{R}_A + \mathbf{A}_A \tilde{\mathbf{s}}_{i,A}) = \delta \mathbf{R}_A + \mathbf{A}_{\varphi_A} \tilde{\mathbf{s}}_{i,A} \delta \varphi_A \quad (9)$$

where the vector  $\delta \varphi_A$  is the virtual rotation associated with body  $A$ , and  $\mathbf{A}_{\varphi_A}$  is the derivative of  $\mathbf{A}_A$  with respect to  $\varphi_A$ .

Here,  $\mathbf{A}_{\varphi_A} \tilde{\mathbf{s}}_{i,A} = -\mathbf{A}_A \tilde{\tilde{\mathbf{s}}}_{i,A}$ , where  $\tilde{\sim}$  is the tilde operator, which can be explained as follows

$$\tilde{\mathbf{s}}_{i,A} = [\tilde{\mathbf{s}}_{i,A}^x \quad \tilde{\mathbf{s}}_{i,A}^y]^T \tilde{\tilde{\mathbf{s}}}_{i,A} = [-\tilde{\mathbf{s}}_{i,A}^y \quad \tilde{\mathbf{s}}_{i,A}^x]^T \quad (10)$$

So, the virtual displacement can be rewritten as

$$\delta r_A^p = \delta \mathbf{R}_A - \mathbf{A}_A \tilde{\tilde{\mathbf{s}}}_{i,A} \delta \varphi_A \quad (11)$$

The virtual work associated with the contact force  $\mathbf{F}_{i,A}$  can now be expressed as

$$\delta W_{i,A} = [\delta r_A^p]^T \mathbf{F}_{i,A} = [\delta \mathbf{R}_A - \mathbf{A}_A \tilde{\tilde{\mathbf{s}}}_{i,A} \delta \varphi_A]^T \mathbf{A}_i \hat{\boldsymbol{\gamma}}_i = \delta \mathbf{R}_A^T \mathbf{A}_i \hat{\boldsymbol{\gamma}}_i + \delta \varphi_A^T \tilde{\tilde{\mathbf{s}}}_{i,A} \mathbf{A}_A^T \mathbf{A}_i \hat{\boldsymbol{\gamma}}_i \quad (12)$$

Correspondingly, the virtual work for body  $B$  is

$$\begin{aligned} \delta W_{i,B} &= [\delta r_B^p]^T (-\mathbf{F}_{i,A}) \\ &= [\delta \mathbf{R}_B - \mathbf{A}_B \tilde{\tilde{\mathbf{s}}}_{i,B} \delta \varphi_B]^T (-\mathbf{A}_i \hat{\boldsymbol{\gamma}}_i) \end{aligned} \quad (13)$$

Then, the virtual work that the presence of the frictional contact force  $\mathbf{F}_{i,A}$  imparts is

$$\begin{aligned} \delta W_i &= \delta W_{i,A} + \delta W_{i,B} = \delta \mathbf{R}_A^T \mathbf{A}_i \hat{\boldsymbol{\gamma}}_i + \delta \varphi_A^T \tilde{\tilde{\mathbf{s}}}_{i,A} \mathbf{A}_A^T \mathbf{A}_i \hat{\boldsymbol{\gamma}}_i \\ &\quad - \delta \mathbf{R}_B^T \mathbf{A}_i \hat{\boldsymbol{\gamma}}_i - \delta \varphi_B^T \tilde{\tilde{\mathbf{s}}}_{i,B} \mathbf{A}_B^T \mathbf{A}_i \hat{\boldsymbol{\gamma}}_i = (\delta \mathbf{R}_A^T + \delta \varphi_A^T \tilde{\tilde{\mathbf{s}}}_{i,A} \mathbf{A}_A^T \\ &\quad - \delta \mathbf{R}_B^T - \delta \varphi_B^T \tilde{\tilde{\mathbf{s}}}_{i,B} \mathbf{A}_B^T) \mathbf{A}_i \hat{\boldsymbol{\gamma}}_i = \delta \mathbf{q}^T \mathbf{D}_i \hat{\boldsymbol{\gamma}}_i \end{aligned} \quad (14)$$

where

$$\delta \mathbf{q} = \begin{bmatrix} \delta \mathbf{R}_1 \\ \delta \varphi_1 \\ \vdots \\ \delta \mathbf{R}_{n_b} \\ \delta \varphi_{n_b} \end{bmatrix} \mathbf{D}_i = \begin{bmatrix} 0_{3 \times 2} \\ \vdots \\ 0_{3 \times 2} \\ + \mathbf{A}_i \\ + \tilde{\tilde{\mathbf{s}}}_{i,A} \mathbf{A}_A^T \mathbf{A}_i \\ 0_{3 \times 2} \\ \vdots \\ 0_{3 \times 2} \\ - \mathbf{A}_i \\ - \tilde{\tilde{\mathbf{s}}}_{i,B} \mathbf{A}_B^T \mathbf{A}_i \\ 0_{3 \times 2} \\ \vdots \\ 0_{3 \times 2} \end{bmatrix} \quad (15)$$

Therefore, the frictional contact force associated with the presence of  $N_K$  contact events is  $\mathbf{D}_i \hat{\boldsymbol{\gamma}}_i$ , which means that  $\mathbf{D}_i$  is the contact transformation matrix associated with contact  $\mathcal{A}(q(t), \Phi_i)$ , which can convert the general force to contact force

$$\mathbf{D} = [\mathbf{D}_1 \quad \cdots \quad \mathbf{D}_{N_K}] \quad (16)$$

Finally, note that

$$\begin{aligned} \mathbf{D}_i^T \dot{\mathbf{q}} &= \begin{bmatrix} 0_{3 \times 2} \\ \vdots \\ 0_{3 \times 2} \\ + \mathbf{A}_i \\ + \tilde{\tilde{\mathbf{s}}}_{i,A} \mathbf{A}_A^T \mathbf{A}_i \\ 0_{3 \times 2} \\ \vdots \\ 0_{3 \times 2} \\ - \mathbf{A}_i \\ - \tilde{\tilde{\mathbf{s}}}_{i,B} \mathbf{A}_B^T \mathbf{A}_i \\ 0_{3 \times 2} \\ \vdots \\ 0_{3 \times 2} \end{bmatrix}^T \begin{bmatrix} \mathbf{R}_1^T \\ \omega_1 \\ \vdots \\ \mathbf{R}_A^T \\ \omega_A \\ \vdots \\ \mathbf{R}_B^T \\ \omega_B \\ \vdots \\ \mathbf{R}_{n_b}^T \\ \omega_{n_b} \end{bmatrix} \\ &= \mathbf{A}_i^T \dot{\mathbf{R}}_A + \mathbf{A}_i^T \mathbf{A}_A \tilde{\tilde{\mathbf{s}}}_{i,A} \omega_A - \mathbf{A}_i^T \dot{\mathbf{R}}_B - \mathbf{A}_i^T \mathbf{A}_B \tilde{\tilde{\mathbf{s}}}_{i,B} \omega_B \\ &= \mathbf{A}_i^T (\dot{\mathbf{R}}_A + \mathbf{A}_{\varphi_A} \tilde{\tilde{\mathbf{s}}}_{i,A} \omega_A - \dot{\mathbf{R}}_B - \mathbf{A}_{\varphi_B} \tilde{\tilde{\mathbf{s}}}_{i,B} \omega_B) \\ &= \mathbf{A}_i^T (\dot{\mathbf{r}}_{i,A} - \dot{\mathbf{r}}_{i,B}) = \begin{bmatrix} v_{i,\tau} \\ v_{i,n} \end{bmatrix} \end{aligned} \quad (17)$$

where

$$\begin{bmatrix} v_{i,\tau} \\ v_{i,n} \end{bmatrix}$$

represents the relative velocity at the contact point between two bodies; that is,  $v_{i,\tau}$  is the tangential relative velocity and  $v_{i,n}$  is the normal relative velocity. The matrix  $\mathbf{D}_i$  can also convert the general velocity to contact velocity.

### Equations of motion

Assume that there are  $N_K$  potential contacts, so that the contact constraints are enforced by non-penetration constraints  $\Phi_i \geq 0, i = 1, 2, \dots, p$ . Here, superscript  $i$  is the number of contact event. Therefore, the equations of motion take the form

$$\mathbf{M} \ddot{\mathbf{q}} = \mathbf{F}(q, \dot{q}, t) + \mathbf{D} \dot{\boldsymbol{\gamma}} \quad (18)$$

where mass matrix  $\mathbf{M} = \text{diag}\{\mathbf{M}_1, \dots, \mathbf{M}_A, \mathbf{M}_B, \dots, \mathbf{M}_{n_b}\}$ , where  $\mathbf{M}_i = \text{diag}\{m_i, m_i, J_i\}$  and  $J_i = m_i r_i^2 / 2$ .  $\mathbf{F}(q, \dot{q}, t)$  is the generalized applied force, and  $\mathbf{D} \dot{\boldsymbol{\gamma}}$  is the frictional contact force associated with the presence of  $N_K$  contact events. Here, a matrix  $\dot{\boldsymbol{\gamma}}$  is built to contain all of the contact force as in equation (19)

$$\hat{\boldsymbol{\gamma}} = [\hat{\boldsymbol{\gamma}}_1 \quad \hat{\boldsymbol{\gamma}}_2 \quad \cdots \quad \hat{\boldsymbol{\gamma}}_{N_k}]^T \quad (19)$$

### Discretized equations of motion

Using a semi-implicit Euler numerical scheme<sup>18</sup> at time step  $t^{(l+1)} = t^{(l)} + \Delta t$ , the equations of motion can be expressed as follows

$$\underbrace{\mathbf{q}(l+1)}_{\text{generalized positions}} = \mathbf{q}^{(l)} + \underbrace{\Delta t}_{\text{step size}} \dot{\mathbf{q}}^{(l+1)} \quad (20a)$$

$$\mathbf{M} \begin{pmatrix} \underbrace{\dot{\mathbf{q}}^{(l+1)}}_{\text{generalized speeds}} \\ -\dot{\mathbf{q}}^{(l)} \end{pmatrix} = \underbrace{\mathbf{f}^{(l)}}_{\text{applied impulse}} + \underbrace{\mathbf{D}^{(l)} \boldsymbol{\gamma}^{(l+1)}}_{\text{frictional contact impulse}} \quad (20b)$$

$$i \in \mathcal{A}^{(l)}(\mathbf{q}(t), \Phi_i) : \begin{cases} \gamma_{i,n}^{(l+1)} \geq 0 \\ (\mu_i \gamma_{i,n}^{(l+1)} - \gamma_{i,\tau}^{(l+1)}) \geq 0 \end{cases} \quad (20c)$$

$$\Phi_i \geq 0 \quad (20d)$$

where  $\mathbf{f}^{(l)} = \Delta t \mathbf{F}(\mathbf{q}^{(l)}, \dot{\mathbf{q}}^{(l)}, t^{(l)})$ ,  $\boldsymbol{\gamma}^{(l+1)} = \Delta t \hat{\boldsymbol{\gamma}}^{(l+1)}$  and  $\mathbf{D}^{(l)} = \mathbf{D}(\mathbf{q}^{(l)}, t^{(l)})$ ,  $\dot{\mathbf{q}}^{(l)}$  is the general known velocity and  $\dot{\mathbf{q}}^{(l+1)}$  is the unknown velocity with time step  $\Delta t$ . In equation (20c),  $\mathcal{A}^{(l)}(\mathbf{q}(t), \Phi_i)$  is the set of active contact events produced by the collision detection step carried out at  $t^{(l)}$  in the configuration  $\mathbf{q}^{(l)}$ . According to equation (4), the Coulomb friction model used in this article is presented in equation (20c).

An approximation of the signed gap function at  $t^{(l+1)}$  is utilized to reflect the complementarity

$$\exists i \in \mathcal{A}^{(l)}(\mathbf{q}(t), \Phi_i) : \Phi_i^{(l+1)} \approx \Phi_i^{(l)} + \Delta t v_{i,n}^{(l+1)} \quad (21)$$

### Reformulation as a CCP

Using the force balance condition in equation (19b), the velocity within time step  $\dot{\mathbf{q}}^{(l+1)}$  can be calculated as

$$\dot{\mathbf{q}}^{(l+1)} = \dot{\mathbf{q}}^{(l)} + \mathbf{M}^{-1} \mathbf{f}^{(l)} + \mathbf{M}^{-1} \mathbf{D}^{(l)} \boldsymbol{\gamma}^{(l+1)} \quad (22)$$

Next,  $\mathbf{d}_i$  can be defined as

$$\mathbf{d}_i = \begin{bmatrix} v_{i,\tau}^{(l+1)} \\ \frac{1}{\Delta t} \Phi_i^{(l)} + v_{i,n}^{(l+1)} \end{bmatrix} \quad (23)$$

At the initial time, the velocity at the contact is all zero, so the initial term of  $\mathbf{d}_i$  is

$$\mathbf{d}_{i,0} = \begin{bmatrix} 0 \\ \frac{1}{\Delta t} \Phi_i^{(l)} \end{bmatrix} \quad (24)$$

According to equation (17), the matrix  $\mathbf{D}$  can convert the general velocity to contact velocity, and  $\mathbf{d}_i$  can also be presented as

$$\mathbf{d}_i = \begin{bmatrix} 0 \\ \frac{1}{\Delta t} \Phi_i^{(l)} \end{bmatrix} + \begin{bmatrix} v_{i,\tau}^{(l+1)} \\ v_{i,n}^{(l+1)} \end{bmatrix} = \mathbf{d}_{i,0} + \mathbf{D}^{(l),T} \dot{\mathbf{q}}^{(l+1)} \quad (25)$$

Then, equation (22) can be submitted into equation (25) as

$$\begin{aligned} \mathbf{d}_i &= \mathbf{d}_{i,0} + \mathbf{D}^{(l),T} (\dot{\mathbf{q}}^{(l)} + \mathbf{M}^{-1} \mathbf{f}^{(l)} + \mathbf{M}^{-1} \mathbf{D}^{(l)} \boldsymbol{\gamma}^{(l+1)}) \\ &= \mathbf{d}_{i,0} + \mathbf{D}^{(l),T} (\dot{\mathbf{q}}^{(l)} + \mathbf{M}^{-1} \mathbf{f}^{(l)}) + \mathbf{D}^{(l),T} \mathbf{M}^{-1} \mathbf{D}^{(l)} \boldsymbol{\gamma}^{(l+1)} \end{aligned} \quad (26)$$

Here,  $\mathbf{d}_{i,1}$  can be defined as

$$\mathbf{d}_{i,1} = \mathbf{d}_{i,0} + \mathbf{D}^{(l),T} (\dot{\mathbf{q}}^{(l)} + \mathbf{M}^{-1} \mathbf{f}^{(l)}) \quad (27)$$

Therefore,  $\mathbf{d}_i$  can be rewritten as

$$\mathbf{d}_i = \mathbf{d}_{i,1} + \mathbf{D}^{(l),T} \mathbf{M}^{-1} \mathbf{D}^{(l)} \boldsymbol{\gamma}^{(l+1)} \quad (28)$$

Below, the vector  $\mathbf{p}$  will be used as a union of all of the particular vectors  $\mathbf{d}_{i,1}$ .

$$\mathbf{p} = \begin{bmatrix} \mathbf{d}_{1,1} \\ \vdots \\ \mathbf{d}_{N_k,1} \end{bmatrix} \quad (29)$$

Analogously, also matrix  $\mathbf{N}$  can be introduced

$$\mathbf{N} = \mathbf{D}^T \mathbf{M}^{-1} \mathbf{D} \quad (30)$$

### Quadratic optimization problem

The CCP represents the first-order optimality conditions<sup>11</sup> for the convex quadratic optimization problem with conic constraints

$$\boldsymbol{\gamma}^{(l+1)} = \min_{\boldsymbol{\gamma}} \frac{1}{2} \boldsymbol{\gamma}^T \mathbf{N} \boldsymbol{\gamma} + \mathbf{p}^T \boldsymbol{\gamma} \quad (31)$$

subject to  $\boldsymbol{\gamma}_k \in \mathbf{C}_k$

where  $\boldsymbol{\gamma}$  is the contact impulse when the bodies collide,  $\boldsymbol{\gamma}^{(l+1)}$  is the unknown contact impulse at the next time step  $\Delta t$ , and  $\mathbf{C}_k$  is from the Coulomb friction model equation (4).

With time integration, the new contact impulse  $\boldsymbol{\gamma}^{(l+1)}$  will be computed using equation (31). Meanwhile, the new velocity  $\dot{\mathbf{q}}^{(l+1)}$  can be obtained via equation (22). The new position  $\mathbf{q}^{(l+1)}$  will finally be calculated through equation (20a).

### Dynamic simulation of multiple pendulum interactions

In this section, the contact description explained above is applied to study multiple pendulums. Multiple bodies may come into contact with each other in three possible

situations: (1) the bodies hit the ground; (2) the bodies collide with each other; (3) adjacent bodies are restricted by a rope. Constraints and contact scenarios used are explained in the following sections of the paper.

### Case of bodies hitting the ground

The first type of multibody contact is between bodies and the ground, as shown in Figure 3.

Each contact point results in two orthogonal forces  $f_1^{G(i)}$  and  $f_2^{G(i)}$  and one torque  $T^{G(i)}$ . The torque can be calculated as

$$T^{G(i)} = r_i f_1^{G(i)} + 0 f_2^{G(i)} = [r_i \ 0] \begin{bmatrix} f_1^{G(i)} \\ f_2^{G(i)} \end{bmatrix} \quad (32)$$

Therefore, the external force and torque can be calculated as

$$\begin{bmatrix} f_x^{G(i)} \\ f_y^{G(i)} \\ T^{G(i)} \end{bmatrix} = \begin{bmatrix} 1 & 0 \\ 0 & 1 \\ r_i & 0 \end{bmatrix} \begin{bmatrix} f_1^{G(i)} \\ f_2^{G(i)} \end{bmatrix} \quad (33)$$

Here, the matrix  $D^{G(i)}$  is

$$D^{G(i)} = \begin{bmatrix} 1 & 0 \\ 0 & 1 \\ r_i & 0 \end{bmatrix} \quad (34)$$

Each body can potentially make contact with the ground. Therefore, matrix  $D_i^G$  takes the following form

$$D^G = \underbrace{\begin{bmatrix} D^{G(1)} & 0_{3 \times 2} & \cdots & 0_{3 \times 2} \\ 0_{3 \times 2} & D^{G(2)} & \cdots & 0_{3 \times 2} \\ \vdots & \vdots & \ddots & \vdots \\ 0_{3 \times 2} & 0_{3 \times 2} & \cdots & D^{G(n_b)} \end{bmatrix}}_{n_b \text{ times}} \quad (35)$$

The gap function  $\Phi^{G(i)}$  is the distance between the contact point and the ground; that is, the number of gap functions is the number of bodies  $n_b$

$$\Phi^{G(i)} = y_i - r_i \quad (36)$$

where  $y_i$  is the distance between the center of the body and the ground, and  $r_i$  is the radius of the body  $i$ .

### Case of bodies colliding with each other

As shown in Figure 4, when bodies collide with each other, two contact forces appear the normal force  $f_2^{S(i)}$  and the tangential force  $f_1^{S(i)}$ . The normal force  $f_2^{S(i)}$  is directed along the line between two body centers.

The force acting on body  $i$  at point  $P$  is

$$F^{S(i)} = \tau_{ij} \hat{\gamma}_1^{(ij)} + n_{ij} \hat{\gamma}_2^{(ij)} = A_{ij} \hat{\gamma}_{ij} \quad (37)$$

The distance of the center mass of two contact bodies can be written as  $L = \sqrt{(x_i - x_j)^2 + (y_i - y_j)^2}$ . For this situation, the orthogonal matrix  $A_{ij}$  is composed with the normal vector  $n_{ij}$  and the tangential vector  $\tau_{ij}$ . The normal vector  $n_{ij}$  is the unit vector which

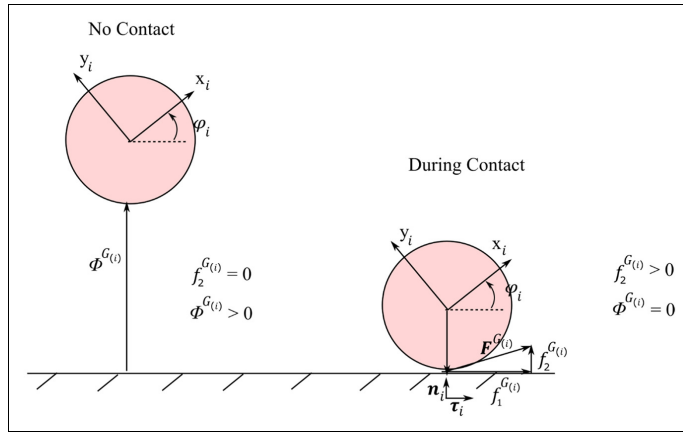


**Figure 3.** Case of body hitting the ground. The gap function  $\Phi^{G(i)}$  is the distance between the contact point and the ground. Two orthogonal forces  $f_1^{G(i)}$ ,  $f_2^{G(i)}$  are produced at the contact point. The gap function and the normal contact force follow the complementarity condition  $\Phi^{G(i)} f_2^{G(i)} = 0$ .

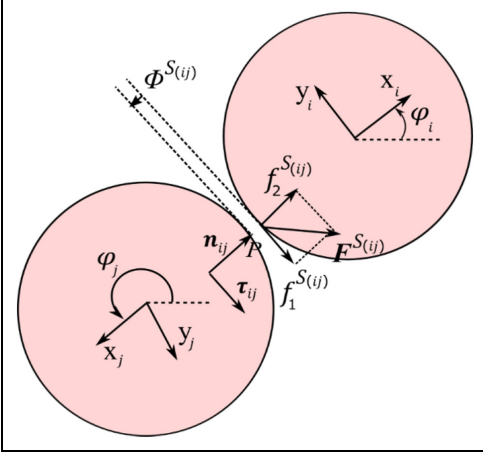


**Figure 4.** Case of bodies colliding with each other. The gap function  $\Phi^{S(ij)}$  is the distance between the contact point of the bodies. Two orthogonal forces  $f_1^{S(ij)}$  and  $f_2^{S(ij)}$  are produced at the contact point. The gap function and the normal contact force follow the complementarity condition  $\Phi^{S(ij)} f_2^{S(ij)} = 0$ .

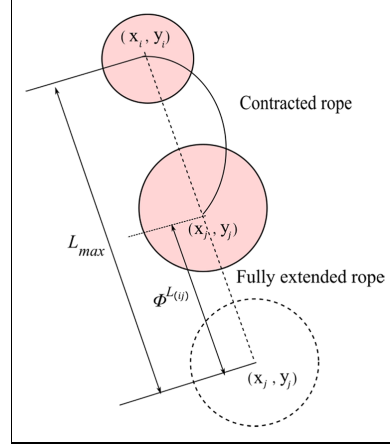


**Figure 5.** Case of rope inextensibility constraint. The gap function  $\Phi^{L(ij)}$  is the distance of the fully extended rope. The normal force  $f_2^{L(ij)}$  is produced along the rope. The gap function and the normal contact force follow the complementarity condition  $\Phi^{L(ij)} f_2^{L(ij)} = 0$ .

is directed from the body  $j$  toward body  $i$ . Thus, it is calculated as

$$\mathbf{n}_{ij} = \begin{bmatrix} \frac{x_i - x_j}{L} \\ \frac{y_i - y_j}{L} \end{bmatrix}$$

The tangential vector  $\boldsymbol{\tau}_{ij}$  is orthogonal to  $\mathbf{n}_{ij}$ , so it should be calculated as

$$\boldsymbol{\tau}_{ij} = \begin{bmatrix} \frac{y_i - y_j}{L} \\ -\frac{x_i - x_j}{L} \end{bmatrix}$$

Accordingly, matrix  $\mathbf{A}_{ij}$  takes the form

$$\mathbf{A}_{ij} = [\boldsymbol{\tau}_{ij} \quad \mathbf{n}_{ij}] = \begin{bmatrix} \frac{y_i - y_j}{L} & \frac{x_i - x_j}{L} \\ -\frac{x_i - x_j}{L} & \frac{y_i - y_j}{L} \end{bmatrix} \quad (38)$$

From equation (15), it can be concluded that

$$\mathbf{D}^{S(ij)} = \begin{bmatrix} +\mathbf{A}_{ij} \\ +r_i \boldsymbol{\tau}_{ij}^T \mathbf{A}_{ij} \end{bmatrix} \mathbf{D}^{S(i)} = \begin{bmatrix} -\mathbf{A}_{ij} \\ -r_j \boldsymbol{\tau}_{ij}^T \mathbf{A}_{ij} \end{bmatrix} \quad (39)$$

Considering that each body can potentially collide with all others, the number of contacts is  $n_c = n_b(n_b - 1)/2$ . That is why the full Jacobian matrix for this case is

$$\mathbf{D}^S = \begin{bmatrix} \mathbf{D}^{S(12)} & \mathbf{D}^{S(13)} & \dots & \mathbf{0}_{3 \times 2} \\ \mathbf{D}^{S(21)} & \mathbf{0}_{3 \times 2} & \dots & \mathbf{0}_{3 \times 2} \\ \mathbf{0}_{3 \times 2} & \mathbf{D}^{S(31)} & \dots & \mathbf{0}_{3 \times 2} \\ \vdots & \vdots & \ddots & \vdots \\ \mathbf{0}_{3 \times 2} & \mathbf{0}_{3 \times 2} & \dots & \mathbf{D}^{S(n_b-1)n_b} \\ \mathbf{0}_{3 \times 2} & \mathbf{0}_{3 \times 2} & \dots & \mathbf{D}^{S(n_b(n_b-1))} \end{bmatrix} \quad (40)$$

$\underbrace{\hspace{10em}}_{\frac{n_b(n_b-1)}{2} \text{ times}}$

The gap function  $\Phi^{S(ij)}$  expresses the distance between the two contact bodies, and the number of such functions is also  $n_c$

$$\Phi^{S(ij)} = L - r_i - r_j \quad (41)$$

where  $r_i$  and  $r_j$  are the radii of the body  $i$  and body  $j$ , respectively.

#### Rope inextensibility constraint

The adjacent bodies are connected pair-wise by a rope. Therefore, the adjacent bodies are restricted by the rope inextensibility constraint, as shown in Figure 5. The

normal force  $f_2^{L(i)}$  is directed along the line between the two adjacent bodies, which is also the direction of the rope.

The force acting on body  $i$  at the contact point is

$$\mathbf{F}^{L(i)} = \mathbf{n}_{ij} \hat{\gamma}_2^{(ij)} = A_{ij} \hat{\gamma}_{ij} \quad (42)$$

where  $A_{ij} = [\mathbf{n}_{ij}]$  is the unit vector of the direction of the rope.

The normal vector  $\mathbf{n}_{ij}$  is the unit vector which is oriented from body  $j$  to body  $i$  and it should be calculated as

$$\mathbf{n}_{ij} = \begin{bmatrix} \frac{x_i - x_j}{L} \\ \frac{y_i - y_j}{L} \end{bmatrix}$$

Thus, matrix  $A_{ij}$  is

$$A_{ij} = [\mathbf{n}_{ij}] = \begin{bmatrix} \frac{x_i - x_j}{L} \\ \frac{y_i - y_j}{L} \end{bmatrix} \quad (43)$$

It can be deduced that

$$\mathbf{D}^{L(i)} = \begin{bmatrix} +A_{ij} \\ 0 \end{bmatrix} \mathbf{D}^{L(j)} = \begin{bmatrix} -A_{ij} \\ 0 \end{bmatrix} \quad (44)$$

The number of contacts of this kind in one branch is equal to  $n_b/2$ , so the total number is  $n_b$ .  $\mathbf{D}^{L(0)}$  and  $\mathbf{D}^{L(n_b/2(n_b/2+1))}$  represent the constraints between the top body and the ceiling. The general form of the Jacobian matrix for this type of constraint is as follows

$$\mathbf{D}^L = \begin{bmatrix} \mathbf{D}^{L(0)} & \mathbf{D}^{L(2)} & \cdots & \mathbf{0}_{3 \times 1} & \mathbf{0}_{3 \times 1} & \mathbf{0}_{3 \times 1} & \cdots & \mathbf{0}_{3 \times 1} \\ \mathbf{0}_{3 \times 1} & \mathbf{D}^{L(2)} & \cdots & \mathbf{0}_{3 \times 1} & \mathbf{0}_{3 \times 1} & \mathbf{0}_{3 \times 1} & \cdots & \mathbf{0}_{3 \times 1} \\ \vdots & \vdots & \ddots & \vdots & \vdots & \vdots & \ddots & \vdots \\ \mathbf{0}_{3 \times 1} & \mathbf{0}_{3 \times 1} & \cdots & \mathbf{D}^{L(\frac{(n_b-1)n_b}{2})} & \mathbf{0}_{3 \times 1} & \mathbf{0}_{3 \times 1} & \cdots & \mathbf{0}_{3 \times 1} \\ \mathbf{0}_{3 \times 1} & \mathbf{0}_{3 \times 1} & \cdots & \mathbf{D}^{L(\frac{(n_b-1)n_b}{2})} & \mathbf{0}_{3 \times 1} & \mathbf{0}_{3 \times 1} & \cdots & \mathbf{0}_{3 \times 1} \\ \mathbf{0}_{3 \times 1} & \mathbf{0}_{3 \times 1} & \cdots & \mathbf{0}_{3 \times 1} & \mathbf{D}^{L(\frac{(n_b-1)n_b}{2})} & \mathbf{D}^{L(\frac{(n_b-1)n_b}{2})} & \cdots & \mathbf{0}_{3 \times 1} \\ \mathbf{0}_{3 \times 1} & \mathbf{0}_{3 \times 1} & \cdots & \mathbf{0}_{3 \times 1} & \mathbf{0}_{3 \times 1} & \mathbf{D}^{L(\frac{(n_b-1)n_b}{2})} & \cdots & \mathbf{0}_{3 \times 1} \\ \vdots & \vdots & \ddots & \vdots & \vdots & \vdots & \ddots & \vdots \\ \mathbf{0}_{3 \times 1} & \mathbf{0}_{3 \times 1} & \cdots & \mathbf{0}_{3 \times 1} & \mathbf{0}_{3 \times 1} & \mathbf{0}_{3 \times 1} & \cdots & \mathbf{D}^{L((n_b-1)n_b)} \\ \mathbf{0}_{3 \times 1} & \mathbf{0}_{3 \times 1} & \cdots & \mathbf{0}_{3 \times 1} & \mathbf{0}_{3 \times 1} & \mathbf{0}_{3 \times 1} & \cdots & \mathbf{D}^{L(n_b(n_b-1))} \end{bmatrix} \quad (45)$$

The gap function is computed as follows

$$\Phi^{L(i)} = L_{max} - L \quad (46)$$

Then, put all  $\mathbf{D}$  matrices together from equations (35), (40), and (45)

$$\mathbf{D} = [\mathbf{D}^G \quad \mathbf{D}^S \quad \mathbf{D}^L] \quad (47)$$

### Solving the CCP

The overall solution scheme can be expressed with Algorithm 1.

#### Algorithm 1

1. For  $i = 1, 2, \dots, n$ , the generalized position  $\mathbf{q}^{(i)}$  and generalized velocity  $\dot{\mathbf{q}}^{(i)}$  of the system are known at the current time step as Eq.(1) and Eq. (2) show.
2. For  $i = 1, 2, \dots, n$ , compute mass matrix  $\mathbf{M}$ .
3. Use Eq. (35), (40), (45), and (47) to obtain the  $\mathbf{D}$  matrix and Eq. (36), (41) and (46) to obtain gap function  $\Phi$ .
4. Use Eq. (48) and (27) to calculate  $\mathbf{d}_{i,0}$  and  $\mathbf{d}_{i,1}$ .
5. Use Eq. (30) and (29) to calculate matrix  $\mathbf{N}$  and  $\mathbf{p}$ , where  $\mathbf{f}^{(i)}$  is the applied impulse. In this situation, only the gravity force should be considered. So,  $\mathbf{f}^{(i)} = [0 -m_i g \ 0 \ \cdots \ 0 -m_i g \ 0]^T \Delta t$ .
6. Use the quadratic programming method to calculate the unknown force impulse  $\gamma^{(i+1)}$ , where matrix  $\mathbf{A}$  and  $\mathbf{b}$  can be obtained through Eq. (53) and (54) below.
7. Use Eq. (22) to update the speed  $\dot{\mathbf{q}}^{(i+1)}$  and Eq. (20a) to update the position  $\mathbf{q}^{(i+1)}$ . Increment  $t^{(i+1)} = t^{(i)} + \Delta t$ , and repeat from step 3 until  $t > t_{end}$ .

According to equation (23), inserting the gap function which can be calculated in equation (36), (41), and (46), one can obtain  $\mathbf{d}_{i,0}$

$$\mathbf{d}_{i,0} = \begin{bmatrix} 0 & \frac{1}{\Delta t} \Phi_1^G & \cdots & \frac{1}{\Delta t} \Phi_n^G & 0 & \frac{1}{\Delta t} \Phi_{12}^S & \cdots & \frac{1}{\Delta t} \Phi_{(n-1)n}^S & 0 & \frac{1}{\Delta t} \Phi_{12}^L & \cdots & \frac{1}{\Delta t} \Phi_{(n-1)n}^L \end{bmatrix} \quad (48)$$

This article employs the Coulomb friction model. When bodies hit the ground or collide with each other, there are two contact forces,  $f_1$  and  $f_2$ . Consequently, according to equation (4)

$$\begin{aligned} -f_2 &\leq 0 \\ f_1 - \mu f_2 &\leq 0 \end{aligned} \quad (49)$$

$$\mathbf{A}^{(i)} = \begin{bmatrix} 0 & -1 \\ 1 & -\mu \end{bmatrix}, \mathbf{b}^{(i)} = \begin{bmatrix} 0 \\ 0 \end{bmatrix} \quad (50)$$

When adjacent bodies are loaded with the rope inextensibility constraint, only one contact force  $f_2$  exists, so according to Coulomb's law

$$-f_2 \leq 0 \quad (51)$$

$$\mathbf{A}^{(j)} = [-1], \mathbf{b}^{(j)} = [0] \quad (52)$$

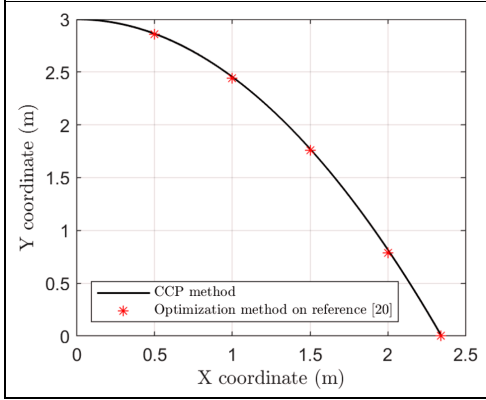


**Figure 6.** Displacements of X and Y directions for one particle with frictional contact. The coefficient of restitution is 0. Some points at  $x = [0.5 \ 1 \ 1.5 \ 2 \ 2.34]$  have been measured from the figure of the study by M Anitescu.<sup>23</sup>

Combining the  $A$  matrix and  $b$  matrix yields

$$A = \begin{bmatrix} 0 & -1 & \cdots & 0 & 0 & 0 & \cdots & 0 \\ 1 & -\mu & \cdots & 0 & 0 & 0 & \cdots & 0 \\ \vdots & \vdots & \ddots & \vdots & \vdots & \vdots & \ddots & \vdots \\ 0 & 0 & 0 & 0 & -1 & 0 & \cdots & 0 \\ 0 & 0 & 0 & 1 & -\mu & 0 & \cdots & 0 \\ 0 & 0 & 0 & 0 & 0 & -1 & \cdots & 0 \\ \vdots & \vdots & \vdots & \vdots & \vdots & \vdots & \ddots & \vdots \\ 0 & 0 & 0 & 0 & 0 & 0 & \cdots & -1 \end{bmatrix} \quad (53)$$

$$b = \underbrace{\begin{bmatrix} 0 & 0 & \cdots & 0 & 0 \end{bmatrix}}_{n_p \text{ times}}^T \quad (54)$$

where  $n_p$  is the potential contact number

$$n_p = 2*n_b + 2 * \frac{n_b(n_b - 1)}{2} + n_b = n_b^2 + 2*n_b \quad (55)$$

### Performance investigation

The numerical method proposed in this article can be utilized to simulate granular pendulum contact. This problem occurs in plenty of engineering applications; for example, a tree harvester truck can be assumed and simplified into a chain structure concept, which can be divided into several arbitrary bodies.<sup>28</sup>

In this section, two types of examples have been discussed. The CCP method developed in this article has been compared with one optimization-based method

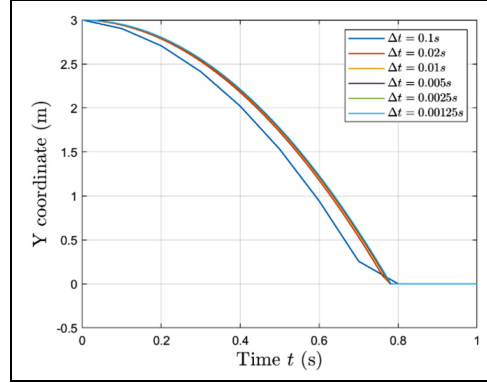


**Figure 7.** Numerical stability of the CCP approach. Y coordinate of one particle contact with different time steps from  $\Delta t = 0.1$  s to  $\Delta t = 0.00125$  s.

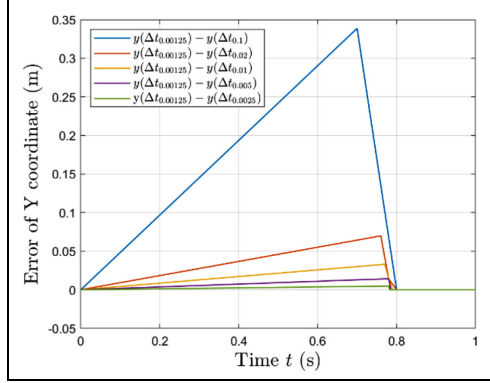
proposed in Kleinert et al.<sup>22</sup> in the first example. The second example investigates the simulation of multiple pendulum contact with CCP solvers.

### Comparison between the CCP method and the optimization-based method

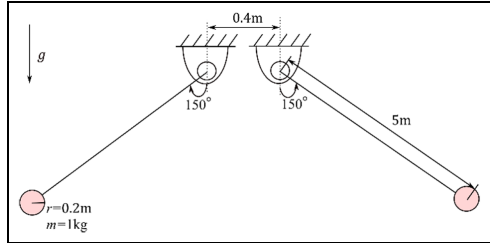
The dynamic example studies one particle fall on the horizontal ground. The initial position of the particle follows  $x = 0\text{m}, y = 3\text{m}$ , and the initial velocity is  $\dot{x} = 3\text{m/s}, \dot{y} = 0\text{m/s}$ . The particle is affected by gravity force, whose acceleration is  $g = 9.8\text{N/kg}$ , and the friction coefficient is  $\mu = 0.3$ . The mass of the particle is 1 kg and the time step  $\Delta t = 0.001$  s.

Figure 6 presents the displacements of the x and y directions for one particle with frictional contact. Some points at  $x = [0.5 \ 1 \ 1.5 \ 2 \ 2.34]$  have been separately measured from the figure of the study by M. Anitescu and added to Figure 6. Good agreement can be observed between the proposed optimization method in Anitescu<sup>23</sup> and CCP. As the figure displays, the particle stops on the ground after the contact. The coefficient of restitution is 0, which agrees with Stewart and Trinkle.<sup>16</sup>

To show how the value of the time step affects the precision of the solution, Figure 7 shows numerical solutions of the Y coordinate of one particle contact with an initial condition of  $x = 0\text{m}, y = 3\text{m}$ ,  $\dot{x} = 3\text{m/s}, \dot{y} = 0\text{m/s}$ . The simulation has been calculated with different time steps from  $\Delta t = 0.1$  s to  $\Delta t = 0.00125$  s. Here, the Y coordinates converge with the decrease of the value of  $\Delta t$ . Figure 8 gives an error estimate of the numerical results of Y coordinates at each time step from Figure 7. The solution for



**Figure 8.** Errors for numerical results of Y coordinates associated with Figure 7. The solution of  $\Delta t = 0.00125$  s is used as a converged value.



**Figure 9.** Initial position of the two pendulum system with two rigid balls.

$\Delta t = 0.00125$  s has been used as a converged value. For different values of  $\Delta t$ , the error measures used are  $error = |y(\Delta t) - y(\text{exact})|$ . The smaller the time step is, the closer the error converge to zero.

**Comparison between the CCP method and penalty method**

To compare the CCP method with the penalty method, a simple case of two pendulums with two balls illustrated in Figure 9 has been analyzed. Aim of this simple contact problem is to clarify importance of the contact parameters of the penalty method in dynamic response after contact. The parameters for the problem are given in Figure 9. The gravity is  $g = 9.8 \text{ kg/m}^3$ , and the coefficient of friction is  $\mu = 0.3$ . The time step is  $\Delta t = 0.0001$  s and the total time is 3 s.

The penalty method is based on dissipative contact force models, combining a linear spring with a linear damper. The contact force can be calculated as

$$F_N = K\delta^{3/2} + D\dot{\delta}\delta \quad (56)$$

where  $K$  is the stiffness coefficient and  $D$  is the damping coefficient. Indentation  $\delta$  is the distance between the contact points of the two balls. In equation (55),  $\dot{\delta}$  is the relative normal velocity between two contact points. The contact parameters of the penalty method have been chosen so that it gives agreement for vertical position solved with the CCP approach. For the penalty method, contact stiffness coefficient  $K = 3.6e^3 \text{ N/m}^{3/2}$  and damping coefficient  $D = 1.45e^5 \text{ N s/m}^2$ .

The difference of vertical position  $Y$  between the contact approaches is shown in Figure 10. An explicit Runge-Kutta method of order 4 has been used as numerical time integrator scheme for solving penalty method. In case of the CCP approach, the semi-implicit Euler has been used. The time step is  $\Delta t = 0.0001$  s is used for both time integration methods. For this simple case, the computation time for CCP is around six times slower than for the penalty method. However, when simulating tens of thousands of contact problems, a complementarity method seems to be a better choice.<sup>21,24</sup> Furthermore, the CCP approach does not produce stability problems due to unnecessary high

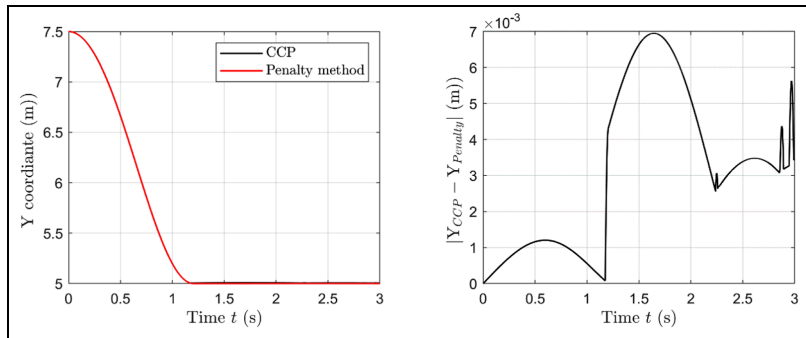


**Figure 10.** Y coordinates and the error of the pendulum ball from CCP approach and penalty method.

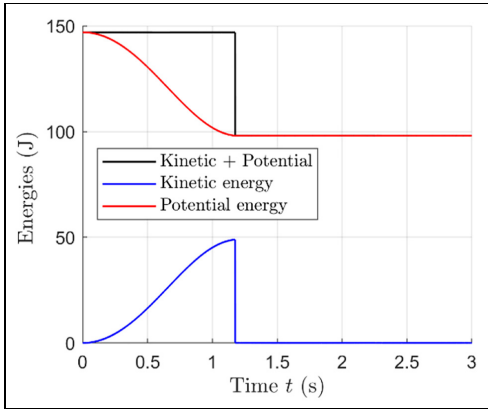


**Figure 11.** Energies of two-pendulum contact with CCP approach.

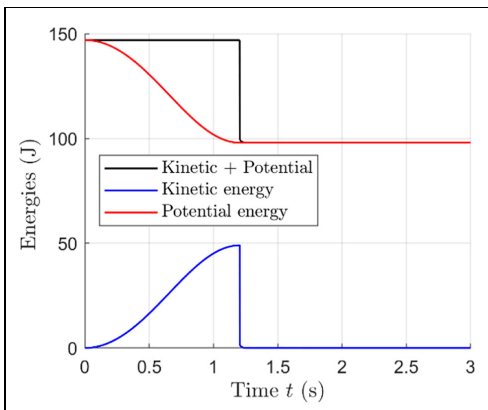


**Figure 12.** Two-pendulum contact with penalty method. Contact stiffness coefficient  $K = 3.6e^5 \text{ N/m}^{3/2}$ , damping coefficient  $D = 1.45e^5 \text{ N s/m}^2$ .

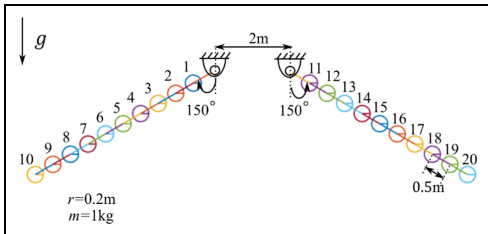


**Figure 13.** Initial position of the two pendulum system with multiple rigid balls.

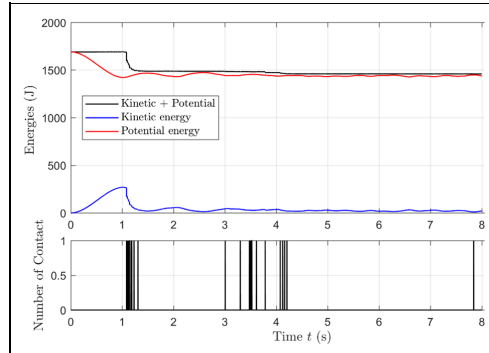


**Figure 14.** Energies and the number of contact of the whole system. The total number of the contact is 63 during an 8 s simulation.

eigenfrequencies which maybe be problematic in the case of the penalty method.

Potential and kinetic energy associated with the CCP approach and penalty method have been shown separately in Figures 11 and 12. As the two figures illustrate, the coefficient of restitution is 0. A change in the sum of kinetic and potential energy exists after inelastic contact. The material damping of the contact bodies is assumed to be the reason which causes energy loss.<sup>19</sup> In Figure 11, the energy changes instantly because of the nonlinear behavior of the CCP approach. However, in Figure 12, the energy changes continuously with the penalty method.

### Analysis of multiple pendulums

As shown in Figure 13, two pendulums of 20 bodies are fixed in the ceiling. The whole system is affected by the gravity force whose acceleration is  $g = 9.8 \text{ kg/m}^3$ , and the coefficient of friction is  $\mu = 0.3$ . The time step is  $\Delta t = 0.001 \text{ s}$  and the total time is 8 s.

Figure 14 displays the energies of the two pendulums when they fall down with zero initial velocity. The figure also shows the number of contacts during the process of two-pendulum contact. The sum of kinetic energy and potential energy decreases when the contact occurs between two pendulums. The change in the sum of kinetic and potential energy exists after each inelastic contact because the coefficient of the restitution is effectively zero with the cone complementarity approach.

Figure 15 shows the frames of the two pendulums from  $t = 1 \text{ s}$  to  $t = 1.3 \text{ s}$ . The contact bodies have been marked in the figure. In this example, neighbor bodies are falling down with gravity force and restricted by the rope inextensibility constraint.

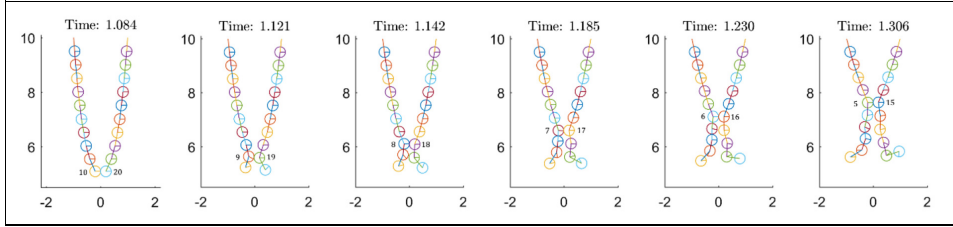


Figure 15. Frames of the simulation of two pendulums with inelastic collisions at  $t = [1.804 \ 1.121 \ 1.142 \ 1.185 \ 1.230 \ 1.306]$  s.

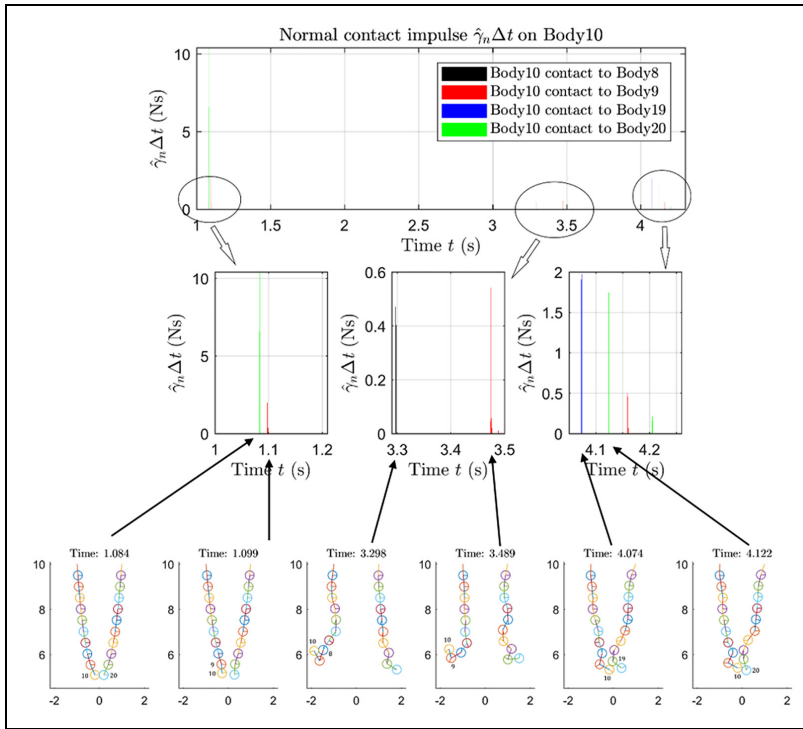


Figure 16. Normal contact impulse happened on body 10 during 8 s. Contact bodies and neighbor bodies at  $t = [1.804 \ 1.099 \ 3.298 \ 3.489 \ 4.074 \ 4.122]$  s have been shown in the frames.

Contact impulse  $\gamma = \hat{\gamma}\Delta t$ , which is the product of contact force  $\hat{\gamma}$  and time step  $\Delta t$  is calculated from equation (31) at each time step. Figure 16 shows the normal contact impulses  $\hat{\gamma}_n\Delta t$  on body 10 and the frames of the simulation at corresponding times. Frames of the simulation at corresponding time have been shown in Figure 16.

In Figure 16, the contact impulse between body 10 and body 20 at  $t = 1.084$  s is much greater than the contact impulses with other bodies. The contact at  $t = 1.084$  s is the first contact in the system. The generalized velocities of body 10 and body 20 are greater than the rest of bodies before contact.

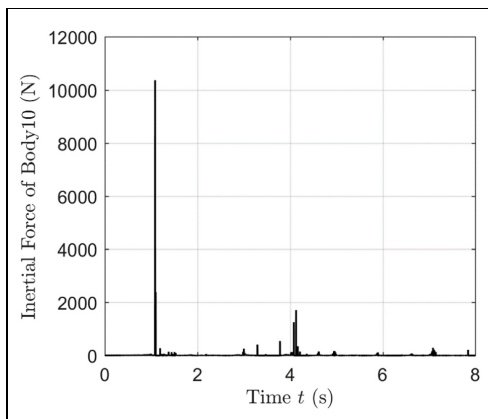


Figure 17. Inertial force of body 10.

Figure 17 shows the inertial force of body 10. The inertial force increases significantly when the contact takes place at the first contact when  $t = 1.084$  s during the simulation. The inertial force is calculated as follows

$$F_{inertial} = m \|\ddot{R}_x \quad \ddot{R}_y\| \quad (57)$$

where  $\ddot{R} = (\dot{R}^{(l+1)} - \dot{R}^{(l)})\Delta t$ .

The numerical simulations presented have been performed with MATLAB. These simulations show the convergence of the introduced algorithm and formulations in the case of multiple unilateral contacts.

## Conclusion

The method studied in this article can solve non-smooth rigid multibody frictional contacts. This article aims for a solution to a planar system with thousands of dynamical contacts and presents a novel method for solving the CCP that appears in the time integration approach. The introduced method is able to simulate colliding rigid bodies on a large scale. In addition, this article proposed and analyzed a method to analyze the contact dynamics of two pendulums. The Coulomb friction model utilized in this article is simplified into two equations, which is simpler than Coulomb friction model for the 3D case.<sup>18</sup> The coefficient of restitution after contact is 0, which agrees with the conclusion made in Stewart and Trinkle.<sup>16</sup> It is also the reason why CCP is widely used in contact applications of powder composites, granular flows.<sup>18</sup> The energy change has been

explained by comparing the introduced approach with penalty method.

In the future, this work can be combined with the implicit time-stepping method and elastic contacts which could be utilized in a virtual interactive environment for training, clinical therapies, military purposes, and video games.

## Acknowledgement

The authors would like to thank the Academy of Finland (application no. 299033 for the funding of Academy Research Fellows) for supporting Marko K. Matikainen.

## Declaration of conflicting interests

The author(s) declared no potential conflicts of interest with respect to the research, authorship, and/or publication of this article.

## Funding

The author(s) received no financial support for the research, authorship, and/or publication of this article.

## ORCID iDs

Xinxin Yu  <https://orcid.org/0000-0002-7740-9643>

Marko K. Matikainen  <https://orcid.org/0000-0003-3683-0199>

## References

1. Jaeger HM, Nagel SR and Behringer RP. Granular solids, liquids, and gases. *Rev Modern Phys* 1996; 68: 1259–1273.
2. Hastings MB, Daya ZA, Ben-Naim E, et al. Entropic tightening of vibrated chains. *Phys Rev E* 2002; 66: 025102.
3. Belmonte A, Shelley MJ, Eldakar ST, et al. Dynamic patterns and self-knotting of a driven hanging chain. *Phys Rev Lett* 2001; 87: 114301.
4. Fortin J, Millet O and de Saxcé G. Numerical simulation of granular materials by an improved discrete element method. *Int J Numer Meth Eng* 2005; 62: 639–663.
5. Braun M. On some properties of the multiple pendulum. *Arch Appl Mech* 2003; 72: 899–910.
6. Nigmatullin RR, Osokin SI, Awrejcewicz J, et al. The fluctuation spectroscopy based on the scaling properties of beta-distribution: analysis of triple pendulum data. *Mech Syst Sig Process* 2015; 52–53: 278–292.
7. Plaut RH and Virgin LN. Pendulum models of ponytail motion during walking and running. *J Sound Vib* 2013; 332: 3768–3780.
8. Humphrey LR and Hemami H. A computational human model for exploring the role of the feet in balance. *J Biomech* 2010; 43: 3199–3206.

9. Segers V, Aerts P, Lenoir M, et al. Dynamics of the body centre of mass during actual acceleration across transition speed. *J Exp Biol* 2007; 210: 578–585.
10. Dao ND, Ryan KL, Sato E, et al. Predicting the displacement of triple pendulumTM bearings in a full-scale shaking experiment using a three-dimensional element. *Earthquake Eng Struct Dyn* 2013; 42: 1677–1695.
11. Pang JS and Trinkle JC. Complementarity formulations and existence of solutions of dynamic multi-rigid-body contact problems with coulomb friction. *Mathematical Programming* 1996; 73: 199–226.
12. Jones CN and Morrari M. Multiparametric linear complementarity problems. In: *Proceedings of the 45th IEEE conference on decision and control*, San Diego, CA, 13–15 December 2000, pp.5687–5692. New York: IEEE.
13. Kocvara M and Zowe J. An iterative two-step algorithm for linear complementarity problems. *Numerische Mathematik* 1994; 68: 95–106.
14. Yao W-L, Chen B, Liu C-S, et al. Dynamics of multi-rigid-body systems under non-smooth constraints and linear complementarity problems. *Int J Comput Math* 2008; 85: 889–898.
15. Anitescu M and Hart GC. A fixed-point iteration approach for multibody dynamics with contact and small friction. *Math Prog* 2004; 101: 3–32.
16. Stewart DE and Trinkle JC. An implicit time-stepping scheme for rigid body. *Int J Numer Meth Eng* 1996; 39: 2673–2691.
17. Tasora A and Anitescu M. A fast NCP solver for large rigid-body problems with contacts, friction, and joints. In: *Multibody dynamics*, Vol. 12. Dordrecht: Springer, 2009, pp.45–55.
18. Negrut D, Serban R and Tasora A. Posing multibody dynamics with friction and contact as a differential complementarity problem. *J Comput Nonlin Dyn* 2017; 13: 014503.
19. Lankarani HM and Nikravesh PE. Continuous contact force models for impact analysis in multibody systems. *Nolin Dyn* 1994; 5: 193–207.
20. Machado M, Moreira P, Flores P, et al. Complaint contact force models in multibody dynamics: evolution of the Herz contact theory. *Mech Mach Theor* 2012; 53: 99–121.
21. Tasora A, Negrut D and Anitescu M. Large-scale parallel multi-body dynamics with frictional contact on the graphical processing unit. *Proc IMechE, Part K: J Multi-Body Dynamics* 2008; 222: 315–326.
22. Kleinert J, Simeon B and Dreßler K. Nonsmooth contact dynamics for the large-scale simulation of granular material. *J Comput Appl Math* 2017; 316: 345–357.
23. Anitescu M. Optimization-based simulation of non-smooth rigid multibody dynamics. *Math Prog* 2006; 105: 113–143.
24. Anitescu M and Tasora A. An iterative approach for cone complementarity problems for nonsmooth dynamics. *Comput Optim Appl* 2010; 47: 207–235.
25. Hogue C. Shape representation and contact detection for discrete element simulations of arbitrary geometries. *Eng Comput* 1998; 15: 374–390.
26. Stronge WJ, James R and Ravan B. Oblique impact with friction and tangential compliance. *Philos Trans Math Phys Eng Sci* 2001; 359: 2447–2465.
27. Moreau JJ. Unilateral contact and dry friction in finite freedom dynamics. In: Moreau JJ and Panagiotopoulos PD (eds) *Nonsmooth mechanics and applications* (CISM Course and Lectures), Vol. 302. Vienna: Springer, 1988, pp.1–82.
28. Pfeiffer F and Glocker F. *Multibody dynamics with unilateral contacts*. Hoboken, NJ: John Wiley & Sons, 1996.



## Publication II

Yu, X., Matikainen, M. K., Harish, A. B., and Mikkola, A.

**Procedure for non-smooth contact for planar flexible beams with  
cone complementarity problem**

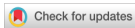
Reprinted with permission from

*Proceedings of the Institution of Mechanical Engineers, Part K: Journal of  
Multi-body Dynamics*

(2020) 1464419320957450

© 2020, the authors.





# Procedure for non-smooth contact for planar flexible beams with cone complementarity problem

Proc IMechE Part K:  
J Multi-body Dynamics  
0(0) 1–18  
© IMechE 2020  
Article reuse guidelines:  
sagepub.com/journals-permissions  
DOI: 10.1177/1464419320957450  
journals.sagepub.com/home/pik



Xinxin Yu<sup>1</sup> , Marko K Matikainen<sup>1</sup>, Ajay B Harish<sup>2</sup> and Aki Mikkola<sup>1</sup>

## Abstract

Contact description plays an important role in modeling of applications involving flexible multibody dynamics. Example of such applications include contact between a belt and pulley, crash-worthiness analysis in aerospace and automotive engineering. Approaches such as the linear complementarity problem (LCP), nonlinear complementarity problem (NCP) and penalty method have been proposed for contact detection and imposition of contact constraints. Contact description within multibody dynamics, however, continues to be a challenging topic, particularly in the case of flexible bodies. This paper describes and compares the use of two contact descriptions in the framework of flexible multibody dynamics; (1) the use of nonlinear cone complementarity approach (CCP) and (2) the penalty method. Both contact models are presented together with a master-slave detection algorithm. The modified form of node-to-node approach presented facilitates creation of pseudo-nodes where gap function can be calculated. This reduces the cumbersome effort of contact search. Since large deformations can be an important phenomenon in flexible multibody applications, beam elements based on the absolute nodal coordinate formulation (ANCF) are implemented in this study. To make a comparison of two approaches, the damping component is included in the penalty method by using the continuous contact model introduced by Hunt and Crossley. Numerical results are based on the simulation of ANCF beam contact with rigid ground, rigid body with an arbitrary shape and pendulum contact. Although kinematic results show a good agreement between both approaches when the coefficient of restitution is zero, the unphysical interpenetration appears in the penalty method. Nonlinear minimization problem solved by CCP approach helps to prevent the penetration during contact event. Furthermore, the proposed contact detection algorithm is proved to be capable of being used for multiple contact between beam and arbitrary shape rigid body; different contact types, such as side-by-side and corner-by-side, can be performed without prediction.

## Keywords

ANCF, contact mechanics, cone complementarity problem, penalty method

Date received: 2 March 2020; accepted: 12 August 2020

## Introduction

Computational contact mechanics is a topic of significant industrial and research interest due to its numerous applications. Simple applications like contact between a belt and pulley to more complex engineering applications like automotive impacts demonstrate the need for accurate modeling of contact within a framework of deformable bodies.

### Beam-to-beam contact

Several works have been presented that consider quasi-static scenarios, particularly from 3D<sup>1</sup> to beam-to-beam contact.<sup>2</sup> Wriggers and Zavarise<sup>2</sup> proposed a computational algorithm to describe the

frictionless contact between three dimensional (3-D) circular beams. The algorithm was subsequently augmented to introduce an extension for the case of frictional contact.<sup>3</sup> Litewka and Wriggers<sup>4,5</sup> later analyzed contact between 3-D beams of rectangular cross-section for both frictionless and frictional

<sup>1</sup>Department of Mechanical Engineering, LUT University, Lappeenranta, Finland

<sup>2</sup>Department of Civil and Environmental Engineering, University of California, Berkeley, CA, USA

**Corresponding author:**  
Xinxin Yu, Department of Mechanical Engineering, LUT University, Yliopistonkatu 34, 53850 Lappeenranta, Finland.  
Email: xinxin.yu@lut.fi

cases. While node-to-node and surface-to-surface strategies are commonly used, Litewka<sup>6</sup> has proposed a smoothing procedure based on Hermite polynomials for contact description. Along similar lines, Konyukhov and Schweizerhof<sup>7</sup> studied curve-to-curve contact within a geometrically exact description in the co-variant form to analyze the normal and tangential contact as well as rotational interactions between the curves. Research has largely focused on small deformations, an exception is,<sup>8</sup> who proposed an approach to simulate frictional contact interactions of beams that considered large deformations. In the work, Durville used (finite element method) FEM concepts to discuss self-contact of beams, defined from the proximity zones using intermediate geometry. Diverging from mainstream computational contact mechanics, Boso et al.<sup>9</sup> extended the earlier ideas to include multiphysics problems with coupled electro-mechanical fields.

A node-to-node contact strategy between beams is commonly used, for example in Refs.<sup>6,9,10</sup> In addition, Wriggers and Zavarise<sup>2</sup> proposed orthogonality conditions for arbitrary contact between two beams. In their work, the minimal distance criterion is utilized to detect the closest points on the center lines of beams in contact. Extending the ideas advanced in Refs.,<sup>5,6</sup> Litewka<sup>11</sup> proposed a surface-to-surface approach for beam-to-beam contact. Based on the mortar method, Puso and Laursen<sup>12,13</sup> developed a segment-to-segment contact method that can prevent over-constraints caused by the node-on-segment contact approach in the event of large sliding with and without friction. Later, Fischer and Wriggers<sup>14</sup> compared contact constraints with the mortar method by using Lagrange multipliers and the penalty method. In their work, they argued that the Lagrange multiplier method needs element-wise contact detection, whereas the penalty method requires point-wise detection. Puso et al.<sup>15</sup> extended the mortar contact method for higher order element formulations in large deformation frictional contact. Hesch and Betsch<sup>16</sup> extended an energy-momentum conserving method to the mortar contact method. Recently, Neto and Wriggers<sup>17</sup> proposed a master-to-master element formulation for the beam-to-beam contact as a generalization of the other types of formulations.

All the above papers use standard finite element interpolations. Wang et al.,<sup>10</sup> however, discussed frictional contact of thin beams using the absolute nodal coordinate formulation (ANCF), a nonlinear finite element formulation. In their work, the closest point projection (CPP) procedure, which can detect the positions of two promising points in contact, has mostly been used for the detection of contact points.

#### **Absolute nodal coordinate formulation**

The ANCF is a finite element based approach that can predict the dynamic responses of structures

such as beams, plates and shell-like bodies subjected to large deformations<sup>18</sup> in multibody applications. Use of absolute position vectors and slope coordinates which define the element orientation<sup>19,20</sup> leads to a constant and symmetric mass matrix and identically zero centrifugal and Coriolis forces. In the ANCF context, the constant and symmetric mass matrix can provide some advantages during analysis of dynamic conditions.<sup>19</sup>

#### **Complementarity approach**

The non-smooth nature of the non-interpenetration and the friction constraints during dynamic contact<sup>21</sup> has resulted in many numerical methods including time integration approaches being proposed.<sup>22,23</sup> It should be noted that time integration based approaches need small time steps to achieve numerical stability in the case of multiple contacts. Researchers have proposed innovative optimization methods to solve this class of problems, for example, the linear complementarity problem (LCP)<sup>24,25</sup> and nonlinear complementarity problem (NCP).<sup>26</sup> The LCP method is frequently used to solve two-dimensional contact simulations by employing Lemke's algorithm, while the NCP, in turn, is recommended for use with three-dimensional contact.<sup>27</sup>

It is important to note that LCP and NCP solvers have limitations when addressing contact problems with a large number of contacts and when polyhedral approximation is used in the friction model.<sup>23</sup> To circumvent these difficulties, the cone complementarity problem (CCP) approach has been introduced. The method has been utilized by Tasora et al.<sup>28</sup> for the simulation of non-smooth rigid multibody dynamics with collision, contact and friction by solving a convex quadratic program with a fixed time step. Anitescu<sup>22</sup> subsequently proposed a time integration formulation method and a fixed-point iteration algorithm to solve a large problem involving numerous contacts with the CCP solver. Working along the same lines, Tasora et al.<sup>28</sup> found that in the CCP, simulation time increases linearly with respect to the number of bodies.

#### **Novelty and objective of this work**

Previously, the cone complementarity problem has only been used to describe contacts between rigid bodies.<sup>29,30</sup> However, the proposed approach<sup>31</sup> is developed for modeling of contact between deformable bodies. This paper introduces an important extension of the CCP approach to flexible bodies in the planar case. The method can also be applied to solve practical problems involving multiple contact interaction between flexible and rigid bodies.

The rest of the paper is organized as follows: The next section briefly introduces the kinematics of the rigid body and beam element based on the ANCF

and equations of motion. Contact geometry and contact detection are presented in ‘‘Contact description’’ section. This is followed by section in which describes contact force calculation with the rigid body and ANCF beam separately. The applied model of imposition of contact based on the penalty method and CCP approach is explained in detail in the same section. To validate the proposed approach, ‘‘Numerical examples’’ section presents three numerical examples. The paper concludes by summarizing the main findings and proposes possible areas for future research in final section.

### Equation of motion for rigid and flexible bodies

This section introduces the kinematic description of a rigid body and ANCF beam, and the equation of motion for a system that describes the contact of a flexible beam and rigid body.

#### Kinematics of rigid body

Cartesian generalized coordinates for a planar rigid body can be written as

$$\mathbf{q}_{RB} = [\mathbf{R}^T \quad \varphi]^T \quad (1)$$

where  $\mathbf{R} = [R_x \quad R_y]^T$  is the global position vector of the origin of the body reference coordinate system and  $\varphi$  is the rotational coordinate of the body.<sup>32</sup>

Assuming that the body reference coordinate system is located at the center of the mass, the equation of motion for the rigid body can be written as:

$$\mathbf{M}_{RB} \dot{\mathbf{q}}_{RB} - \mathbf{F}_{exter.RB} - \mathbf{F}_{c.RB} = 0 \quad (2)$$

where  $\mathbf{F}_{exter.RB}$  is the vector of generalized external forces,  $\mathbf{F}_{c.RB}$  is the vector of contact forces and  $\mathbf{M}_{RB}$  is the mass matrix that can be written as:

$$\mathbf{M}_{RB} = \text{diag}\{m\mathbf{I}_{2 \times 2}, J\} \quad (3)$$

where  $m$  is the mass of the rigid body,  $J$  is the mass moment of inertia defined with respect to the center of mass, and  $\mathbf{I}_{2 \times 2}$  is the identity matrix of size  $2 \times 2$ .

#### Kinematics of ANCF

The ANCF beam element used in this study and shown in Figure 1 consists of three nodes that are located at the end points and at the midpoint of the longitudinal axis of the beam.<sup>33</sup>

One position vector and one slope vector are used as the nodal coordinates at each nodal location. The position vector is denoted by  $r$  and the slope vector can be defined as the derivative of position vector  $r_{,y} = \frac{\partial r}{\partial y}$ . Accordingly, the vector of the nodal position coordinates  $\mathbf{q}_{fb}$  for the element, as shown in Figure 1, is:

$$\mathbf{q}_{fb} = [r^{(1)T} \quad r_{,y}^{(1)T} \quad r^{(2)T} \quad r_{,y}^{(2)T} \quad r^{(3)T} \quad r_{,y}^{(3)T}]^T \quad (4)$$

Since four degrees of freedom are specified at each node, a three-noded beam element has a total of 12 degrees of freedom. The shape functions are defined for the reference element in the local coordinate system of the element  $(\xi, \eta)$  as:

$$N_1(\xi, \eta) = \frac{(\xi + 1)^2}{2} - \frac{3\xi}{2} - \frac{1}{2}$$

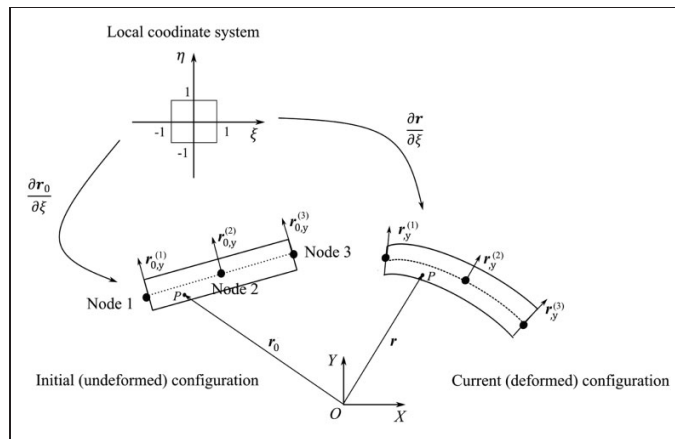


Figure 1. Beam element kinematics defined in reference and deformed configuration.

$$\begin{aligned}
N_2(\xi, \eta) &= \frac{\ell_y \eta}{2} + \frac{\ell_y \eta (\xi + 1)^2}{4} - \frac{3\ell_y \eta (\xi + 1)}{4}, \\
N_3(\xi, \eta) &= 2\xi - (\xi + 1)^2 + 2, \\
N_4(\xi, \eta) &= 2\xi - (\xi + 1)^2 + 2, \\
N_5(\xi, \eta) &= \ell_y \eta (\xi + 1) - \frac{\ell_y \eta (\xi + 1)^2}{2}, \\
N_6(\xi, \eta) &= \frac{\ell_y \eta (\xi + 1)^2}{4} - \frac{\ell_y \eta (\xi + 1)}{4}
\end{aligned} \quad (5)$$

where the non-dimensional quantities  $(\xi, \eta)$  are defined as:

$$\xi = \frac{2x}{\ell_x}; \quad \eta = \frac{2y}{\ell_y} \quad (6)$$

where  $\ell_x$  is the length and  $\ell_y$  is the height of the beam element in the undeformed configuration.

The shape function matrix for the beam element can be written with the help of equation (5) in the following way:

$$\mathbf{N}_m = [N_1 \mathbf{I} \quad N_2 \mathbf{I} \quad N_3 \mathbf{I} \quad N_4 \mathbf{I} \quad N_5 \mathbf{I} \quad N_6 \mathbf{I}] \quad (7)$$

where  $\mathbf{I}$  is a  $2 \times 2$  identity matrix.

In the ANCF, any arbitrary point of the element can be defined with respect to the global coordinates using the shape function equation (7) and the vector of the nodal position coordinates equation (4) as:

$$\mathbf{r} = \mathbf{N}_m \mathbf{q}_{fb} \quad (8)$$

### Equation of motion for the element

In ANCF, the equation of motion in the weak form can be derived using the concept of the weak form (variational energy) as follows:

$$\begin{aligned}
\delta \Pi(\mathbf{r}, \delta \mathbf{r}) &= \delta \int_{t_1}^{t_2} (W_{kin} - W_{elast} + W_{exter} + W_c) dt \\
&= 0
\end{aligned} \quad (9)$$

where  $W_{kin}$  is the kinetic energy of the element,  $W_{elast}$  is the strain energy of the element,  $W_{exter}$  is the work done by the externally applied forces, and  $W_c$  is the energy added during contact. It is important to note here that the energy related to the contact is absent when the gap function is zero or positive but only considered in the presence of interpenetration. Thus, this energy is equivalent to moving the body by an amount equivalent to the un-physical interpenetration. In equation (9),  $t_1$  and  $t_2$  are integration limits with respect to time  $t$ .

For the structural mechanics based ANCF beam element,<sup>33</sup> the variations of strain energy associated

with beam bending and torsion in terms of the nodal coordinate  $\mathbf{q}_{fb}$  can be expressed as follows:

$$\begin{aligned}
\delta W_{elast}^{bend,tors.} &= \left( \int_0^L \left( EA \frac{\partial \Gamma_1}{\partial \mathbf{q}_{fb}} + k_s GA \frac{\partial \Gamma_2}{\partial \mathbf{q}_{fb}} \right. \right. \\
&\quad \left. \left. + EI_z \frac{\partial K_r}{\partial \mathbf{q}_{fb}} \right) dx \right) \cdot \delta \mathbf{q}_{fb}
\end{aligned} \quad (10)$$

where  $E$  and  $G$  are the Young's modulus and shear modulus, respectively,  $\Gamma_1$  and  $\Gamma_2$  are the generalized strains,  $I_z$  is the second moment of inertia,  $k_s$  is the shear correction factor and  $K_r$  measures the rotation of cross-section plane with respect to the reference length.

The additional variations of the strain energy accounting for thickness deformation can be considered as follows:

$$\delta W_{elast}^{thickness} = \int_0^L EA \frac{\partial E_{yy}}{\partial \mathbf{q}_{fb}} dx \cdot \delta \mathbf{q}_{fb} \quad (11)$$

where the transverse strain component  $E_{yy}$  is defined from the Green-Lagrange strain tensor.

The total strain energy is:

$$W_{elast} = W_{elast}^{bend,tors.} + W_{elast}^{thickness} \quad (12)$$

The weak form from equation (9) must hold for any virtual coordinate  $\delta \mathbf{q}_{fb}$ , the equation of motion for ANCF can be written as:

$$\mathbf{M}_e \ddot{\mathbf{q}}_{fb} + \mathbf{F}_{elast,e} - \mathbf{F}_{exter,e} - \mathbf{F}_{c,e} = \mathbf{0} \quad (13)$$

where  $\mathbf{M}_e$  is the mass matrix,  $\mathbf{F}_{elast,e}$  is the elastic force vector,  $\mathbf{F}_{exter,e}$  is the external force vector and  $\mathbf{F}_{c,e}$  is the contact force vector of the ANCF beam.

### Equation of motion for rigid and flexible bodies

The generalized coordinate  $\mathbf{q}$  consists of the rigid body coordinate  $\mathbf{q}_{RB}$  and nodal position coordinate  $\mathbf{q}_{fb}$ :

$$\mathbf{q} = \begin{bmatrix} \mathbf{q}_{RB} \\ \mathbf{q}_{fb} \end{bmatrix} \quad (14)$$

Rearranging the equation of motion for the rigid body and ANCF beam (see equations (2) and (13)), the equation of motion in ODE (Ordinary Differential Equations) form can be written for a system of rigid and flexible bodies as follows:

$$\begin{bmatrix} \dot{\mathbf{q}} \\ \ddot{\mathbf{q}} \end{bmatrix} = \begin{bmatrix} \mathbf{I} \\ \mathbf{M}^{-1} \end{bmatrix} \begin{bmatrix} \dot{\mathbf{q}} \\ \mathbf{F}_{exter} - \mathbf{F}_{elast} + \mathbf{F}_c \end{bmatrix} \quad (15)$$

where  $\mathbf{M} = \text{diag}\{\mathbf{M}_{RB}, \mathbf{M}_e\}$  is the mass matrix,  $\mathbf{F}_{exter} = [\mathbf{F}_{exter,RB} \ \mathbf{F}_{exter,e}]^T$  is the external force,  $\mathbf{F}_{elast} = [\mathbf{F}_{elast,e}]^T$  is the elastic force and  $\mathbf{F}_c = [\mathbf{F}_{c,RB} \ \mathbf{F}_{c,e}]^T$  is the contact force.

The equation of motion in ODE form of equation (15) is solved by the semi-implicit Euler method as follows:

$$\begin{aligned} \dot{\mathbf{q}}^{(l+1)} &= \dot{\mathbf{q}}^{(l)} + \ddot{\mathbf{q}}^{(l)} \Delta t \\ \mathbf{q}^{(l+1)} &= \mathbf{q}^{(l)} + \dot{\mathbf{q}}^{(l+1)} \Delta t \end{aligned} \quad (16)$$

where  $\Delta t$  is time step.

### Contact description

Node-to-node, node-to-surface and surface-to-surface strategies are commonly used for contact descriptions within deformable bodies.<sup>2,7,34</sup> The modified form of node-to-node contact strategy between the beam and the rigid body is implemented in this work. The method presented here facilitates the creation of pseudo-nodes where the gap function can be calculated. This reduces the cumbersome effort of contact search. As shown in Figure 2, predefined slave points, are distributed equally along the beam surface. Slave contact points are used to find the corresponding master point (potential contact point) on the rigid body using an orthogonality condition.<sup>6,9,10,35</sup> The orthogonality condition states that the line connecting potential contact points is perpendicular to the tangent lines at the contact points.

Given the slave point  $\mathbf{r}_P$  (obtained from equation (8)) on the beam, the corresponding master point  $\mathbf{r}_Q$  on the rigid body has to be determined using orthogonality condition:

$$h(x) = (\mathbf{r}_P - \mathbf{r}_Q(x))^T \mathbf{t}_Q(x) = 0 \quad (17)$$

where  $\mathbf{r}_Q$  and  $\mathbf{t}_Q$  are the position vector and tangential vector of master point on the rigid body, which can be expressed as:

$$\mathbf{r}_Q = \mathbf{R} + \mathbf{A}\bar{\mathbf{u}}_Q(x), \quad \mathbf{t}_Q = \mathbf{A}\bar{\mathbf{t}}_Q(x) \quad (18)$$

where  $\mathbf{A}$  is body transformation matrix,  $\bar{\mathbf{u}}_Q(x) = [x \ g(x)]^T$  and  $\bar{\mathbf{t}}_Q(x) = [1 \ \partial g(x)/\partial x]^T$ .

Equation (17) leads to a nonlinear equation in one unknown variable  $x$  which can be solved using the Newton-Raphson method. The coordinates of the slave points on the beam are used as the initial values to start the Newton-Raphson iteration.

For, a given  $i$ -th contact, gap function  $\Phi_i$  is the signed distance between the two potential contact points  $\mathbf{r}_P$  and  $\mathbf{r}_Q$ . This distance can be computed based on the distance vector  $\mathbf{d}_{PQ}$  and the normal vector  $\mathbf{n}_Q$  as follows:

$$\Phi_i = -(\mathbf{d}_{PQ})^T \mathbf{n}_Q \quad (19)$$

where  $\mathbf{d}_{PQ} = \mathbf{r}_P - \mathbf{r}_Q$  is the distance vector and  $\mathbf{n}_Q$  is the normal vector which is perpendicular with respect to  $\mathbf{t}_Q$ .

After the gap function  $\Phi_i$  is obtained, the contact criterion can be written as:

$$\begin{cases} \Phi_i < 0 & \Rightarrow \text{Contact occurs} \\ \Phi_i \geq 0 & \Rightarrow \text{No contact} \end{cases} \quad (20)$$

When the gap function is less than zero, the contact takes place between the beam and the rigid body.

### Contact force calculation

To improve the computation efficiency, only the set of potential contact points will be considered in the contact calculation. The tolerance  $\epsilon$  is used to define a

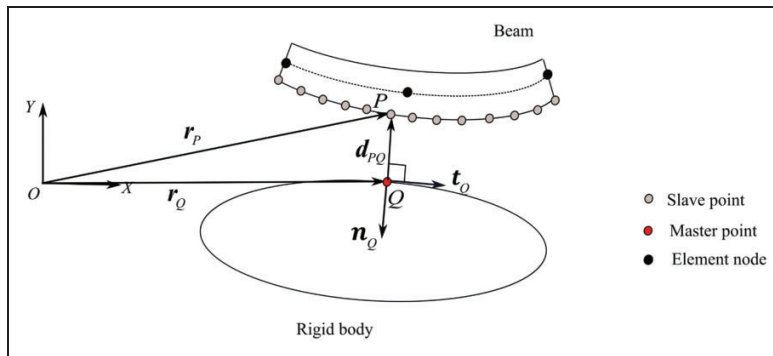


Figure 2. Element contact detection.

distance threshold to select the potential contact points from the pairs of slave-master points:<sup>25,36</sup>

$$\Phi_i \leq \epsilon \quad (21)$$

where  $\epsilon$  is the parameter that determines the activation of contact computation. The physical meaning of  $\epsilon$  is the normal distance between the potential contact points. In this work, the value of  $\epsilon$  is set as  $1 \times 10^{-4}$ . It has been observed that the value used offers an improved numerical convergence.

After having obtained the pairs of potential contact points from contact detection, this section will introduce the contact force is calculated and imposed on the flexible bodies.

### Contact force model

Consider the case of contact of a beam with a rigid body, as shown in Figure 3.

In the above case, for  $i$ -th contact, the normal contact force vector  $\mathbf{F}_{i,n}^Q$  and tangential contact force vector  $\mathbf{F}_{i,t}^Q$  are imposed on the rigid body by means of components of normal vector  $\mathbf{n}_Q$  and tangential vector  $\mathbf{t}_Q$  on the contact point  $Q$ , such that:

$$\mathbf{F}_i^Q = \mathbf{F}_{i,t}^Q + \mathbf{F}_{i,n}^Q = [\mathbf{t}_Q \quad \mathbf{n}_Q] \begin{bmatrix} f_{i,t} \\ f_{i,n} \end{bmatrix} = \mathbf{A} \mathbf{f}_i \quad (22)$$

where  $\mathbf{A}_i = [\mathbf{t}_Q \quad \mathbf{n}_Q]$  is the orthogonal rotation matrix consisting of unit orthogonal tangential  $\mathbf{t}_Q$  and normal vector  $\mathbf{n}_Q$  at the contact point  $Q$ ,  $\mathbf{f}_i = [f_{i,t} \quad f_{i,n}]^T$  is the vector corresponding to the magnitudes of tangential and normal contact forces.

The variation of energy associated with contact force  $\mathbf{F}_i^Q$  for rigid body<sup>36,37</sup> is:

$$\begin{aligned} \delta W_{c,i,Q} &= (\mathbf{F}_i^Q)^T \delta \mathbf{r}_Q = \mathbf{f}_i^T \mathbf{A}_i^T (\delta \mathbf{R} - \mathbf{A} \tilde{\mathbf{u}}_Q \delta \varphi) \\ &= \begin{bmatrix} \mathbf{A} \mathbf{f}_i \\ -\tilde{\mathbf{u}}_Q^T \mathbf{A}^T \mathbf{A} \mathbf{f}_i \end{bmatrix}^T \delta \mathbf{q}_{RB} \end{aligned} \quad (23)$$

where  $\delta \mathbf{q}_{RB} = [\delta \mathbf{R}^T \quad \delta \varphi]^T$  and  $\delta \mathbf{r}_Q = \delta \mathbf{R} - \mathbf{A} \tilde{\mathbf{u}}_Q \delta \varphi$ , in which  $\tilde{\cdot}$  is the tilde operator, which can be explained as follows:

$$\mathbf{a} = [x \quad y]^T, \quad \tilde{\mathbf{a}} = [-y \quad x]^T \quad (24)$$

It is worth noting that the contact force  $\mathbf{F}_i^P$  on the beam is the reaction force of  $\mathbf{F}_i^Q$  as:

$$\mathbf{F}_i^P = -\mathbf{F}_i^Q \quad (25)$$

The variation of energy  $\delta W_{c,i,P}$  associated with contact force  $\mathbf{F}_i^P$  on the beam can be expressed as:

$$\begin{aligned} \delta W_{c,i,P} &= (\mathbf{F}_i^P)^T \delta \mathbf{r}_P = -\mathbf{f}_i^T (\mathbf{A}_i)^T \mathbf{N}_m^P \delta \mathbf{q}_{fb} \\ &= -[(\mathbf{N}_m^P)^T \quad \mathbf{A} \mathbf{f}_i]^T \delta \mathbf{q}_{fb} \end{aligned} \quad (26)$$

where  $\delta \mathbf{r}_P = \mathbf{N}_m^P \delta \mathbf{q}_{fb}$ . Then, the total variation of energy in the system is:

$$\delta W_{c,i} = \delta W_{c,i,Q} + \delta W_{c,i,P} = \begin{bmatrix} \mathbf{A} \mathbf{f}_i \\ -\tilde{\mathbf{u}}_Q^T \mathbf{A}^T \mathbf{A} \mathbf{f}_i \\ -(\mathbf{N}_m^P)^T \mathbf{A} \mathbf{f}_i \end{bmatrix}^T \delta \mathbf{q} \quad (27)$$

where

$$\delta \mathbf{q} = \begin{bmatrix} \delta \mathbf{q}_{RB} \\ \delta \mathbf{q}_{fb} \end{bmatrix}, \quad \mathbf{F}_{c,i} = \mathbf{D} \mathbf{f}_i, \quad \mathbf{D}_i = \begin{bmatrix} \mathbf{A}_i \\ -\tilde{\mathbf{u}}_Q^T \mathbf{A}^T \mathbf{A}_i \\ -(\mathbf{N}_m^P)^T \mathbf{A}_i \end{bmatrix} \quad (28)$$

For  $i$ -th contact,  $\mathbf{D}_i$  is a transformation matrix which can define the location and direction of the contact force in global coordinate system. The  $\mathbf{D}_i$  matrix is computed based on the  $i$ -th pair of potential contact points. If there is  $N_k$  presence of contact

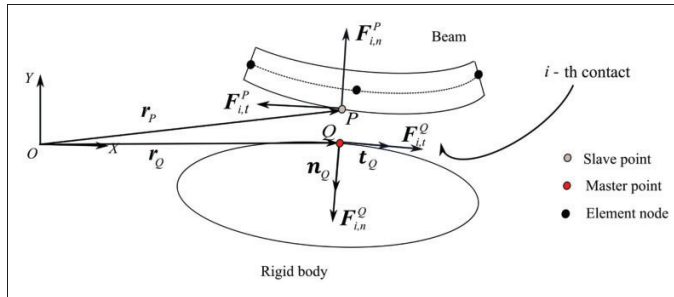


Figure 3. Illustration of element A contact with rigid body B.

events happen at same time step,  $\mathbf{D}$  matrix and vector  $\mathbf{f}$  can be built as:

$$\mathbf{D} = \underbrace{\begin{bmatrix} \mathbf{D}_1 & \mathbf{D}_2 & \cdots & \mathbf{D}_{N_k} \end{bmatrix}}_{N_{dof} \times 2N_k}$$

$$\mathbf{f} = \left. \begin{bmatrix} f_1 \\ f_2 \\ \vdots \\ f_{N_k} \end{bmatrix} \right\} 2N_k \times 1 \quad (29)$$

where  $N_{dof}$  is the total number of freedom of rigid body and beam.

### Penalty method

In multibody dynamics applications, the penalty method and the method based on complementary conditions are two well-known approaches to simulate contact phenomenon. The penalty method and other classical methods such as the method of Lagrange multipliers and Augmented Lagrangian method are often used in contact description between flexible bodies in the finite element method. However, both methods are computationally intensive and lead to other numerical issues due to non positive definiteness of the stiffness matrix. Such methods are thus, unsuitable for any type of real-time modeling motivation. In the penalty method, contact force can be expressed as a continuous function of penetration between two surfaces.<sup>38-40</sup> This variant of the penalty method introduced in Ref.<sup>39</sup> is also known as a continuous contact force model and is implemented in this paper. The drawback of this approach is that the stiffness constant depends non-linearly on the penetration, material property and surface geometries. Accordingly, the use of a small stiffness constant will lead to a large penetration, which can be considered being as physically unrealistic. Alternatively, high values of the stiffness contact might lead to a stiff system of ordinary differential equations which increase the computational effort during the simulation. In the complementarity approach, the nonlinear minimizing problem is solved to prevent the penetration between the contact surfaces.<sup>25</sup>

The normal contact force  $f_{i,n}$  is computed based on the Hertzian model, included the elastic and dissipative components<sup>41,42</sup> as:

$$f_{i,n} = K\delta_i^n + \chi_i\delta_i^n\dot{\delta}_i, \quad n = 1.5 \quad (30)$$

where  $K$  is the generalized stiffness constant,  $\chi_i$  is the hysteresis damping factor,  $\delta_i^n$  is the relative normal penetration between the bodies in contact and  $\dot{\delta}_i$  is the relative velocity. Parameter  $n=1.5$  is adopted from the work,<sup>43</sup> where it is defined experimentally for metallic materials.

The generalized stiffness constant  $K$  is based on the radius and material properties of two spheres as:<sup>44</sup>

$$K = \frac{4}{3(\sigma_i + \sigma_j)} \left[ \frac{R_i R_j}{R_i + R_j} \right]^{0.5}, \quad \sigma_k = \frac{1 - \nu_k^2}{E_k} \quad (31)$$

where  $\nu_k$  is the Poisson's ratio and  $E_k$  is the Young's modulus of sphere  $k$ . In Hunt-Crossley's work,<sup>41</sup> equation (31) is estimated based on two steel spheres with the stiffness constant  $K = 2.19 \times 10^7$  N/m<sup>1.5</sup>.

In this study, the simplified stiffness constant  $K$  is derived based on equation (31), as follows:

$$K = \frac{\sqrt{H}}{3\sigma}, \quad \sigma = \frac{1 - \nu^2}{E} \quad (32)$$

where  $H$  the height of the beam, and Young's modulus  $E$  and  $\nu$  are associated with the ANCF beam. In this study, the stiffness constant is estimated as  $K = 3.13 \times 10^7$  N/m<sup>1.5</sup> with the beam's Young's modulus  $E = 2.1 \times 10^7$  N/m<sup>2</sup>, Poisson's ratio  $\nu = 0.3$  and height  $H = 0.1$  m.

Damping factor  $\chi_i$  is given by:<sup>41,45</sup>

$$\chi_i = \frac{3K(1 - c_r)}{2\delta_i^{(-)}\dot{\delta}_i^{(-)}}, \quad c_r = -\frac{\dot{\delta}_i^{(-)}}{\dot{\delta}_i^{(+)}} \quad (33)$$

where  $c_r$  is the coefficient of restitution, which is determined experimentally with solid spheres of different materials in Ref.<sup>44</sup> and  $\dot{\delta}_i^{(-)}$  is the velocity before contact and  $\dot{\delta}_i^{(+)}$  is the velocity after contact. Thus,  $c_r$  has values from 0 to 1.

The normal and tangential forces between the rigid and flexible bodies are defined by using a Hertzian based contact force model and Coulomb friction model. The coefficient of friction is assumed to be  $\mu = 0.3$  in all numerical examples solved using the penalty method and CCP. The friction force  $f_{i,t}$  acts in a direction opposite to the contact velocity with a magnitude of  $\mu f_{i,n}$ . Therefore, the sliding friction force  $f_{i,t}$  can be computed with the help of velocity direction vector, such as:<sup>45</sup>

$$f_{i,t} = -\mu f_{i,n} \frac{\mathbf{v}_{i,t}}{|\mathbf{v}_{i,t}|} \quad (34)$$

where  $\mathbf{v}_{i,t}$  is the tangential velocity at the contact point,  $\mathbf{v}_{i,t}/|\mathbf{v}_{i,t}|$  returns a unit vector along the direction of  $\mathbf{v}_{i,t}$ .

To avoid an infinite number produced by  $\mathbf{v}_{i,t}/|\mathbf{v}_{i,t}|$ , when  $|\mathbf{v}_{i,t}|$  is zero, the unit vector  $\mathbf{v}_{i,t}/|\mathbf{v}_{i,t}|$  is replaced by  $\text{dir}_e(\mathbf{v}_{i,t}, v_\epsilon)$ ,<sup>45</sup> which is:

$$\text{dir}_e(\mathbf{v}_{i,t}, v_\epsilon) = \begin{cases} \frac{\mathbf{v}_{i,t}}{|\mathbf{v}_{i,t}|} & |\mathbf{v}_{i,t}| \geq v_\epsilon \\ \frac{\mathbf{v}_{i,t}}{v_\epsilon} \left( \frac{3|\mathbf{v}_{i,t}|}{2v_\epsilon} - \frac{1}{2} \left( \frac{|\mathbf{v}_{i,t}|}{v_\epsilon} \right)^3 \right) & |\mathbf{v}_{i,t}| < v_\epsilon \end{cases} \quad (35)$$

where velocity tolerance  $v_\epsilon$  is the small velocity tolerance.

### Cone complementarity approach

In this work, the Coulomb friction model combined with a non-penetration condition are added to the differential algebraic equation of the multibody dynamic with frictional contact. The above problem is relaxed to a cone complementarity problem, which can be solved using a convex quadratic optimization method with conic constraints.<sup>36</sup>

**Non-penetration constraints.** The non-penetration constraints are defined in terms of Karush-Kuhn-Tucker conditions. If the gap function, which is a signed function, is defined as  $\Phi_i$  and the normal contact force as  $f_{i,n}$ , the non-penetration conditions defined by the Karush-Kuhn-Tucker condition can be given as:

$$\Phi_i \geq 0, \quad f_{i,n} \geq 0, \quad \Phi_i f_{i,n} = 0 \quad (36)$$

If the gap function  $\Phi_i$  is positive, i.e. ( $\Phi_i > 0$ ), there is no contact between bodies and accordingly the normal contact pressure is zero, i.e. ( $f_{i,n} = 0$ ). When the contact occurs ( $\Phi_i = 0$ ), the normal contact force is above than 0 ( $f_{i,n} > 0$ ). When the gap function is less than zero ( $\Phi_i < 0$ ), the two bodies penetrate into each other.

**Frictional constraints.** The above non-penetration conditions only account for normal contact and not for sliding conditions. When the contact is active between two contact points, that is  $\Phi_i = 0$ , a normal force and tangential force may exist at the contact point.

In this paper, the Coulomb friction law is adopted as the relation between the normal and tangential force at the contact point. For a contact event  $i$ , the relation between two contact forces can be defined as:

$$\begin{aligned} f_{i,n} &\geq 0, \\ \mu f_{i,n} - f_{i,t} &\geq 0 \end{aligned} \quad (37)$$

**Posing problem.** Substituting acceleration (see equation (15)) and the contact force (see equation (28)):

$$\ddot{\mathbf{q}}^{(l)} = \mathbf{M}^{-1}(\mathbf{F}_{\text{exter}}^{(l)} - \mathbf{F}_{\text{elast}}^{(l)} + \mathbf{F}_c^{(l+1)}) \quad (38)$$

into equation (16), the discretized equation of velocity combined with the complementarity conditions of non-penetration and friction model can be rewritten as:

$$\begin{aligned} \dot{\mathbf{q}}^{(l+1)} &= \dot{\mathbf{q}}^{(l)} + \mathbf{M}^{-1}\mathbf{F}_{\text{exter}}^{(l)}\Delta t - \mathbf{M}^{-1}\mathbf{F}_{\text{elast}}^{(l)}\Delta t \dots \\ &\quad + \mathbf{M}^{-1}\mathbf{D}^{(l)}\mathbf{f}^{(l+1)}\Delta t \end{aligned} \quad (39a)$$

$$\mathbf{q}^{(l+1)} = \mathbf{q}^{(l)} + \dot{\mathbf{q}}^{(l+1)}\Delta t$$

$$\left. \begin{aligned} 0 &\leq \gamma_{i,n}^{(l+1)} \perp \Phi_i^{(l+1)} \geq 0 \\ -\gamma_{i,n}^{(l+1)} &\leq 0, \quad \gamma_{i,t}^{(l+1)} - \mu\gamma_{i,n}^{(l+1)} \leq 0 \\ &\in \{1, 2, \dots, N_k\} \end{aligned} \right\} \times \forall i \quad (39b)$$

where  $\perp$  means perpendicular, which is  $a \perp b = ab = 0$  and contact impulse  $\gamma^{(l+1)} = \mathbf{f}^{(l+1)}\Delta t$  is used in the rest of the paper.

Gap function  $\Phi_i^{(l+1)}$  can be approximated as:

$$\Phi_i^{(l+1)} \approx \Phi_i^{(l)} + \Delta t v_{i,n}^{(l+1)} + \Delta t \mu_i v_{i,t}^{(l+1)} \quad (40)$$

The relaxation of  $\Delta t \mu_i v_{i,t}^{(l+1)}$  is used to pose the problem of non-penetration constraints equation (39) as a cone complementarity problem (CCP).<sup>23</sup>

In the cone complementary problem, the following definitions of  $\mathbf{d}_i$  and  $\gamma_i^{(l+1)}$  are used:

$$\mathbf{d}_i = \begin{bmatrix} v_{i,t}^{(l+1)} \\ \frac{1}{\Delta t} \Phi_i^{(l)} + v_{i,n}^{(l+1)} \end{bmatrix}, \quad \gamma_i^{(l+1)} = \begin{bmatrix} \gamma_{i,t}^{(l+1)} \\ \gamma_{i,n}^{(l+1)} \end{bmatrix} \quad (41)$$

For the  $i$ -th contact, according to equation (39b),  $\gamma_{i,n}^{(l+1)} > 0$ , and  $\frac{\Phi_i^{(l+1)}}{\Delta t} = \frac{1}{\Delta t} \Phi_i^{(l)} + v_{i,n}^{(l+1)} + \mu_i v_{i,t}^{(l+1)} = 0$ . Consequently:

$$\begin{aligned} \mathbf{d}_i^T \gamma_i^{(l+1)} &= v_{i,t}^{(l+1)} \gamma_{i,t}^{(l+1)} + \left( \frac{1}{\Delta t} \Phi_i^{(l)} + v_{i,n}^{(l+1)} \right) \gamma_{i,n}^{(l+1)} \\ &= v_{i,t}^{(l+1)} \gamma_{i,t}^{(l+1)} - \mu_i v_{i,t}^{(l+1)} \gamma_{i,n}^{(l+1)} \\ &= v_{i,t}^{(l+1)} \left( \gamma_{i,t}^{(l+1)} - \mu_i \gamma_{i,n}^{(l+1)} \right) = 0 \end{aligned} \quad (42)$$

**Formulating the cone complementarity problem.** In what follows, it is necessary to reformulate the optimization problem with equilibrium constraints<sup>28</sup> to account for the above cone complementarity constraints. To this end, the initial term of  $\mathbf{d}_i$  is defined as:

$$\mathbf{d}_{i,0} = \begin{bmatrix} 0 \\ \frac{1}{\Delta t} \Phi_i^{(l)} \end{bmatrix} \quad (43)$$

According to equations (41) and (39), the term of  $\mathbf{d}_i$  can be rewritten:

$$\begin{aligned} \mathbf{d}_i &= \begin{bmatrix} 0 \\ \frac{1}{\Delta t} \Phi_i^{(l)} \end{bmatrix} + \begin{bmatrix} v_{i,t}^{(l+1)} \\ v_{i,n}^{(l+1)} \end{bmatrix} = \mathbf{d}_{i,0} + \mathbf{D}^{(l),T} \dot{\mathbf{q}}^{(l+1)} \\ &= \mathbf{p}_i + \mathbf{D}^{(l),T} \mathbf{M}^{-1} \mathbf{D}^{(l)} \gamma_i^{(l+1)}, \end{aligned} \quad (44)$$

where

$$\mathbf{p}_i = \mathbf{d}_{i,0} + \mathbf{D}^{(l),T} (\dot{\mathbf{q}}^{(l)} + \mathbf{M}^{-1} \mathbf{F}_{\text{exter}}^{(l)} \Delta t - \mathbf{M}^{-1} \mathbf{F}_{\text{elast}}^{(l)} \Delta t) \quad (45)$$

The matrix  $\mathbf{N} = \mathbf{D}^{(l)T} \mathbf{M}^{-1} \mathbf{D}^{(l)}$  is then defined, and equation (42) can be given as:

$$\mathbf{d}_i^T \boldsymbol{\gamma}_i^{(l+1)} = (\mathbf{p}_i + \mathbf{N} \boldsymbol{\gamma}_i^{(l+1)})^T \boldsymbol{\gamma}_i^{(l+1)} = 0 \quad (46)$$

Below, the following vector  $\mathbf{p}$  will be used:

$$\mathbf{p} = [\mathbf{p}_1 \quad \mathbf{p}_2 \quad \cdots \quad \mathbf{p}_{N_k}]^T \quad (47)$$

According to Karush-Kuhn-Tucker (KKT) conditions, equation (46) can be solved as a convex quadratic optimization problem with conic constraints as follows<sup>36</sup>:

$$\begin{aligned} \min \quad & f = \frac{1}{2} (\boldsymbol{\gamma}^{(l+1)})^T \mathbf{N} \boldsymbol{\gamma}^{(l+1)} + \mathbf{p}^T \boldsymbol{\gamma}^{(l+1)}, \\ \text{subject to} \quad & \boldsymbol{\gamma}_i^{(l+1)} \in \Gamma_i \end{aligned} \quad (48)$$

whose solution is the contact impulse  $\boldsymbol{\gamma}^{(l+1)}$ . According to equation (39):

$$\Gamma_i = \begin{cases} -\gamma_{i,n}^{(l+1)} \leq 0 \\ \gamma_{i,t}^{(l+1)} - \mu \gamma_{i,n}^{(l+1)} \leq 0 \end{cases} \quad (49)$$

The overall scheme for advancing a single time step can be expressed with algorithm 1:

---

#### Algorithm 1

- 1: Set time  $t=0$  and step counter  $l=0$ , initial values for  $\mathbf{q}^{(l)}$  and  $\dot{\mathbf{q}}^{(l)}$ .
- 2: Compute external force  $\mathbf{F}_{\text{exter}}$  and elastic force  $\mathbf{F}_{\text{elast}}$ .
- 3: Perform the contact detection to solve nonlinear equation (17). For each contact point, compute gap function  $\Phi_i$  and  $\mathbf{D}$  matrix.
- 4: **if**  $\Phi_i \leq \epsilon$  **then**
- 5:     **if** Using continuous contact force model **then**
- 6:     For each pair of potential contact points  $i$ , compute normal and tangential contact forces  $\mathbf{f}_i$  from equations (30) and (34). Build contact force vectors  $\mathbf{f}$ .
- 7:     **else** Using CCP approach
- 8:     Compute contact impulses  $\boldsymbol{\gamma}$  using optimization method from equation (48). Then contact force is  $\mathbf{f} = \boldsymbol{\gamma} / \Delta t$ .
- 9:     **end if**
- 10: **else**
- 11:      $\mathbf{f} = 0$
- 12: **end if**
- 13: Construct contact force vector using  $\mathbf{F}_c = \mathbf{D} \mathbf{f}$ .

- 14: The new velocity  $\dot{\mathbf{q}}^{(l+1)}$  can be obtained via equation (16).
  - 15: The new position  $\mathbf{q}^{(l+1)}$  will finally be calculated through equation (16).
  - 16: Increment  $t = t + \Delta t$ ,  $l = l + 1$ , repeat from step 2 till  $t > t_{\text{end}}$ .
- 

As can be observed from algorithm 1, if multiple contact events occur simultaneously, contact forces according to each event are computed by using for-loop with penalty method. However, when using CCP, the contact forces are computed simultaneously with optimization function.

### Numerical examples

In this section, three numerical examples of frictional contact between a flexible beam and a rigid body are examined to shed light on the performance of the introduced cone complementarity problem approach. The beam is discretized using an ANCF element which has been widely used in the description of flexible bodies undergoing large deformations under a multibody dynamics framework.

The problems considered include: (a) contact of a beam with a flat rigid surface; (b) contact between a pendulum beam and a fixed rigid ball; (c) contact between the beam and a continuous analytical rigid surface. For the first and third cases, the parameters of the ANCF beam are given in Table 1.

#### Beam contact with flat rigid ground

The first example of the proposed cone complementarity approach is a beam subject to free-fall onto a rigid surface (hereafter referred to as 'ground') as illustrated in Figure 4.

Figure 5 includes the results of the beam kinematics when using the continuous contact force model. Predictably, when the coefficient of restitution  $c_r$  decreases, the displacement and velocity reduces. When the coefficient of restitution is equal to 1, there is no energy dissipation in the contact process, which corresponds to the pure Hertz contact law. However, when the coefficient of restitution is equal to 0, the velocity did not drop to zero after contact.

**Table 1.** Simulation parameters.

Parameters	Model
Length $L$ (m)	1
Height $H$ (m)	0.1
Material density $\rho$ ( $\text{kg}/\text{m}^3$ )	7850
Young's modulus $E$ ( $\text{N}/\text{m}^2$ )	$2.1 \times 10^7$
External force	Gravity
Poisson's ratio $\nu$	0.3
Friction coefficient $\mu$	0.3
Stiffness constant $K$ ( $\text{N}/\text{m}^{1.5}$ )	$3.13 \times 10^7$

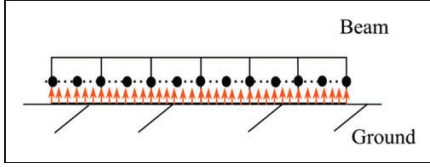


**Figure 4.** Illustration of element A contact with the flat ground.

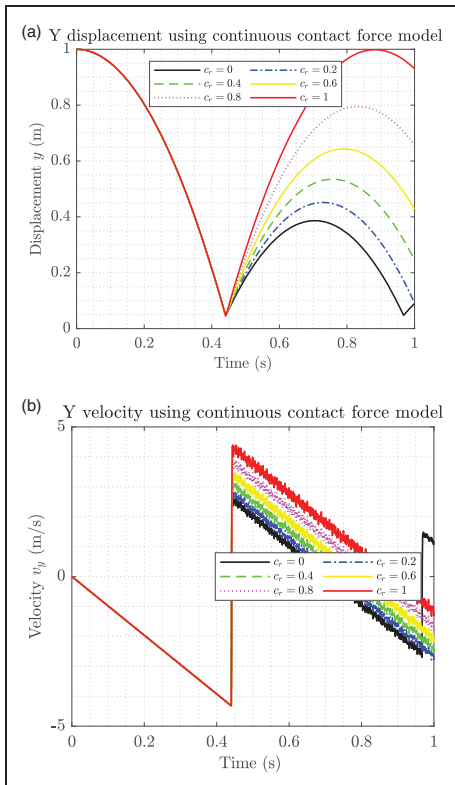


**Figure 5.** Kinematic simulation results of the beam falling on the ground with different coefficient of restitution  $c_r$  when using continuous contact force model. (a) Comparison of displacements in Y direction. (b) Comparison of velocities in Y direction.

This is because part of the kinetic energy is transferred as strain energy at the time of contact with the ground. Thus, the strain energy compensates for the lost kinetic energy during contact as shown in Figure 6.

As can be seen, Figure 7 plots the normal contact force profile as a function of penetration, various restitution coefficients ranging from 0 to 1 have been

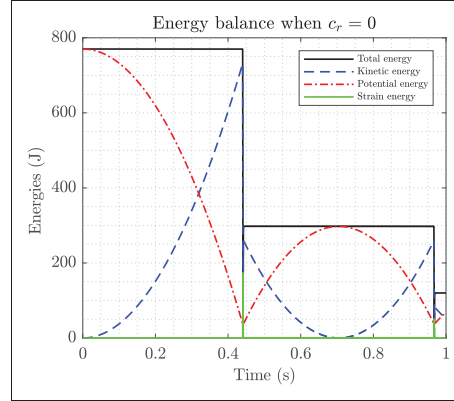


**Figure 6.** Energy balance of the ANCF beam using the continuous contact force model when  $c_r = 0$ .

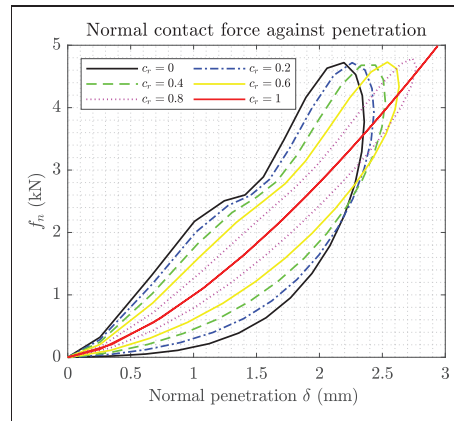


**Figure 7.** Normal contact force against normal penetration with different coefficient of restitution  $c_r$  by using continuous contact force model.

used. In the large coefficient restitution, the contact force profile is essentially symmetric. A significant dissipation of energy takes place in the low coefficient of restitution during the contact process. The results produced here agree with literature.<sup>39,45</sup>

In the CCP approach, the contact is considered to be inelastic, thus the coefficient of restitution is assumed to be 0.<sup>25,36</sup> To obtain the identical Y displacement of the beam from both approaches, the stiffness constant for continuous contact force model (equation (30)) needs to be regularized by the factor  $\alpha$  as:

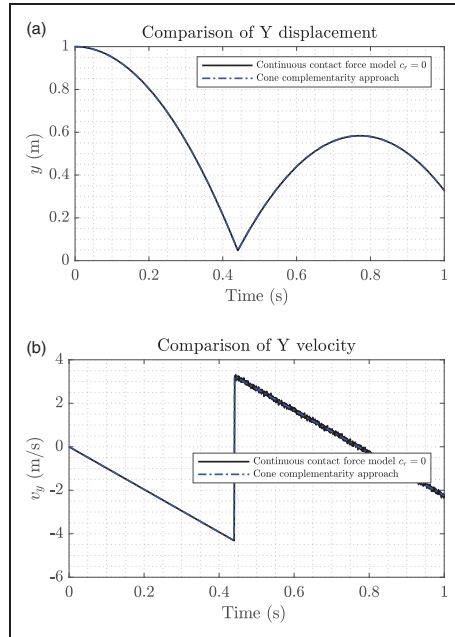
$$K_{reg} = \alpha K \quad (50)$$

where  $K$  is the stiffness constant from equation (32). In this study, the corrector factor  $\alpha$  is concluded from multiple numerical analysis of beam contact with flat rigid ground simulation.

In Figure 8, Y-displacement and velocity of the beam using the continuous contact force model with  $c_r=0$  and cone complementarity approach are shown. As seen from Figure 8(a) displacement and Figure 8(b) velocity of the beam leads to identical results when using the corrector factor  $\alpha = 3.8$ .

A comparison of the normal penetration for both methods is shown in Figure 9. In the penalty method, Hertzian stiffness only accounts for local deformation effects, without considering the structural deformation of the beam. The unphysical interpenetration is allowed during the contact event. In this paper, the nonlinear minimization problem is solved in CCP approach. The total energy of the system is minimized by considering the potential, kinetic and strain energy associated with the contact constraint. The non-penetration constraints prevent the ANCF beam from penetrating into the ground and the beam exerting pressure on the ground due to the contact force. For this reason, the normal contact force is 25 times smaller than CCP method.

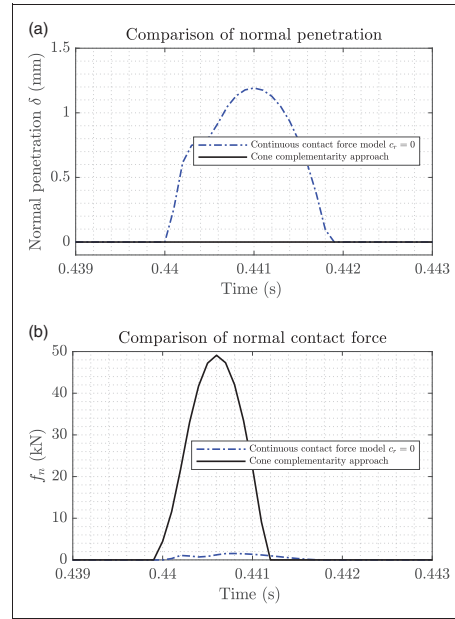
Normal contact force distribution along the beam side with both method at  $t=0.44$ s is shown in



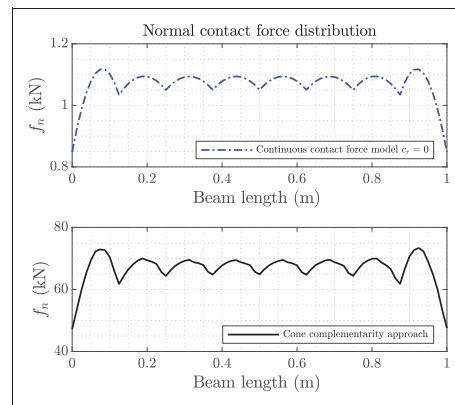
**Figure 8.** Comparison of kinematic simulation results of the beam falling on the ground with both approaches. (a) Comparison of displacements in Y direction. (b) Comparison of velocities in Y direction.

Figure 10. The number of elements considered is  $n=8$  and the number of slave points per element is  $nc=11$ . The contact points are evenly distributed at beam side. For each element, the normal contact force in the middle is larger than at the tip.

The comparison of the computation time between the two methods implemented in MATLAB with and without threshold  $\epsilon$  from equation (21) is presented in



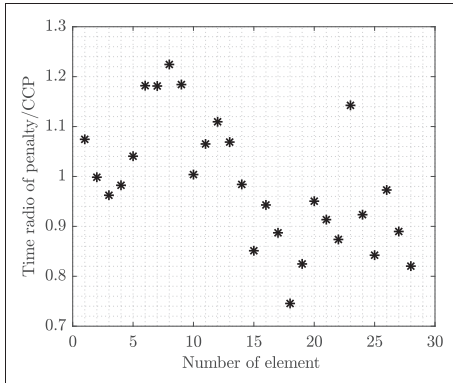
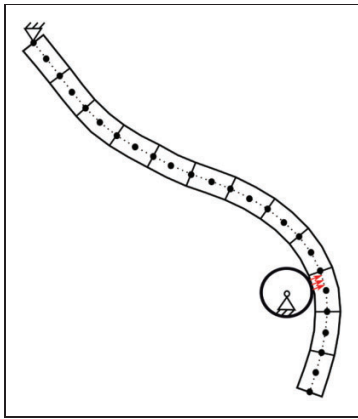
**Figure 9.** Comparison of normal penetration and normal contact forces with both approaches. (a) Comparison of normal penetration (b) Comparison of normal contact forces.



**Figure 10.** Normal contact impulse distribution at different slave points when time  $t=0.44$  s.

**Table 2.** Comparison of computation time of two methods with and without threshold  $\epsilon$ .

CPU time(s)	Without $\epsilon$	With $\epsilon$
CCP	202.5s	43.5s

**Figure 11.** Time ratio of penalty/CCP with different number of element per ANCF beam, the number of slave points per element is  $n_c = 11$ .**Figure 12.** Contact between a beam and fixed rigid circle.**Table 3.** Simulation parameters.

Parameters	Model
Length $L$ (m)	1
Height $H$ (m)	0.05
Material density $\rho$ ( $\text{kg/m}^3$ )	7850
Young's modulus $E$ ( $\text{N/m}^2$ )	$2.1 \times 10^7$
External force	Gravity
Poisson's ratio $\nu$	0.3
Radii of fixed rigid circle (m) $r$	0.05
Friction coefficient $\mu$	0.3

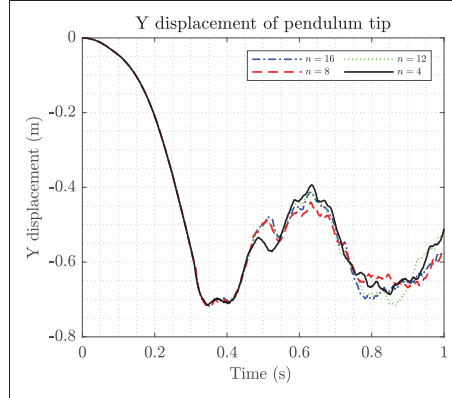
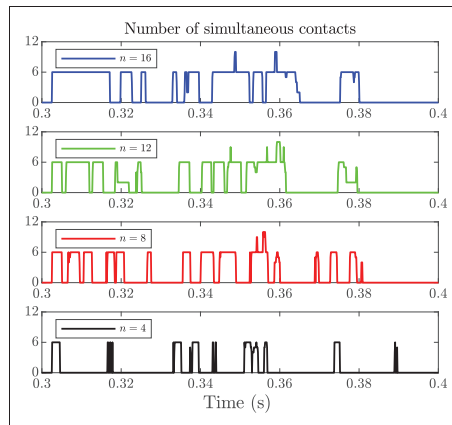
**Figure 13.** Displacements of pendulum tip in Y direction with different number of elements, when using CCP approach. The number of slave points is  $n_c = 41$  per element.**Figure 14.** Number of simultaneous contact with different number of elements, when using CCP approach. The number of slave points is  $n_c = 41$  per element.

Table 2. Time step is 0.1 ms and total time is 1 s. The number of elements considered is  $n=8$  and the number of slave points per element is  $n_c=11$ . With the threshold  $\epsilon$ , the CPU time for CCP approach is around five times smaller than without the threshold  $\epsilon$ . It can be concluded that the use of equation (21) helps to improve the computational efficiency.

Figure 11 shows the time ratio of Penalty/CCP with a different number of elements per ANCF beam, which is:

$$\text{ratio} = \frac{T_{\text{penalty}}}{T_{\text{CCP}}} \quad (51)$$

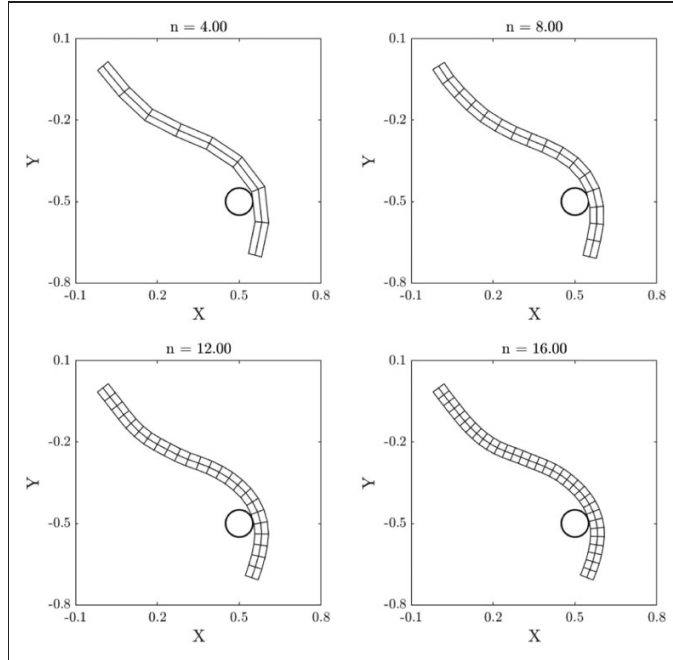


Figure 15. Deformed configuration of flexible beam for different numbers of element.

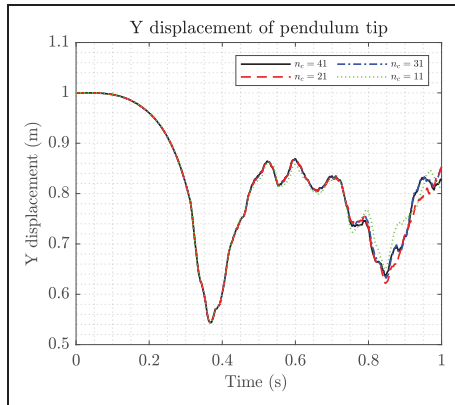


Figure 16. Displacements of pendulum tip in Y direction with different number of slave points per elements, when using CCP approach. The number of element is  $n = 8$ .

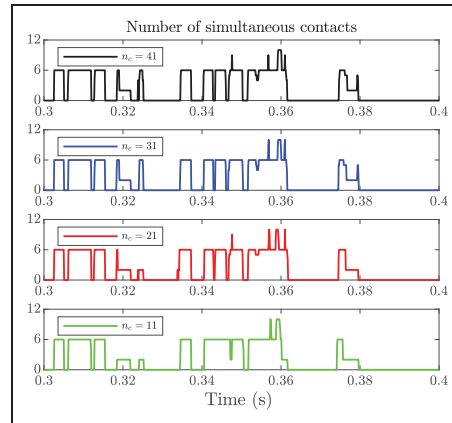


Figure 17. Number of simultaneous contact with different number of slave points per element, when using CCP approach. The number of element is  $n = 12$ .

where  $T_{penalty}$  is the computation time when using the penalty method and  $T_{CCP}$  is the computation time when using CCP approach.

It can be concluded from Figure 11, that there is no significant difference between the two approaches with a different number of elements. When the number of elements is smaller than 14, CCP is a

faster method, whereas, if the number of elements is more than 14, the penalty method is a faster.

### Pendulum contact

A continuous contact force model (pure Hertz contact law) is utilized for a contact problem between

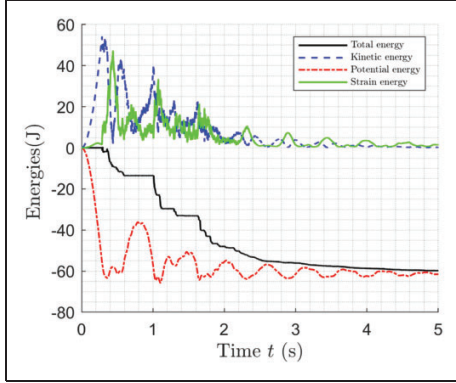


**Figure 18.** Energy balance when using CCP approach, the number of element is  $n = 5$ . The number of slave points on the beam is  $n_c = 41$ .

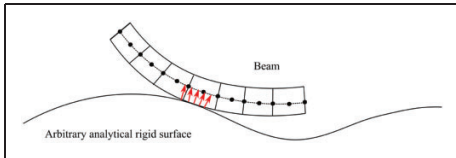


**Figure 19.** Contact between beam and arbitrary shape of rigid body.

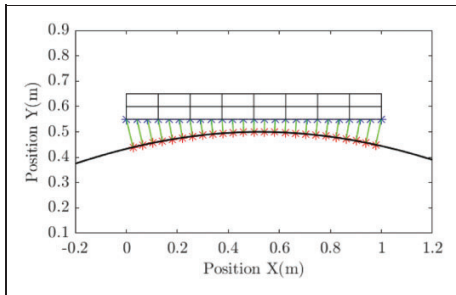


**Figure 20.** Contact points on beam and arbitrary analytical surface, blue points are slave points on the beam and red points are master points on the rigid body.

ANCF beams.<sup>46</sup> In their work, spheres are overlapped and located equally along the axis of the beam elements and contact between two ANCF beams is assumed as the contact between two spheres. This example considers contact between a flexible beam and fixed rigid ball as shown in Figure 12, which is extended from Ref.<sup>46</sup> The pendulum beam is fixed using a revolute joint and loaded by gravity. The beam is discretized using ANCF beam elements.

As the pendulum swings, it comes into contact with the rigid ball. Details of the simulation parameters are given in Table 3. In this test, the pendulum comes into contact with a rigid circle fixed at position  $(0.5, -0.5)$ .

Figure 13 compares the tip displacement of the pendulum obtained with different numbers of beam elements while using the CCP approach. The number of beam elements varies from 4–12. The number of slave points is  $n_c = 41$  per element. However this does not serve as a convergence analysis, due to different bending stiffness for different number of element. Figure 14 shows the corresponding number of simultaneous contacts with varying beam element numbers. In the simulation, the number of beam elements leads to different contact times. The more the number of elements, the more the number of simultaneous contacts.

Figure 15 shows the snapshots of the simulation for different numbers of elements in the beam. As the beam comes into contact with the rigid ball, the flexible beam tends to wrap around the circle. As the number of elements increase, it is observed that the bending stiffness decreases.

Figure 16 compares the tip displacement of the pendulum obtained with a different number of slave points per elements while using the CCP approach. The number of element is  $n = 8$ . Figure 16 indicates that the tip displacements converge as the number of slave points is increased. Figure 17 shows the corresponding number of simultaneous contacts with a different number of slave points per element. The number of the slave points per element does not affect the contact time during the simulation. However, the more slave points there are, the more the simultaneous contacts at the same instant.

Figure 18 shows the energy balance of the beam during the dynamic simulation when using both methods. There are multiple contacts happen during 5 s simulation. The total energy decreases due to contact when using CCP.

#### Contact with an arbitrary analytical rigid surface

The last example considers contact between a flexible beam and an analytical rigid surface as shown in Figure 19.

The position of the contact points on the beam and the analytical rigid surface is shown in Figure 20. Blue points are slave points on the beam, red points are the contact points detected on the analytical rigid surface. According to the contact point detection algorithm in equation (17), each slave point can find its potential master point automatically.

The beam considered here is in a free-fall from a height of  $h = 5$  m with zero initial velocity. Figure 21 shows the contact between the beam and the analytical rigid surface defined by function  $f(x) = \sin(x)$ . Figure 22 shows the beam contact with the analytical

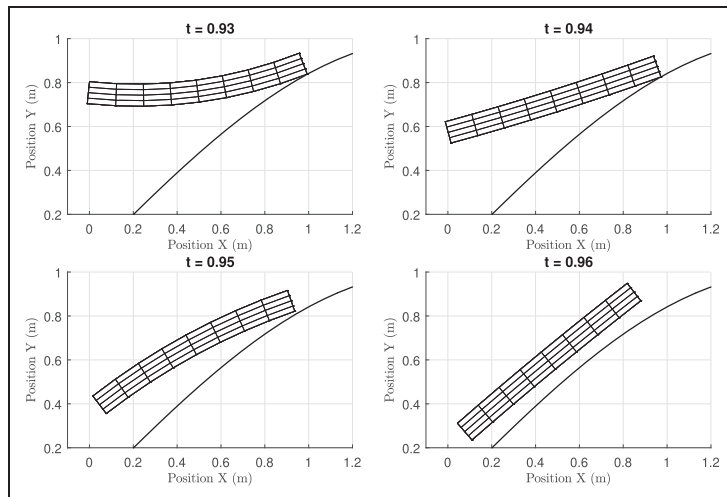


**Figure 21.** Illustration of the shape of the beam during the first contact with the continuous ground of  $f(x) = \sin(x)$  at different time.

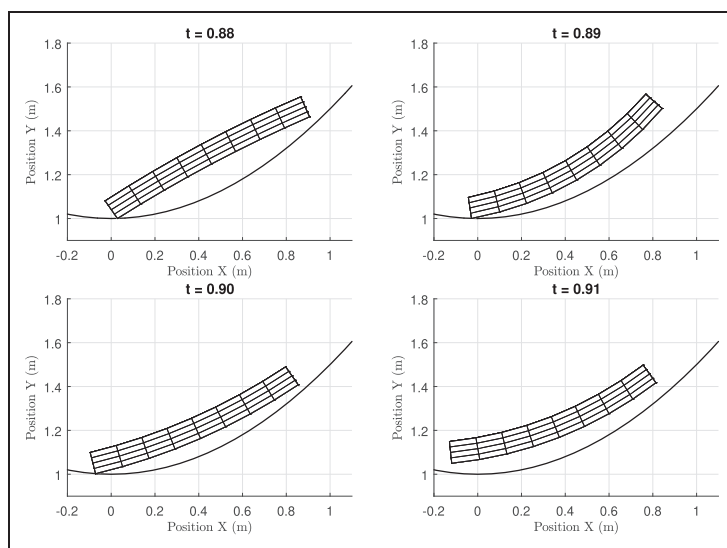


**Figure 22.** Illustration of the shape of the beam during the second contact with the continuous ground of  $f(x) = \frac{x^2}{2} + 1$  at different time.

rigid surface defined by  $f(x) = \frac{x^2}{2} + 1$ . As can be observed from the figures, different contact types can make the switch from corner-by-side to side-by-side during contact period.

**Conclusions**

In multibody system dynamics, contact description plays an important role. Contact itself is a highly

nonlinear problem and is not easy to solve. Solving such non-linearities requires iterative procedures, thus making the solution process a computationally intensive endeavor. Analysis of contact dynamics is not a trivial task. Several methods have been developed over the years, of which the complementarity approach is a prominent example, particularly for rigid body contact. Contact problems can be solved with reasonably acceptable accuracy using the

complementarity approach. However, this approach is often limited to rigid body contacts because of the high computational cost. The non-smooth behavior of dynamic contact remains a challenge when simulating flexible bodies.

This work introduced an approach in which contacts of a deformable body are described using the cone complementarity problem (CCP) approach. To this end, the ANCF was combined with the cone complementarity problem (CCP) method. To shed light on the performance of the introduced approach, three example case studies were analyzed where a shear deformable beam comes into contact with different types of rigid bodies. The contact detection algorithm was shown to be able to detect beam contact with arbitrary rigid body. At the same time, different contact case including that of the case of parallel beams in contact, corner contact with side and side contact with side are shown in numerical results. Energy balance was shown to demonstrate conservation of energy when coefficient of restitution is zero, because of strain energy in ANCF beam. The CCP approach was compared against the penalty method by setting a regularized correction factor for the stiffness constant in the penalty method. Both approaches can achieve the same kinematic results. In the penalty method, Hertzian stiffness ignores the structural deformation of the beam allowing a penetration in the contact process. However, in the CCP approach, the nonlinear minimization problem helps to prevent the penetration.

Future work will extend the CCP approach into 3-D contact. 3-D ANCF beam with deformable circular cross sections will be used to analyze large deformations in multibody applications, such as the hair simulations, self contact and rope knotting.

#### Declaration of Conflicting Interests

The author(s) declared no potential conflicts of interest with respect to the research, authorship, and/or publication of this article.

#### Funding

The author(s) disclosed receipt of the following financial support for the research, authorship, and/or publication of this article: This work was supported by the Academy of Finland (Application No. 299033 for funding of Academy Research Fellow) for supporting Marko K. Matikainen.

#### ORCID iD

Xinxin Yu  <https://orcid.org/0000-0002-7740-9643>

#### References

1. Harish AB and Wriggers P. Modeling of two-body abrasive wear of filled elastomers as a contact-induced fracture process. *Tribol Int* 2019; 138: 16–31.
2. Wriggers P and Zavarise G. On contact between three-dimensional beams undergoing large deflections. *Commun Numer Methods Eng* 1997; 13: 429–438.
3. Zavarise G and Wriggers P. Contact with friction between beams in 3-D space. *Int J Numer Methods Eng* 2000; 49: 977–1006.
4. Litewka P and Wriggers P. Contact between 3-D beams with rectangular cross-sections. *Int J Numer Methods Eng* 2002; 53: 2019–2041.
5. Litewka P and Wriggers P. Frictional contact between 3-D beams. *Comput Mech* 2002; 28: 26–39.
6. Litewka P. Hermite polynomial smoothing in beam-to-beam frictional contact. *Comput Mech* 2007; 40: 815–826.
7. Konyukhov A and Schweizerhof K. Geometrically exact covariant approach for contact between curves. *Comput Methods Appl Mech Eng* 2010; 199: 2510–2531.
8. Durville D. Contact friction modeling within elastic beam assemblies: an application to knot tightening. *Comput Mech* 2012; 49: 687–707.
9. Boso DP, Litewka P, Schrefler BA, et al. A 3-D beam to beam contact finite element for coupled electric-mechanical fields. *Int J Numer Methods Eng* 2005; 64: 1800–1815.
10. Wang Q, Tian Q and Hu H. Dynamic simulation of frictional contacts of thin beams during large overall motions via absolute nodal coordinate formulation. *Nonlinear Dyn* 2014; 77: 1411–1425.
11. Litewka P. Enhanced multiple-point beam-to-beam frictionless contact finite element. *Comput Mech* 2013; 52: 1365–1380.
12. Puso MA and Laursen TA. A mortar segment-to-segment contact method for large deformation solid mechanics. *Comput Methods Appl Mech Eng* 2004; 193: 601–629.
13. Puso MA and Laursen TA. A mortar segment-to-segment frictional contact method for large deformations. *Comput Methods Appl Mech Eng* 2004; 193: 4891–4913.
14. Fischer KA and Wriggers P. Frictionless 2D contact formulations for finite deformations based on the mortar method. *Comput Mech* 2005; 36: 226–244.
15. Puso MA, Laursen TA and Solberg J. A segment-to-segment mortar contact method for quadratic elements and large deformations. *Comput Methods Appl Mech Eng* 2008; 197: 555–566.
16. Hesch C and Betsch P. Transient three-dimensional contact problems: mortar method. Mixed methods and conserving integration. *Comput Mech* 2011; 48: 461–475.
17. Neto AG and Wriggers P. Computing pointwise contact between bodies: a class of formulations based on master–master approach. *Comput Mech* 2019; 64: 585–263.
18. Simo JC and Vu-Quoc L. On the dynamics of flexible beams under large overall motions – the plane case: part I and II. *Computer Methods Appl Mech Eng* 1986; 53: 849–863.
19. Berzeri M, Campanelli M and Shabana AA. Definition of the elastic forces in the finite element absolute nodal coordinate formulation and the floating frame of reference formulation. *Multibody Syst Dyn* 2001; 5: 21–54.

20. Shabana AA. Definition of the slopes and the finite element absolute nodal coordinate formulation. *Multibody Syst Dyn* 1997; 1: 339–348.
21. Pfeiffer TF and Glocke C. *Multibody dynamics with unilateral contacts*. New York: John Wiley & Sons, 1996.
22. Anitescu M. Optimization-based simulation of non-smooth rigid multibody dynamics. *Math Program* 2006; 105: 113–143.
23. Anitescu M and Tasora A. An iterative approach for cone complementarity problems for nonsmooth dynamics. *Comput Optim Appl* 2010; 47: 207–235.
24. Ko M and Zowe J. An iterative two-step algorithm for linear complementarity problems. *Numer Math* 1994; 68: 95–106.
25. Anitescu M, Potra FA and Stewart DE. Time-stepping for three-dimensional rigid body dynamics. *Comput Methods Appl Mech Eng* 1999; 177: 183–197.
26. Yao W, Chen B, Liu C, et al. Dynamics of multi-rigid-body systems under non-smooth constraints and linear complementary problems. *Int J Comput Math* 2008; 85: 889–898.
27. Mashayekhi MJ and Kovecses J. A comparative study between the augmented Lagrangian method and the complementarity approach for modeling the contact problem. *Multibody Syst Dyn* 2017; 40: 327–345.
28. Tasora A, Negrut D and Anitescu M. Large-scale parallel multibody dynamics with frictional contact on the graphical processing unit. *Proc IMechE, Part K: J Multi-body Dynamics* 2008; 222: 315–326.
29. Tasora A and Anitescu M. A fast NCP solver for large rigid-body problems with contacts, friction, and joints. *Multibody Dyn Comput Methods Appl* 2008; 12: 45–55.
30. Tasora A and Anitescu M. A matrix-free cone complementarity approach for solving large-scale, nonsmooth, rigid body dynamics. *Comput Methods Appl Mech Eng* 2011; 200: 439–453.
31. Zhang X, Qi Z, Wang G, et al. Model smoothing method of contact-impact dynamics in flexible multibody systems. *Mech Mach Theory* 2019; 138: 124–148.
32. Shabana AA. *Computational dynamics*. New York: John Wiley & Sons, Inc, 2009.
33. Nachbagauer K, Pechstein AS, Irschik H, et al. A new locking-free formulation for planar, shear deformable, linear and quadratic beam finite elements based on the absolute nodal coordinate formulation. *Multibody Syst Dyn* 2011; 26: 245–263.
34. Wriggers P, Rust WT and Reddy BD. A virtual element method for contact. *Comput Mech* 2016; 58: 1039–1050.
35. Liu J, Liu J, Shu X, et al. An efficient multibody dynamic model of three-dimensional meshing contacts in helical gear-shaft system and its solution. *Mech Mach Theory* 2019; 142: 103607.
36. Negrut D, Serban R and Tasora A. Posing multibody dynamics with friction and contact as a differential complementarity problem. *J Comput Nonlinear Dyn* 2018; 13: 014503.
37. Yu X, Dmitrochenko O, Matikainen MK, et al. Cone complementarity approach for dynamic analysis of multiple pendulums. *Adv Mech Eng* 2019; 11: 168781401985674–168781401985615.
38. Huněk I. On a penalty formulation for contact-impact problems. *Comput Struct* 1993; 48: 193–203.
39. Flores P, Machado M, Silva MT, et al. On the continuous contact force models for soft materials in multibody dynamics. *Multibody Syst Dyn* 2011; 25: 357–375.
40. Machado M, Moreira P, Flores P, et al. Compliant contact force models in multibody dynamics: evolution of the hertz contact theory. *Mech Mach Theory* 2012; 53: 99–121.
41. Hunt K and Crossley E. Coefficient of restitution interpreted as damping in vibroimpact. *J Appl Mech* 1975; 42: 440–445.
42. Lankarani HM and Nikravesh PE. A contact force model with hysteresis damping for impact analysis of multibody systems. *J Mech Des* 1990; 112: 369–376.
43. Hertz H. On the contact of solids – on the contact of rigid elastic solids and on hardness (translated by D. E. Jones and G. A. Schott. In: *Miscellaneous Papers*. London, UK: Macmillan and Co. Ltd, 1896, pp. 146–183.
44. Goldsmith W and Frasier JT. *Impact: the theory and physical behaviour of colliding solids*. London: Edward Arnold Ltd, 1960.
45. Gonthier Y, McPhee J, Lange C, et al. A regularized contact model with asymmetric damping and dwell-time dependent friction. *Multibody Syst Dyn* 2004; 11: 209–233.
46. Khude N, Stanciulescu I, Melanz D, et al. Efficient parallel simulation of large flexible body systems with multiple contacts. *J Comput Nonlinear Dyn* 2013; 8: 041003.

## Appendix

### Notations

$A$	The body transformation matrix of the rigid body
$A_i$	the orthogonal rotation matrix for $i$ -th contact, which can define the contact force direction
$c_r$	The coefficient of restitution
$d_{pq}$	The distance vector between one pair of slave-master points
$dt$	The time step
$D_i$	the transformation matrix which can define the location and direction of the contact force in global coordinate system for $i$ -th contact
$E, G$	Young's modulus and shear modulus for the beam respectively
$E_{yy}$	The transverse strain component
$f_i$	The vector corresponding to the magnitudes of tangential and normal contact forces for $i$ -th contact
$f_{in}, f_{it}$	The magnitudes of tangential and normal contact forces for $i$ -th contact
$F_{c, RB}, F_{c, e}$	The contact force vector exerted at rigid body and ANCF beam respectively
$F_{exter, RB}, F_{exter, e}$	The external force vector for rigid body and ANCF beam respectively

$\mathbf{F}_i^Q, \mathbf{F}_i^P$	The contact force vectors of the slave point $P$ and master point $Q$		
$\mathbf{F}_{i,n}^Q, \mathbf{F}_{i,t}^Q$	The normal and tangential contact force vectors of the master point $Q$		
$H$	The height of the beam	$v_\epsilon$	The velocity tolerance when computing tangential contact force
$I_z$	The second moment of inertia	$v_{i,t}$	The tangential velocity at the contact point
$k_s$	The shear correction factor	$W_{elast}^{bend\&tors}$	The strain energy associated with beam bending and torsion
$K$	The generalized stiffness constant which depends on the material properties and the shape of the contact surface	$W_{elast}^{thickness}$	The strain energy accounting for thickness deformation
$K_r$	The rotation of cross-section plane with respect to the reference length	$W_{kin}, W_{elast}, W_{exter}, W_c$	The kinetic energy, strain energy, the work done by the externally applied forces and the energy added during contact respectively for the beam element
$\ell_x, \ell_y$	The length and height of the beam element in the undeformed configuration	$\zeta_i$	The hysteresis damping factor
$\mathbf{M}_{RB}, \mathbf{M}_e$	The mass matrix for rigid body and ANCF beam respectively	$\delta_i$	The relative normal penetration between bodies in contact and its relative contact velocity
$\mathbf{n}_Q, \mathbf{t}_Q$	The normal and tangential vectors of master point $Q$ on the rigid body in global coordinate system	$\dot{\delta}_i^{(-)}$	The initial contact velocity
$N_m$	The shape function matrix for the beam element	$\epsilon$	The tolerance $\epsilon$ to define a distance threshold to obtain the potential contact points
$N_1, N_2, \dots$	The shape functions are defined	$\gamma_i$	The vector corresponding to the magnitudes of tangential and normal contact impulses for $i$ -th contact
$\mathbf{q}, \dot{\mathbf{q}}, \ddot{\mathbf{q}}$	The position, velocity and acceleration vectors for the system	$\gamma_{i,n}, \gamma_{i,t}$	The magnitudes of tangential and normal contact impulses for $i$ -th contact
$\mathbf{q}_{fb}$	The vector of the nodal position coordinates for ANCF beam	$\mu$	The coefficient of the friction force
$\mathbf{q}_{RB}$	The vector of Cartesian generalized coordinates for a planar rigid body	$\nu$	The Poisson's ratio
$\mathbf{r}, \mathbf{r}_y$	The position vector of the nodal location of the beam and its slope vector	$\varphi$	The rotational coordinate of the rigid body
$\mathbf{r}_P, \mathbf{r}_Q$	The position vectors of slave point $P$ on the beam and its corresponding master point $Q$ on the rigid body in global coordinate system	$\Phi_i$	The gap function for $i$ -th contact
$\mathbf{R}$	The global position vector of the origin of body reference coordinate system	$\Gamma_1, \Gamma_2$	Generalized strains
$\bar{\mathbf{u}}_Q, \bar{\mathbf{t}}_Q$		$\xi, \eta$	The local coordinate system of the element

### Publication III

Bozorgmehri, B., Yu, X., Matikainen, M. K., Harish, A. B., and Mikkola, A.  
**A study of contact methods in the application of large deformation  
dynamics in self-contact beam**

Reprinted with permission from  
*Nonlinear Dynamics*  
103(1) (2021) 581-616  
© 2021, Springer.





# A study of contact methods in the application of large deformation dynamics in self-contact beam

Babak Bozorgmehri · Xinxin Yu · Marko K. Matikainen · Ajay B. Harish · Aki Mikkola

Received: 18 January 2020 / Accepted: 24 September 2020 / Published online: 29 December 2020  
© The Author(s) 2020

**Abstract** This paper introduces a procedure in the field of computational contact mechanics to analyze contact dynamics of beams undergoing large overall motion with large deformations and in self-contact situations. The presented contact procedure consists of a contact search algorithm which is employed with two approaches to impose contact constraint. The contact search task aims to detect the contact events and to identify the contact point candidates that is accomplished using an algorithm based on intersection of the oriented bounding boxes (OBBs). To impose the contact constraint, an approach based on the complementarity problem (CP) is introduced in the context of beam-to-beam contact. The other approach to enforce the contact constraint in this work is the penalty method, which is often used in the finite element and multibody

literature. The latter contact force model is compared against the frictionless variant of the complementarity problem approach, linear complementarity problem approach (LCP). In the considered approaches, the absolute nodal coordinate formulation (ANCF) is used as an underlying finite element method for modeling beam-like structures in multibody applications, in particular. The employed penalty method makes use of an internal iteration scheme based on the Newton solver to fulfill the criteria for minimal penetration. Numerical examples in the case of flexible beams demonstrate the applicability of the introduced approach in a situation where a variety of contact types occur. It was found that the employed contact detection method is sufficiently accurate when paired with the studied contact constraint imposition models in simulation of the contact dynamics problems. It is further shown that the optimization-based complementarity problem approach is computationally more economical than the classical penalty method in the case of studied 2D-problems.

B. Bozorgmehri (✉) · X. Yu · M. K. Matikainen · A. Mikkola  
Mechanical Engineering, School of Energy Systems, LUT University, Lappeenranta, Finland  
e-mail: babak.bozorgmehri@lut.fi

X. Yu  
e-mail: xinxin.yu@lut.fi

M. K. Matikainen  
e-mail: marko.matikainen@lut.fi

A. Mikkola  
e-mail: aki.mikkola@lut.fi

A. B. Harish  
Department of Civil and Environmental Engineering,  
University of California, Berkeley, CA, USA  
e-mail: ajaybh@berkeley.edu

**Keywords** Self-contact · Contact detection · Oriented bounding box · Complementarity problem · Penalty method · Absolute nodal coordinate formulation

## 1 Introduction

Contact between highly flexible bodies or self-contact situation in a flexible body is an important subject

matter in many applications such as in wire ropes, belts, drapes and biomechanical implementations. The solutions to the contact problems above-mentioned are intrinsically rife with the three categories of nonlinearity known from the nonlinear finite element including material, geometry and boundary nonlinearities [71]. The presence of all these nonlinearities leads to undesired non-physical vibrations resulting in poor energy conservation, dynamic instability and moreover expensive, computational efforts for contact description including contact search procedures [9].

The above applications which account for large deformations have been the motivation for developing several formulations to discretize the beam-like structures using the nonlinear finite element method. Many of the nonlinear finite element formulations developed for beam-like continua have been characterized using the one-dimensional elastic line theory. This is also often referred to as the Simo-Reissner beam model [57,62–64]. The Simo-Reissner beam model also forms the basis for many beam formulations in the framework of the geometrically exact beam (GEB) theory [24,29,58,59]. Rather recently, the geometrically exact beam finite element was formulated according to the Kirchhoff–Love beam type by Meier et al. [44]. There, the proposed formulations fulfilled all the essential requirements that were already satisfied by the Simo-Reissner beam type, such as large deformation, dynamic problems involving slender beams, applicability in various anisotropic cross sections and avoidance of locking effects [46]. An alternative formulation for discretizing slender continua undergoing large deformation dynamics is the absolute nodal coordinate formulation (ANCF) introduced by Shabana [60]. Within a number of developments and extensions made to the original ANCF, it is capable of fulfilling all the above-mentioned essential requirements [58]. Among a large number of comparisons between the absolute nodal coordinate and the geometrically exact beam formulations, we cite in passing on the investigations by Gerstmayr et al. [23] on the performance and accuracy of the ANCF element. They further indicated a fourth order of convergence rate of a locking-free planar ANCF beam element when the strain energy is derived according to Simo and Vu-Quoc formulation [63,64]. With the evolution of the formulation [19,42,43], capturing cross-sectional deformation in high-frequency modes became feasible using the higher-order derivations of position vector with respect to the beam transverse

directions that was recently discussed by Bozorgmehri et al. [10]. The strain energy in the ANCF can be described using a number of nonlinear material laws known from the two- and three-dimensional elasticity. Moreover, ANCF is regarded as a suitable underlying formulation to incorporate the isogeometric analysis (IGA), and in particular to be combined with the isogeometric collocation method [5] due to the feasibility of enforcing Neumann boundary conditions [14] on the higher-order degrees-of-freedom of the ANCF nodes.

In the context of formulation related to contact between beams, Lee et al. [35] introduced a solution procedure for frictionless contact problems in two-dimensional beams undergoing large displacements. They used quadratic programming to solve the equivalent minimization problem. Speaking of three-dimensional beam contact, Wriggers et al. [72] proposed a computational algorithm to describe the contact between beams with circular cross sections subjected to large deformations. Subsequently, Zavarise et al. [77] extended the proposed algorithm to formulate the contact force model when friction is present. Later, a contact search strategy was developed with the contact model with rectangular cross-sectional beams in the case of large displacements and rotations [40,41]. All the above-mentioned contributions were based on point-to-point contact interaction leading to discrete contact force acting on the contacting beams. Although using the point-to-point contact model results in an efficient and precise numerical implementation, it has an essential limitation when beams with arbitrary orientation i.e., when the contact angle between them is small (almost parallel), come into contact. In this situation, the requirement of the uniqueness and existence of closest point projection for all contact points is violated. To alleviate the point-to-point contact model limitation, Litewka [37] proposed a smoothing procedure based on the Hermite polynomials for contact description to improve the smoothness of the normal and tangent contact vectors through the contact points. The limitation mentioned above, particularly when the contact beams are rather parallel was resolved to some extent by Litewka [38,39], although it still necessitates solving two closest point projection problems (bilateral minimal distance problem) for the contacting beams. The above point-wise contact developments were classified as master-and-slave definition of the contacting entities. In contrary, Gay Neto et al. recently introduced a class of master-and-master formulations within which

no distinction is made whether a point and surface is on a master or slave beam [51,52].

As it is often the case with the general beam-to-beam contact when beams of arbitrary configuration come into contact, the enhanced multiple-point contact method in [38,39] unable to guarantee the uniqueness of a closest point projection. Consequently, a contact region may remain undetected leading to inaccurate contact constraint enforcement, i.e., nonphysical penetration within a contact event. To alleviate this shortcoming, Durville introduced an intermediate geometry where a proximity zone can be defined to detect the contact point candidates in [18] and was later used in the case of a self-contact beam in [17]. Inspired by Durville's geometrical contact detection approach, Weeger et al. [69] applied the point force as the contact force in a rod-to-rod surface contact in the framework of Cosserat beam model parameterized using the collocation isogeometric analysis (IGA-C). Chamekh et al. [12,13] introduced a Gauss-point-to-segment approach to measure gap function between the contacting beams and in self-contact beam problems. To solve the particular contact when contacting beams are interacting along two curves, Konyukhov et al. [32] studied a curve-to-curve contact within a geometrically exact description in the covariant form. Further, they used a geometrical criteria whereby the existence and uniqueness of closest point projection [33] is ensured. As an alternative to the geometrical-based formulation proposed in [32,33] Meier et al. [45] developed the Gauss-point-to-segment approach into a variant of line-to-line contact formulation with an emphasis on integration interval segmentation in the vicinity of strong discontinuity in the applied beam element formulation, i.e., in the end-points of contacting beams. The line-to-line formulations are considered as a very accurate and rather efficient (more computationally expensive than the point-to-point) contact model in the range of small contact angles for contacting beams (parallel or roughly parallel beams). But, the formulation becomes drastically inefficient when the contact angle exceeds a certain value [45,47]. To deal with such a scenario, Meier et al. [47] introduced a transition procedure between the point-to-point and the line-to-line contact schemes in contact force level and the contact energy level.

Generally speaking, contact constraint can be imposed by different approaches such as penalty methods, Lagrange multipliers method and augmented Lagrangian method. The variation of contact energy

in the penalty method is computed based on the selected penalty parameter which is critically important to ensure that the interpenetration between two bodies in contact is minimal [70]. This method typically needs small time steps in the time integration scheme and a carefully chosen penalty parameter due to the stability requirements. The penalty is widely used alongside the standard mortar contact approach [73] for analyzing contact problems. Yet, the combination of the penalty method with the mortar finite element method is computationally time consuming and not suitable for efficient computing such as real-time simulations. In the case of solid continua, in the presence of frictional contact, Puso et al. [56] enforced contact constraint by an augmented Lagrangian scheme using the mortar method. Speaking of contact between one-dimensional slender continua, Litewka [36] compared the penalty and Lagrange multiplier methods and concluded that in expanse of higher computational effort, the Lagrange multiplier is more accurate than the penalty method and is trial-and-error free in contrast to the penalty method. On the other hand, Meier et al. [45] argued that the penalty method is more efficient than the Lagrange multiplier method, because of a lower amount of unknowns in the line-to-line contact model and also the penalty parameter has a physical role by taking into account the beam cross-sectional flexibility. Instead of using the standard penalty force law, Khude et al. [30] combined the discrete continuous contact force model with the absolute nodal coordinate formulation (ANCF) to describe the interactions between flexible bodies in multibody applications. The contact constraint can be characterized by inequality constraints, which in turn can be served with a complementarity problem [54]. This is analogous to the Lagrange multipliers method. But, the complementarity problem-based approaches are distinguished from the Lagrange multipliers method with the following features: in Lagrange multiplier method, the contact between two bodies is computed by solving a set of nonlinear constraint equations that establish that both surfaces are in contact without penetration or separation. The contact forces are described through the Lagrange multipliers, which are associated with the contact constraints. On the other hand, with the linear complementary problem approach (LCP), the contact constraints are included into the differential algebraic equations in terms of the complementarity conditions. The contact forces can be solved using a con-

vex quadratic optimization method. The algorithms in this class lead to solving the differential variational inequality (DVI) classified in [53] that describes the interaction of bodies with contact and friction over the evolution of time. The complementarity problem (CP) is regarded as a special case of variational inequality (VI) and subsequently, the acronym DVI. Tasora et al. [4,67] proposed cone complementarity problems by means of a fixed-point iteration algorithm to simulate contact problems with tens of thousands of colliding rigid bodies. They have enhanced the computational efficiency of the algorithms and formulas by tailoring the fixed-point iteration to obtain a matrix-free algorithm with  $O(n)$  space complexity [65]. Negrut et al. [50] proposed the non-penetration condition and the Coulomb dry friction model in a cone complementarity problem which can solve the multibody problems with frictional contact. All of the above applications of the complementarity problem approach were in the context of rigid body contact. Latterly, Tasora et al. [66] introduced a rigid-to-flexible contact model using second-order CCP in the frame work of geometrically exact beam with the isogeometric analysis (IGA) discretization. They concluded that the employed CCP method can be regarded as an acceptable alternative to the conventional penalty method. Accordingly, in the work of Yu et al. [76], the CCP approach is used to compare with the penalty method in the frame work of ANCF beam contact with rigid bodies. The damping component is included in the penalty method using the continuous contact model introduced by Hunt and Crossley [28]. They concluded that the kinematic results show a good agreement between both approaches when the coefficient of restitution is zero.

Prior to a contact event description, a collision detection procedure is needed if the contact points and/or the contact types are unknown. Collision detection is essential and often one of the most crucial steps when imposing an accurate contact procedure. As is often the case, a large overall motion in highly flexible bodies encompasses several contact events of different types, for example, a beam in self-contact situation. A general contact detection procedure was introduced by Zhong et al. [78]. They used a hierarchical algorithm within the contacting entities between bodies or in one self-contacting body. In the past decades, with the development of computer graphics, several numerically efficient algorithms to search for contact between moving bodies have been presented in the literature.

In multibody system dynamics [34], computer games [21] and in efficient multi-physics engines [68], the concept of a bounding box approach is widely used to decrease the computational time associated with collision detection. Klosowski et al. [31] proposed a method based on a bounding-volume hierarchy for efficient collision detection for objects moving within highly complex environments. The bounding volumes used in their study were k-dops (discrete orientation polytopes). The k-dops form a natural generalization of axis-aligned bounding boxes. Van den Bergen [7] presented a collision detection scheme that relies on a hierarchical model representation and axis-aligned bounding boxes (AABBs). The work found AABB trees to be the method of choice for collision detection of complex models undergoing deformation. Yang et al. [74] introduced a contact searching algorithm based on bounding volume hierarchies. The procedure introduced was designed for use with the mortar finite element method, and it was employed to solve problems featuring large deformations and significant sliding. Their algorithm searches for potential contacting elements pairs and from which all the contributing points to the mortar integral are identified. They found that for large deformation problems, the bounding volume trees need to be updated in every iteration, which is computationally more costly than the contact searching algorithm itself. Haikal et al. [25] introduced an oriented volume contact search scheme to deal with non-smooth contact events e.g., corner-to-corner contact type. The contact constrained in their implementation relies on an oriented gap function which is evaluated according to the inner products of in-plane vectors defining the contact surface and the position vector of the closest node to the contact surface candidate. When dealing with large torsion loads, large displacements and rotations, self-contact may occur. Neto et al. [22] analyzed a self-contact situation of a highly flexible beam using a geometrically exact formulation. They used a contact search technique based on the overlap between imaginary spheres located at each element to find the candidates of contacting elements when the beam undergoes line-to-line contact in a loop formation. Recently, Sun et al. [16] introduced global and local strategies for contact detection. They have employed an AABBs in the global search stage to find an overlapping pair of AABBs in the frame work of an ANCF plate element.

This contribution proposes a contact procedure including a novel contact detection algorithm. This

contact detection algorithm facilitates side-to-side (segment-to-segment), corner-to-side (point-to-segment) and corner-to-corner (point-to-point) contact scenarios. The method is applied with linear complementarity condition (LCP) and the penalty to enforce the contact constraint. The transition between the above beam contact scenarios is treated by means of the minimal contact angle criterion described in [47] and is further discussed in Sect. 4.5. The presented contact detection procedure accounts for the following three phases:

1. A broad-phase (element-wise) search is performed to find the pairs of close-by elements either located in two beams or in the case of self-contact in one beam that might potentially come into contact.
2. Upon identifying the closest contacting element pairs, the oriented bounding boxes enveloping the contacting element candidates are activated. Therein, an algorithm based on the separating axis test (SAT) is used to detect contact events.
3. The intersection of the contacting bounding boxes is determined using Cyrus–Beck line clipping algorithm [27]. For the master beam, the reported intersection points are projected onto the corresponding contacting element surface to solve the closest point projection problem for the beam local parameter of the contact point. Depending on the orientation of the bounding boxes which is measured in terms of contact angles, there are the following possibilities:
  - For sufficiently small contact angles, the contact is regarded as a line-to-line model.
  - Otherwise, the contact model is of the point-to-segment (including point-to-point scenario).

The segment-to-segment contact scenario is formulated with respect to the line-to-line contact model (discussed in Sect. 3.3.3) and the other contact scenarios are regarded as the point-wise contact (discussed in Sects. 3.3.1 and 3.3.2). The line-to-line formulation also known as Gauss-point-to-segment (GPTS) formulation is preferred over the mortar methods in this work for a number of reasons: in the mortar methods, the contact constraints are expressed by introducing the special functions so-called mortar space functions on contact interface [75]. These constraint functions, which are composed of product of the shape functions on the slave and master bodies, are to be integrated across the contact surface. The required segmentation over the contact surface in the mortar methods is com-

putationally expensive, yet it concretely contributes to the accuracy of the mortar integrals [15]. A discussion over the computational cost of the mortar methods was recently presented by Harish et al. in [26]. Meanwhile, the developed Gauss-point-to-segment formulation in this work incorporates the segmentation technique to parameterize the contact patch. The mortar methods are known for their optimal convergence properties thanks to satisfying the stability conditions known as the Ladyzhenskaya–Babuška–Brezzi (LBB) conditions in expense of performing mesh refinement [75]. On the contrary, the presented GPTS formulation achieves a converged solution with a reasonable number of elements. Alongside the presented complementarity problem approach, a conventional penalty method with an embedded Newton solver is employed with the contact search scheme outlined above. The novelties with reference to the presented contact procedure can be stated as follows:

- Proposal of a contact constraint enforcement model according to the complementarity problem method for beam-to-beam contact and in particular in the case of line-to-line contact i.e., Gauss-point-to-segment (GPTS).
- Describing a narrow-phase contact search strategy to find the collision points to be applied with the point-to-segment, line-to-line and point-to-point contact scenarios.
- Comparing the optimization-based LCP approach with the classical penalty formulation with respect to their performance and accuracy.

In a number of numerical examples, the DVI optimization scheme is compared to the conventional Newton iteration embedded in the penalty formulation within each time step. In order to compare against the frictionless penalty formulation, the linear complementarity problem (LCP) is selected with the Lemke’s optimizing algorithm.

## 2 The absolute nodal coordinate formulation (ANCF)

### 2.1 Kinematics of the element

In solving the dynamics of multibody applications, deformable bodies can be described in a number of different ways. The floating frame of reference formulation, the geometrically exact beam formulations (GEB)

also known as the large rotation vector formulation in multibody literature, conventional nonlinear solid finite elements and the absolute nodal coordinate formulation (ANCF) are some of the examples. The ANCF is a finite element-based approach which is particularly designed to analyze large deformations in multibody applications. In this approach, the kinematics of deformable planar and spatial bodies, such as beams, plates and shells, can be described using polynomial-based shape functions. Absolute positions and their gradients are used as nodal degrees-of-freedom in the ANCF element [60]. The use of ANCF leads to a constant and symmetric mass matrix, however, the centrifugal and Coriolis forces are not expressed explicitly [8, 61]. Hence, the simpler dynamic equations in ANCF makes the formulation suitable in the optimized design of flexible multibody systems [20]. Although in the two-dimensional (2D) space the GEB formulations lead to constant mass matrix and the three-dimensional large rotations do not come into play in beam kinematics, 2D ANCF has some merits over the 2D GEB formulations. Some of the general advantages of the ANCF beam over the GEB formulations were already discussed in Sect. 1. In the following, we briefly point out those benefits which are prominent in the contact procedure presented:

- As mentioned above, in the ANCF including 2D beams, the position of any particle in a physical beam or its surface is given in terms of the element shape function in the current (deformed) configuration. This solid element-like feature is beneficial when combining with the employed narrow-phase contact search procedure and particularly during the Cyrus-beck line clipping process. This feature is illustrated in Sect. 3.
- In the case of ANCF, the transition from 2D to 3D is just a few simple steps because of using components of the deformation gradient to define the rotational degrees-of-freedom. One can easily replicate the presented procedure using the 3D variant of the element used [48].

This study employs a three-node quadratic ANCF planar beam element. In this element, the nodes are located at the ends and in the middle of the beam's longitudinal axis as shown in Fig. 1 [49].

Each node has four degrees-of-freedom: two components of position vector  $\mathbf{r}$  and two components of the position vector gradient  $\mathbf{r}_{,y}$ . Accordingly, the vector of the nodal coordinates can be written as:

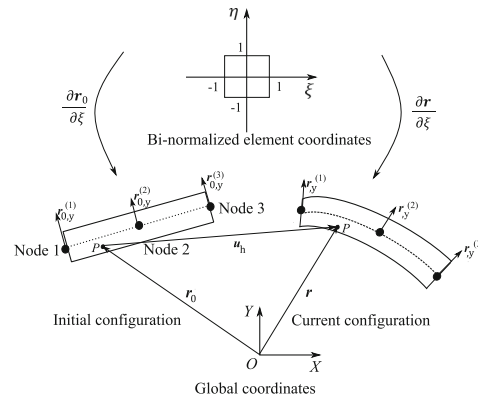


**Fig. 1** Beam kinematics defined in the reference and deformed configurations with description of the bi-normalized, the local elemental coordinates and the transformation between them, where  $u_h$  is the displacement field

$$\mathbf{q} = \left[ \mathbf{r}^{(1)T} \mathbf{r}_{,y}^{(1)T} \mathbf{r}^{(2)T} \mathbf{r}_{,y}^{(2)T} \mathbf{r}^{(3)T} \mathbf{r}_{,y}^{(3)T} \right], \quad (1)$$

where  $\mathbf{r}_{,y}$  is the derivative of position vector with respect to  $y = \frac{\partial \mathbf{r}}{\partial y}$ . The shape functions are defined for the beam element in the element's local bi-normalized coordinate system  $\boldsymbol{\xi} = \{\xi, \eta\}$  as:

$$N_1(\xi, \eta) = \frac{(\xi + 1)^2}{2} - \frac{3\xi}{2} - \frac{1}{2} \quad (2a)$$

$$N_4(\xi, \eta) = 2\xi - (\xi + 1)^2 + 2 \quad (2b)$$

$$N_2(\xi, \eta) = \frac{\ell_y \eta}{2} + \frac{\ell_y \eta (\xi + 1)^2}{4} - \frac{3\ell_y \eta (\xi + 1)}{4} \quad (2c)$$

$$N_5(\xi, \eta) = \ell_y \eta (\xi + 1) - \frac{\ell_y \eta (\xi + 1)^2}{2} \quad (2d)$$

$$N_3(\xi, \eta) = 2\xi - (\xi + 1)^2 + 2 \quad (2e)$$

$$N_6(\xi, \eta) = \frac{\ell_y \eta (\xi + 1)^2}{4} - \frac{\ell_y \eta (\xi + 1)}{4} \quad (2f)$$

where the non-dimensional quantities  $\boldsymbol{\xi} = \{\xi, \eta\}$  are defined as:

$$\xi = \frac{x}{\ell_x}, \quad \eta = \frac{y}{\ell_y}, \quad (3)$$

where  $\ell_x$  is the length and  $\ell_y$  is the height of the beam element in the undeformed configuration.

The shape function matrix for the beam element can be written with the help of Eq. 2 in the following way:

$$N = [N_1 I \ N_2 I \ N_3 I \ N_4 I \ N_5 I \ N_6 I], \tag{4}$$

where  $I$  is the 2-by-2 identity matrix. In the ANCF, an arbitrary particle within the element can be defined with respect to the global coordinates using the shape function matrix  $N$ , and the vector of the nodal degree-of-freedom  $q$  as

$$r = Nq. \tag{5}$$

### 2.2 Equations of motion

In the absolute nodal coordinate formulation, the equations of motion in weak form can be derived using the concept of variational energy as follows:

$$\delta \Pi(r, \delta r) = \delta \int_{t_1}^{t_2} (\Pi_{kin} - \Pi_{int} + \Pi_{ext} - \Pi_{con}) dt = 0, \tag{6}$$

where  $\Pi_{kin}$  is the kinetic energy of the element,  $\Pi_{int}$  is the strain energy of the element,  $\Pi_{ext}$  is the work done by externally applied forces, and  $\Pi_{con}(g_N, g_T)$  relates to contact constraint terms due to normal  $g_N$  and tangential  $g_T$  gap functions. In Eq. (6),  $t_1$  and  $t_2$  are integration limits with respect to time  $t$ . The variations of the energies can be written as:

$$\begin{aligned} \delta \Pi(r, \delta r) &= \int_{t_1}^{t_2} \left( \int_V \rho \dot{r} \delta \dot{r} dV - \int_V S : \delta E dV \right. \\ &\quad \left. + \int_V b \delta r dV - \delta \Pi_{con} \right) dt = 0 \\ &= \left[ \int_V \rho \dot{r} \delta r dV \right]_{t_1}^{t_2} \\ &\quad + \int_{t_1}^{t_2} \left( - \int_V \rho \ddot{r} \delta r dV \right. \\ &\quad \left. - \int_V S : \delta E dV + \int_V b \delta r dV + \delta \Pi_{con} \right) dt \\ &= 0, \end{aligned} \tag{7}$$

where  $\left[ \int_V \rho \dot{r} \delta r dV \right]_{t_1}^{t_2} = 0$ , because the position vector is specified at the end-points  $t_1$  and  $t_2$ ,  $\rho$  is the density of mass,  $S$  is the second Piola–Kirchhoff stress tensor,  $E$  is the Green–Lagrange strain tensor,  $:$  denotes the double dot product,  $b$  is the body force vector, which is  $b = \rho g$ , where  $g$  is the field of gravity. The variation

of kinetic energy  $\delta \Pi_{kin}$  can be represented as follows:

$$\begin{aligned} \delta \Pi_{kin} &= \int_V \rho \ddot{r} \delta r dV = \ddot{q}^T \int_V \rho N^T N dV \cdot \delta q \\ &= \ddot{q}^T M \delta q, \end{aligned} \tag{8}$$

where  $M$  is the mass matrix. The elastic force  $F_{int}$  can be derived from the variation of strain energy

$$\begin{aligned} \delta \Pi_{int} &= \int_V S : \delta E dV = \int_V S : \frac{\partial E}{\partial q} dV \delta q \\ &= F_{int} \delta q. \end{aligned} \tag{9}$$

In this work, the strain energy is derived in terms of generalized strains according to Simo and Vu-Quoc [63,64] and was adapted for the employed ANCF beam originally introduced in [49]. This structural mechanics-based approach proposed in [49] is preferred over the continuum mechanics-based approach due to its higher rate of solution convergence in the case of lower-order ANCF beams. This topic was investigated in detail for two-dimensional cases in [23] and for three-dimensional beams in [10,19]. The variations of strain energy associated with beam bending and torsion in terms of the nodal coordinate  $q$  can be expressed as follows:

$$\begin{aligned} \delta \Pi_{int}^{bt} &= \left( \int_0^L \left( E A \frac{\partial \Gamma_1}{\partial q} + k_s G A \frac{\partial \Gamma_2}{\partial q} \right. \right. \\ &\quad \left. \left. + E I_z \frac{\partial K}{\partial q} \right) dx \Big|_{y,z=0} \right) \cdot \delta q, \end{aligned} \tag{10}$$

where  $E$  and  $G$  are the Young’s modulus and shear modulus, respectively,  $\Gamma_1$  and  $\Gamma_2$  are the generalized strains,  $I_z$  is the second moment of inertia,  $k_s$  is the shear correction factor and  $K$  measures the rotation of the cross section plane with respect to the reference length. The integration in Eq. 10 is computed along the beam center line  $x$ . The additional variations of the strain energy accounting for thickness deformation can be considered as follows:

$$\delta \Pi_{int}^t = \left( \int_0^L E A \frac{\partial E_{yy}}{\partial q} dx \right) \cdot \delta q, \tag{11}$$

where the transverse strain component  $E_{yy}$  is defined in the Green–Lagrange strain tensor:

$$E = \frac{1}{2}(\mathbf{F}^T \mathbf{F} - I), \tag{12}$$

where  $I$  is the identity matrix and  $\mathbf{F}$  stands for the deformation gradient which is expressed as follows:

$$\mathbf{F} = \frac{\partial \mathbf{r}}{\partial \mathbf{r}_0} = \frac{\partial \mathbf{r}}{\partial \boldsymbol{\xi}} \left( \frac{\partial \mathbf{r}_0}{\partial \boldsymbol{\xi}} \right)^{-1} = \mathbf{I} + \frac{\partial \mathbf{u}_h}{\partial \boldsymbol{\xi}} \left( \frac{\partial \mathbf{r}_0}{\partial \boldsymbol{\xi}} \right)^{-1}, \tag{13}$$

where  $\mathbf{r}$  and  $\mathbf{r}_0$  are the current and initial reference configurations, respectively, and  $\mathbf{u}_h$  is the displacement vector from the initial configuration to the current configuration.

The external force  $\mathbf{F}_{\text{ext}}$  can be obtained using the variation of energy  $\delta \Pi_{\text{ext}}$  as follows:

$$\begin{aligned} \delta \Pi_{\text{ext}} &= \int_V \mathbf{b}^T \delta \mathbf{r} \, dV = \int_V \mathbf{b}^T \mathbf{N} \, dV \delta \mathbf{q} \\ &= \mathbf{F}_{\text{ext}} \delta \mathbf{q}. \end{aligned} \tag{14}$$

The variation of energy  $\delta \Pi_{\text{con}}$  is contributed by contact force and can be written as:

$$\delta \Pi_{\text{con}} = \mathbf{F}_{\text{con}} \delta \mathbf{q}, \tag{15}$$

where  $\mathbf{F}_{\text{con}}$  represents the contact force, which will be explained in Sect. 4.

Substituting (8), (9) and (14) into Eq. (7), the weak form of the equations of motion can be expressed as follows:

$$\ddot{\mathbf{q}}^T \mathbf{M} \delta \mathbf{q} + \mathbf{F}_{\text{int}} \delta \mathbf{q} - \mathbf{F}_{\text{ext}} \delta \mathbf{q} - \mathbf{F}_{\text{con}} \delta \mathbf{q} = 0. \tag{16}$$

### 2.3 Semi-implicit time integration with embedded Newton iteration

According to the semi-implicit Euler integration scheme, the new position  $\mathbf{q}^{l+1}$  and the new velocity  $\dot{\mathbf{q}}^{l+1}$  at the end of the new time step can be written as follows:

$$\dot{\mathbf{q}}_{\text{trial}}^{l+1} = \dot{\mathbf{q}}^{l+1} = \dot{\mathbf{q}}^l + \Delta t \ddot{\mathbf{q}}^l, \tag{17a}$$

$$\mathbf{q}_{\text{trial}}^{l+1} = \mathbf{q}^{l+1} = \mathbf{q}^l + \Delta t \dot{\mathbf{q}}^{l+1}, \tag{17b}$$

where  $\Delta t$  is the time step size. To amend the position vector  $\mathbf{q}^{l+1}$  of the contact points and in turn the velocity vector  $\dot{\mathbf{q}}^{l+1}$  at each time step, the Newton iteration is employed and is embedded into the equations of motion of the system. After substituting the acceleration  $\ddot{\mathbf{q}}^l =$

$\frac{\mathbf{q}^{l+1} - \mathbf{q}^l - \Delta t \dot{\mathbf{q}}^l}{\Delta t^2}$  at the current time into Eq. (16), the iterative form of the equations of motion is:

$$\mathbf{M} \frac{(\mathbf{q}_i^{l+1} - \mathbf{q}^l - \Delta t \dot{\mathbf{q}}^l)}{\Delta t^2} - \mathbf{F}_{\text{ext}_i}^{l+1} + \mathbf{F}_{\text{int}_i}^{l+1} + \mathbf{F}_{\text{con}_i}^{l+1} = 0, \tag{18}$$

where index  $i$  indicates the evaluation of the corresponding variable at each Newton iteration.

Accordingly,  $\mathbf{F}_{\text{ext}_i}$ ,  $\mathbf{F}_{\text{int}_i}$  and  $\mathbf{F}_{\text{con}_i}$  are the external force, elastic force and contact force at iteration  $i$  during the time period from  $t^l$  to  $t^{l+1}$ . The trial position and velocity vectors to be amended through the iteration are denoted  $\mathbf{q}_{\text{trial}}^{l+1} = \mathbf{q}_i^{l+1}$  and  $\dot{\mathbf{q}}_{\text{trial}}^{l+1} = \dot{\mathbf{q}}_i^{l+1}$ , respectively. The time integration form is created in terms of the velocities and positions, where multiple contact forces can be treated uniformly per step [2]. For the  $i$ th iteration, a new displacement is evaluated by taking the Jacobian matrix of the vector of residual forces  $\mathbf{R}_e$  with respect to the total degrees-of-freedom of the system as follows:

$$\begin{aligned} \mathbf{R}_{e_i}^{l+1} &= \mathbf{M} \frac{(\mathbf{q}_i^{l+1} - \mathbf{q}^l - \Delta t \dot{\mathbf{q}}^l)}{\Delta t^2} - \mathbf{F}_{\text{ext}_i}^{l+1} \\ &\quad + \mathbf{F}_{\text{int}_i}^{l+1} + \mathbf{F}_{\text{con}_i}^{l+1}. \end{aligned} \tag{19}$$

One can express the tangent stiffness matrix of the flexible multibody system at the  $i$ th iteration using the finite difference method as follows:

$$\begin{aligned} \mathbf{K}_i^{l+1} &= \frac{\partial \mathbf{R}_{e_i}^{l+1}}{\partial \mathbf{q}_i^l} \\ &\approx \sum_{m=0}^n \frac{\mathbf{R}_{e_i}^{l+1}(\mathbf{q}_i^{l+1} + h \hat{\mathbf{I}}^{(m)})}{2h} \\ &\quad - \frac{\mathbf{R}_{e_i}^{l+1}(\mathbf{q}_i^{l+1} - h \hat{\mathbf{I}}^{(m)})}{2h}, \end{aligned} \tag{20}$$

where  $\hat{\mathbf{I}}^{(m)}$  is the identity vector corresponding to the  $m$ th degree-of-freedom of the total  $n$  degrees-of-freedom of the system and  $h$  is the reasonable infinitesimal step [6, 70]. The next predicted-amended position vector  $\mathbf{q}_{i+1}^{l+1}$  is given as follows to check if the converged solution has been achieved:

$$\mathbf{q}_{i+1}^{l+1} = \mathbf{q}_i^{l+1} - (\mathbf{K}_i^{l+1})^{-1} \mathbf{R}_{e_i}^{l+1}. \tag{21}$$

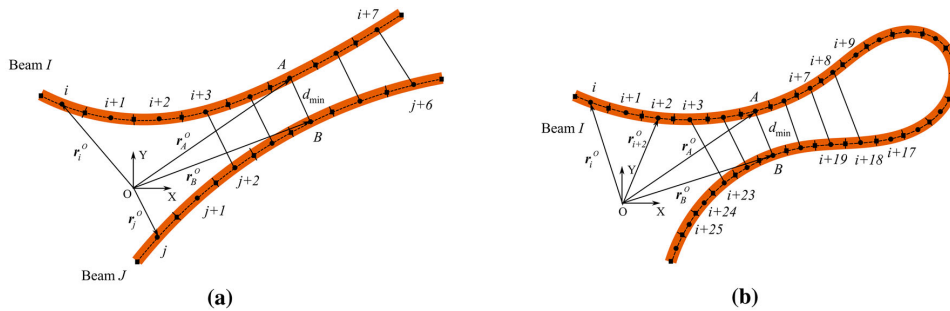


**Fig. 2** Search for the contact element candidates. **a** Checking the closest potential contact elements  $i$  and  $j$  by comparing the distance between the mid-nodes from each pair of elements between two beams,  $r_i^O$  and  $r_j^O$  are the middle nodes from element  $i$  and

**j**. **b** Checking the closest potential contact elements  $i$  and  $j$  by comparing the distance between the mid-nodes from each pair of elements in case of self-contact,  $r_i^O$  and  $r_j^O$  are the middle nodes from element  $i$  and  $j$

### 3 Contact search procedure

#### 3.1 Determination of the elements in contact

In the beam-to-beam contact, the first task in contact search is to identify the possible pairs of contact zones i.e., the global contact search. In this work, the definition of a pair of entities is addressed based on the current position of the middle node  $r_i^O$  of element  $i$  from beam  $I$  and the middle node  $r_j^O$  of element  $j$  from beam  $J$  as shown in Fig. 2a. The position vectors of the middle nodes  $r_i^O$  and  $r_j^O$  are defined from Eq. (5) with local coordinate  $(\xi = 0, \eta = 0)$  [17]. The pair of the elements  $A$  and  $B$  with minimum distance of  $d_{min}$  can be expressed as follows:

$$d_{min} = \min(\|r_i^O - r_j^O\|), \tag{22}$$

$$i = 1, 2, \dots, n_I, j = 1, 2, \dots, n_J,$$

where  $n_I$  is the number of elements of beam  $I$  and  $n_J$  is the number of element of beam  $J$ .

In the case of self-contact (Fig. 2b), the pair of closest elements needs to be considered within the beam. When contact occurs, the adjacent elements are assumed as not making contact with each other, which means element  $i$  cannot contact element  $i - 1$  and element  $i + 1$ . To prevent the adjacent middle nodes from being detected, the pair of adjacent elements are not included in the calculation of the minimum distance  $d_{min}$ . As shown in Fig. 2b, the pair of elements  $A$  and  $B$  with a minimum distance  $d_{min}$  can be expressed as follows:

$$d_{min} = \min(\|r_i^O - r_j^O\|), \tag{23}$$

$$i = 1, 2, \dots, n_I - 2, j = i + 2, i + 3, \dots, n_I,$$

where  $n_I$  is the element ID of element  $I$ .

*Remark 1* Equations (22) and (23) form the loops to detect the pairs of closest elements in the case of the beam-to-beam and beam self-contact situations, respectively. The closest element pairs are recorded for activation in the narrow-phase discussed in the forthcoming Sections. So the value of  $d_{min}$  is not of interest.

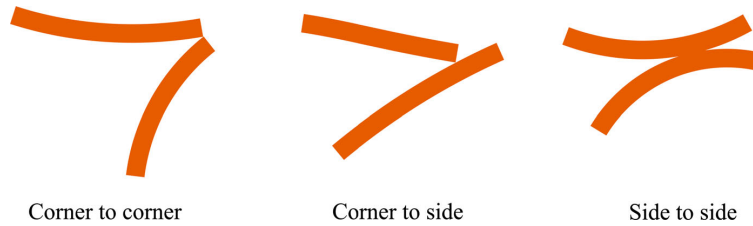
#### 3.2 Determination of the contact event

Planar contact phenomena between flexible bodies includes corner-to-corner, corner-to-side and side-to-side contact scenarios, as shown in Fig. 3. In multibody dynamic problems with flexible bodies, the contact type is not known before contact simulation.

To search for the existence of a contact event, a bounding box scheme is developed in this work. A bounding box is a single simple volume in three-dimensional space or a planar box in two-dimensional space encapsulating one or more objects of a more complex nature or those undergoing significant deformation. The main concept of this approach is to replace complex objects with simple geometrical representation, such as boxes and spheres to have efficient overlap tests [21].

In the oriented bounding box (OBB) approach, a rectangular block with an arbitrary orientation is

**Fig. 3** Possibilities of contact between beams



employed. This approach is based on the separating axis test (SAT). A separating axis of two boxes is an axis for which the projections of two polygons onto that axis never overlap. In the planar case, the existence of the separating axis sufficiently ensures that two convex polygons never intersect. In other words, two polygons do not intersect if there exists a line that completely divides a polygon on one side of the line and the other polygon on the other side of the line. This line is known as the separating line, which is perpendicular to the separating axis. The above explanation is illustrated in Fig. 4 in which  $L$  denotes the separating axis. It is worth mentioning that in the spatial case, a separating axis is still defined, but there are 15 cases to check for existence of the separating axes instead of the four trials with the planar case. Moreover, instead of separating lines that are perpendicular to the separating axes, the separating planes separate the oriented bounding volumes. For the above reasons, the SAT algorithm may not be the most efficient way for three-dimensional contact detection, and therefore, some other contact detection approaches such as Gilbert–Johnson–Keerthi distance algorithm is usually preferred [27]. Using bounding volumes allows for fast overlap rejection tests because one only needs to check if there is a separating axis, and if it gives a positive result, the objects never intersect. As shown in Fig. 4, to have an intersection between the bounding boxes encapsulating the closest elements recorded by Eqs. (22) or (23),  $L$  must not be an instant separating axis. Then, the following condition should be satisfied:

$$T_c \cdot L > \left| \left( \frac{W_A}{2} A_x \right) \cdot L \right| + \left| \left( \frac{H_A}{2} A_y \right) \cdot L \right| + \left| \left( \frac{W_B}{2} B_x \right) \cdot L \right| + \left| \left( \frac{H_B}{2} B_y \right) \cdot L \right|, \tag{24}$$

where  $T_c$  is a vector from the center of box  $B$  to the center of box  $A$ ,  $A_x$  and  $A_y$  are the unit vectors representing the local  $x$ -axis or  $y$ -axis of  $A$ ,  $B_x$  and  $B_y$  are the unit vectors denoting the local  $x$ -axis or  $y$ -axis of  $B$ ,  $W_A$

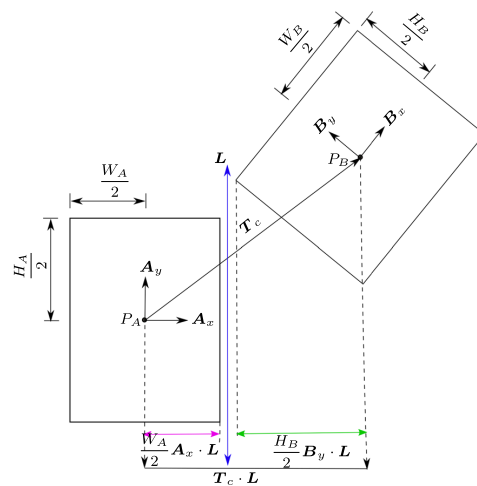


**Fig. 4** Illustration of two rectangles to check the possible intersections through existence of separating axes. The vector  $T_c$  and half of rectangle  $A$  ( $\frac{W_A}{2} A_x \cdot L$ ) and half of rectangle  $B$  ( $\frac{W_B}{2} B_x \cdot L + \frac{H_B}{2} B_y \cdot L$ ) are projected onto axis  $L = A_x$  in this illustration. The other axis  $L = A_y$  and  $L = B_y$  are not separating axes for this case. The objects in this illustration do not intersect as the projection of  $A$  and  $B$  onto the separating axis  $L = A_x$  do not overlap

is half the width of  $A$ ,  $W_B$  is half of the width of  $B$ ,  $H_A$  and  $H_B$  are half of the height of  $A$  and  $B$ , respectively, see Fig. 4. To establish a contact detection algorithm based on the oriented bounding box, a solid based mesh is used as a set of points in two-dimensional space. A convex hull is defined using the imported coordinates of the solid mesh. The mesh is created for an undeformed plane element in the bi-normalized coordinate system using the commercial finite element software ANSYS. For the  $i$ -th convex hull  $C_{H_i}$  and the  $j$ -th convex hull  $C_{H_j}$  correspond to the closest element pair, one side of the bounding box contains an edge of the convex hull. Hereafter, to simplify the notation, the subscripts  $i$  and

$j$  are dropped. The edge of convex hull  $C_H$  is defined as follows:

$$E^{(2 \times nc)} = C_H(X, Y^{ic}) - C_H(X, Y^{ic-1}) \quad (25)$$

$ic = 2, \dots, nc,$

where  $nc$  denotes the number of columns of the convex hull and  $ic$  is the column index and  $X$  and  $Y$  are the global coordinates of the points along the convex hull edges. The angle of the convex hull edges can be computed as follows:

$$T = \tan^{-1} \left( \frac{E^{(2)}}{E^{(1)}} \right). \quad (26)$$

Assigning a rotation matrix to  $n_a$  angles given by Eq. (26) gives a global rotation matrix of  $R^{(2n_a \times 2)}$ . The rotated convex hull then is of the form

$$R_{CH} = RC_H. \quad (27)$$

The border size of each bounding box for all possible edges is computed as follows:

$$b_s = \max_{C_H} R_{CH}(R, C_H) - \min_{C_H} R_{CH}(R, C_H). \quad (28)$$

Subsequently, the area of the bounding boxes for all possible edges can be determined among which the smallest one belongs to the minimal-volume-oriented bounding box. Then, the coordinates of the corners of the minimal-volume bounding box can be determined in a straightforward manner. To this end, by the following transformation

$$B = R_{OBB} C_H \quad (29)$$

all the possible bounding boxes are transformed on the rotated frame  $R_{OBB}$  which corresponds to the smallest bounding box whose index is identified by the minimum bounding boxes area according to Eq. (28). After identification of the borders of the minimum-oriented bounding box, its corners can be simply found using the corresponding rotation matrix.

### 3.3 Determination of the contact points

After detecting the pair of closest elements  $A$  and  $B$  described in Sect. 3.1, and determining an active contact between the contacting OBBs explained in

Sect. 3.2, the next task is the placement of the contact point to measure the gap function in order to apply the contact constraint. Consequently, a line clipping process according to Cyrus–Beck algorithm [27] is started to determine the intersection between the colliding bounding boxes.

#### 3.3.1 Point-to-segment contact model

Contact between the beam corner and beam edge is considered to be point-to-segment contact.

In the point-to-segment contact model, since the collision point between two OBBs is determined according to the Cyrus–Beck algorithm, the exact contact point is identified by solving a number of closest point projection problems (CPP), see Fig. 5. This approach leads to an accurate enough approximation of a contact point which would physically belong to the beam surface. The following closest projection point problem

$$p(\eta_A^{CB}) = (r_A^{P'} - r_A^{CB})^T r_{A,\eta}^P = 0 \quad (30)$$

is solved for the closest value of master beam parameter  $\eta_A^{CB}$  to the intersection point, where

$$r_{A,\eta}^P = \frac{\partial r_A^P}{\partial \xi_A} = \frac{\partial N_m}{\partial \eta_A} q_A \quad (31)$$

and superscript  $^{CB}$  denotes the intersection between lines given by the Cyrus–Beck clipping process. Then, the position of resulted point  $P'$  is:

$$r_A^{P'} = N(1, \eta_A^{CB}) q_A. \quad (32)$$

Since the contact takes place on the side of the ANCF beam, the value of the local coordinates  $\eta^P$  and  $\eta^Q$  can only be  $-1$  or  $1$  in the current configuration [24]. Thereto, local coordinates  $\xi_A^P$ , ranging from  $-1$  to  $1$ , respectively, is the solution of the following closest point projection problem [72]:

$$h_1(\xi_A^P) = (r_A^P - r_A^{P'})^T r_{A,\xi}^P = 0, \quad (33)$$

where

$$r_{A,\xi}^P = \frac{\partial r_A^P}{\partial \xi_A} = \frac{\partial N_m}{\partial \xi_A} q_A. \quad (34)$$

As shown in Fig. 6 assuming the connecting line between point  $P$  on beam  $A$  (master) and point  $Q$  of

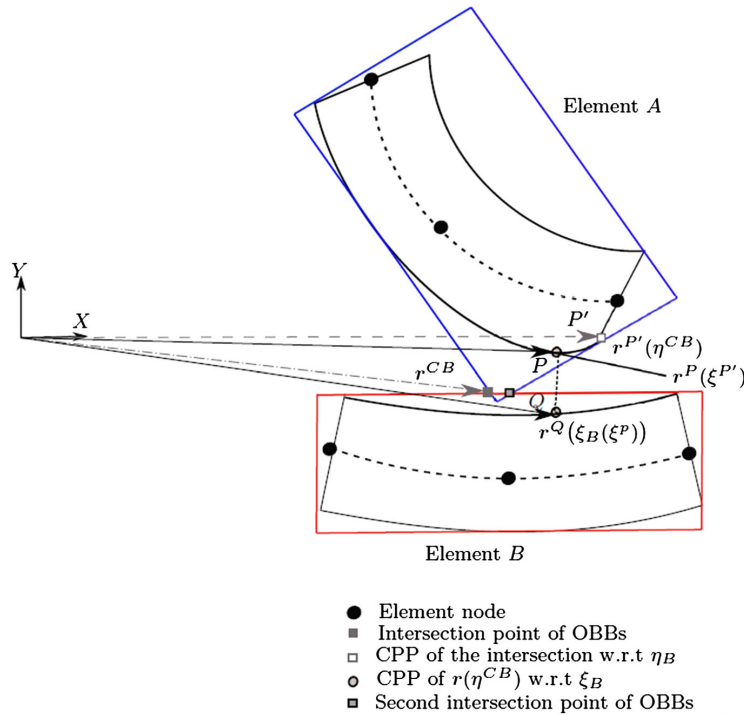


**Fig. 5** Kinematics of a contact event when a corner makes contact with a side. The master point  $r^P(\xi^{P'})$  is found after solving two closest point projection problems (CPP) for  $\eta$  and  $\xi$ , respectively

beam  $B$  (slave) is perpendicular to the tangent vector at point  $Q$ , the following unilateral minimal distance problem

$$\min_{\xi_B} d(\xi_A, \xi_B) = d(\xi_A, \xi_B^c) = \left\| r_A(\xi_A^P) - r_B(\xi_B^c) \right\| \tag{35}$$

should be solved for the unknown closest coordinate parameters  $\xi_B^c \equiv \xi_B^Q$  via the following orthogonality problem:

$$h_2(\xi_A^P, \xi_B^Q) = (r_B^Q - r_A^P)^T r_{B,\xi}^Q = 0, \tag{36}$$

where

$$r_{B,\xi}^Q = \frac{\partial r_B^Q}{\partial \xi_B} = \frac{\partial N}{\partial \xi_B} q_B. \tag{37}$$

The solution of the quadratic problems for  $\xi_A^P$  and  $\xi_B^Q$ , respectively, appeared in Eqs. (33) and (36) necessitates Newton's iterative procedure. The contact points are

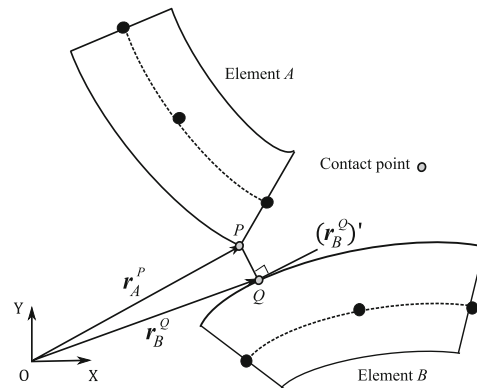


**Fig. 6** Contact detection when a corner makes contact with a side

thus as follows:

$$r_A^P = N(\xi_A^P) q_A \quad \text{and} \quad r_B^Q = N(\xi_B^Q) q_B. \tag{38}$$

### 3.3.2 Point-to-point contact model

In this section, the collision point detection in the corner-to-corner contact scenario is analyzed. In this case, it is assumed that the closest points  $P$  and  $Q$  are located at the corner of two beams. The contact candidate points are represented by their coordinates  $r_A^P$  and  $r_B^Q$ , which can be calculated analogous to the approach described in Sect. 3.3.1 for the point  $P$ . However, that procedure should be replicated here in the case of the other corner  $Q$ . Repeating the same routine as that formulated through Eqs. (30)–(34) ends up with the following bilateral minimal distance problem:

$$\begin{aligned} \min_{\xi_A, \xi_B} d(\xi_A, \xi_B) &= d(\xi_A^c, \xi_B^c) \\ &= \left\| r_A(\xi_A^P) - r_B(\xi_B^Q) \right\|. \end{aligned} \tag{39}$$

Consequently, the additional orthogonality condition

$$h_3(\xi_A^P, \xi_B^Q) = (r_B^Q - r_A^P)^T r_{A,\xi}^P = 0 \tag{40}$$

should be satisfied, where

$$r_{A,\xi}^P = \frac{\partial r_A^P}{\partial \xi_A} = \frac{\partial N}{\partial \xi_A} q_A. \tag{41}$$

Therefore, in contrast to the unilateral distance problem (35) in the point-to-segment contact model, the bilateral distance problem (39) leads to two orthogonality conditions (36) and (40). This is equivalent to the point-to-point formulation originally introduced by Wriggers et al. [72]. It is classified as master-to-master formulation [51] as no distinction between the slave and master entities in contacting beams is made.

### 3.3.3 Line-to-line contact model

The approach presented in Sect. 3.3.1 was to find the exact contact points when point-wise contact happens i.e., in the case of a small contact patch between two beams or self-contact of one physical beam. However, when the contact patch is large compared to the other dimensions of the contacting beams (roughly parallel contacting elements), the point-to-point procedure described in the previous Section should be adjusted to find the contact patch end-points. As illustrated in Fig. 7, two points are given as the results of the line clipping process. Although in the previous Section, two intersection points were also screened, see Fig. 5, the

second point is too close to  $P_{CB}$ . In Sect. 4, a measure to consider a contact being point- or patch-wise is further discussed. Analogous to the point-to-segment model, the following closest point projection problems

$$p_1(\xi_A^{P_{CB}}) = (r_A^P - r^{P_{CB}})^T r_{A,\xi}^P = 0 \tag{42a}$$

$$p_2(\xi_A^{Q_{CB}}) = (r_A^Q - r^{Q_{CB}})^T r_{A,\xi}^Q = 0, \tag{42b}$$

should be solved for the abscissa coordinate parameters  $\xi_A^{P_{CB}}$  and  $\xi_A^{Q_{CB}}$  corresponding to the intersections  $P_{CB}$  and  $Q_{CB}$ . The contact patch boundaries

$$r_A^P = N(\xi_A^{P_{CB}}, \eta_A^P) q_A \tag{43a}$$

and

$$r_A^Q = N(\xi_A^{Q_{CB}}, \eta_A^Q) q_A \tag{43b}$$

on master beam  $A$  are to be assigned onto the slave beam  $B$  to confine the contact patch  $RS$  via the following set of closest point projections:

$$p_3(\xi_B^R) = (r_B^R - r_A^P)^T r_{B,\xi}^R = 0 \tag{44a}$$

$$p_4(\xi_B^S) = (r_B^S - r_A^Q)^T r_{B,\xi}^S = 0, \tag{44b}$$

where  $\xi_B^R$  and  $\xi_B^S$  are the abscissa coordinate parameters on beam  $B$ . The contact patch  $RS$  is thus confined at the following points:

$$r_B^R = N(\xi_B^R, \eta_B^R) q_B \tag{45a}$$

and

$$r_B^S = N(\xi_B^S, \eta_B^S) q_B. \tag{45b}$$

Algorithm 1 is written in view of the procedure in [21]. It describes the proposed contact search approach based on the oriented bounding box, which detects and identifies the collision points, which are significantly important in the calculation of the vector of the contact force.

## 4 Contact constrain enforcement

This section discusses two methods used in this work for contact constraint enforcement. This includes the penalty presented in Sects. 4.1 and 4.2 and the linear complementarity problem (LCP) approach introduced in Sects. 4.3 and 4.4.

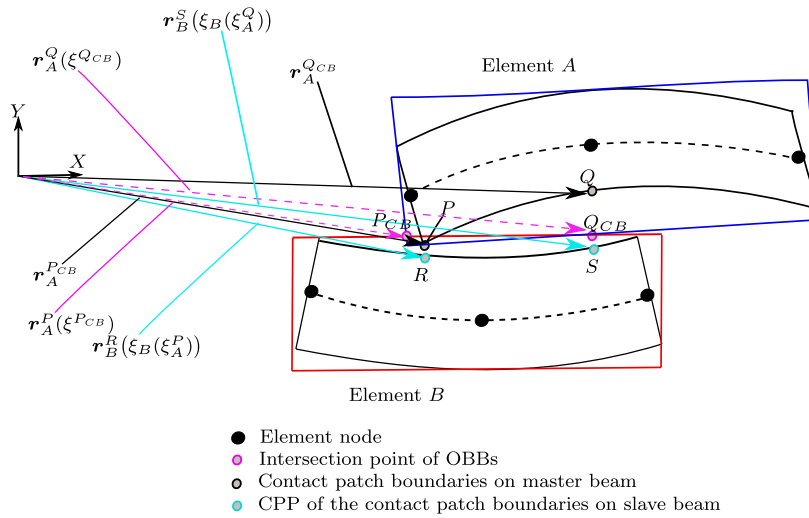


Fig. 7 A side-to-side contact situation happens when contact angle is small enough according to Eq. (83)

**Algorithm 1** Contact detection algorithm based on the intersection of the OBBs to detect the contact events and to find the contact points

```

1: Loop over the beam elements to identify the closest element pairs; the element candidates come into contact
2: for i = 1 : n_A do
3:   for j = 1 : n_B do ▷ Having found the closest distance between the two beams or one physical beam in the case of self-contact
         situation, the corresponding element ID's are recorded.
4:   end for
5: end for
6: The recorded element ID's are retrieved to establish the OBBs to encapsulate each contacting element candidate
7: The vertices of each OBBs are obtained ▷ See Section 3.2
8: Evaluating T_c · L, W_A, H_A, W_B, H_B, A_x, A_y, B_x and B_y
9: if Eq. (24) is satisfied for OBBs encapsulating the contacting element candidates then
10:   Starting the Cyrus-Beck's line clipping process to find the OBB's intersections
11:   for i = 1 : 4 do
12:     for j = 1 : 4 do
13:       Follow the procedure presented in Sections 3.3
14:     end for
15:   end for
16: end if

```

4.1 Penalty method based on the point-to-segment formulation

This section describes the application of the penalty method for enforcing contact constraints in the case of the point-to-segment contact formulation. The normal gap function  $g_N$  can be written in terms of the derived contact points in Eq. (38) as follows:

$$g_N = \|r_A^P - r_B^0\| - \|r_B^Q - r_B^0\|, \tag{46}$$

where  $r_B^{Q_0} = N_m(\xi_B^{Q_0}, 0)q_B$  is the closest projection of the master point  $r_A^P$  on the slave beam  $B$  axis where  $\xi_B^{Q_0}$  is the solution of

$$h_2(\xi_B^{Q_0}(\xi_A^P))|_{\eta_B=0} = 0. \tag{47}$$

If the gap function  $g_N$  is positive ( $g_N > 0$ ), there is no contact between bodies ( $f_N = 0$ ), and consequently the variation of energy  $\delta I_{con}$  based on the contact force

is not introduced. In the opposite case ( $g_N \leq 0$ ), the contact occurs when ( $f_N > 0$ ), the contact contribution terms  $\delta \Pi_{\text{con}}$  should be taken into account in the weak form  $\delta \Pi$ . In the absence of tangential force, the Signorini non-penetration conditions for the unilateral contact take the form

$$g_N \geq 0, \quad f_N \geq 0, \quad g_N f_N = 0, \tag{48}$$

which coincides with the Karush–Kuhn–Tucker (KKT) non-penetration constraints. The penalty potential energy  $\Pi_{\text{con}}^{\text{PM}}$  related to normal contact is expressed as follows:

$$\Pi_{\text{con}}^{\text{PM}} = \frac{1}{2} c_N g_N^2, \tag{49}$$

where  $c_N$  is the normal penalty parameter. The variation of the penalty potential energy (49)

$$\delta \Pi_{\text{con}}^{\text{PM}} = c_N g_N (\delta \mathbf{r}_A^P - \delta \mathbf{r}_B^Q)^T \mathbf{n}(\xi_A^P) \tag{50}$$

is equivalent to the contact energy contribution in Eq. (15) where

$$\mathbf{n}(\xi_A, \xi_B) = \frac{\mathbf{r}_B^Q - \mathbf{r}_A^P}{\|\mathbf{r}_B^Q - \mathbf{r}_A^P\|} \tag{51}$$

is the contact normal vector. Thereto, the point-wise discrete contact force can be read from Eq. (50):

$$\mathbf{F}_{\text{con}}^{\text{PM}} = c_N g_N \mathbf{n}. \tag{52}$$

The variation of the normal gap function is expressed as follows:

$$\begin{aligned} \delta g_N &= \delta((\mathbf{r}_A^P - \mathbf{r}_B^Q)^T \mathbf{n}_A^P) \\ &= (\delta \mathbf{r}_A^P - \delta \mathbf{r}_B^Q)^T \mathbf{n}_A^P + (\mathbf{r}_A^P - \mathbf{r}_B^Q)^T \delta \mathbf{n}_A^P, \end{aligned} \tag{53}$$

where  $(\mathbf{r}_A^P - \mathbf{r}_B^Q)^T \delta \mathbf{n}_A^P = 0$  and  $\delta \mathbf{r} = \frac{\partial \mathbf{r}}{\partial \mathbf{q}} \delta \mathbf{q} = \mathbf{N} \delta \mathbf{q}$ . Therefore, the variation of the normal gap can be reduced to the following form:

$$\delta g_N = (\mathbf{N}_A^P \delta \mathbf{q}_A - \mathbf{N}_B^Q \delta \mathbf{q}_B)^T \mathbf{n}_A^P. \tag{54}$$

*Remark 2* In the case of the point-to-point contact model in Sect. 3.3.2, it is cumbersome to define the normal vector using Eq. (51) at the corner of beams

and the gap function calculation cannot follow Eq. (46) function. On this account, an approach based on penetration check originally proposed by [41] is discussed in Sect. 5.4.

*Remark 3* As it can be realized from Fig. 5, there is a scenario when the bounding boxes intersect, but still there is no intersection between the two beams. This usually happens when deformation is large. In such a situation, the bounding boxes continue to interpenetrate as a result of a positive gap function. This is also the case for the line-to-line formulation in the forthcoming Section.

#### 4.2 Penalty method based on the line-to-line contact formulation

In the case of the beam line-to-line contact formulation, the unilateral minimum problem for two contacting beams is expressed in terms of the closest distance field between two contacting beams. The closest vector field on beam  $A$  (master)  $\mathbf{r}_A^c(\xi_B)$  corresponds to the position field belonging to beam  $B$  (slave),  $\mathbf{r}^B$  is obtained by solving the following minimal distance problem

$$\min_{\xi_A} d(\xi_A, \xi_B) = d(\xi_A^c, \xi_B) = \|\mathbf{r}_B(\xi_B) - \mathbf{r}_A^c(\xi_A)\|, \tag{55}$$

where superscript  $c$  denotes the closest point coordinate assigned to the master element, and hereafter, it denotes the entity assigned to the coordinate given by closest point projection problem. In the line-to-line contact, the unique solution to (55) leads to one orthogonality condition in which the task is seeking for unknown  $\xi_A^c(\xi_B)$  that is the master closest point coordinate corresponds to the slave point in terms of the coordinate field parameter  $\xi_B$

$$\begin{aligned} f(\xi^A, \xi^B) &= (\mathbf{r}_A(\xi_A) - \mathbf{r}_B(\xi_B))^T \mathbf{r}_{A,\xi}(\xi_A) \\ \text{with } f(\xi_A^c, \xi_B) &= 0, \end{aligned} \tag{56}$$

where  $\mathbf{r}_{A,\xi}(\xi_A)$  is the tangent of the position vector field  $\mathbf{r}_A$  with respect to the local coordinate  $\xi_A$ . The gap function field  $g(\xi_A(\xi_B), \xi_B)$  is defined to express the non-penetration condition

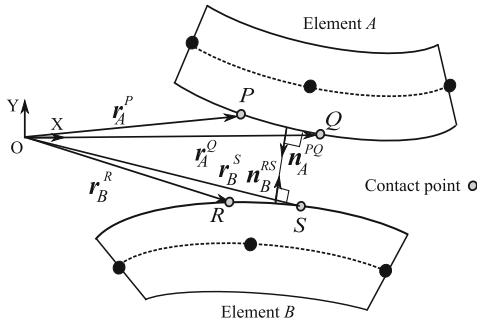


**Fig. 8** Illustration of the minimum distance gap function when side-to-side contact takes place

$$\begin{aligned}
 g_N(\xi_A(\xi_B), \xi_B) &= d(\xi_A^c(\xi_B), \xi_B) \\
 &= \left\| \mathbf{r}_A^{P_0Q_0} - \mathbf{r}_B^{R_0S_0} \right\| \\
 &\quad - \left( \left\| \mathbf{r}_A^{PQ} - \mathbf{r}_A^{P_0Q_0} \right\| \right. \\
 &\quad \left. + \left\| \mathbf{r}_B^{RS} - \mathbf{r}_B^{R_0S_0} \right\| \right) \quad (57a) \\
 g(\xi_A(\xi_B), \xi_B) &\geq 0. \quad (57b)
 \end{aligned}$$

where position field  $\mathbf{r}_A^{P_0Q_0} = \mathbf{N}_m(\xi_A^{P_0Q_0}, 0)\mathbf{q}_A$  results from the projection of the intersections  $P_{CB}$  and  $Q_{CB}$  on the master element axis and the position field  $\mathbf{r}_B^{R_0S_0} = \mathbf{N}_m(\xi_B^{R_0S_0}, 0)\mathbf{q}_B$ , in the same way resulted from the projection of the closest points  $P$  and  $Q$  on the slave element axis. In the light of the segment-to-segment integration along the parameterized contact patch that was previously applied in the mortar contact method in [11, 16, 55], and with reference to the line-to-line contact formulation proposed by Meier et al. [45], the penalty potential energy in terms of the established contact patch shown in Fig. 8 is of the following form

$$\Pi_{con}^{PM} = c_N \frac{1}{2} \int_{RS} g_N(\xi_A^c(\xi_B), \xi_B)^2 d\xi_B. \quad (58)$$

Accordingly, the contribution of contact energy to the weak form of equation of motion (6) can be expressed as follows:

$$\begin{aligned}
 \delta \Pi_{con} &= c_N \int_{RS} g_N(\xi_A^c(\xi_B), \xi_B) \delta g_N(\xi_A^c(\xi_B), \xi_B) d\xi_B, \\
 &\text{with } g_N(\xi_B) \equiv g_N(\xi_A^c(\xi_B), \xi_B), \quad (59)
 \end{aligned}$$

where

$$\delta g_N(\xi_B) = (\delta \mathbf{r}_A^{PQ}(\xi_A^c) - \delta \mathbf{r}_B^{RS}(\xi_B))^T \delta \mathbf{r}_{B,\xi}(\xi_B) \quad (60)$$

and  $RS$  indicates the integration domain on the slave beam  $B$ . The vector of distributed contact force can be identified in Eq. (59) in the form of

$$\mathbf{F}_{con}^{PM} = \int_N^{PM}(\xi_B) \mathbf{n}, \quad (61)$$

where

$$\int_N^{PM} = c_N g_N(\xi_B) \quad (62)$$

is the average magnitude of contact pressure on the entire contact patch and

$$\mathbf{n}(\xi_B) = \frac{\mathbf{r}_B^{RS}(\xi_B) - \mathbf{r}_A^{PQ}(\xi_A^c)}{\left\| \mathbf{r}_B^{RS}(\xi_B) - \mathbf{r}_A^{PQ}(\xi_A^c) \right\|} \quad (63)$$

the contact normal vector.

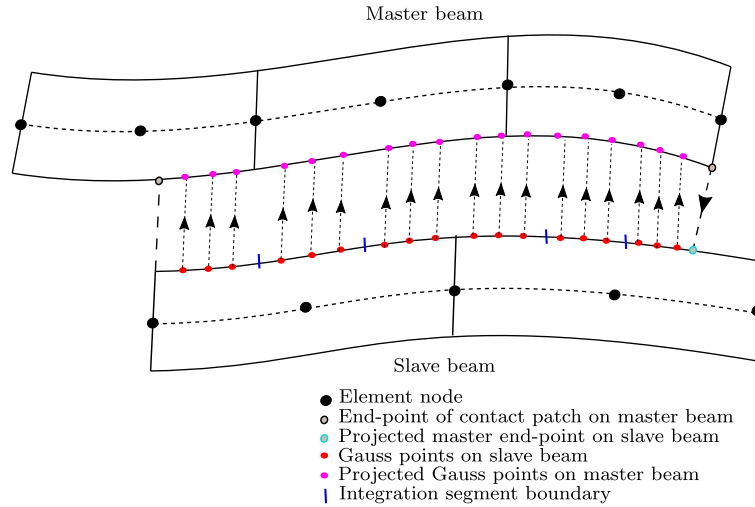
#### 4.2.1 Parameterization of contact patch

The variation of energy (59) can be expressed in discretized form by substituting the position vector  $\mathbf{r}$  from Eq. (5) into Eq. (59):

$$\begin{aligned}
 \delta \Pi_{con} &= \delta \mathbf{q}_A^T \sum_{j=1}^{n_G} g_N(\xi_B^j) \mathbf{N}(\xi_A^c(\xi_B^j))_A^T \mathbf{n}(\xi_B^j) w_j J(\xi_A^c(\xi_B^j)) \\
 &\quad - \delta \mathbf{q}_B^T \sum_{j=1}^{n_G} g_N(\xi_B^j) \mathbf{N}(\xi_B^j)_B^T \mathbf{n}(\xi_B^j) w_j J(\xi_B^j), \quad (64)
 \end{aligned}$$

where  $n_G$  is the number of Gauss points in a contacting element,  $w_j$  are the corresponding Gauss points weight,  $\xi_B^j$  is the Gauss point coordinate in terms of the slave beam parameter  $\xi_B$ ,  $\xi_A^c(\xi_B^j)$  is the closest projected master point assigned to the Gauss slave point parameter  $\xi_B^j$  and  $J(\xi_A^c(\xi_B^j))$  and  $J(\xi_B^j)$  are the scaling factor between the increment of the Gauss point coordinates in the bi-normalized and the physical coordinate systems in the master and slave beams, respectively. The integration interval used in Eq. (64) can be further parameterized by assigning  $n_S$  segments for each beam slave element, see Fig. 9. Therefore, for  $n_S$  number

**Fig. 9** Illustration of integration segmentation along the contact patch in the contacting master and slave beams



of segments within a slave element, a new coordinate parameter in a slave beam element can be introduced as

$$\xi_B^{sj} = \xi_B^s(\xi_B^j) = \frac{\xi_B^{2e} - \xi_B^{1e}}{2} \xi_B^j + \frac{\xi_B^{2e} + \xi_B^{1e}}{2}, \quad (65)$$

for  $j = 1, \dots, n_G$ , for  $i = 1, \dots, n_S$

where  $\xi_B^{1e}$  and  $\xi_B^{2e}$  are the integration boundaries at each integration segment. The parameter  $\xi^s$  is equidistantly spaced within interval  $[-1, 1]$  unless there exists a projection for a master beam end-point to be assigned onto a slave beam segment such that  $\xi_B^{1e} \equiv \xi_B(\xi_A^P)$  and/or  $\xi_B^{2e} \equiv \xi_B(\xi_A^Q)$  where  $\xi_A^P$  and  $\xi_A^Q$  are the master beam end-points abscissa coordinate parameters. Therefore, according to Eq. (56)

$$\begin{aligned} f(\xi_B^{1e}, \xi_A^P) &= 0 \\ \text{and/or} & \\ f(\xi_B^{2e}, \xi_A^Q) &= 0. \end{aligned} \quad (66)$$

Now, the discretized contact energy variation (64) can be expressed with a further parameterization consisting of the beam discretization and the contact segmentation. It is represented in the form of two sums over the number of Gauss points and over the integral segments:

$$\begin{aligned} \delta \Pi_{\text{con}} &= \delta \mathbf{q}_A^T \sum_{j=1}^{n_G} \sum_{i=1}^{n_S} g_N(\xi_B^{sj}) \mathbf{N}(\xi_A^c(\xi_B^{sj}))_A^T \mathbf{n}(\xi_B^{sj}) w_j J(\xi_A^c(\xi_B^{sj})) \\ &\quad - \delta \mathbf{q}_B^T \sum_{j=1}^{n_G} \sum_{k=1}^{n_S} g_N(\xi_B^{sj}) \mathbf{N}(\xi_B^{sj})_B^T \mathbf{n}(\xi_B^{sj}) w_j J(\xi_B^{sj}), \end{aligned} \quad (67)$$

where

$$\begin{aligned} J(\xi_A^c(\xi_B^{sj})) &= J(\xi_B^{sj}) \\ &= H \frac{\partial \mathbf{r}_B^{(1)}}{\partial \xi_B} \frac{\partial \xi_B}{\partial \xi_B^s} \\ &= H \frac{L_B}{2} \frac{\xi_B^{2e} - \xi_B^{1e}}{2}, \end{aligned} \quad (68)$$

in which  $L_B$  is the slave beam length and  $H$  is the element height.

*Remark 4* As illustrated in Fig. 9, the established Gauss points on the slave beam characterized by coordinate parameter  $\xi_B^{sj}$  are to be projected onto the master beam using Eq. (56). To this end, an internal search should be considered in the computation algorithm to find the closest master element to each Gauss points on the slave beam.

### 4.3 Linear complementarity method based on the point-to-segment formulation

In the absence of friction, the normal contact force vector  $\mathbf{F}_{k,N}^P$  for the  $k$ -th contact is imposed on the beam  $A$  by the components of normal vector  $\mathbf{n}_P$  on the contact point  $P$ , such that:

$$\mathbf{F}_k^P = \mathbf{F}_{k,N}^P = \mathbf{n}_P \hat{\gamma}_{k,N}, \quad (69)$$

where  $\hat{\gamma}_{k,N}$  is the Lagrange multiplier vector corresponding to the values of the normal contact forces.

It is worth noting that the discrete contact force  $F_k^Q$  on the beam in the point-to-point and point-to-segment formulation is the reaction force of  $F_k^P$  as:

$$F_k^Q = -F_k^P. \tag{70}$$

The variation of energy  $\delta\Pi_{\text{con},N}^{\text{LCP}}$  related to the contact force within the linear complementarity problem (LCP) associated with the contact force can be expressed as:

$$\begin{aligned} \delta\Pi_{\text{con}}^{\text{LCP}} &= (F_k^P)^T \delta r_A^P - (F_k^P)^T \delta r_B^Q \\ &= \begin{bmatrix} (N_A^P)^T \mathbf{n}_P \hat{\gamma}_{k,N} \\ -(N_B^Q)^T \mathbf{n}_P \hat{\gamma}_{k,N} \end{bmatrix}^T \delta \mathbf{q} = \mathbf{F}_{\text{con},k}^T \delta \mathbf{q}, \end{aligned} \tag{71}$$

where

$$\delta \mathbf{q} = \begin{bmatrix} \delta q_A \\ \delta q_B \end{bmatrix}, \tag{72a}$$

$$\mathbf{F}_{\text{con},k} = \mathbf{D}_k \hat{\gamma}_{k,N} \tag{72b}$$

and

$$\mathbf{D}_k = \begin{bmatrix} (N_A^P)^T \mathbf{n}_{Pk} \\ -(N_B^Q)^T \mathbf{n}_{Pk} \end{bmatrix}. \tag{72c}$$

For the  $k$ -th contact,  $\mathbf{D}_k$  is a vector which can define the location and direction of the contact force in the global coordinate system.  $\mathbf{D}_k$  is computed based on the  $k$ -th pair of potential contact points. If there is  $N_k$  presence of contact events at same time step,  $\mathbf{D}$  and  $\hat{\gamma}$  can be constructed at the system level as:

$$\begin{aligned} \mathbf{D} &= \underbrace{[\mathbf{D}_1 \ \mathbf{D}_2 \ \dots \ \mathbf{D}_{N_k}]}_{N_{\text{dof}} \times N_k}, \\ \hat{\gamma} &= \begin{bmatrix} \hat{\gamma}_{1,N} \\ \hat{\gamma}_{2,N} \\ \vdots \\ \hat{\gamma}_{N_k,N} \end{bmatrix} N_k \times 1, \end{aligned} \tag{73}$$

where  $N_{\text{dof}}$  refers to total number of degrees-of-freedom of the system.

#### 4.4 Linear complementarity method based on the line-to-line formulation

When dealing with line-to-line contact formulation, the contact energy contribution to the weak form has to be defined in terms of a distributed force model. In this way, the variation of contact energy is in the form of

$$\delta\Pi_{\text{con}}^{\text{LCP}} = (F_k^{PQ})^T \delta r_A^{PQ} - (F_k^{RS})^T \delta r_B^{RS}, \tag{74}$$

where the first and the second terms represent the contact energy contribution with respect to beam  $A$  (master) and beam  $B$  (slave), respectively, in which  $F^{PQ}$  and  $r_B^{RS}$  are the corresponding continuous contact force over the entire contact patch defined with the position fields  $r_A^{PQ}$  and  $r_B^{RS}$ . The variational contact energy (74) is in the form of

$$\begin{aligned} \delta\Pi_{\text{con}}^{\text{LCP}} &= \delta q_A^T \int_{RS} N(\xi_A(\xi_B)) \mathbf{n}_A(\xi_B, \xi_A(\xi_B)) \hat{\gamma}_{k,N} d\xi_B \\ &\quad - \delta q_B^T \int_{RS} N(\xi_B) \mathbf{n}_A(\xi_B, \xi_A(\xi_B)) \hat{\gamma}_{k,N} d\xi_B \end{aligned} \tag{75}$$

in which  $RS$  denotes the contact patch on the slave element  $B$ . Analogously to the definition for the discrete contact force given in Eq. (72b), the distributed contact force acting on each beam element are

$$F_{\text{con},k}^{PQ} = \mathbf{D}_{A,k} \hat{\gamma}_{k,N} \tag{76a}$$

$$F_{\text{con},k}^{RS} = \mathbf{D}_{B,k} \hat{\gamma}_{k,N}, \tag{76b}$$

where  $\mathbf{D}_{A,k}$  and  $\mathbf{D}_{B,k}$  are to be parameterized according to the Gauss-point-to-segment (or line-to-line) approach described in Sect. 4.2 in the form of

$$\mathbf{D}_{A,k} = \sum_{j=1}^{n_G} N(\xi_A(\xi_B^j))^T \mathbf{n}(\xi_A(\xi_B^j), \xi_B^j) w_j J(\xi_B^j) \tag{77a}$$

$$\mathbf{D}_{B,k} = - \sum_{j=1}^{n_G} N(\xi_B)^T \mathbf{n}(\xi_A(\xi_B^j), \xi_B^j) w_j J(\xi_B^j). \tag{77b}$$

Applying of the same integration segmentation scheme as presented in Sect. 4.2.1 yields:

$$\mathbf{D}_{A,k} = \sum_{j=1}^{n_G} \sum_{s=1}^{n_S} N(\xi_A(\xi_B^{sj}))^T \mathbf{n}(\xi_A(\xi_B^{sj}), \xi_B^{sj}) w_j J(\xi_A(\xi_B^{sj})) \tag{78a}$$

$$D_{B,k} = \sum_{j=1}^{n_G} \sum_{s=1}^{n_S} N(\xi_B^{sj})^T \mathbf{n}(\xi_B^{sj}) w_j J(\xi_B^{sj}) \quad (78b)$$

that are analogous to Eq. (72c). For  $N_k$  number of contact events per time step Eq. (73) is valid and consists of  $N_k$  surface-to-surface contact scenarios.

*Remark 5* The gap function is calculated according to Eq. (57), but first, the contributions

$$\mathbf{r}_A^{PQ} = \int_{\xi_A^P}^{\xi_A^Q} N d\xi_A \mathbf{q}_A \quad (79)$$

and

$$\mathbf{r}_B^{RS} = \int_{\xi_B^R}^{\xi_B^S} N d\xi_B \mathbf{q}_B \quad (80)$$

and also those denoted  $\mathbf{r}_A^{P_0Q_0}$  and  $\mathbf{r}_B^{R_0S_0}$  defining the contact patch should be integrated separately with respect to the procedure described in Sect. 4.2.1.

#### 4.5 Transition between point-wise and line-to-line formulations

As briefly pointed out in Sect. 1, the point-to-point and line-to-line beam contact formulations have their own limitations with respect to the angle range within which contact takes place. These limitations were already derived in [45] and circumvented in [47]. In this work, the transition between the point-to-segment and line-to-line contact scenarios is handled by means of measuring the contact angle with reference to the point-wise (point-to-segment or point-to-point) contact type. So that, in case of a sufficiently small contact angle, the line-to-line formulation is required. In the ANCF, the angle between two contacting beam elements is defined in terms of the angle between the tangent vectors at the contact points:

$$\chi = \frac{\|\mathbf{r}_{A,\xi}^T(\xi_A^P) \mathbf{r}_{B,\xi}^T(\xi_B^Q)\|}{\|\mathbf{r}_{A,\xi}(\xi_A^P)\| \cdot \|\mathbf{r}_{B,\xi}(\xi_B^Q)\|} \quad (81)$$

with  $\alpha = \arccos(\chi)$ ,

in which  $\alpha \in [0; \frac{\pi}{2}]$ . The rate of rotation of the cross section rotation with respect to the beam undeformed

center line is adopted according to [24] as follows:

$$K = \frac{\mathbf{r}_{,\eta} \times \mathbf{r}_{,\xi\eta}}{\|\mathbf{r}_{,\eta}\|^2}, \quad (82)$$

where  $\mathbf{r}_{,\xi\eta} = \frac{\partial \mathbf{r}_{,\xi}}{\partial \eta}$ . According to [45], as long as the contact angle  $\alpha$  is larger than the following lower bound

$$\alpha_{\min} = \arccos(1 - \lambda_{\max}) \quad (83)$$

a unique solution for the closest point projection problem (36) is guaranteed, where

$$\lambda_{\max} = \frac{H}{2R} \text{ with } R = \frac{1}{K}. \quad (84)$$

Concretely, for the contact angle values above  $\alpha_{\min}$ , the unique solution for the closest point projection problem (40) in the case of point-to-point contact is also guaranteed.

#### 4.6 Customized time integration with contact impulse

The discretized equation of motion in terms of the  $k$ -th contact impulse  $\gamma_k = \Delta t \hat{\gamma}$  in the semi-implicit Euler scheme can be rewritten as:

$$\begin{aligned} \dot{\mathbf{q}}^{(l+1)} &= \dot{\mathbf{q}}^{(l)} + \mathbf{M}^{-1} \mathbf{F}_{\text{ext}}^{(l)} \Delta t - \mathbf{M}^{-1} \mathbf{F}_{\text{int}}^{(l)} \Delta t \\ &\quad + \mathbf{M}^{-1} \mathbf{D}^{(l)} \hat{\gamma}_k^{(l+1)} \Delta t, \end{aligned} \quad (85a)$$

$$\mathbf{q}^{(l+1)} = \mathbf{q}^{(l)} + \dot{\mathbf{q}}^{(l+1)} \Delta t, \quad (85b)$$

$$0 \leq \gamma_{k,N}^{(l+1)} \perp g_{N,k}^{(l+1)} \geq 0, \quad k = 1, 2, \dots, N_k, \quad (85c)$$

where  $\perp$  means perpendicular [50], which is indeed  $\gamma_{k,N} \perp g_{N,k} = \gamma_{k,N} \cdot g_{N,k}$ , based on the calculation of the contact contribution presented in Sects. 4.3 and Sect. 4.4, and contact impulse  $\gamma^{(l+1)} = \hat{\gamma}^{(l+1)} \Delta t$  is used in the rest of the paper [50].

The signed gap function at  $t^{(l+1)}$  can be approximated in terms of Taylor's expansion as [4]:

$$\begin{aligned} g_{N,k}^{(l+1)} &\approx g_{N,k}^{(l)} + \frac{\partial g_{N,k}^{(l)}(\mathbf{q}^{(l+1)} - \mathbf{q}^{(l)})}{\partial \mathbf{q}} \\ &= g_{N,k}^{(l)} + \Delta t v_{k,N}^{(l+1)}, \end{aligned} \quad (86)$$

where  $v_{k,N}^{(l+1)}$  is the normal component of relative velocity at a contact event between two contact points at  $t^{l+1}$ .

Recalling the definition of vector  $\mathbf{D}$  in Eq. (72c), it can be interpreted as the differentiation of the gap function with respect to the nodal coordinates in the normal direction. Hereupon, the complementarity condition in Eq. (85c) can be expressed in the following form:

$$0 \leq \gamma_{k,N}^{(l+1)} \cdot \frac{1}{\Delta t} g_{N,k}^{(l+1)} + \mathbf{D}_k^{(l+1),T} \dot{\mathbf{q}}_k^{(l+1)} \geq 0$$

$$k = 1, 2, \dots, N_k. \tag{87}$$

The corresponding composite velocity with respect to Eq. (86) takes the form of

$$d_k = \frac{1}{\Delta t} g_{N,k}^{(l)} + \mathbf{D}_k^{(l+1),T} \dot{\mathbf{q}}_k^{(l+1)}. \tag{88}$$

For the  $k$ -th contact  $\gamma_{k,N}^{(l+1)} > 0$  and  $\frac{1}{\Delta t} g_{N,k}^{(l+1)} = \frac{1}{\Delta t} g_{N,k}^{(l)} + \mathbf{D}_k^{(l+1),T} \dot{\mathbf{q}}_k^{(l+1)} = 0$ . It is for this reason that:

$$d_k \gamma_k^{(l+1)} = \left( \frac{1}{\Delta t} g_{N,k}^{(l)} + \mathbf{D}_k^{(l+1),T} \dot{\mathbf{q}}_k^{(l+1)} \right) \gamma_{k,N}^{(l+1)}, \tag{89}$$

according to which  $\gamma_k^{(l+1)} \cdot d_k \geq 0$ .

At the initial time, the relative contact velocity will be zero, so the initial term of  $d_k$  is:

$$d_{k,0} = \frac{1}{\Delta t} g_{N,k}^{(l)}. \tag{90}$$

According to Eq. (88), the term of  $d_k$  can be rewritten as:

$$d_k = d_{k,0} + \mathbf{D}_k^{(l),T} \dot{\mathbf{q}}_k^{(l+1)}. \tag{91}$$

After substituting the nodal velocity vector at  $t^{l+1}$  from the first row of Eq. (85a) into Eq. (91) one gets

$$d_k = p + N_c \gamma_k^{(l+1)}, \tag{92}$$

where

$$p = d_{k,0} + \mathbf{D}_k^{(l),T} \left( \dot{\mathbf{q}}_k^{(l)} + \mathbf{M}^{-1} \mathbf{F}_{\text{ext}}^{(l)} \Delta t - \mathbf{M}^{-1} \mathbf{F}_{\text{int}}^{(l)} \Delta t \right) \tag{93}$$

and in the absence of friction the second term in Eq. (92) containing

$$N_c = \mathbf{D}^T \mathbf{M}^{-1} \mathbf{D} \tag{94}$$

is a scalar.

### 4.7 Time integration scheme

Due to the use of the absolute nodal coordinate formulation, the mass matrix  $\mathbf{M}$  and the gravity external force  $\mathbf{F}_{\text{ext}}$  are constant. It is for this reason that the mass matrix and gravity external force can be initialized before time integration. The initial elastic force  $\mathbf{F}_{\text{int}}$  and the velocity  $\dot{\mathbf{q}}$  can be set to be equal to zero by assuming that the simulation starts in an undeformed configuration. Algorithm 2 succinctly explicates the implementation of a semi-implicit integrator with the embedded iteration loop to calculate the corrected position vector of the collision points during a contact event [40,72]. With the employed semi-implicit Euler time integration scheme, the contact force, the elastic force, the velocity and the position vectors are calculated and amended at each time step using the Newton's iteration as summarized in Algorithm 2 when the penalty method is used. In the case of the LCP method, the vector  $\mathbf{D}$ , and the gap function  $g_N$  is used to compute the new contact impulse  $\gamma^{(l+1)}$  using Eq. (96).

## 5 Numerical examples

The numerical examples presented in this Section aim to examine the performance and accuracy of the computational procedures introduced including point-wise (point-to-segment and point-to-point), contact formulation and line-wise formulation (line-to-line). One quasi-static and four dynamics cases of ANCF beams coming into contact are considered in this section. Contact cases between beams are described as corner contacts a corner, corner contacts a side and side contacts a side. All examples are solved using the linear complementarity problem (LCP) and the penalty method. The contact detection explained in Sect. 3 is used to help impose the contact constraints. A Semi-implicit Euler numerical scheme is utilized

**Algorithm 2** Implementation of the semi-implicit Euler integration scheme with an embedded Newton iteration during each contact event.

- 1: Set  $t^l = 0$ , initial values for position  $q^l$  and velocity  $\dot{q}^l$ , compute the constant mass matrix  $M$  and the body forces  $F_b^l$
- 2: Loop over the beam elements to compute the elastic forces  $F_{int}^l$ , and the externally applied forces  $F_{ext}^l$  to set up the right side of the equation of motion
- 3: Loop over the simulation time-span to get the vector of nodal acceleration  $\ddot{q}^l$  and the vectors of the nodal velocity  $\dot{q}^{l+1}$  and position  $q^{l+1}$ 
  - ▷ Solving the equation of motion for the full set of the acceleration vectors during the simulation
- 4: **for**  $l = 1 : t$  **do**  $\ddot{q}^{(l^0 \dots l^l)} = M^{-1}(F_{ext}^l + F_b^l - F_{int}^l)$
- 5:     Get the trial displacement  $q_{trial}^{l+1}$  and velocity  $\dot{q}_{trial}^{l+1}$  at the next time step  $t^{l+1}$  ▷ See Eqs. (17)
- 6:     Preliminary check if there is contact / penetration using the minimum distance between the OBBs corresponding to the closest elements
- 7:     **if**  $g_N(q_{trial}^{l+1}) \geq 0$  **then**
- 8:          $q^{l+1} = q_{trial}^{l+1}$
- 9:          $\dot{q}^{l+1} = \dot{q}_{trial}^{l+1}$
- 10:     **else** ▷ The gap function  $g_N(q_{trial}^{l+1}) < 0$  ▷ Choose the appropriate contact model after determining the contact type using the OBBs
- 11:         Within the  $i^{th}$  number of the Newton-Rophson iterations calculate the corrected velocity vector  $\dot{q}_i^{l+1}$  and position vector  $q_i^{l+1}$
- 12:         Evaluate the initial contact force vector  $F_{con}^{l+1}(q_{trial}^{l+1})$  and calculate the initial residual vector  $R_{etrial}^{l+1}(q_{trial}^{l+1})$
- 13:         Loop within the maximum number of iterations
- 14:         **for**  $i = 1 : \text{maximum iteration number}$  **do**
- 15:             **if**  $i = 1$  **then**
- 16:                  $R_{ei}^{l+1} = R_{etrial}^{l+1}$
- 17:                  $q_i^{l+1} = q_{trial}^{l+1}$
- 18:             **end if**
- 19:             update the vector of residual  $R_{ei}^{l+1}$  and recalculate the tangent stiffness matrix  $K_i^{l+1}(q_i^{l+1})$  with respect to the amended nodal position vector in each iteration ▷ See Eq. (19) and Eq. (20)
- 20:             Calculate the next approximation for the position vector and check if this is the converged solution ▷ See Eq. (21)
- 21:         **end for**
- 22:     **end if**
- 23: **end for**

as the time integration scheme for both approaches used.

When using the penalty method, the corrector, Newton’s iteration presented in Sect. 2.3 is employed to provide a converged solution for the vector of nodal degrees-of-freedom at each time step during each contact event. This is needed to minimize the interpenetration of the contact elements. The converged solution is achieved when the magnitude of the vector of the residual of the equation of motion given in Eq. (19)  $\|R_e^{l+1}\| \leq 10^{-4}$ .

The material and integrator setting used in the simulations are given in Table 1. The contact events are detected through the oriented bounding boxes (OBBs) scheme which is composed of a parent box that encapsulates the whole beam structure, and the children boxes that encompass the finite ANCF beam elements.

Then the complementarity problem can be displayed as:

**Table 1** Material and integrator parameters

Parameters	Value
Material density (kg/m <sup>3</sup> )	7850
Young’s modulus (Pa)	2.07E+7
External force (N)	Gravity
Integration step-size	1.0E−4

$$d_k \gamma^{(l+1)} = (p + N_c \gamma^{(l+1)})^T \gamma^{(l+1)}. \tag{95}$$

According to Eq. (95), the linear complementarity problem (LCP) represents the first-order optimality conditions for the one-dimensional quadratic optimization problem and can be solved by Lemke’s algorithm [1,3] to find the minimum for the impulse  $\gamma^{l+1}$  which satisfies the KKT constraints:

$$\begin{aligned} \min \quad & f(\gamma^{(l+1)}) = N_c \gamma^2 + p\gamma, \\ \text{subject to} \quad & \gamma_{k,N}^{(l+1)} \geq 0, \end{aligned} \tag{96}$$

whose solution is the normal contact impulse  $\gamma^{(l+1)}$ .

**Table 2** Double cantilever simulation parameters

Parameters	Value
Young's modulus $E$ (Pa)	1
Poisson ratio $\nu$	0
External nodal moment $m_z$ ( $N \cdot m$ )	0.01
Applied ambient pressure $p_a$ (Pa)	$2 \cdot 10^{-4}$
$L = L_A = L_B$ (m)	10
$H = H_A = H_B$ (m)	1

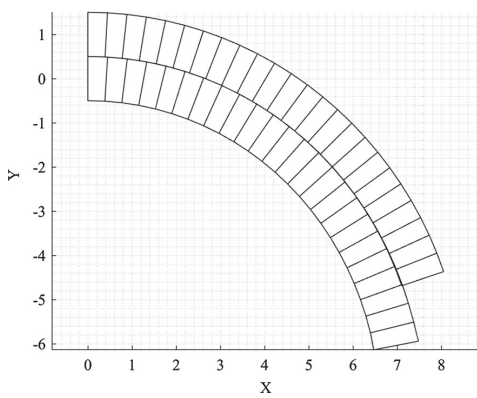


**Fig. 10** Double cantilever beam in deformed configuration using 24 beam discretization and three integration segments per slave beam element

5.1 Double-cantilever beam

In this example, the performance and accuracy of the presented Gauss-point-to-segment (GPTS) contact formulation is examined by considering a classical example originally discussed in [55] and later in [25] using the bounding volumes scheme. The parameters used in the simulation are collected in Table 2. The structure underwent a large deformation at the end of the simulation in the maximum loading as shown in Fig. 10. In order to investigate the GPTS formulation discussed in Sect. 4.1, a convergence analysis was performed with an increasing number of ANCF elements.

The number of Gauss point per integration interval  $n_S$  over each segment is given by the Gauss rule as follows:

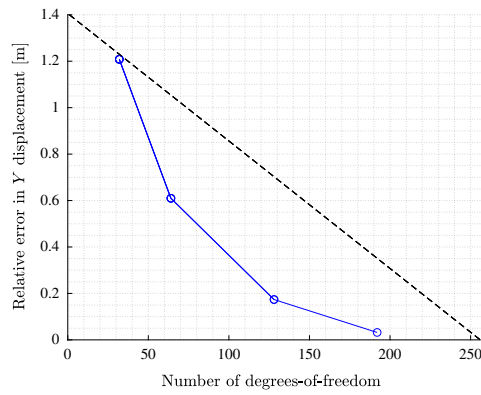


**Fig. 11** Rate of convergence of the double cantilever beam solution for the tip vertical displacement of the upper beam with increasing number of beam discretizations. Dashed line indicates third order of convergence

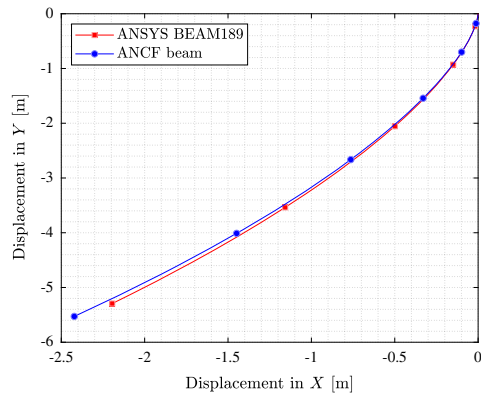


**Fig. 12** Comparison between the solutions for the slave beam center line position using the proposed contact formulation and ANSYS. A certain discretization of 24 and 72 number of ANCF and ANSYS BEAM189 are used, respectively

$$n_G = \frac{p + 1}{2} \tag{97a}$$

with the total number of

$$n_{GT} = n_S \cdot n_G \tag{97b}$$

Gauss points per slave beam element, where  $p$  is the order of the integrand polynomial appeared in Eq. (67)

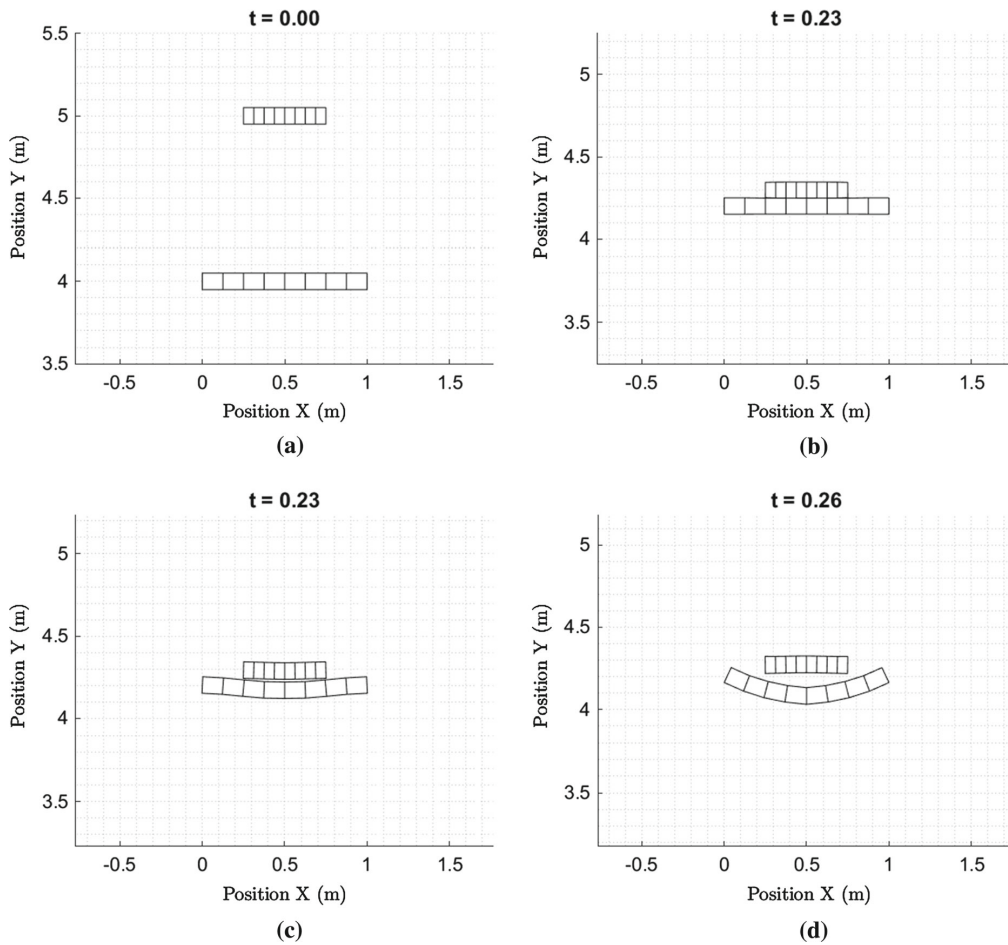
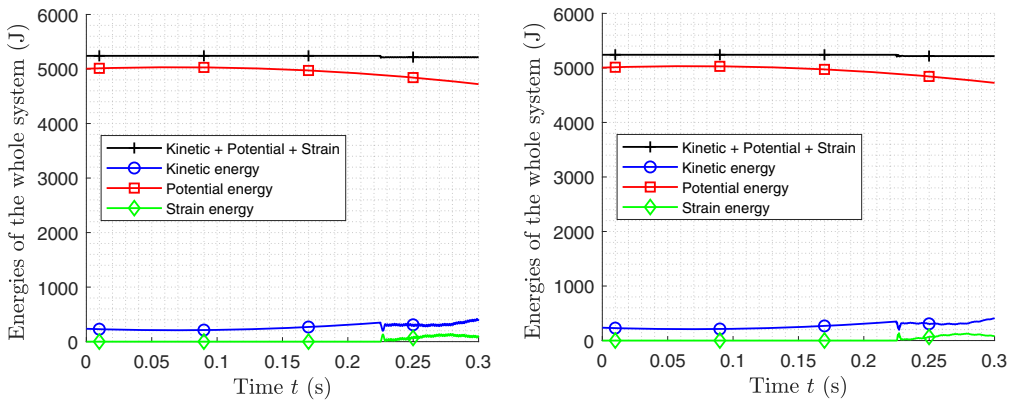


Fig. 13 Initial configuration of two unconstrained beams and three stages of the contact process

Figure 11 shows the convergence rate of the solution for end point vertical displacement, therein, the relative errors were measured versus increasing number of beam discretization: 4, 8, 16, 24 and 32 to investigate the used beam element performance when applying the contact formulation. The solution given by the finest discretization (32 ANCF beams) is as to the reference value. It can be seen from the figure that the solution converges with a sharp pace when using 16 discretizations, and thereafter, the convergence rate follows a slighter rate. To investigate the accuracy of the above

performance analysis, the simulation was replicated by a commercial finite element code ANSYS using a three-node beam element BEAM189. To properly replicate the contact model with ANSYS implementation, the contact element type CONTA170 acts to define a contact surface on the master beam (upper beam), and TARGE170 was used for definition of contact surface on the slave beam (lower beam). The contact elements' options are set to replicate the contact constraint used in the proposed GPTS formulation. Therein, the contact model is set for parallel beam with distributed force and



**Fig. 14** Energy balance of the side-to-side contact type based on the LCP and the penalty methods. Eight ANCF elements are used for each beam structure

the penalty methods are chosen to enforce the contact constraint. Figure 12 shows the lower beam’s center line displacement based on the proposed formulation and ANSYS solution for maximum loading. The results are based on 24 ANCF elements with three integration segments per element and 72 BEAM189 elements when a nonlinear static solver is selected. Although, the comparison between two center line displacements are in an acceptable range for such a significant deformation, the *X*-displacement value for the beam end point is not in close agreement with the ANSYS solution. It is expected from the low-order ANCF beam that was comprehensively shown in [10].

5.2 Side-to-side contact problem

In this example, two unconstrained beams enter into contact demonstrating the side-to-side contact (segment-to-segment) type, see Fig. 13a. The beams are of two different lengths. The length of the upper beam is 1 m and the lower beam is 0.5 m. The beams are discretized using eight ANCF elements. The initial configuration and three stages of the contact process are shown in Fig. 13. To define the contact patch on the contacting element, the boundaries of the patch were found according to the procedure described in Sect. 4.2. The OBBs corresponding to the boundaries of the lower beam are considered with their counterparts from the upper beam for the line clipping process as was detailed in Sect. 3.3.3. The established contact patch was param-

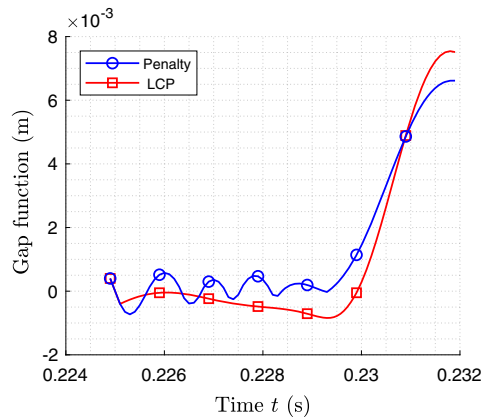


**Fig. 15** Comparison of evolution of the gap function along the contact patch when using LCP and the penalty methods. The discretization of eight elements is used with the both beams

eterized with three segments per contacting elements. The gap function in both the LCP and penalty methods were computed with respect to Eq. (57). In the case of the penalty method, four Gaussian points according to Eq. (97) are required to integrate the contact contribution appearing in Eq. (67). With the LCP method, the contributions to the distributed contact force Eq. 76 represented by Eq. (78) were integrated using three Gauss points. The deformation dependent abscissa coordinates confining the entire contact patch are iteratively obtained according to Eq. (66).

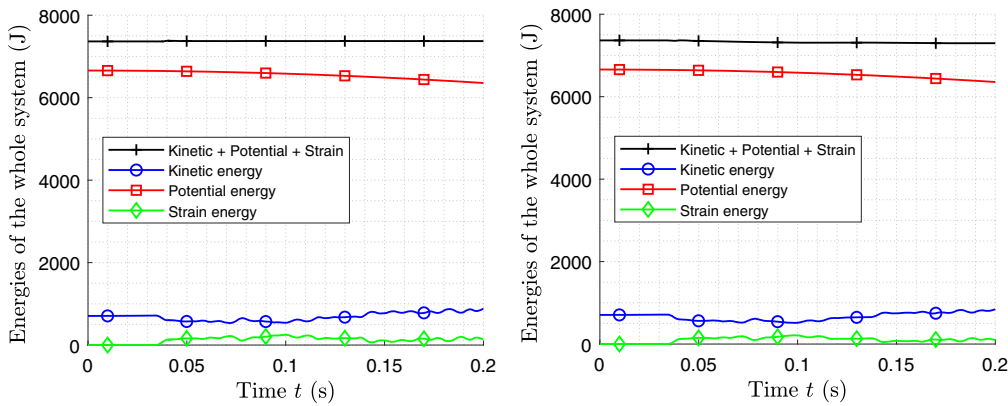


**Fig. 16** Energy balance of the corner-to-side contact type based on the penalty and the LCP methods. Eight ANCF elements are used for each beam structure

Figure 14a and b shows the potential, kinetic and strain energies associated with the LCP approach and the penalty method with the OBB contact detection algorithm, respectively.

The small drop appeared in the total energy with the penalty method could emanate from choosing a relatively large penalty parameter ( $2 \cdot E$ ) to compensate for the surface penetration in the pure line-to-line contact which contains more energy lost compared to the point-to-segment case discussed in Sect. 5.3. On the other hand, the LCP exhibits the flat level of the total energy excluding a tiny drop upon the first contact event. The fluctuations with the kinetic and strain energy interchange is expected from the LCP formulation. It is analogous to that in the Lagrange multipliers method. Figure 15 indicates that the evaluation of gap function with the LCP and penalty methods is in a close agreement in their values. The penalty method exhibits a number of swings within the contact duration which is expected from such formulation. Moreover, the average of the penetration with the penalty method is slightly less than that in the LCP method. As corroborated with the above energy conservation results, this is due to the relatively large penalty factor used. This supports the small drop in the total energy level shown in Fig. 14b.

### 5.3 Corner-to-side contact problem

In this example, a rotated free falling flexible beam and a horizontally moving beam make contact as shown in Fig. 17. The upper beam is rotated by an angle of  $45^\circ$  with respect to the ground level. The velocities of the upper and lower beams are  $-3$  m/s and  $3$  m/s, respectively. The contact events were detected according to the OBB scheme described in Sect. 3.2, and the contact points were identified based on the line clipping process explained in Sect. 3.3.1. In the LCP and penalty approaches, the contact energy contribution was evaluated according to the approach described in Sects. 4.3 and 4.1, respectively. In the case of negative values for the gap function, the contact force vector is iteratively updated during the contact events. Potential, kinetic and strain energies associated with the LCP approach and the penalty method are shown in Fig. 16a and b, respectively. As evidenced by the figures, the total energy remains constant in the case of the penalty formulation. This is due to the use of the Newton iteration within the contact events to re-evaluate the system's tangent stiffness matrix (20).

Figure 18 shows the gap function variation during the contact events in the LCP and the penalty approaches. As can be seen in the figure, a significant sliding takes place in the contact events due to the non-frictional contacts (see Fig. 17).

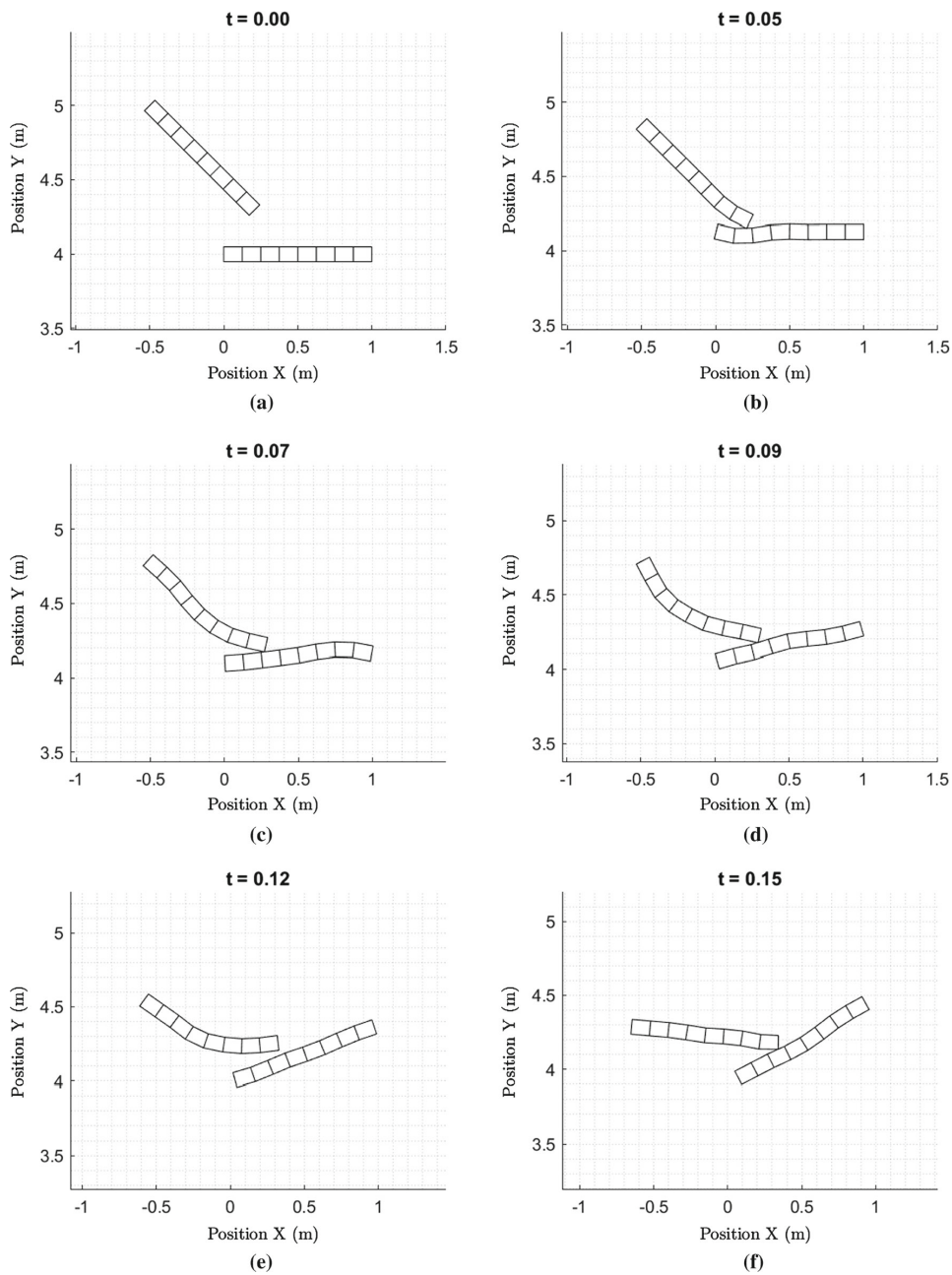


**Fig. 17** Initial configuration of two free moving beams and six stages of the contact process. The contact and the collision points are detected by the algorithm based on the intersecting of OBBs

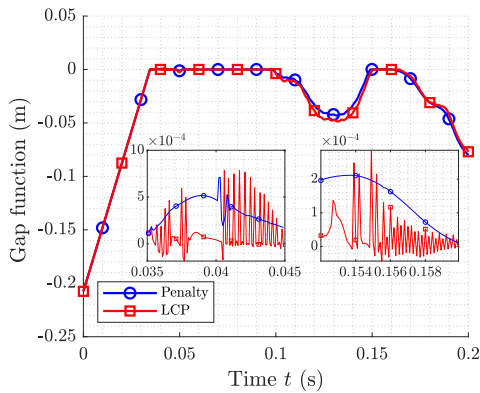


**Fig. 18** Gap function variation during the simulation of the penalty and the LCP methods with OBB contact detection when mesh of eight ANCF beam elements is used for the beams

Figure 19a and b, respectively, shows the disposition of the solution convergence for the right-end-point of the upper beam when the LCP and penalty methods are used. Both methods delivered the converged results up to 12 discretizations that imply the robust computational performance of the contact implementation. While the solutions with the penalty method for 8 and 12 discretizations seem to closely resemble each other, in the case of the LCP method, the solutions for 8 and 12 beam elements are still discernible. This can be justified by the applied strict convergence criterion (19) with the penalty method.

A comparison was made between the converged solutions for the upper beam trajectory with the LCP and penalty methods in the *X* and *Y* directions that are illustrated in Fig. 20a and b. The figures indicate that the solutions from both methods are almost coincident in the *X* direction and for the *Y* direction they are in close agreement (see also Fig. 19).

The LCP method showed a significantly lower computational cost compared to the penalty method. The computational effort is given in terms of the CPU time in Table 3. This indicates that the optimization-based approach in evaluating the contact force components in CP method is more efficient than the classic Newton iterative solver used with the penalty method. This emanating from the fact that the local optimization used with the CP approach is dealing with evaluation of optimized value for the normal component of reaction force

(the Lagrange multiplier) at each contact event per time integration step, whereas in the case of penalty method, the whole right-hand side of the motion differential equation is iteratively evaluated per each contact event within a time integration step. This accounts for the re-evaluation of the gap function at each Newton iteration. That means that the narrow-phase contact detection algorithm has to be repeated at each iteration.

#### 5.4 Corner-to-corner contact problem

In this example, the corner-to-corner contact scenario is analyzed.

The gap calculation is accompanied by a specific penetration check according to [41]. Figure 21 shows the possibility of penetration for the closest points at the corners to satisfy Karush–Kuhn–Tucker conditions. The values of the angles between several vectors are also illustrated in Fig. 21. According to Fig. 21, the angle  $\alpha_1$  and  $\alpha_1$  can be defined as:

$$\begin{aligned} \alpha_1 &= \angle(PQ, PM) \\ \alpha_2 &= \angle(-PQ, QN), \end{aligned} \tag{98}$$

where contact points *P* and *Q* are found according to the discussion in Sect. 3.3.2. When penetration takes place between the corners [40], the angles  $\alpha_1$  and  $\alpha_2$  can be computed as follows:

$$\begin{aligned} \cos \alpha_1 &> 0 \\ \cos \alpha_2 &> 0. \end{aligned} \tag{99}$$

Therefore, if the angles fulfill the condition of Eq. (99), the gap function is negative, and can be written as:

$$g_N = -\|r_A^P - r_B^Q\|. \tag{100}$$

If the angles do not fulfill the condition, the gap function will be positive.

The example of two pendulums contacting each other is used to analyze the corner-to-corner contact type. The initial configuration and three stages of the contact process are shown in Fig. 23.

With this example, the transition between the contact scenarios discussed in Sect. 4.5 is illustrated. It is shown in Fig. 23 that first contact scenario is regarded as the

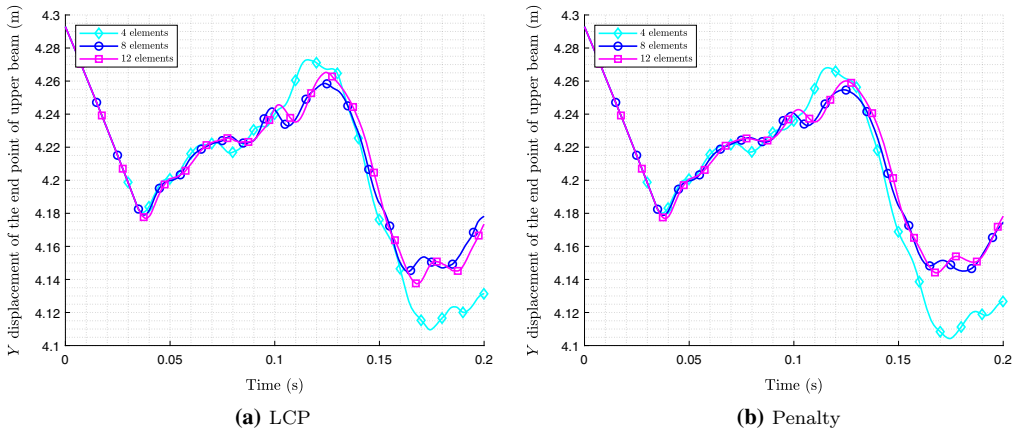


**Fig. 19** Convergence of the displacements in the Y direction with increasing number of beam discretizations with respect to the contact constraint imposition using **a:** penalty and **b:** LCP methods

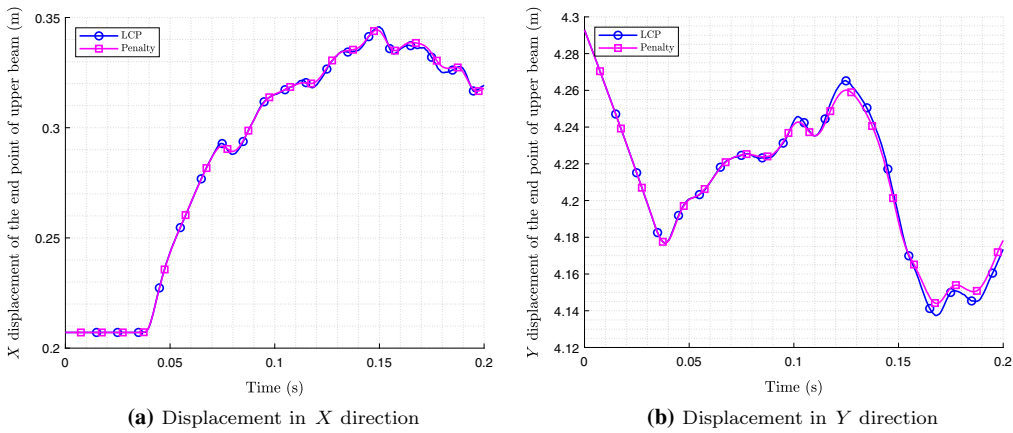


**Fig. 20** Comparison of the displacement of upper beam right-end-point **a:** in the X and **b:** Y directions when enforcing the contact constraint based on the LCP and penalty methods. The discretization of 12 beam elements are used with the both methods

**Table 3** CPU and the elapsed time with the evaluation of the functions associated with the Newton and Lemke’s solvers when the penalty and LCP methods are, respectively, used for simulation of the corner-to-side contact problem

Elapsed time	LCP (s)	Penalty (s)
Total simulation until the end of 1st contact event	13.947	53.9697
Function evaluation during the 1st contact event	Lemke’s algorithm: 0.012	Newton solver: 39.76

Eight beams discretization is used with the simulation

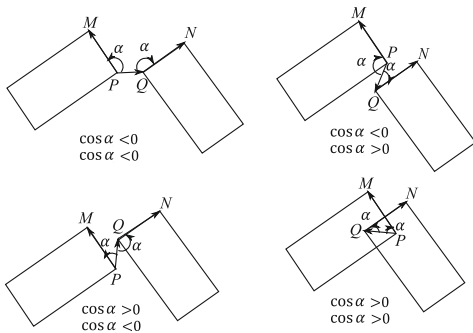


**Fig. 21** Penetration check:  $\alpha_1 = \angle(PQ, PM)$ ,  $\alpha_2 = \angle(-PQ, QN)$

point-to-point followed by a side-to-side contact scenario. Potential, kinetic and strain energy associated with the LCP approach and the penalty method are shown in Fig. 22a and b, respectively. There are small fluctuations during the transition from the point-wise formulation (described in Sects. 4.1 and 4.3) into the line-to-line formulation presented in Sects. 4.2 and 4.4. Nonetheless, the penalty and LCP method conserved the level of total energy within the contact events with respect to the different contact formulations; the point-to-point and line-to-line. The above-mentioned fluctuation could be arisen from switching between the contact formulation in the narrow-phase of contact detection level.

### 5.5 Self-contact problem

In this example, a highly flexible beam undergoing multiple self contact events is studied. The example parameters were adopted from [62] where the dynamics of the flexible beam denoted "flying spaghetti" was originally contrived, see Fig. 24.

The quadratic ANCF beam element with discretization of 16, 24 and 32 beam elements is used in the formulation. A force of  $F(t) = 8 \text{ N}$  and a torque of  $M(t) = 80 \text{ N}\cdot\text{m}$  are applied as shown in Fig. 24 within the time interval of  $t = [0, 4.0] \text{ s}$  to provide a motion composed of a large deformation and a large local displacement and rotation. According to the approach described in Sect. 3.1, the global search for the proximity zone leads to an efficient computational algorithm. This is because only the OBBs corresponding to the closest elements remain active in the identification of the collision points.

As shown in Fig. 25, the self-contact events including sliding and non-frictional contacts take place several times during the simulation from  $t = 2.84 \text{ s}$ . To determine the contact points, Algorithm 1 is employed to detect the contact and the contact point candidates in the LCP and the penalty formulation approaches.

To evaluate the accuracy of the presented approaches with the highly flexible beam, an energy balance analysis is provided in Fig. 26a and b. As can be seen from the figures, the total energy and its components for

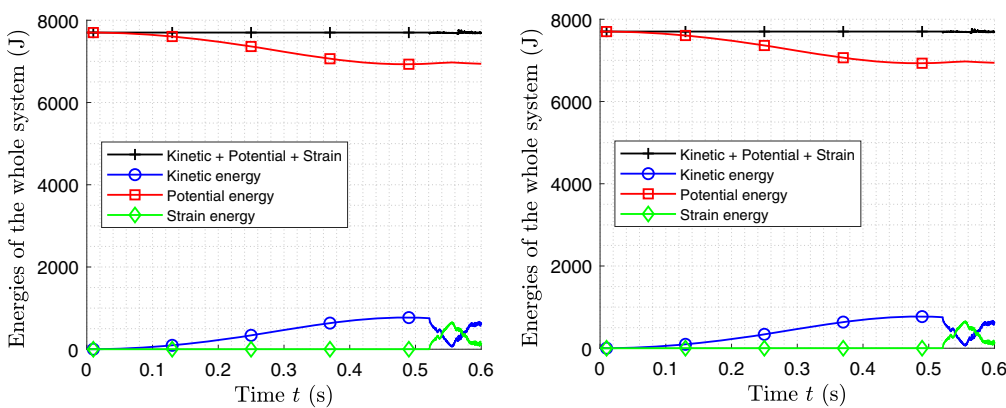


**Fig. 22** Energy balance of the corner-to-corner contact type based on the LCP and penalty methods. 16 ANCF elements are used for each beam

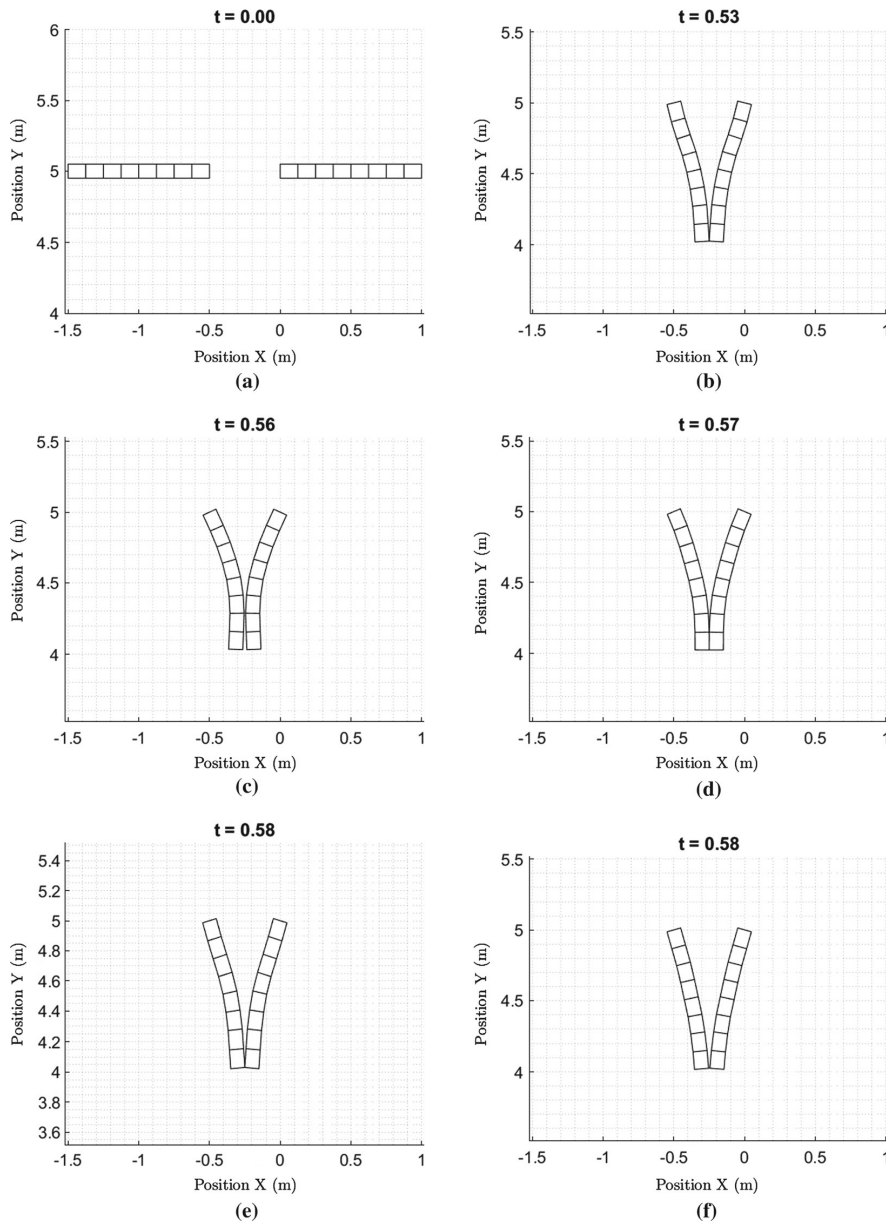


**Fig. 23** Initial configuration: **a** of two pendulums and five stages of the contact process: **a–f**. Two pendulum come into contact starting with the point-to-point contact events: **b**, and after sepa-

ration: **c**, a line-to-line contact happens within their lower part: **d**, and subsequently, another round of point-to-point contact events: **e** is repeated

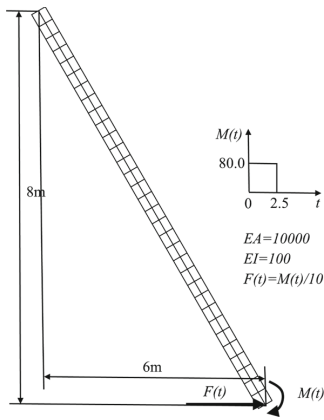
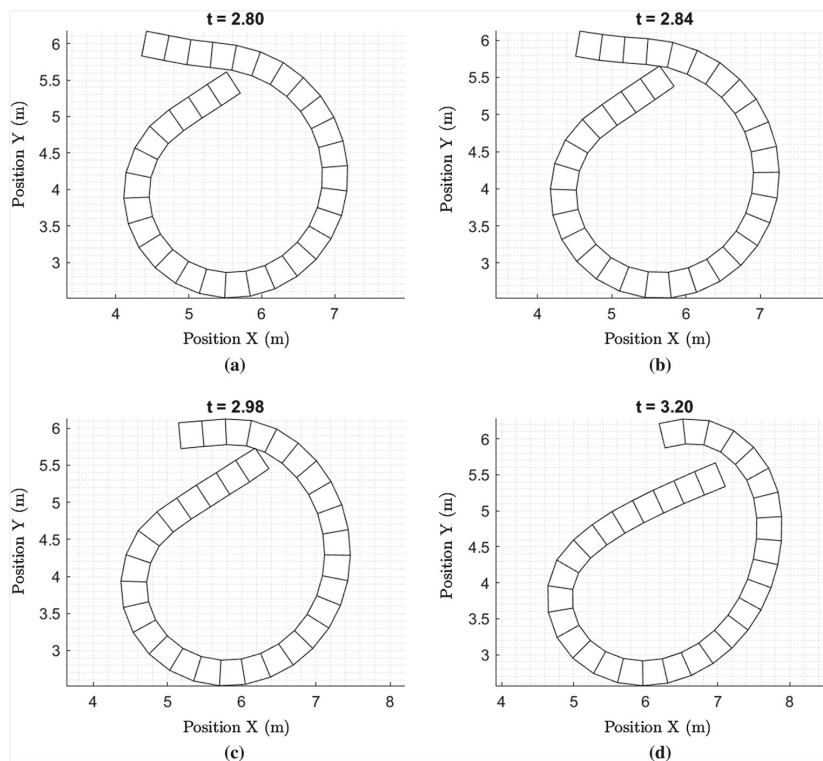


**Fig. 24** A flexible unconstrained beam with an applied force, moment and its problem data

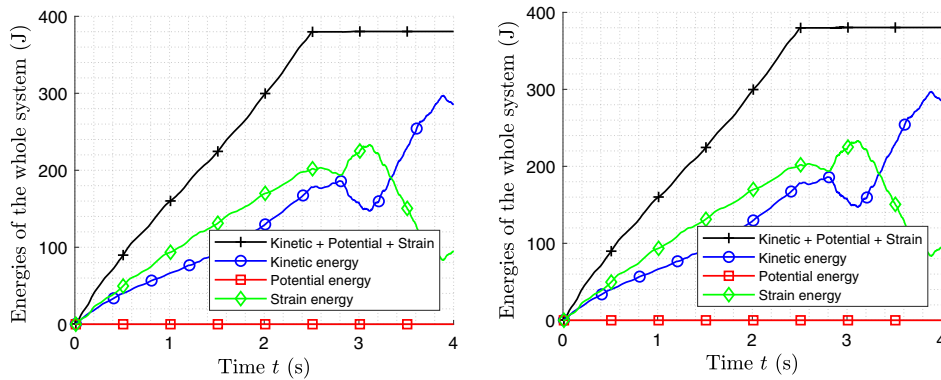
the LCP- and the penalty-based approaches are in an acceptable agreement.

Figure 27a and b compares the rate of convergence of the solution for the displacement in the Y direction of the beam lower end point in the case of the penalty and LCP methods, respectively. The figures indicate that the solution is converged up to 32 beam elements with both methods, and no distinction can be reported between the penalty and LCP methods from the convergence analysis perspective.

To gain an insight into the motion of the flying spaghetti problem during the contact events, the motion of the end node of the structure is considered. Figure 28 depicts the trajectory of the end node in the LCP and the penalty formulation approaches. The figure shows the coincident patterns recorded by the two methods within the contact events and by the end of the simulation time. The usage of Newton’s solver with the penalty method mitigates the inter-penetrations of contact ele-



**Fig. 25** Snapshots of the self-contact events in the flying spaghetti problem in the simulation when using the penalty force model. The number of meshes in beam is 32



**Fig. 26** Energy balance of the flying spaghetti based on the LCP and the penalty methods. The number of beam elements are 32

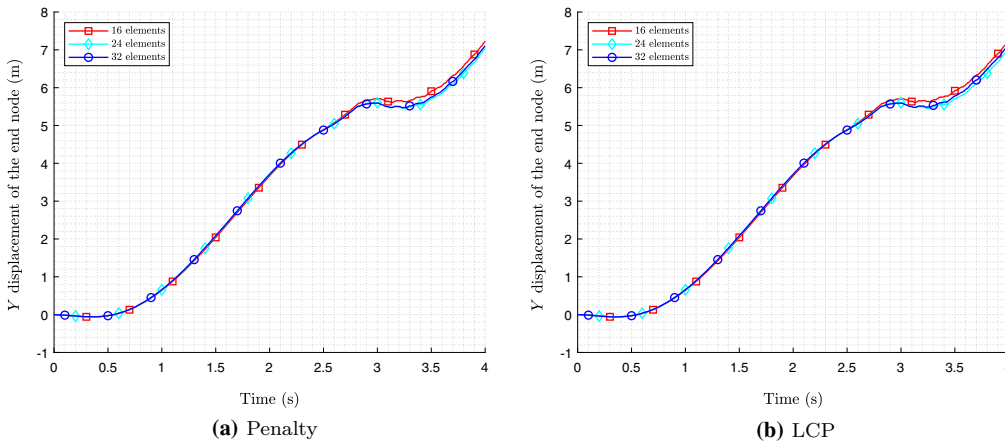


**Fig. 27** Convergence of the displacements of the lower end point of the beam in the Y direction with increasing number of beam discretizations with respect to the contact constraint imposition using **a**: penalty and **b**: LCP methods

ments. This is demonstrated in Fig. 29a and b where the convergence of the solution in the contact methods are shown in terms of the magnitude of the vector of the residuals  $\|\mathbf{R}_e\|$ . From Fig. 29a, it can be interpreted that the penalty method proves the converged solution in

every time step during contact events by satisfying the criterion given in Eq. (19). Figure 29b shows that the LCP method ensures zero norm of the residual vector within the contact events.

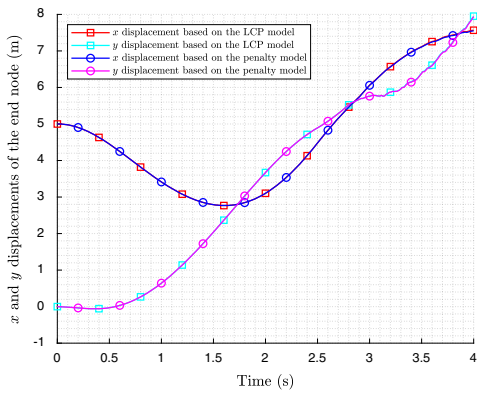


**Fig. 28** Trajectory of the lower end point of the beam during the simulation based on the LCP and the penalty methods

**6 Conclusions**

In this work, a contact procedure was introduced to analyze contact in the case of flexible beams and particularly in self-contact situations. The contact events and the collision points were, respectively, detected using the oriented bounding box scheme and the Cyrus–Beck line clipping process. The complementarity problem (CP) and penalty approaches were used for contact constraint imposition. Five numerical examples were presented to investigate the performance and accuracy of the introduced CP method in combination with the proposed contact detection procedure. To compare against the LCP method, a penalty method was developed with a particular stress on the line-to-line (GPTS) formulation with the contact patch segmentation inspired by Meier et al.’s work [45]. In the first static example,

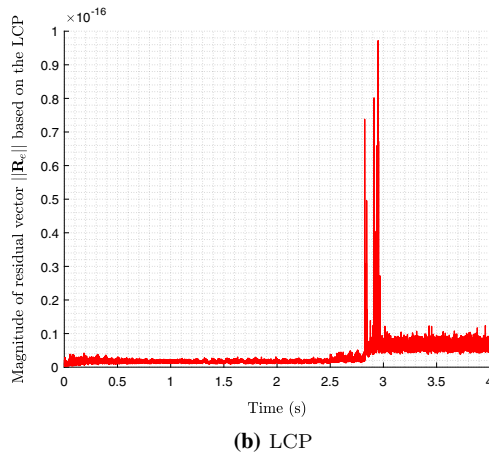
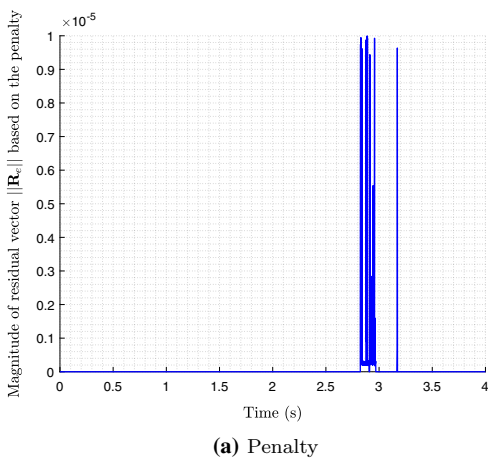


**Fig. 29** Magnitude of the vector of the residual of the equation of motion over the simulation time based on the penalty and the LCP models when mesh of 16 beam elements is used

the developed line-to-line formulation was examined for further implementations in the large deformation dynamic problems with the LCP and penalty methods. Therein, a three-dimensional beam element in ANSYS was used to verify the results. In the dynamic examples, energy balance is presented to show the conservation of strain energy when a contact event occurs. Furthermore, the performance of the proposed contact formulations in respect of the LCP and penalty methods were investigated by a number of solution convergence analyses. In the numerical examples, the introduced contact detection procedure showed its accuracy and robustness in application of different contact formulations (point-to-segment, point-to-point and line-to-line), and also different contact constraint imposition (LCP and penalty) approaches. The gap functions evolution based on the two employed approaches are in acceptable agreement which is discussed in Sects. 5.2 and 5.3 where the segment-to-point and line-to-line formulation contact were studied. The numerical results show that the LCP method possesses similar solution convergence properties as the penalty method when combined with the introduced contact detection procedure. However, the computational effort with the LCP is significantly lower than the penalty method and for this reason, the LCP method is more suitable in (real-time) simulation of large deformation contact problems in two-dimensional space. As demonstrated in this work, the combination of the introduced hierarchical contact detection procedure with the complementarity problem (CP) approach can be efficiently applied in the simulation of highly flexible beams undergoing self-contact. In our forthcoming contribution, we will introduce a novel surface-to-surface contact formulation in the framework of three-dimensional ANCF beam with arbitrary cross-sectional geometry.

**Acknowledgements** We would like to thank the Academy of Finland (Application No. 299033 for funding of Academy Research Fellow) for supporting Marko K. Matikainen.

**Funding** Open access funding provided by LUT University.

**Compliance with ethical standards**

**Conflict of interest** The authors declare that they have no conflict of interest.

**Open Access** This article is licensed under a Creative Commons Attribution 4.0 International License, which permits use, sharing, adaptation, distribution and reproduction in any medium

or format, as long as you give appropriate credit to the original author(s) and the source, provide a link to the Creative Commons licence, and indicate if changes were made. The images or other third party material in this article are included in the article's Creative Commons licence, unless indicated otherwise in a credit line to the material. If material is not included in the article's Creative Commons licence and your intended use is not permitted by statutory regulation or exceeds the permitted use, you will need to obtain permission directly from the copyright holder. To view a copy of this licence, visit <http://creativecommons.org/licenses/by/4.0/>.

## References

1. Anitescu, M.: Optimization-based simulation of nonsmooth rigid multibody dynamics. *Math. Program.* **105**(1), 113–143 (2006)
2. Anitescu, M., Hart, G.D.: A constraint-stabilized time-stepping approach for rigid multibody dynamics with joints, contact and friction. *Int. J. Numer. Methods Eng.* **60**(14), 2335–2371 (2000)
3. Anitescu, M., Potra, F.: Formulating dynamic multi-rigid-body contact problems with friction as solvable linear complementarity problems. *Nonlinear Dyn.* **14**(3), 231–247 (1997)
4. Anitescu, M., Tasora, A.: An iterative approach for cone complementarity problems for nonsmooth dynamics. *Comput. Optim. Appl.* **47**(2), 207–235 (2010)
5. Auricchio, F., Da Veiga, L.B., Hughes, T.J.R., Reali, A., Sangalli, G.: Isogeometric collocation methods. *Math. Models Methods Appl. Sci.* **20**(11), 2075–2107 (2010). <https://doi.org/10.1142/S0218202510004878>
6. Bathe, K., Bouzinov, P.: On the constraint function method for contact problems. *Comput. Struct.* **64**(5–6), 1069–1085 (1997)
7. Bergen, G.V.D.: Efficient collision detection of complex deformable models using aabb trees. *J. Graph Tools* **2**(4), 1–13 (1998)
8. Berzeri, M., Campanelli, M., Shabana, A.A.: Definition of the elastic forces in the finite element absolute nodal coordinate formulation and the floating frame of reference formulation. *Multibody Syst. Dyn.* **5**(1), 21–54 (2001)
9. Bourago, N., Kukudzhanov, V.: A review of contact algorithms. *Mech. Solids* **40**(1), 35–71 (2005)
10. Bozorgmehri, B., Hurskainen, V.V., Matikainen, M.K., Mikkola, A.: Dynamic analysis of rotating shafts using the absolute nodal coordinate formulation. *J. Sound Vib.* **453**, 214–236 (2019). <https://doi.org/10.1016/j.jsv.2019.03.022>
11. Cavalieri, F.J., Cardona, A.: Numerical solution of frictional contact problems based on a mortar algorithm with an augmented Lagrangian technique. *Multibody Syst. Dyn.* **35**(4), 353–375 (2015)
12. Chamekh, M., Mani-Aouadi, S., Moakher, M.: Modeling and numerical treatment of elastic rods with frictionless self-contact. *Comput. Methods Appl. Mech. Eng.* **198**(47–48), 3751–3764 (2008)
13. Chamekh, M., Mani-Aouadi, S., Moakher, M.: Stability of elastic rods with self-contact. *Comput. Methods Appl. Mech. Eng.* **279**, 227–246 (2014)

14. De Lorenzis, L., Evans, J., Hughes, T., Reali, A.: Isogeometric collocation: neumann boundary conditions and contact. *Comput. Methods Appl. Mech. Eng.* **284**, 21–54 (2015). <https://doi.org/10.1016/j.cma.2014.06.037>
15. De Lorenzis, L., Wriggers, P., Hughes, T.J.: Isogeometric contact: a review. *GAMM-Mitt.* **37**(1), 85–123 (2014)
16. Dewei, S., Cheng, L., Haiyan, H.: Dynamic computation of 2D segment-to-segment frictionless contact for a flexible multibody system subject to large deformation. *Mech. Mach. Theory* **140**(2), 350–376 (2019)
17. Durville, D.: Contact friction modeling within elastic beam assemblies: an application to knot tightening. *Comput. Mech.* **49**(6), 687–707 (2012)
18. Durville, D.: Modelling of contact-friction interactions in entangled fibrous materials. In: VI World Wide Congress on Computational Mechanics, Beijing, China (2004)
19. Ebel, H., Matikainen, M.K., Hurskainen, V.V., Mikkola, A.: Higher-order beam elements based on the absolute nodal coordinate formulation for three-dimensional elasticity. *Nonlinear Dyn.* **88**(2), 1075–1091 (2017). <https://doi.org/10.1007/s11071-016-3296-x>
20. Ebrahimi, M., Butscher, A., Cheong, H., Iorio, F.: Design optimization of dynamic flexible multibody systems using the discrete adjoint variable method. *Comput. Struct.* **213**, 82–99 (2019)
21. Ericson, C.: Real-Time Collision Detection. Morgan Kaufmann Publishers, San Francisco (2004)
22. Gay Neto, A., Pimenta, P., Wriggers, P.: Self-contact modeling on beams experiencing loop formation. *Comput. Mech.* **55**(1), 193–208 (2015)
23. Gerstmayr, J., Irschik, H.: On the correct representation of bending and axial deformation in the absolute nodal coordinate formulation with an elastic line approach. *J. Sound Vib.* **318**(3), 461–487 (2008). <https://doi.org/10.1016/j.jsv.2019.03.022>
24. Gerstmayr, J., Matikainen, M., Mikkola, A.: A geometrically exact beam element based on the absolute nodal coordinate formulation. *Multibody Syst. Dyn.* **20**(4), 359–384 (2008)
25. Haikal, G., Hjelmstad, K.D.: A finite element formulation of non-smooth contact based on oriented volumes for quadrilateral and hexahedral elements. *Comput. Methods Appl. Mech. Eng.* **196**, 4690–4711 (2007)
26. Harish, A.B., Wriggers, P.: Modeling of two-body abrasive wear of filled elastomers as a contact-induced fracture process. *Tribol. Int.* **138**, 16–31 (2019)
27. Hughes, J.F., Van Dam, A., Foley, J.D., McGuire, M., Feiner, S.K., Sklar, D.F.: *Computer Graphics: Principles and Practice*. Pearson Education, London (2014)
28. Hunt, K., Crossley, E.: Coefficient of restitution interpreted as damping in vibroimpact. *J. Appl. Mech.* **7**, 440–445 (1975)
29. Jelenic, G., Crisfield, M.: Geometrically exact 3d beam theory: implementation of a strain-invariant finite element for statics and dynamics. *Comput. Methods Appl. Mech. Eng.* **171**(1–2), 141–171 (1999)
30. Khude, N., Stanculescu, I., Melanz, D., Negrut, D.: Efficient parallel simulation of large flexible body systems with multiple contacts. *J. Comput. Nonlinear Dyn.* **8**(4), 041003 (2013)
31. Klosowski, J.T., Held, J.M., Mitchell, J.S., Sowizral, H., Zikan, K.: Efficient collision detection using bounding volume hierarchies of k-dops. *IEEE Trans. Vis. Comput. Graph.* **4**(1), 21–36 (1998)
32. Konyukhov, A., Schweizerhof, K.: On the solvability of closest point projection procedures in contact analysis: analysis and solution strategy for surfaces of arbitrary geometry. *Comput. Methods Appl. Mech. Eng.* **197**(33), 3045–3056 (2008)
33. Konyukhov, A., Schweizerhof, K.: Geometrically exact covariant approach for contact between curves. *Comput. Methods Appl. Mech. Eng.* **199**(37), 2510–2531 (2010)
34. Korkealaakso, P.M., Rouvinen, A.J., Moisio, S.M., Peusaari, J.K.: Development of a real-time simulation environment. *Multibody Syst. Dyn.* **17**(2), 177–194 (2007)
35. Lee, G.B., Kwak, B.M.: Formulation and implementation of beam contact problems under large displacement by a mathematical programming. *Comput. Struct.* **31**(3), 365–376 (1989)
36. Litewka, P.: The penalty and Lagrange multiplier methods in the frictional 3D beam-to-beam contact problem. *Civil and Environmental Engineering Reports*, pp. 189–207 (2005)
37. Litewka, P.: Hermite polynomial smoothing in beam-to-beam frictional contact. *Comput. Mech.* **40**(5), 815–826 (2007)
38. Litewka, P.: Enhanced multiple-point beam-to-beam frictionless contact finite element. *Comput. Mech.* **52**(6), 1365–1380 (2013)
39. Litewka, P.: Frictional beam-to-beam multiple-point contact finite element. *Comput. Mech.* **56**(2), 243–264 (2015)
40. Litewka, P., Wriggers, P.: Contact between 3-D beams with rectangular cross-sections. *Int. J. Numer. Methods Eng.* **53**(9), 2019–2041 (2002)
41. Litewka, P., Wriggers, P.: Frictional contact between 3-D beams. *Comput. Mech.* **28**(1), 26–39 (2002)
42. Matikainen, M.K., Dmitrochenko, O.: A study of three-node higher-order gradient beam elements based on the absolute nodal coordinate formulation. In: The 3rd Joint International Conference on Multibody System Dynamics. Busan, Korea (2014)
43. Matikainen, M.K., Dmitrochenko, O., Mikkola, A.: Beam elements with trapezoidal cross section deformation modes based on the absolute nodal coordinate formulation. In: International Conference of Numerical Analysis and Applied Mathematics, pp. 1266–1270. Rhodes, Greece (2010). <https://doi.org/10.1063/1.3497930>
44. Meier, C., Popp, A., Wall, W.A.: An objective 3D large deformation finite element formulation for geometrically exact curved kirchhoff rods. *Comput. Methods Appl. Mech. Eng.* **278**, 445–478 (2014)
45. Meier, C., Popp, A., Wall, W.A.: A finite element approach for the line-to-line contact interaction of thin beams with arbitrary orientation. *Comput. Methods Appl. Mech. Eng.* **308**, 377–413 (2016)
46. Meier, C., Popp, A., Wall, W.A.: Geometrically exact finite element formulations for slender beams: Kirchhoff–Love theory versus simo-reissner theory. *Arch. Comput. Methods Eng.* **26**, 163–243 (2017)
47. Meier, C., Popp, A., Wall, W.A.: A unified approach for beam-to-beam contact. *Comput. Methods Appl. Mech. Eng.* **315**, 972–1010 (2017)
48. Nachbagaer, K., Gruber, P., Gerstmayr, J.: A 3D shear deformable finite element based on the absolute nodal coordinate

- dinate formulation. In: Samin, J.C., Fiset, P. (eds.) *Multibody System Dynamics, Computational Methods in Applied Sciences*, pp. 77–96. Springer, Dordrecht (2013). [https://doi.org/10.1007/978-94-007-5404-1\\_4](https://doi.org/10.1007/978-94-007-5404-1_4)
49. Nachbagger, K., Pechstein, A.S., Irschik, H., Gerstmayr, J.: A new locking-free formulation for planar, shear deformable, linear and quadratic beam finite elements based on the absolute nodal coordinate formulation. *Multibody Syst. Dyn.* **26**(3), 245–263 (2011)
  50. Negrut, D., Serban, R., Tasora, A.: Posing multibody dynamics with friction and contact as a differential complementarity problem. *J. Comput. Nonlinear Dyn.* **13**(1), 014503 (2017)
  51. Neto, A.G., Wriggers, P.: Computing pointwise contact between bodies: a class of formulations based on master-master approach. *Comput. Mech.* **64**(3), 585–609 (2019)
  52. Neto, A.G., Wriggers, P.: Numerical method for solution of pointwise contact between surfaces. *Comput. Methods Appl. Mech. Eng.* **365**, 112971 (2020)
  53. Pang, J.S., Stewart, D.E.: Differential variational inequalities. *Math. Program.* **113**(2), 345–424 (2008)
  54. Pfeiffer, F., Glocker, C.: *Multibody Dynamics with Unilateral Contacts*. Wiley, New York (1996)
  55. Puso, M.A., Laursen, T.: A mortar segment-to-segment contact method for large deformations solid elements. *Comput. Methods Appl. Mech. Eng.* **193**, 601–629 (2003)
  56. Puso, M.A., Laursen, T., Solberg, J.: A segment-to-segment mortar contact method for quadratic elements and large deformations. *Comput. Methods Appl. Mech. Eng.* **197**(6), 555–566 (2008)
  57. Reissner, E.: On one-dimensional finite strain beam theory: the plane problem. *J. Appl. Math. Phys.* **23**(5), 795–804 (1972)
  58. Romero, I.: A comparison of finite elements for nonlinear beams: the absolute nodal coordinate and geometrically exact formulations. *Multibody Syst. Dyn.* **20**(1), 51–68 (2008). <https://doi.org/10.1007/s11044-008-9105-7>
  59. Romero, I., Armero, F.: An objective finite element approximation of the kinematics of geometrically exact rods and its use in the formulation of an energy-momentum conserving scheme in dynamics. *Int. J. Numer. Methods Eng.* **54**(12), 1683–1716 (2002). <https://doi.org/10.1002/nme.486>
  60. Shabana, A.A.: Definition of the slopes and the finite element absolute nodal coordinate formulation. *Multibody Syst. Dyn.* **1**(3), 339–348 (1997)
  61. Shabana, A.A.: Flexible multibody dynamics: review of past and recent developments. *Multibody Syst. Dyn.* **1**(2), 189–222 (1997)
  62. Simo, J.: A finite strain beam formulation, the three-dimensional dynamic problem. Part I. *Comput. Methods Appl. Mech. Eng.* **49**(1), 55–70 (1985)
  63. Simo, J., Vu-Quoc, L.: On the dynamics of flexible beams under large overall motions-the plane case: I. *J. Appl. Mech.* **53**(4), 849–854 (1986)
  64. Simo, J., Vu-Quoc, L.: On the dynamics of flexible beams under large overall motions-the plane case: II. *J. Appl. Mech.* **53**(4), 855–863 (1986)
  65. Tasora, A., Anitescu, M.: A matrix-free cone complementarity approach for solving large-scale, nonsmooth, rigid body dynamics. *Comput. Methods Appl. Mech. Eng.* **200**(5–8), 439–453 (2011)
  66. Tasora, A., Benatti, S., Mangoni, D., Garziera, R.: A geometrically exact isogeometric beam for large displacements and contacts. *Comput. Methods Appl. Mech. Eng.* **358**, 112635 (2020)
  67. Tasora, A., Negrut, D., Anitescu, M.: Large-scale parallel multibody dynamics with frictional contact on the graphical processing unit. *Proc. Inst. Mech. Eng. Part K J. Multi-body Dyn.* **222**(4), 315–326 (2008)
  68. Tasora, A., Serban, R., Mazhar, H., Pazouki, A., Melanz, D., Fleischmann, J., Taylor, M., Sugiyama, H., Negrut, D.: Chrono: an open source multi-physics dynamics engine. In: Kozubek, T., Blaheta, R., Šístek, J., Rozložník, M., Čermák, M. (eds.) *High Performance Computing in Science and Engineering*, pp. 19–49. Springer, Cham (2016)
  69. Weeger, O., Narayanan, B., De Lorenzis, L., Kiendl, J., Dunn, M.L.: An isogeometric collocation method for frictionless contact of Cosserat rods. *Comput. Methods Appl. Mech. Eng.* **321**, 361–382 (2017)
  70. Wriggers, P.: *Computational Contact Mechanics*, 2nd edn. Springer, Berlin (2006)
  71. Wriggers, P.: *Nonlinear Finite Element Methods*. Springer, Berlin (2008)
  72. Wriggers, P., Zavarise, G.: On contact between three-dimensional beams undergoing large deflections. *Commun. Numer. Methods Eng.* **13**(6), 429–438 (1997)
  73. Yang, B.: *Mortar Finite Element Methods for Large Deformation Contact Mechanics*, 2nd edn. VDM Publishing, Saarbrücken (2009)
  74. Yang, B., Laursen, T.A.: A contact searching algorithm including bounding volume trees applied to finite sliding mortar formulations. *Comput. Mech.* **41**(2), 189–205 (2008)
  75. Yang, B., Laursen, T.A., Meng, X.: Two dimensional mortar contact methods for large deformation frictional sliding. *Int. J. Numer. Methods Eng.* **62**(9), 1183–1225 (2005)
  76. Yu, X., Matikainen, M.K., Harish, A.B., Mikkola, A.: Procedure for non-smooth contact for planar flexible beams with cone complementarity problem. *Proc. Inst. Mech. Eng. Part K J. Multibody Dyn.* (2020). <https://doi.org/10.1177/1464419320957450>
  77. Zavarise, G., Wriggers, P.: Contact with friction between beams in 3-D space. *Int. J. Numer. Methods Eng.* **49**(8), 977–1006 (2000)
  78. Zhong, Z.H., Nilsson, L.: A contact searching algorithm for general contact problems. *Comput. Struct.* **33**(1), 197–209 (1989)

**Publisher's Note** Springer Nature remains neutral with regard to jurisdictional claims in published maps and institutional affiliations.

## **Publication IV**

Escalona, J. L., Yu, X., and Aceituno, J. F.

**Wheel–rail contact simulation with lookup tables and KEC profiles:  
a comparative study**

Reprinted with permission from

*Multibody System Dynamics*

(2020) 1-37

© 2020, Springer.





## Wheel–rail contact simulation with lookup tables and KEC profiles: a comparative study

José L. Escalona<sup>1</sup> · Xinxin Yu<sup>2</sup> ·  
Javier F. Aceituno<sup>3</sup>

Received: 9 June 2020 / Accepted: 30 November 2020  
© The Author(s), under exclusive licence to Springer Nature B.V. part of Springer Nature 2020

**Abstract** This paper describes and compares the use and limitations of two constraint-based formulations for the wheel–rail contact simulation in multibody dynamics: (1) the use of contact lookup tables and (2) the Knife-edge Equivalent Contact constraint method (KEC-method). Both formulations are presented and an accurate procedure to interpolate within the data in the lookup table is also described. Since the wheel–rail constraint contact approach finds difficulties at simultaneous tread and flange contact scenarios, the lookup table method is implemented with a penetration-based elastic contact model for the flange, turning the method into a hybrid (constant in the tread and elastic in the flange) approach. To deal with the two-point contact scenario in the KEC-method, a regularisation of the tread–flange transition allows the use of the constraint approach in the tread and also in the flange. To show the applicability and limitations of both methods, they are studied and compared with special emphasis in the calculation of normal and tangential contact forces. Numerical results are based on the simulation of a two-wheeled bogie vehicle in different case studies that consider irregular tracks and two wheel–rail profiles combinations: profiles that do not show two-point wheel–rail contacts and profiles that do show two-point wheel–rail contacts. Although results show a good agreement between both approaches, the use of the KEC-method is more extensive since it allows to reproduce the wheel-climbing scenario that cannot be simulated with the lookup table method with the hybrid contact approach. It is concluded that simulations with this later method may not be on the safe side.

---

J.F. Aceituno  
[jaceitun@ujaen.es](mailto:jaceitun@ujaen.es)

J.L. Escalona  
[escalona@us.es](mailto:escalona@us.es)

X. Yu  
[xinxin.yu@lut.fi](mailto:xinxin.yu@lut.fi)

- <sup>1</sup> Dept. of Mechanical and Manufacturing Engineering, University of Seville, Seville, Spain
- <sup>2</sup> Dept. of Mechanical Engineering, LUT University, Lappeenranta, Finland
- <sup>3</sup> Dept. of Mechanical and Mining Engineering, University of Jaén, Jaén, Spain

**Keywords** Contact lookup table · KEC-method · Interpolation · Wheel–rail contact · Wheel-climbing

**Nomenclature**

$\bar{\mathbf{r}}^{lir}, \bar{\mathbf{r}}^{rir}$	The relative position vector of the irregular rail centreline with respect to the ideal rail centreline.
$\bar{\mathbf{r}}^{lrp}, \bar{\mathbf{r}}^{rrp}$	The relative position vector of the ideal rail centreline with respect to the the <i>track frame</i> .
$\bar{\mathbf{r}}_c^{wi}, \bar{\mathbf{r}}_c^{rp}$	The position vectors of contact points on the wheel and rail in <i>track frame</i> .
$\bar{\mathbf{t}}_{1,c}^{wi}, \bar{\mathbf{n}}_c^{rp}$	The unit-tangent vector and normal vector at the contact point in <i>track frame</i> .
$\beta$	The orientation angle of the rail profiles
$\lambda$	The array of Lagrange multipliers.
$\delta$	The linearised rotation angle due to the irregularity
$\delta^{wi}, \dot{\delta}^{wi}$	The wheel-rail penetration at the flange contact and its time derivative.
$\hat{\mathbf{u}}_P^{rrp}, \hat{\mathbf{u}}_Q^{lrp}$	The position vector of points <i>P</i> and <i>Q</i> in the rail profiles.
$\hat{\mathbf{u}}_R^{wli}, \hat{\mathbf{u}}_L^{wli}$	The position of the points in the wheel surface with respect to the <i>wheelset intermediate frame</i> .
$\mathbf{A}^{t,lrp}, \mathbf{A}^{t,rrp}$	The rotation matrix from the <i>railhead frame</i> with respect to the <i>track frame</i> .
$\mathbf{A}^t$	The rotation matrix from the <i>track frame</i> to the <i>global frame</i> .
$\mathbf{A}^{wti,wi}, \mathbf{A}^{wti,wli}, \mathbf{A}^{wli,wi}$	The rotation matrices from <i>wheel frame</i> to the <i>wheelset track frame</i> , from <i>wheelset intermediate frame</i> to the <i>wheelset track frame</i> and from <i>wheel frame</i> to the <i>wheelset intermediate frame</i> .
$\mathbf{C}^{clt}$	The wheel-rail contact constraint equations modelled with lookup tables.
$\mathbf{C}_q^{clt}, \dot{\mathbf{C}}_q^{clt}$	The Jacobian matrix and its time derivative of all wheel-rail contact constraints modelled with lookup tables.
$\mathbf{C}^{KEC}$	The contact constraint equations of a wheelset with KEC profiles.
$\mathbf{C}_q^{KEC}, \dot{\mathbf{C}}_q^{KEC}$	The Jacobian matrix and its time derivative of KEC contact constraint equations with respect to generalised coordinates $\mathbf{q}$ .
$\mathbf{C}_s^{KEC}, \dot{\mathbf{C}}_s^{KEC}$	The Jacobian matrix and its time derivative of KEC contact constraint equations with respect to KEC surface parameters.
$\mathbf{n}_c^{rp}$	The normal vector to the rail surface at the contact point in <i>global frame</i> .
$\mathbf{Q}$	The force vectors of generalised applied forces and generalised quadratic-velocity inertia forces.
$\mathbf{Q}_{fla}^{nor}, \mathbf{Q}^{tang}, \mathbf{Q}_{tread}^{nor}$	The force vectors of generalised wheel-rail normal flange forces, generalised tangential tread and flange forces, and generalised normal forces at the wheel tread.
$\mathbf{R}^t$	The absolute position vector of an arbitrary point on the ideal track centreline with respect to a <i>global frame</i> .
$\mathbf{R}_c^{wi}, \mathbf{R}_c^{rp}$	The position vectors of contact points on the wheel and rail in <i>global frame</i> .
$\mathbf{t}_{1,c}^{wi}, \mathbf{t}_{2,c}^{wi}$	The two unit-tangent vectors to the wheel surface at the contact point in <i>global frame</i> .
$\psi^t, \theta^t, \varphi^t$	The Euler angles that describe the orientation of the <i>track frame</i> with respect to a <i>global frame</i> .

$al, vp, gv, cl$ $f^{lk}, f^{rk}$	Alignment, vertical profile, gauge variation and cross level. The value of the equivalent profiles at the lateral positions of $s^{lk}$ and $s^{rk}$ .
$K_{hertz}, C_{damp}$	The Hertzian stiffness and the constant that introduces non-linear damping.
$L_w$	The lateral distance of the <i>wheel frames</i> with respect to the wheelset frame.
$R_x^t, R_y^t, R_z^t$	The absolute position of an arbitrary point on the ideal track centreline with respect to a <i>global frame</i> in $X, Y$ and $Z$ direction.
$r_0$	The rolling radius of the wheel when centred in the track.
$s$	The arc-length along the track.
$s^{lk}, s^{rk}$	The lateral positions of the contact point in the left and right KEC profiles.
$y^{lir}, z^{lir}, y^{rir}, z^{rir}$	The track irregularities in $Y$ and $Z$ direction.
$h^r, h^w$	The functions that define the railhead and wheel profiles.
$s_1^r, s_2^r, s_1^w, s_2^w$	The surface parameters of the railhead and wheel profiles.
$\bar{F}_z^{wi}, \bar{M}_x^{wi}$	The vertical force and roll torque at the wheelset due to the normal contact forces.
$\nu$	The Poisson's ratio.
$A, B$ and $\beta_h$	The parameters to compute Hertzian stiffness which depend on the curvatures of rail/wheel surfaces.
$E$	The Young's modulus of the surface.

## 1 Introduction

In multibody dynamic simulations of railway vehicles, the modelling of wheel–rail contact plays a fundamental role throughout the literature. Contact forces and their locations within wheel and rail profiles strongly influence in the dynamic behaviour of the vehicles. Hence, the development of contact models in terms of accuracy and efficiency is of great interest for the research community [1–6]. Among these works, two well-known approaches are commonly used to simulate wheel/rail contact in multibody railway simulations. The first is the elastic approach, in which interpenetration and separation between the wheel and rail surfaces is allowed and normal contact forces are computed, for example, using a Hertzian-based model that calculates normal contact forces using the interpenetration and interpenetration rate [7–9]. The second is the constraint approach, where the contact between wheel and rail is computed by solving a set of non-linear constraint equations that establish that both surfaces in contact coincide in one or more singular contact points without penetration or separation [10, 11]. In this approach, normal contact forces are described through the Lagrange multipliers, which are associated with the contact constraints at each contact point.

One main feature of the elastic and the constraint approaches is the determination of the location of the contact points. In this sense, two methodologies can be used for this contact search. On the one hand, this search can be addressed using the *online* method. In this approach, the location of the contact points is determined at each time step of the dynamic simulation by solving a set of algebraic non-linear equations that evaluates the contact points as a function of the wheelset-track relative position. Many works can be found in the literature that use the online search method. In this sense, Marques et al. [12] present an approach to determine contact points in the conformal zone between wheel tread and flange,

based on the evaluation of the contact between each wheel strip and rail avoiding inaccuracies of the minimum distance method. Magalhães et al. [13] proposed an elastic contact model for non-Hertzian conditions providing accurate results and efficient simulations. In this line, Sun et al. [14] presents a modified Kik–Piotrowski model [15] for the wheel–rail normal contact analysis, which is extended to the analysis of the influence of the wheelset yaw angle in [16]. In the work of Pombo and Ambrósio, a three-dimensional online contact detection approach is proposed to analyse the lead/lag flange contact scenarios [17], small radius track simulation [18] and the inclusion of track irregularities [19]. Moreover, in the work of O’Shea and Shabana [20, 21], the initiation of the wheel–climb phenomenon is investigated at large angles of attack. They show that the Nadal  $L/V$  derailment criterion is not conservative. In the work of Malvezzi et al. [22], two contact elastic detection methods are proposed with the known analytical expressions of the wheel and rail surfaces, one is based on the idea of minimising the distance while the other is minimising the difference between the surfaces. Both methods give efficient computational times and good agreement in terms of kinematic variables and contact forces between Matlab and Simpack Rail models in [23]. Also, Baeza et al. [24] proposed an elastic detection approach to calculate the interpenetration areas between the wheel and rail. In their work, the geometries of the wheel surface are discretised by using cones and those of rail head by using knife-edge lines. Moreover, with the goal of reducing the computational cost of online contact search methods, Muñoz et al. [25] present a multibody model of railway vehicles that uses simplified contact constraints for the online wheel–tread solution combined with an elastic approach for the flange. In the same context, Escalona et al. [26] present the simplified constraint-based wheel–rail contact method called KEC-method (Knife-edge Equivalent Contact method), in which the rails, that are considered infinitely narrow, contact an equivalent wheel profile, producing the same wheelset relative-track kinematics than using real wheel–rail profiles with a great computational efficiency.

On the other hand, the search of the contact points can be done using the so-called *offline* method. In this approach, the contact solution is provided in a preprocessing stage as a function of the wheelset relative position with respect to the track, and it is stored in a lookup table, which is later used during the dynamic simulations by the interpolation in the stored data. In this sense, there are also many references in the literature about contact lookup tables. Most of them are based on the constraint approach [27–33], but also on the elastic approach [34]. The reason is that the constraint approach involves a reduced number of relative degrees of freedom of the wheelset with respect to the track, as shown in [26]. This reduces the number of entries, and in turn the stored data, of the lookup tables. In [27], a constraint contact lookup table approach that accounts for track irregularities using two independent variables (2-DOFs) is proposed and compared with the online solution of the contact constraints. It is demonstrated that dealing carefully with geometric assumptions, simplified contact lookup tables produce accurate and efficient results. In [34], a 3-DOFs elastic contact lookup table is presented to study the advantages and disadvantages against an online procedure. The results showed that the time required for the lookup table approach is substantially lower than for the online solution procedure. In [29], a combination of a constraint contact lookup table for the tread contact and an elastic online approach for the flange one is proposed and called the *hybrid* method. It is extended in [30] to the combination of nodal and non-conformal contact detection, to solve significant jumps of contact points in turnouts. Moreover, in [31], a regularisation of the non-elliptical wheel–rail contact areas named Kalker book of tables for non-Hertzian contact (KBTNH) is proposed and used in [32, 33] to analyse the accuracy and contact patch moments.

This paper supports and focuses on the use of the constraint approach in some applications. Clearly, the elastic approach is better suited for a more detailed contact analysis

because it allows more insight into the actual surface areas in contact. However, under some common circumstances, the use of the constraint approach is superior:

1. When the profiles geometry is not well-known, for example, due to wear;
2. When the overall vehicle dynamics is of interest, instead of the intimate wheel–rail contact analysis.

In addition, as it is accepted in the community, the constraint approach is computationally more efficient. However, one of its main drawbacks is its difficult application when dealing with two-point contact scenario. This scenario is very important in curving and safety analysis of the railway vehicles. That is why this paper focuses on this scenario.

To this end, this paper compares the accuracy, efficiency, applicability and limitations of two constraint-based formulations (offline and online, respectively) for the dynamic simulation of the wheel–rail contact of railway vehicles in multibody dynamics. The offline methodology used in this paper is based on precalculated contact lookup tables and the online one is based on the Knife-edge Equivalent Contact method (KEC-method) presented in [26]. The use of precalculated contact lookup tables is presented first. This method is well-known, computationally efficient and widely used [27–34]. It also presents an innovative procedure to interpolate between the stored data. However, an important drawback of lookup tables appears when using wheel–rail profile combinations that show two-point contact scenarios (tread and flange contacts) because constraint contact lookup tables are not suitable to deal with simultaneous contacts using variable number of kinematic constraints. Since most of real wheel–rail profile combinations are of this type, this scenario is essential when analysing vehicle curving or wheel climbing and derailment. Instead, the two-point contact simulation with contact lookup tables is done in this work using a hybrid method in which the flange contact is analysed using a penetration-based elastic model. The second method used in this paper is the KEC-method [26]. It is an online constraint-based method that considers the rails as infinitely narrow lines (like the edge of a knife) that contact equivalent wheels such that they show the same subspace of allowable motion that the real wheel and rail profiles. As it is a constraint-based method, the two-point contact scenario used together with a regularisation method for the tread-flange transition as presented in [35] allows possible wheel climbing.

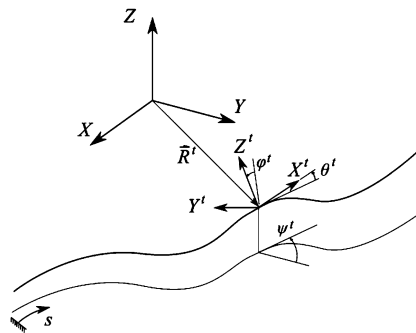
The organisation of this paper is given as follows: Sect. 2 introduces the kinematics of the wheel–rail contact. Wheel–rail contact simulation with lookup tables and its interpolation procedure are presented in Sect. 3. The KEC-method approach is briefly explained in Sect. 4. Section 5 presents the generation of lookup tables for flanging wheelsets, and Sect. 6 presents three case studies of a bogie vehicle to analyse differences and limitations of both approaches: (1) simulation results in a tangent-curved track with irregularities using profiles that do not show two-point contacts, (2) simulation results in a tangent-curved track with irregularities using profiles that show two-point contacts and (3) simulation results of a wheel climbing scenario in a small radius curved track without irregularities. Finally, Sect. 7 provides a summary and conclusion.

## 2 Kinematics of the wheel–rail contact

### 2.1 Track kinematics

Track geometry is the superposition of the ideal geometry and the irregularities. The components of the absolute position vector of an arbitrary point on the ideal track centreline with

**Fig. 1** Ideal track centreline



respect to a global frame is a function of the arc-length  $s$  as follows:

$$\mathbf{R}^t(s) = \begin{bmatrix} R_x^t(s) \\ R_y^t(s) \\ R_z^t(s) \end{bmatrix}, \tag{1}$$

where  $\mathbf{R}^t(s)$  contains the components of vector  $\vec{R}^t$  shown in Fig. 1. The geometry of the track centreline 3D-curve is defined by the *horizontal profile* and the *vertical profile*. The so-called track preprocessors implement these functions of  $s$  given the ideal track geometry using a set of segment-dependent parameters (length, curvature, slope, etc.)

Figure 1 shows the track frame  $\langle O^t; X^t, Y^t, Z^t \rangle$  associated with the track centreline at each value of  $s$ . The orientation of the track frame with respect to a global frame can be measured with the Euler angles  $\psi^t$  (*azimut* or *heading* angle),  $\theta^t$  (*vertical slope*, positive when downwards in the forward direction) and  $\varphi^t$  (*cant* or *superelevation* angle). These three angles are also functions of  $s$  that are implemented in the track preprocessor. The rotation matrix from the track frame to the global frame is given by

$$\mathbf{A}^t(s) = \begin{bmatrix} c\theta^t c\psi^t & s\varphi^t s\theta^t c\psi^t - c\varphi^t s\psi^t & s\varphi^t s\psi^t + c\varphi^t s\theta^t c\psi^t \\ c\theta^t s\psi^t & c\varphi^t c\psi^t + s\varphi^t s\theta^t s\psi^t & c\varphi^t s\theta^t s\psi^t - s\varphi^t c\psi^t \\ -s\theta^t & s\varphi^t c\theta^t & c\varphi^t c\theta^t \end{bmatrix}, \tag{2}$$

where the terms ‘c’ and ‘s’ in Eq. (2) refer to the cosine and sine functions, respectively.

Figure 2 on the left shows the relative position of the irregular right rail centreline with respect to the track frame. Figure 2 on the right shows the displacement of the railheads due to irregularity in a cross-section of the track ( $Y^t$ – $Z^t$  plane). As observed in the figure, a frame is defined at each railhead (*lrp*, *left rail profile* frame, and *rrp*, *right rail profile* frame). The left and right rail profile frames are separated by a distance of  $2L_r$  in the ideal track. The irregularity vectors  $\vec{r}^{lir}$  (*lir*, *left rail irregularity*) and  $\vec{r}^{rir}$  (*rir*, *right rail irregularity*) describe the displacement of the rail centrelines. The components of these vectors in the track frame are functions of  $s$  given by

$$\vec{r}^{lir}(s) = \begin{bmatrix} 0 \\ y^{lir} \\ z^{lir} \end{bmatrix}, \quad \vec{r}^{rir}(s) = \begin{bmatrix} 0 \\ y^{rir} \\ z^{rir} \end{bmatrix}. \tag{3}$$

In the railway industry, the following four combinations of the railhead centrelines irregularities are measured:

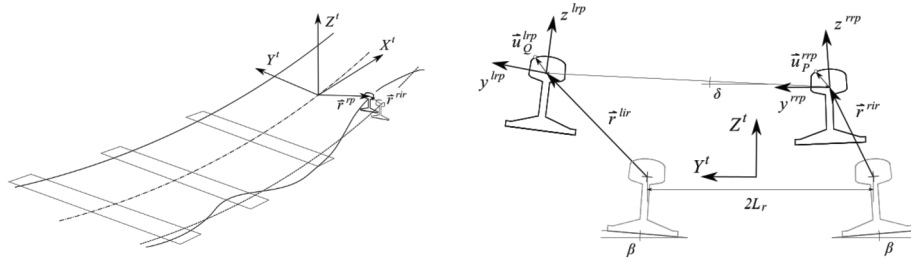


Fig. 2 Track irregularity

- Alignment ( $al$ ),  $al = (y^{lir} + y^{rir})/2$ ;
- Verticle profile ( $vp$ ),  $vp = (z^{lir} + z^{rir})/2$ ;
- Gauge variation ( $gv$ ),  $gv = y^{lir} - y^{rir}$ ;
- Cross level ( $cl$ ),  $cl = z^{lir} - z^{rir}$ .

The orientation of the railhead frames with respect to the track frame is given by the following rotation matrices:

$$\begin{aligned}
 \mathbf{A}^{t,lrp}(s) &= \begin{bmatrix} 1 & 0 & 0 \\ 0 & \cos(\beta + \delta) & -\sin(\beta + \delta) \\ 0 & \sin(\beta + \delta) & \cos(\beta + \delta) \end{bmatrix}, \\
 \mathbf{A}^{t,rrp}(s) &= \begin{bmatrix} 1 & 0 & 0 \\ 0 & \cos(-\beta + \delta) & -\sin(-\beta + \delta) \\ 0 & \sin(-\beta + \delta) & \cos(-\beta + \delta) \end{bmatrix},
 \end{aligned} \tag{4}$$

where  $\beta$  is the orientation angle of the rail profiles and  $\delta = (z^{lir} - z^{rir})/2L_r$  is the linearized rotation angle due to the irregularity. Both angles can be observed in Fig. 2 on the right.

The absolute position vectors of two points,  $P$  and  $Q$ , defined in the right and left railheads, respectively, are given by:

$$\begin{aligned}
 \vec{R}_P^{rrp} &= \vec{R}^t + \vec{r}^{rrp} + \vec{r}^{rir} + \vec{u}_P^{rrp}, \\
 \vec{R}_Q^{lrp} &= \vec{R}^t + \vec{r}^{lrp} + \vec{r}^{lir} + \vec{u}_Q^{lrp}.
 \end{aligned} \tag{5}$$

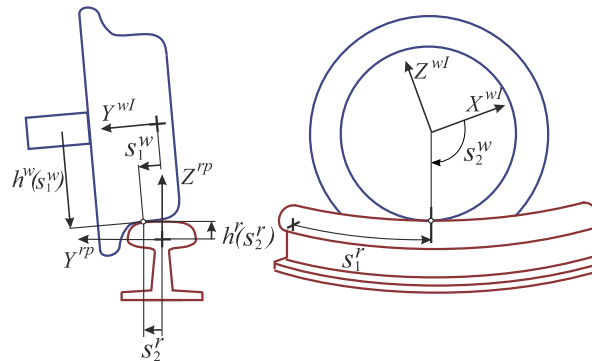
The components of these vectors in the global frame are given by:

$$\begin{aligned}
 \mathbf{R}_P^{rrp} &= \mathbf{R}^t + \mathbf{A}^t(\vec{r}^{rrp} + \vec{r}^{rir} + \mathbf{A}^{t,rrp}\hat{\mathbf{u}}_P^{rrp}), \\
 \mathbf{R}_Q^{lrp} &= \mathbf{R}^t + \mathbf{A}^t(\vec{r}^{lrp} + \vec{r}^{lir} + \mathbf{A}^{t,lrp}\hat{\mathbf{u}}_Q^{lrp}),
 \end{aligned} \tag{6}$$

where  $\hat{\mathbf{u}}_P^{rrp}$  and  $\hat{\mathbf{u}}_Q^{lrp}$  contain the components of the position vector of points  $P$  and  $Q$  in the rail profiles as shown in Fig. 2 on the right. These vectors are parametrized following the railhead profile geometry:

$$\hat{\mathbf{u}}_P^{rrp} = \begin{bmatrix} 0 \\ s_2^{rr} \\ h^{rr}(s_2^{rr}) \end{bmatrix}, \quad \hat{\mathbf{u}}_Q^{lrp} = \begin{bmatrix} 0 \\ s_2^{lr} \\ h^{lr}(s_2^{lr}) \end{bmatrix}, \tag{7}$$

**Fig. 3** Wheel profile and rail profile geometry



where *lr* and *rr* stand for *left rail* and *right rail*,  $s_2^{lr}$  and  $s_2^{rr}$  are the transverse coordinates of the points in the railheads and  $h^{lr}$  and  $h^{rr}$  are the functions that define the railhead profile, as shown in Fig. 3.

The calculation of the track geometry requires interpolation at two levels: (1) the description of the centreline shown in Eq. (1) as a function of the longitudinal arc-length  $s$  and (2) the description of the rail-head cross-sections  $h^{lr}$  and  $h^{rr}$  shown in Eq. (7) as a function of the transverse parameters  $s_2^{lr}$  and  $s_2^{rr}$ . Both are implemented in this investigation using cubic splines. For the description of the track centreline, the analytic functions used in the industry to describe the track horizontal and vertical profiles (straight lines, circles, clothoids and cubic polynomials) are used to tabulate the absolute position a set of equally-spaced nodal points. For the description of the rail-head profiles, the straight lines and circles used to define the new (not worn) rail-head profiles are used to tabulate the functions  $h^{lr}$  and  $h^{rr}$  at a set of nodal points. Alternatively, experimentally measured rail-head profiles can be used if worn rail-head profiles are simulated. The benefits of the cubic interpolation compared with the evaluation of analytic functions is the smoothness of the higher-order space-derivatives of the geometry at the transition points.

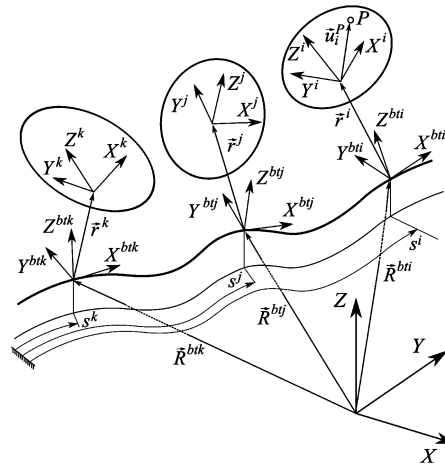
### 2.2 Vehicle kinematics

For the modelling of a railway vehicle, a set of relative body-track frame coordinates, as shown in Fig. 4, is selected in this work. In this formulation [26], each modelled body belonging to the railway vehicle is accompanied by a track-frame along the track centreline. These frames are called *body-track frames*  $\langle O^{bti}; X^{bti}, Y^{bti}, Z^{bti} \rangle$  for each body  $i$ . The body-track frame is defined such that the relative position vector  $\bar{\mathbf{r}}^i = [0 \quad \bar{r}_y^i \quad \bar{r}_z^i]^T$  of the body frame with respect to the body-track frame has zero  $x$ -component along the track centreline. Therefore, for each body  $i$ , the following set of coordinates is defined:

$$\mathbf{q}^i = [s^i \quad \bar{r}_y^i \quad \bar{r}_z^i \quad (\bar{\Phi}^i)^T]^T = [s^i \quad \bar{r}_y^i \quad \bar{r}_z^i \quad \bar{\varphi}^i \quad \bar{\theta}^i \quad \bar{\psi}^i]^T, \tag{8}$$

where the vector  $\mathbf{q}^i$  describes the absolute position of the body track frame (arc-length coordinate  $s^i$ ), the relative body frame to body-track frame position (position vector  $\bar{\mathbf{r}}^i$ ) and relative body frame to body-track frame orientation (Euler angles  $\bar{\Phi}^i$ ). Therefore, the

**Fig. 4** Kinematics of the bodies of a railway vehicle with relative body-track frame coordinates



set of coordinates for all vehicle bodies is

$$\mathbf{q} = \begin{bmatrix} \mathbf{q}^2 \\ \vdots \\ \mathbf{q}^{nb} \end{bmatrix}, \tag{9}$$

where  $nb$  is the number of modelled bodies in the railway vehicle. Superscripts start at 2 because body 1 is assumed to be the ground body, this is, the track.

Using these coordinates, the absolute position vector of point  $P$  that belongs to body  $i$  is given by

$$\vec{R}_p^i = \vec{R}^{bti} + \vec{r}^i + \vec{u}_p^i, \tag{10}$$

where  $\vec{R}_p^i$  (not shown in Fig. 1) is the absolute position vector of  $P$ ,  $\vec{R}^{bti}$  is the absolute position vector of the body-track frame,  $\vec{r}^i$  is the relative position vector of the origin of the body  $i$  frame with respect to its body-track frame and  $\vec{u}_p^i$  is the local position vector of point  $P$  in body  $i$ . Equation (10) can be projected in the global frame as follows:

$$\mathbf{R}_p^i = \mathbf{R}^{bti} + \mathbf{A}^{bti}(\vec{r}^i + \mathbf{A}^{bti,i}\hat{\mathbf{u}}_p^i). \tag{11}$$

In this formula, the terms have the following meaning and functional dependency:

- $\mathbf{R}^{bti} = \mathbf{R}^{bti}(s^i)$  Components of position vector of the body-track frame in the global frame;
- $\mathbf{A}^{bti} = \mathbf{A}^{bti}(s^i)$  Transformation matrix of the body-track frame to the global frame;
- $\vec{r}^i = \vec{r}^i(\mathbf{q})$  Components of position vector of the body with respect to the body-track frame in the body-track frame;
- $\mathbf{A}^{bti,i} = \mathbf{A}^{bti,i}(\mathbf{q})$  Transformation matrix of the base body frame with respect to the body-track frame;
- $\hat{\mathbf{u}}_p^i$  Components of the position vector of point  $P$  with respect to body  $i$  in the body frame. These components are constant.

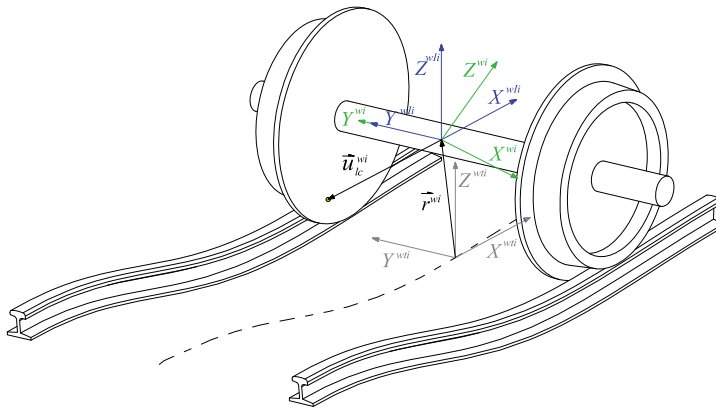


Fig. 5 Frames for rigid wheelset kinematics

### 2.3 Wheelset kinematics

The track-relative coordinates of a rigid wheelset  $i$  (superscript  $wi$ ) are

$$\mathbf{q}^{wi} = [s^{wi} \quad \bar{r}_y^{wi} \quad \bar{r}_z^{wi} \quad \bar{\varphi}^{wi} \quad \bar{\theta}^{wi} \quad \bar{\psi}^{wi}]^T. \tag{12}$$

For each rigid wheelset, an additional frame that rotates with the wheelset without following the rolling angle  $\bar{\theta}^{wi}$  is defined, namely the *wheelset intermediate frame*,  $wli$ . Figure 5 shows the wheelset  $i$  body frame  $wi$  and the intermediate one  $wli$ . The orientation of the wheelset body frame with respect to the wheelset track frame  $wti$  is given by the following matrix:

$$\mathbf{A}^{wti,wi} = \mathbf{A}^{wti,wli}(\bar{\psi}^{wi}, \bar{\varphi}^{wi})\mathbf{A}^{wli,wi}(\bar{\theta}^{wi}), \tag{13}$$

where the brackets mean the functional dependency of the rotation matrices.

The use of the wheelset intermediate frame allows a clearer description of the position of the wheel–rail contact points. This position varies very little in the  $wli$  frame, but it greatly varies in the  $wi$  frame (this variation is approximately periodic, being the time taken by the wheel to complete a revolution the time-period). The position vector of an arbitrary point  $P$  on the surface of the left or right wheel profile can be obtained as

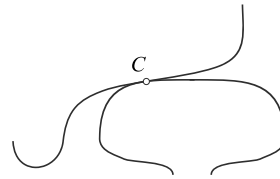
$$\mathbf{R}_P^{wi} = \mathbf{R}^{wti} + \mathbf{A}^{wti}(\bar{\mathbf{r}}^{wi} + \mathbf{A}^{wti,wli}\hat{\mathbf{u}}_P^{wli}), \tag{14}$$

where  $\hat{\mathbf{u}}_P^{wli}$  may take the following forms for the left ( $P = L$ ) or right wheels ( $P = R$ ):

$$\hat{\mathbf{u}}_R^{wli} = \begin{bmatrix} h^{rw}(s_1^{rw}) \cos s_2^{rw} \\ -L_w + s_1^{rw} \\ -h^{rw}(s_1^{rw}) \sin s_2^{rw} \end{bmatrix}, \quad \hat{\mathbf{u}}_L^{wli} = \begin{bmatrix} h^{lw}(s_1^{lw}) \cos s_2^{lw} \\ L_w + s_1^{lw} \\ -h^{lw}(s_1^{lw}) \sin s_2^{lw} \end{bmatrix}, \tag{15}$$

where  $lw$  and  $rw$  stand for *left wheel* and *right wheel*,  $s_1^{lw}$ ,  $s_2^{lw}$ ,  $s_1^{rw}$  and  $s_2^{rw}$  are the parameters needed to define the points in the wheel surface,  $h^{lw}$  and  $h^{rw}$  are the functions that defines the left and right wheel profile, as shown in Fig. 3 and  $L_w$  is the lateral distance of the wheel frames with respect to the wheelset frame.

**Fig. 6** Wheel and rail in contact



### 2.4 Wheel–rail contact constraints

The wheel–rail non-conformal contact constraints (see Fig. 6) establish that the absolute position of the contact point on the rail is the same as the absolute position of the contact point on the wheel. In addition, the tangent plane to the rail at the contact point is parallel to the tangent plane to the wheel at the contact point. These are five constraint equations that can be written as:

$$\begin{aligned}
 \mathbf{R}_c^{wi}(\mathbf{q}^{wi}, \mathbf{s}^w) - \mathbf{R}_c^{rp}(s^r) &= \mathbf{0}, \\
 \left[ \mathbf{t}_{1,c}^{wi}(\mathbf{q}^{wi}, \mathbf{s}^w) \right]^T \mathbf{n}_c^{rp}(s^r) &= 0, \\
 \left[ \mathbf{t}_{2,c}^{wi}(\mathbf{q}^{wi}, \mathbf{s}^w) \right]^T \mathbf{n}_c^{rp}(s^r) &= 0,
 \end{aligned} \tag{16}$$

where  $c$  can be  $lc$  (left contact) or  $rc$  (right contact),  $w$  can be  $lw$  (left wheel) or  $rw$  (right wheel),  $rp$  can be  $lrp$  (left rail profile) or  $rrp$  (right rail profile),  $\mathbf{s}^w = [s_1^w \ s_2^w]^T$ ,  $\mathbf{s}^r = [s_1^r \ s_2^r]^T$  include all surface parameters needed to locate the contact points,  $\mathbf{t}_{1,c}^{wi}$  and  $\mathbf{t}_{2,c}^{wi}$  are the two unit-tangent vectors to the wheel surface at the contact point,  $\mathbf{n}_c^{rp}$  is the normal vector to the rail surface at the contact point.

The tangent vectors  $\mathbf{t}_{1,c}^{wi}$  and  $\mathbf{t}_{2,c}^{wi}$  from Eq. (16), which are defined with respect to the surface parameters  $\mathbf{s}^w$ , span the tangent plane at the contact point;  $\mathbf{t}_{1,c}^{wi}$  is perpendicular to the cross-section and  $\mathbf{t}_{2,c}^{wi}$  lies in it. The normal vector  $\mathbf{n}_c^{rp}$  is defined as the cross-product of the two tangent vectors.

The approximate contact constraints represent a simplified version to Eq. (16). The approximate contact constraints neglect the influence of the wheelset yaw angle in the contact geometry. In other words, the 3D surface-to-surface contact constraints are reduced to 2D curve-to-curve contact constraints. The main implication of this approach is that the so-called lead-lag contact effect that occurs due to the longitudinal displacement of the flange contact point with respect to the thread contact point, is neglected. The lead-lag contact effect has, in practice, influence in the vehicle motion when negotiating very narrow curves. This curve negotiation usually happens at very low velocities following a quasi-static motion. As shown in [27], the planar contact approach is commonly sufficiently accurate. The approximate contact constraints can be written as a set of three constraint equations per wheel–rail pair as follows:

$$\begin{aligned}
 \bar{\mathbf{r}}_c^{wi}(\mathbf{q}^{wi}, s_1^w) - \bar{\mathbf{r}}_c^{rp}(s_2^r) &= \mathbf{0}, \\
 \left[ \bar{\mathbf{t}}_{1,c}^{wi}(\mathbf{q}^{wi}, s_1^w) \right]^T \bar{\mathbf{n}}_c^{rp}(s_2^r) &= 0,
 \end{aligned} \tag{17}$$

In these equations, vectors are projected to the track frame. Due to the assumed 2D contact approach, the  $X$ -component of the vector equation on top is automatically fulfilled,

because both vectors  $\bar{\mathbf{r}}_c^{wi}$  and  $\bar{\mathbf{r}}_c^{rp}$  are contained in the  $Y$ – $Z$  plane of the track frame. Therefore, only the  $Y$ – $Z$  components are used. Accordingly, the perpendicularity of  $\bar{\mathbf{n}}_c^{rp}$  and  $\bar{\mathbf{t}}_{2,c}^{wi}$  is guaranteed as well. Hence, the total set of equations in Eq. (17) is reduced to 3. The 2D contact approach also implies that  $s_2^w = \pi/2$  and  $s_1^r = s^w$ . Only one surface parameter per profile needs to be indentified. In practice, the set of surface parameters is reduced from 4 to 2. For that reason, the simplified nomenclature  $s^w = s_1^w$  and  $s^r = s_2^r$  will be used. More details about the use of these contact constraints for non-conformal contacts can be found in [27].

### 3 Wheel–rail contact simulation with lookup tables

This section explains the use of contact lookup tables for the simulation of railway vehicles using relative body-track frame coordinates.

#### 3.1 Calculation of lookup tables

Lookup tables are calculated in a preprocessing stage. To create a contact lookup table, a set of discrete numerical values is assigned to the lateral displacement of the wheelset  $y^{wi}$  in a range that will be discussed in Sect. 5. The position along the track  $s^{wi}$  and pitch angle  $\theta^{wi}$  are assumed to be zero because these coordinates have no influence on the contact geometry. The yaw angle  $\psi^{wi}$  is also assumed to be zero because its influence in the contact geometry is assumed to be negligible, as explained in Sect. 2.4. For each of these positions, 6 simplified contact constraints Eq. (17) (3 for left contact and 3 for right contact) are solved to find the values of 6 coordinates: the wheelset position and orientation coordinates  $z^{wi}$  and roll angle  $\varphi^{wi}$  and the surface parameters  $s^{lw}$ ,  $s^{rw}$ ,  $s^{lr}$  and  $s^{rr}$  needed to locate the contact points on the left and right wheel and rail surfaces. The contact lookup table can be interpreted as a set of tabulated functions of the form:

$$\begin{aligned} z^{wi} &= z_{clt}(y^{wi}), & \varphi^{wi} &= \varphi_{clt}(y^{wi}), \\ s^{lw} &= s_{clt}^{lw}(y^{wi}), & s^{lr} &= s_{clt}^{lr}(y^{wi}) & s^{rw} &= s_{clt}^{rw}(y^{wi}), & s^{rr} &= s_{clt}^{rr}(y^{wi}), \end{aligned} \tag{18}$$

where the subscript *clt* stands for ‘contact lookup table’. The contact lookup table can be used in dynamic simulations to find the values of these six coordinates from the value of the lateral displacement. In order to deal with a track with irregularities, the contact lookup table has to be extended from 1 entry to 2 entries. The process of creation of the contact lookup table has to be repeated for a set of values of the gauge variation ( $gv$ ) in a range that covers the extreme values of the gauge that appear in practical applications. This is, the contact lookup table is recalculated a number of times after approaching and separating the rails from the nominal distance  $2L_r$  shown in Fig. 2. That way, the functions given above become functions of two variables, as follows:

$$\begin{aligned} z^{wi} &= z_{clt}(y^{wi}, gv), & \varphi^{wi} &= \varphi_{clt}(y^{wi}, gv), \\ s^{lw} &= s_{clt}^{lw}(y^{wi}, gv), & s^{lr} &= s_{clt}^{lr}(y^{wi}, gv) & s^{rw} &= s_{clt}^{rw}(y^{wi}, gv), & s^{rr} &= s_{clt}^{rr}(y^{wi}, gv). \end{aligned} \tag{19}$$

The use of the lookup tables with irregular track is slightly different. In a dynamic simulation, given the longitudinal position of the wheelset  $s^{wi}$ , the values of the irregularities  $al$ ,  $vp$ ,  $gv$  and  $cl$  can be obtained. The lateral displacement that has to be used to enter the

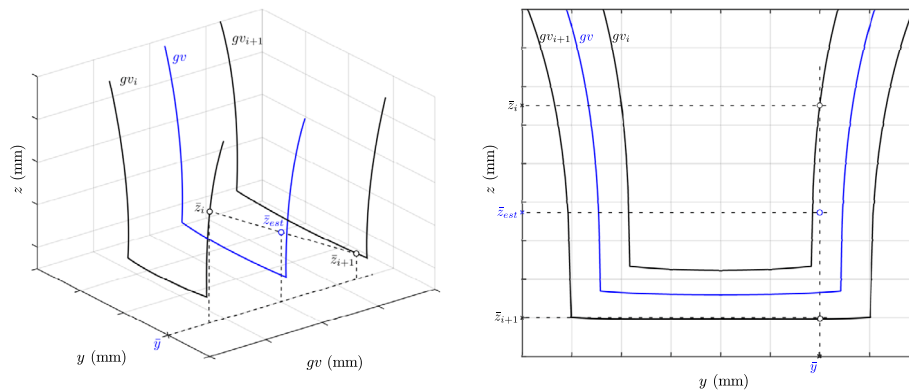


**Fig. 7** Interpolation error at contact lookup tables with track irregularities (Color figure online)

lookup table is not  $y^{wi}$  that gives the lateral displacement with respect to the ideal track centreline, but  $\bar{y}^{wi} = y^{wi} - al$ , that gives the lateral displacement with respect to the irregular track centreline. In turn, the outputs of the lookup table  $\bar{z}^{wi}$  and  $\bar{\varphi}^{wi}$  have to be interpreted differently, being  $\bar{z}^{wi} = z^{wi} + vp$  and  $\bar{\varphi}^{wi} = \varphi^{wi} + cl/2L_r$ . The kinematic constraints associated with wheelset  $wi$  finally yield:

$$\mathbf{C}^{clt,wi} = \begin{bmatrix} z^{wi} - vp - z_{clt}(\bar{y}^{wi} + al, gv) \\ \varphi^{wi} - cl/2L_r - \varphi_{clt}(\bar{y}^{wi} + al, gv) \end{bmatrix} = \mathbf{0}. \tag{20}$$

More details in railway multibody simulation using contact lookup tables can be found in [27].

### 3.2 Interpolation in the lookup tables

As explained in the previous sections, for the generation of KEC-profiles and also during the simulation with the KEC-method, the lookup tables have to be used to find the location of the contact points in the real profiles and other geometric properties. This subsection describes the interpolation in the lookup tables in these cases. However, when using the lookup table contact method with elastic contact in the flange, the lookup tables that are used do not account for contact constraints in the flange (penetration is assumed to occur instead). Therefore, the content of this section is not applicable in that case.

In this context, the use of contact lookup tables that consider flange contact constraints (this is, wheel climb is admissible without flange penetration) and also include track irregularities requires a special treatment in the interpolation procedure. In what follows and with the help of Fig. 7 (superscript  $wi$  is omitted in the figure for simplicity), it is shown the error obtained when the interpolation is applied in the vicinity of the two-point of flange contact scenario.

Figure 7 shows in solid dark lines the wheelset vertical coordinate  $\bar{z}^{wi}$  stored in the lookup table for two different values of gauge irregularity ( $gv_i$  and  $gv_{i+1}$ ) and in solid blue line the same for an arbitrary track gauge irregularity  $gv$  between  $gv_i$  and  $gv_{i+1}$  that is not stored in the table. Let us assume that in a specific instant of a simulation with track gauge  $gv$  (solutions given in blue line that are not stored in the table), the wheelset lateral displacement  $\bar{y}^{wi}$  is in the vicinity of the two-point wheel–rail contact scenario such that, in order

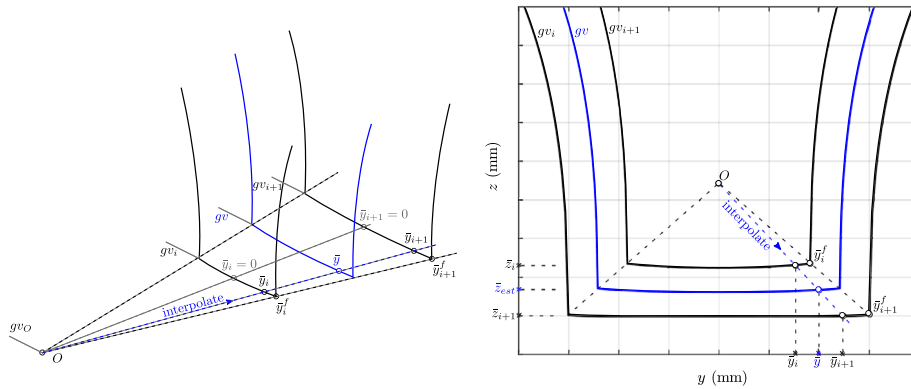


**Fig. 8** Interpolation method at contact lookup tables with track irregularities (Color figure online)

to interpolate in table  $gv_{i+1}$  with  $\bar{y}^{wi}$  the wheelset is at a single point tread contact  $\bar{z}_{i+1}^{wi}$ , while in table  $gv_i$  the wheelset is at a wheel climb scenario  $\bar{z}_i^{wi}$ . Obviously, the interpolation between  $\bar{z}_i^{wi}$  and  $\bar{z}_{i+1}^{wi}$  provides an estimated wheelset vertical displacement  $\bar{z}_{est}^{wi}$  that is far from the correct value given by the blue line as shown in Fig. 7.

In order to avoid these interpolation errors, the wheelset lateral displacement  $\bar{y}^{wi}$  cannot be used directly as an input to interpolate in the tables. It has to be updated to the values  $\bar{y}_i^{wi}$  and  $\bar{y}_{i+1}^{wi}$  that correspond to gauge variations  $gv_i$  and  $gv_{i+1}$  that are stored in the table. This procedure, which is shown in Fig. 8, is defined as follows:

- Given  $\bar{y}^{wi}$  and  $gv$ , find the point of convergence  $O$  and its theoretical irregularity  $gv_O$  as

$$gv_O = gv_{i+1} - \frac{\bar{y}_{i+1}^f \cdot (gv_{i+1} - gv_i)}{\bar{y}_{i+1}^f - \bar{y}_i^f}, \quad (21)$$

where superscript  $f$  refers to the flange starting point. Note that  $gv_O$  is a conceptual gauge irregularity in which both wheels experience flange contact and the wheelset has no possible lateral displacement.

- Interpolate in the direction  $O - \bar{y}^{wi}$  to obtain the corresponding two lateral displacements  $\bar{y}_i^{wi}$  and  $\bar{y}_{i+1}^{wi}$ .
- Enter the lookup tables  $gv_i$  and  $gv_{i+1}$  with  $\bar{y}_i^{wi}$  and  $\bar{y}_{i+1}^{wi}$  to obtain the contact solutions at the stored tables (i.e.  $\bar{z}_i^{wi}$  and  $\bar{z}_{i+1}^{wi}$  for the vertical displacement,  $\bar{\varphi}_i^{wi}$  and  $\bar{\varphi}_{i+1}^{wi}$  for the roll angle).
- Interpolate between the stored solutions to obtain the accurate coordinate (i.e.  $\bar{z}_{est}^{wi}$  and  $\bar{\varphi}_{est}^{wi}$ ).

As it is shown by Figs. 7 and 8, the described linear interpolation procedure avoids errors that can be considerably high in the vicinity of the flange contact scenario.

### 3.3 Calculation of contact forces when using lookup tables

Contact forces are divided into normal contact forces and tangential contact forces. When using lookup tables, normal contact forces in the tread are computed as reaction forces associated with the contact constraints, while normal contact forces in the flange are computed as elastic forces as a function of the wheel–rail penetration. For both, tread and flange contact,

tangential contact forces are computed as applied forces using any established creep contact theory (as Kalker non-linear theory [36] or Polach theory [37]). The resulting equations of motion of the railway vehicle yield

$$\begin{bmatrix} \mathbf{M} & (\mathbf{C}_q^{clt})^T \\ \mathbf{C}_q^{clt} & \mathbf{0} \end{bmatrix} \begin{bmatrix} \ddot{\mathbf{q}} \\ \lambda \end{bmatrix} = \begin{bmatrix} \mathbf{Q} + \mathbf{Q}_{fla}^{nor} + \mathbf{Q}^{tang} \\ -\dot{\mathbf{C}}_q^{clu} \dot{\mathbf{q}} \end{bmatrix}, \tag{22}$$

where  $\mathbf{M}$  is the vehicle mass matrix,  $\mathbf{C}_q^{clt}$  is the Jacobian matrix of all wheel–rail contact constraints modelled with lookup tables,  $\lambda$  is the array of Lagrange multipliers,  $\mathbf{Q}_{fla}^{nor}$  is the vector of generalised wheel–rail normal flange forces,  $\mathbf{Q}^{tang}$  is the vector of generalised tangential tread and flange forces, and  $\mathbf{Q}$  include all other generalised applied forces and generalised quadratic-velocity inertia forces. For clarity, in this equation it has been assumed that the only constraints in the vehicle system are those due to the wheel rail contact. However, everything is valid under the existence of other constraints.

The generalised normal forces at the wheel tread are computed using the Lagrange multipliers technique. Therefore, these forces are treated as reaction forces whose value can be computed as

$$\mathbf{Q}_{tread}^{nor} = -(\mathbf{C}_q^{clt})^T \lambda. \tag{23}$$

The Jacobian matrix  $\mathbf{C}_q^{clt}$  is an assembly of the Jacobian matrices  $\mathbf{C}_q^{clt,wi}$  associated with each wheelset that is given by

$$\mathbf{C}_q^{clt,wi} = \begin{bmatrix} -\frac{dvp}{ds^{wi}} - \frac{\partial z_{clt}}{\partial y} \frac{dal}{ds^{wi}} - \frac{\partial z_{clt}}{\partial gv} \frac{dgv}{ds^{wi}} & -\frac{\partial z_{clt}}{\partial y} & 1 & 0 & 0 & 0 \\ -\frac{1}{2L_r} \frac{dcl}{ds^{wi}} - \frac{\partial \varphi_{clt}}{\partial y} \frac{dal}{ds^{wi}} - \frac{\partial \varphi_{clt}}{\partial gv} \frac{dgv}{ds^{wi}} & -\frac{\partial \varphi_{clt}}{\partial y} & 0 & 1 & 0 & 0 \end{bmatrix}. \tag{24}$$

In this matrix the fact that the irregularities  $al$ ,  $vp$ ,  $gv$  and  $cl$  are a functions of the wheelset position along the track  $s^{wi}$  has been accounted for. However, because these functions use to be such that the derivatives with respect to  $s^{wi}$  are very small, the Jacobian matrix can be simplified to

$$\mathbf{C}_q^{clt,wi} = \begin{bmatrix} 0 & -\frac{\partial z_{clt}}{\partial y} & 1 & 0 & 0 & 0 \\ 0 & -\frac{\partial \varphi_{clt}}{\partial y} & 0 & 1 & 0 & 0 \end{bmatrix}. \tag{25}$$

The use of Eq. (24) would be needed if the wave-length of the track irregularities were short compared with the distance advanced by the wheel in one time-step. In practice, the measured irregularities have wave-lengths above 1 m, which is much longer than that distance.

The generalised normal forces at the wheel flange are treated as applied forces. The contact point detection at flange can be obtained offline, while building the contact lookup table. Thus, the maximum relative-indentation condition [27] is used for potential contact point search at flange, which is

$$\begin{aligned} \left[ \bar{\mathbf{t}}_{1,c}^{wi}(\mathbf{q}^{wi}, s_{fla,1}^w) \right]^T (\bar{\mathbf{r}}_c^{wi}(\mathbf{q}^{wi}, s_{fla,1}^w) - \bar{\mathbf{r}}_c^{rp}(s_{fla,2}^r)) &= 0, \\ \left[ \bar{\mathbf{t}}_{1,c}^{wi}(\mathbf{q}^{wi}, s_{fla,1}^w) \right]^T \bar{\mathbf{n}}_c^{rp}(s_{fla,2}^r) &= 0, \end{aligned} \tag{26}$$

Note that the vectors are projected to the  $Y-Z$  plane of the track frame. Equation (26) is a set of two non-linear equations of two unknown variables, the flange surface parameters at the wheel and the rail,  $s_{fla,1}^w$  and  $s_{fla,2}^r$ , which can be solved using the Newton–Raphson method. The indentation  $\delta^{wi}$  at flange is computed as

$$\delta^{wi} = \left[ \bar{\mathbf{r}}_c^{wi} - \bar{\mathbf{r}}_c^{rp} \right]^T \bar{\mathbf{n}}_c^{wi}. \tag{27}$$

In this research, the flange normal contact force at wheelset  $i$  ( $wi$ ) is computed based on a Hunt–Crossley force model [8, 27, 38], including the elastic and dissipative components:

$$\begin{aligned} \mathbf{Q}_{fla}^{nor,wi} &= \left( \frac{\partial \bar{\mathbf{r}}_{fla}^{wi}}{\partial \mathbf{q}^{wi}} \right)^T \mathbf{F}_{fla}^{nor,wi}, \\ \mathbf{F}_{fla}^{nor,wi} &= \begin{cases} K_{hertz}(\delta^{wi})^{3/2} + C_{damp}\dot{\delta}^{wi}\delta^{wi} & \text{if } \delta^{wi} > 0, \\ \mathbf{0} & \text{if } \delta^{wi} \leq 0, \end{cases} \end{aligned} \tag{28}$$

where  $\bar{\mathbf{r}}_{fla}^{wi}$  is the position vector of the contact point in the flange,  $\mathbf{F}_{fla}^{nor,wi}$  is the elastic normal force in the flange,  $\delta^{wi}$  is the wheel–rail penetration at the flange contact,  $K_{hertz}$  is the Hertzian stiffness and  $C_{damp}$  is a constant that introduces non-linear damping. Note that the terms  $\bar{\mathbf{r}}_{fla}^{wi}$ ,  $\delta^{wi}$  and  $K_{hertz}$  are interpolated from the lookup table.

The Hertzian stiffness  $K_{hertz}$  can be obtained based on the curvatures and material properties of the wheel and rail surfaces [39]

$$K_{hertz} = \frac{4\beta_h}{3(K_i + K_j)\sqrt{A + B}}, \quad K_k = \frac{1 - \nu_k^2}{\pi E_k}, \tag{29}$$

where  $\nu_k$  is the Poisson’s ratio and  $E_k$  is the Young’s modulus of surface  $k$ ,  $A$ ,  $B$  and  $\beta_h$  are computed based on the curvatures of both surfaces (see [39, 40]). However, this formula that comes from Hertz contact theory, assumes that the bodies in contact behave like infinite semi-spaces. Thus, the contact stiffness can be modified (decreased) to account for the structural deformation of the bodies. This structural deformation can be important in the wheel flange.

For the calculation of the contact-tangential creep forces that result in  $\mathbf{Q}^{tang}$ , the following data are needed for each wheel–rail contact pair (either tread or flange contact):

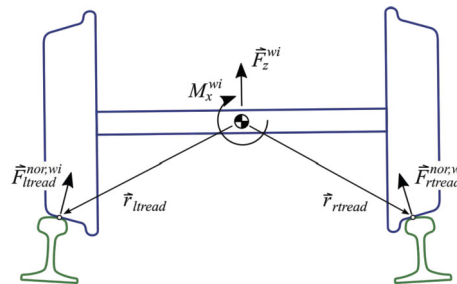
1. The normal contact force;
2. The relative velocity of the contact points;
3. Kalker’s constants and coefficient of friction.

Here, two problems arise just for the tread contacts:

1. The generalised normal forces  $\mathbf{Q}_{tread}^{nor}$  (reaction forces) are known only after solving Eq. (20) and
2. The calculation of the normal force at wheelset  $wi$ ,  $\mathbf{F}_{tread}^{nor,wi}$ , from the generalised normal force  $\mathbf{Q}_{tread}^{nor}$  is not straightforward.

The solution to the first problem, which being strict would require an iterative solution of the equations of motion Eq. (22), is practically solved by assuming that the normal forces this time-step equal the normal forces obtained last time-step. This simple assumption works efficiently in practice because general time-steps used in railway multibody simulations are

**Fig. 9** Forces and torque on wheelset



usually small (a maximum of around 1 ms). Also, to the best authors’ knowledge, there are no simulation codes that implement such an iterative procedure to find the tangential forces.

For the second problem, the following approach is derived: the vertical force  $\bar{F}_z^{wi}$  (vertical component in the track frame) and roll torque  $\hat{M}_x^{wi}$  (longitudinal component in the wheelset intermediate frame) at the wheelset due to the normal contact forces on the treads can be easily identified as the third and fourth components of  $\mathbf{Q}_{tread}^{nor,wi}$ , as follows:

$$\mathbf{Q}_{tread}^{nor,wi} = -(\mathbf{C}_q^{clu,wi})^T \boldsymbol{\lambda}^{wi}, \tag{30}$$

$$\bar{F}_z^{wi} = \mathbf{Q}_{tread}^{nor,wi} (3), \quad \hat{M}_x^{wi} = \mathbf{Q}_{tread}^{nor,wi} (4).$$

This is clear due to the physical interpretation of the reaction forces. These force and torque are due to the normal contact forces at the left tread  $F_{ltread}^{nor,wi}$  and the right tread  $F_{rtread}^{nor,wi}$  as shown by Fig. 9. The directions of these forces,  $\vec{n}_{ltread}$  and  $\vec{n}_{rtread}$ , are the normal vectors to the wheel surfaces that are stored in the lookup table since they only depend on the lateral displacement and the irregularity. A simple force and torque balance allows writing a set of two linear algebraic equations that can be used to find the normal contact forces at the treads each time step. Input data are the reaction force and torque, that appear as independent terms, and the contact geometry (position of contact points and normal to the wheels at these points), that appears in the coefficient matrix and can be extracted from the contact lookup table, as follows:

$$\begin{bmatrix} (\bar{\mathbf{n}}_{ltread})_z & (\bar{\mathbf{n}}_{rtread})_z \\ (\hat{\mathbf{r}}_{ltread} \times \hat{\mathbf{n}}_{ltread})_x & (\hat{\mathbf{r}}_{rtread} \times \hat{\mathbf{n}}_{rtread})_x \end{bmatrix} \begin{bmatrix} F_{ltread}^{nor,wi} \\ F_{rtread}^{nor,wi} \end{bmatrix} = \begin{bmatrix} \bar{F}_z^{wi} \\ \hat{M}_x^{wi} \end{bmatrix}. \tag{31}$$

Once the location of the contact points and the normal contact forces at the tread and the flange of the wheels are known, the generalised tangential forces  $\mathbf{Q}^{tang}$  at these points can be computed. In this investigation, Polach method is used [37] because of its good balance between the accuracy and simplicity. To this end, the relative velocities of the contact points on the wheels with respect to the contact points on the rails have to be calculated. These velocities are divided by the wheelset forward velocity to find the so-called creepages. Polach method uses the Kalker’s linear coefficients. These coefficients depend on the material properties of the wheel and rail, the curvatures of the surfaces at the contact points and the normal contact force. The curvatures and the normal contact forces are used to find the semi-axis of the contact ellipse (Hertz theory is assumed to be valid). If the wheel and rail profiles are assumed to be new, as in the examples presented in Sect. 6, the curvatures are piecewise constant functions that are smoothed to avoid discontinuities. If the profiles are assumed

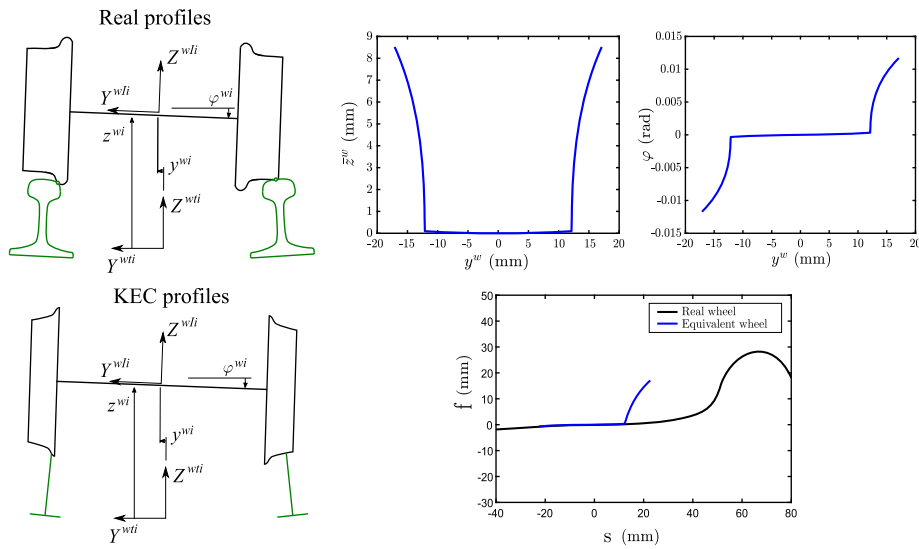


**Fig. 10** Real profile and KEC wheel profile (Color figure online)

to be worn, the curvatures are calculated using numerical differentiation of the geometry evaluated at the nodal points and possibly using numerical filtering to avoid high frequency space-oscillations of the output. Kalker’s linear coefficients cannot be precomputed because the value of the normal contact forces is not known in the preprocessing stage. The strategy followed in this research is to precompute the Kalker’s linear coefficients for each wheel–rail contact geometry used in the lookup table for a normal contact force equal to one. These ‘unit-force Kalker’s linear coefficients’ are stored in the lookup table such that the calculation of the actual ones is very simply obtained online.

#### 4 Wheel–rail contact simulation with KEC profiles

This section presents the use of KEC profiles for the simulation of railway vehicles using relative body-track frame coordinates.

##### 4.1 KEC profiles

The KEC profile associated with the wheel–rail profiles combination has the property that, when contacting ideal railheads with zero width, results in a wheelset with the same space of allowable motion than the wheelset with the real wheel–rail profiles combination. All details about this method can be seen in [26, 35]. Figure 10 on the left shows two wheelsets contacting rails. The sketch on the top with the real wheel–rail profiles combination while the sketch below with the KEC profile. The subspace of allowable motion is characterised by the functions  $z^{wi} = z_{clt}(y^{wi})$ ,  $\varphi^{wi} = \varphi_{clt}(y^{wi})$ , that are plot on the right-upper part of the figure. The real and KEC wheel profiles are shown in the right-lower part of the figure.

The contact constraint equations of a wheelset with KEC profiles have a simple form compared with Eq. (17): (a) only the condition of the coincidence of two points belonging to the two surfaces has to be fulfilled, (b) the orthogonality condition for the normal and

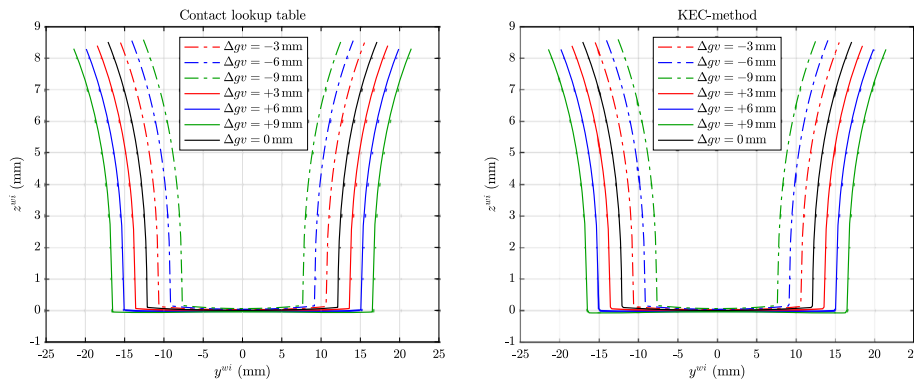


**Fig. 11** Wheelset vertical displacement with respect to track centreline for different values of gauge irregularity: (left) contact lookup table; (right) KEC-method (Color figure online)

tangential vectors of two contact surfaces is not needed [26]. Thus, these equations are given by

$$\mathbf{C}^{KEC,wi}(\mathbf{q}^{wi}, \mathbf{s}^k) = \begin{bmatrix} 0 & r_0 + f^{lk} & 1 & 0 \\ 0 & r_0 + f^{rk} & 0 & 1 \\ 1 & L_w & \varphi^{wi} & 0 \\ 1 & -L_w & 0 & \varphi^{wi} \end{bmatrix} \begin{bmatrix} \bar{z}^{wi} \\ \varphi^{wi} \\ s^{lk} \\ s^{rk} \end{bmatrix} - \begin{bmatrix} y^{wi} - y^{lir} \\ y^{wi} - y^{rir} \\ -f^{lk} - z^{lir} \\ -f^{rk} - z^{rir} \end{bmatrix}, \quad (32)$$

where  $\mathbf{s}^k = [s^{lk} \quad s^{rk}]^T$  are the lateral positions of the contact point in the left and right KEC profiles,  $f^{lk}$  and  $f^{rk}$  are the values of the equivalent profiles at these locations and  $r_0$  is the rolling radius of the wheel when centered in the track. The main advantage of the use of KEC profiles instead of the real ones are [26, 35]:

1. Contact forces on the tread and the flange are treated equally (avoiding hybrid methods);
2. Contact constraints can be solved online keeping a good computational efficiency;
3. Wheel climbing can be simulated;
4. Two-point contact scenario can be simulated with a smooth transition of the normal contact forces from tread to flange.

Regarding the simulation of wheel climbing, some authors claim that the lead-lag contact may have important influence on this phenomenon. Lead-lag contact cannot be simulated with the KEC-method. However, recent work and the authors’ experience [27] shows that this influence of the lead-lag contact may not be that important.

#### 4.2 Equivalence of lookup tables and KEC-method in irregular tracks

In the KEC-method, the computation of the equivalent wheel profiles requires the wheelset kinematics with respect to an ideal track [26]. However, these profiles can be used in irregular tracks with accuracy. This is an advantage with respect to traditional contact lookup tables that need to store the wheelset kinematics and contact solution for tracks with a set of different values of the gauge. This is, the lookup table contact method requires a two-entry table, while the KEC-method requires a one-entry table. Nonetheless, the resulting KEC profiles appear to be valid for different values of the gauge, as shown below.

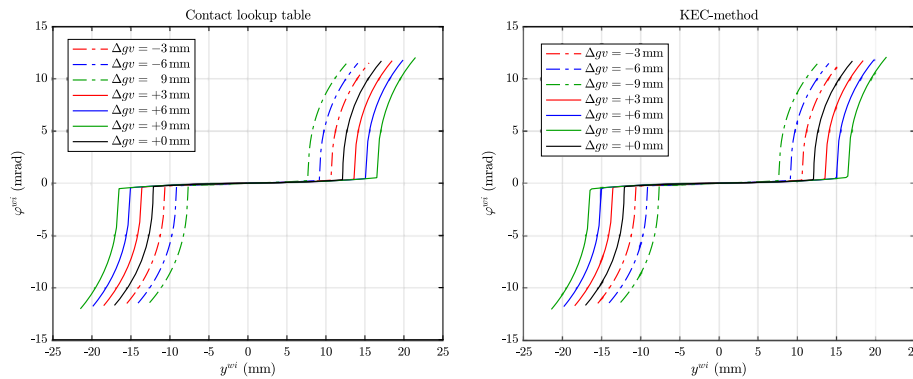


**Fig. 12** Wheelset roll angle with respect to track centreline for different values of gauge irregularity: (left) contact lookup table; (right) KEC-method (Color figure online)

To show this equivalence in irregular tracks, the wheelset kinematics using contact lookup tables and KEC-method is compared next. To that end, a wheelset with wheels S1002 profile and rails LB.140-AREA profile are considered [35]. Figures 11 and 12 show the wheelset vertical displacement and roll angle coordinate with respect to the track centreline within a range of track gauge variations  $\Delta gv$  of  $\pm 9$  mm, respectively.

Figures 13 and 14 show the absolute differences between the contact solution using lookup tables and KEC-method. As shown in both figures, the error obtained for both wheelset vertical displacement and roll angle is bigger the higher the gauge variation. This outermost case, which is given by a 9-mm track gauge variation, provides a 60  $\mu\text{m}$  vertical distance and 0.16 mrad errors when the contact point is at the flange before wheel climb. These are quite small errors when compared to the high-order magnitudes given in Figs. 11 and 12, respectively. Moreover, those differences are almost inappreciable when the contact point lies on the tread. It can be concluded that the KEC-method provides an accurate kinematic solution for its use in tracks with irregularities.

### 4.3 Calculation of contact forces when using the KEC method

When using the KEC method, two main difficulties are found:

1. Normal contact forces cannot be obtained with the classical Lagrange multiplier method;
2. The tangential contact forces cannot be applied on the equivalent profile.

The second problem has an easy solution. When finding the KEC profile, a table is created to find the position of the contact points in the real profiles once the position of the contact points in the KEC profile is found solving Eq. (32). The solution of the first problem is more involved as explained next. Equation (32) is written in terms of the wheelset coordinates  $\mathbf{q}^{wi}$  and the profile parameters  $\mathbf{s}^k$ . If these profile parameters could be eliminated from Eq. (32), reducing it to a set of two equations and three unknowns ( $y^{wi}$ ,  $z^{wi}$  and  $\phi^{wi}$ ), just like Eq. (20), then the problem would be solved and the Lagrange multipliers method could be used to find the normal contact forces. Unfortunately, the elimination of  $\mathbf{s}^k$  is not possible due to the non-linearity of Eq. (32). It can be concluded that, for the KEC-method,

$$\mathbf{Q}^{nor} \neq -(\mathbf{C}_q^{KEC})^T \boldsymbol{\lambda}, \tag{33}$$

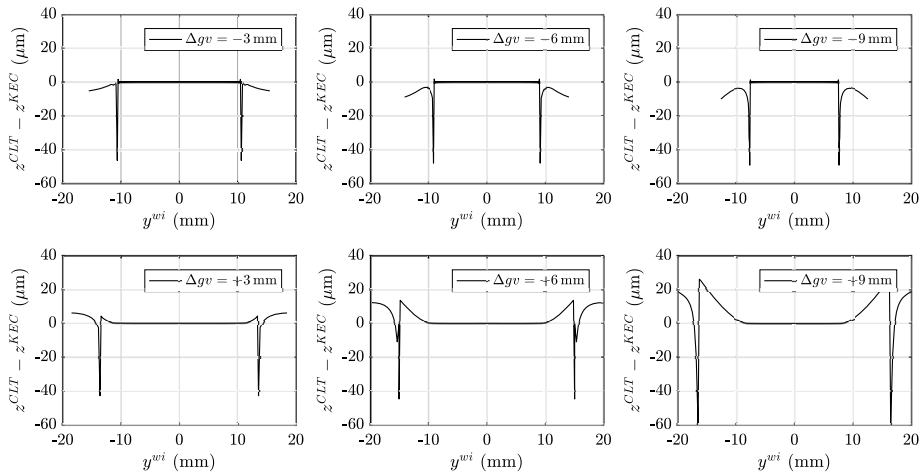


**Fig. 13** Absolute differences between contact lookup tables and KEC kinematics in the wheelset vertical displacement with respect to track centreline for different values of gauge irregularity

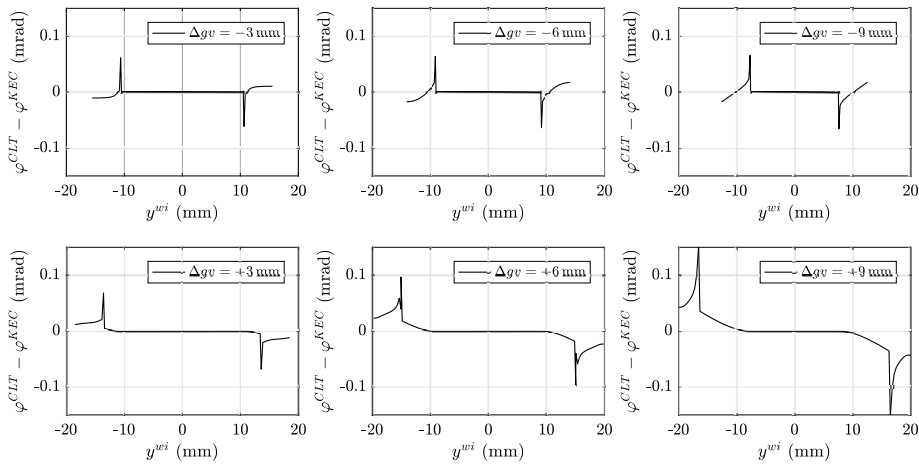


**Fig. 14** Absolute differences between contact lookup tables and KEC kinematics in the wheelset roll angle with respect to track centreline for different values of gauge irregularity

where the Jacobian matrix  $\mathbf{C}_q^{KEC}$  is the result of assembling the Jacobian matrices  $\mathbf{C}_q^{KEC,wi}$  associated with all wheelsets in the vehicle.

In the classical method of the Lagrange multipliers, the rows of the Jacobian matrix provide the direction of the reaction forces in the space of the generalised coordinates, while the multipliers mean the number that these rows have to be multiplied by to obtain the generalised reaction forces. In the problem at hand, the Jacobian matrix is not needed to find the direction of the reaction forces because these directions are known in advance, we know the normal vectors to the real wheel profiles. Therefore, the reaction forces for wheelset  $wi$

can be obtained as

$$\mathbf{Q}^{nor} = - \begin{bmatrix} \bar{\mathbf{n}}_{lw} & \bar{\mathbf{n}}_{rw} \\ \hat{\mathbf{r}}_{lw} \times \hat{\mathbf{n}}_{lw} & \hat{\mathbf{r}}_{rw} \times \hat{\mathbf{n}}_{rw} \end{bmatrix} \begin{bmatrix} \lambda_{lw}^{wi} \\ \lambda_{rw}^{wi} \end{bmatrix} = -\mathbf{N}^{wi} \boldsymbol{\lambda}^{wi}. \tag{34}$$

The coefficient matrix  $\mathbf{N}^{wi}$  of this equation looks similar to that appearing in Eq. (31). However,  $\mathbf{N}^{wi}$  includes the complete set vector components (it is  $6 \times 2$ ) instead of single components (the one in Eq. (31) is  $2 \times 2$ ). An important benefit of this alternative formulation of the Lagrange multipliers method is that the multipliers can be directly identified with the normal contact forces, that is,

$$\begin{aligned} F_{lw}^{nor,wi} &= \lambda_{lw}^{wi}, \\ F_{rw}^{nor,wi} &= \lambda_{rw}^{wi}. \end{aligned} \tag{35}$$

Therefore, once the Lagrange multipliers are obtained after solving the equations of motion each time-step, no additional equations, like Eq. (31), have to be solved to find the normal contact forces.

Substituting the reaction forces from Eq. (34) into the equations of motion yields:

$$\begin{aligned} \mathbf{M}\ddot{\mathbf{q}} + \mathbf{N}\boldsymbol{\lambda} &= \mathbf{Q} + \mathbf{Q}^{tang}, \\ \mathbf{C}^{KEC} &= \mathbf{0}, \end{aligned} \tag{36}$$

where  $\mathbf{N}$  and  $\mathbf{C}^{KEC}$  are the results of assembling the matrices  $\mathbf{N}^{wi}$  and the vectors  $\mathbf{C}^{KEC,wi}$  associated with all the wheelsets in the vehicle.

Equation (36) represents a system of differential-algebraic equations (DAE). Because the constraints are augmented at the position level, this DAE system is called index-3 [41]. It is common in multibody dynamics to substitute the constraint equations by their second time-derivative. In that case the system is called DAE-index 1. In these derivatives, the wheelset accelerations have to be isolated with respect to  $\mathbf{s}^k$ . In this case, this isolation has no difficulty because the constraint equations at the acceleration level are linear. The process starts with the calculation of the first time-derivative of the KEC constraints as follows:

$$\dot{\mathbf{C}}^{KEC,wi} = \frac{\partial \mathbf{C}^{KEC,wi}}{\partial \mathbf{q}^{wi}} \dot{\mathbf{q}}^{wi} + \frac{\partial \mathbf{C}^{KEC,wi}}{\partial \mathbf{s}^k} \dot{\mathbf{s}}^k + \begin{bmatrix} \dot{y}^{lir} \\ \dot{z}^{lir} \\ \dot{y}^{rir} \\ \dot{z}^{rir} \end{bmatrix} = \mathbf{C}_q^{KEC,wi} \dot{\mathbf{q}}^{wi} + \mathbf{C}_s^{KEC,wi} \dot{\mathbf{s}}^k + \dot{\mathbf{x}}^{ir} = \mathbf{0}, \tag{37}$$

where  $\mathbf{x}^{ir}$  includes the four track irregularities. The second time-derivative of the constraints is given by

$$\ddot{\mathbf{C}}^{KEC,wi} = \mathbf{C}_q^{KEC,wi} \ddot{\mathbf{q}}^{wi} + \mathbf{C}_s^{KEC,wi} \ddot{\mathbf{s}}^k + \dot{\mathbf{C}}_q^{KEC,wi} \dot{\mathbf{q}}^{wi} + \dot{\mathbf{C}}_s^{KEC,wi} \dot{\mathbf{s}}^k + \ddot{\mathbf{x}}^{ir} = \mathbf{0}. \tag{38}$$

The Jacobian matrices  $\mathbf{C}_q^{KEC,wi}$  ( $4 \times 6$ ) and  $\mathbf{C}_s^{KEC,wi}$  ( $4 \times 2$ ) can be separated into two submatrices, with two rows each, as follows:

$$\mathbf{C}_q^{KEC,wi} = \begin{bmatrix} \mathbf{C}_q^a \\ \mathbf{C}_q^b \end{bmatrix}, \quad \mathbf{C}_s^{KEC,wi} = \begin{bmatrix} \mathbf{C}_s^a \\ \mathbf{C}_s^b \end{bmatrix}. \tag{39}$$

Accordingly, the second time-derivative of the constraints given in Eq. (38) can be separated into two vectors with two rows:

$$\ddot{\mathbf{C}}^a = \mathbf{C}_q^a \ddot{\mathbf{q}}^{wi} + \mathbf{C}_s^a \ddot{\mathbf{s}}^k + \dot{\mathbf{C}}_q^a \dot{\mathbf{q}}^{wi} + \dot{\mathbf{C}}_s^a \dot{\mathbf{s}}^k + (\ddot{\mathbf{x}}^{ir})^a = \mathbf{0}, \tag{40a}$$

$$\ddot{\mathbf{C}}^b = \mathbf{C}_q^b \ddot{\mathbf{q}}^{wi} + \mathbf{C}_s^b \ddot{\mathbf{s}}^k + \dot{\mathbf{C}}_q^b \dot{\mathbf{q}}^{wi} + \dot{\mathbf{C}}_s^b \dot{\mathbf{s}}^k + (\ddot{\mathbf{x}}^{ir})^b = \mathbf{0}. \tag{40b}$$

The second time-derivative of the constraints of Eq. (40b) can be manipulated to isolate  $\ddot{\mathbf{s}}^k$  as follows:

$$\begin{aligned} \mathbf{C}_q^b \ddot{\mathbf{q}}^{wi} + \mathbf{C}_s^b \ddot{\mathbf{s}}^k &= -\dot{\mathbf{C}}_q^b \dot{\mathbf{q}}^{wi} - \dot{\mathbf{C}}_s^b \dot{\mathbf{s}}^k - (\ddot{\mathbf{x}}^{ir})^b \\ \implies \ddot{\mathbf{s}}^k &= -(\mathbf{C}_s^b)^{-1} [\mathbf{C}_q^b \ddot{\mathbf{q}}^{wi} + \dot{\mathbf{C}}_q^b \dot{\mathbf{q}}^{wi} + \dot{\mathbf{C}}_s^b \dot{\mathbf{s}}^k + (\ddot{\mathbf{x}}^{ir})^b]. \end{aligned} \tag{41}$$

Substituting Eq. (41) into Eq. (40a), one gets:

$$\begin{aligned} \mathbf{C}_q^a \ddot{\mathbf{q}}^{wi} - \mathbf{C}_s^a (\mathbf{C}_s^b)^{-1} [\mathbf{C}_q^b \ddot{\mathbf{q}}^{wi} + \dot{\mathbf{C}}_q^b \dot{\mathbf{q}}^{wi} + \dot{\mathbf{C}}_s^b \dot{\mathbf{s}}^k + (\ddot{\mathbf{x}}^{ir})^b] &= -\dot{\mathbf{C}}_q^a \dot{\mathbf{q}}^{wi} - \dot{\mathbf{C}}_s^a \dot{\mathbf{s}}^k - (\ddot{\mathbf{x}}^{ir})^a \\ \implies (\mathbf{C}_q^a - \mathbf{C}_s^a (\mathbf{C}_s^b)^{-1} \mathbf{C}_q^b) \ddot{\mathbf{q}}^{wi} &= \\ = -(\ddot{\mathbf{x}}^{ir})^a - \mathbf{C}_s^a (\mathbf{C}_s^b)^{-1} (\ddot{\mathbf{x}}^{ir})^b - (\dot{\mathbf{C}}_q^a - \mathbf{C}_s^a (\mathbf{C}_s^b)^{-1} \dot{\mathbf{C}}_q^b) \dot{\mathbf{q}}^{wi} &- (\dot{\mathbf{C}}_s^a - \mathbf{C}_s^a (\mathbf{C}_s^b)^{-1} \dot{\mathbf{C}}_s^b) \dot{\mathbf{s}}^k \end{aligned} \tag{42}$$

These are two constraint equations in which  $\ddot{\mathbf{s}}^k$  does not appear. They can be augmented to the generalised force balance in the equations of motion. This equation can be written with a simplified notation as follows:

$$\mathbf{B}^{wi} \ddot{\mathbf{q}}^{wi} = -\mathbf{D}_{ir}^{wi} - \mathbf{E}^{wi} \dot{\mathbf{q}}^{wi} - \mathbf{G}^{wi} \dot{\mathbf{s}}^k, \tag{43}$$

where

$$\begin{aligned} \mathbf{B}^{wi} &= \mathbf{C}_q^a - \mathbf{C}_s^a (\mathbf{C}_s^b)^{-1} \mathbf{C}_q^b, \\ \mathbf{D}_{ir}^{wi} &= -(\ddot{\mathbf{x}}^{ir})^a - \mathbf{C}_s^a (\mathbf{C}_s^b)^{-1} (\ddot{\mathbf{x}}^{ir})^b, \\ \mathbf{E}^{wi} &= \dot{\mathbf{C}}_q^a - \mathbf{C}_s^a (\mathbf{C}_s^b)^{-1} \dot{\mathbf{C}}_q^b, \\ \mathbf{G}^{wi} &= \dot{\mathbf{C}}_s^a - \mathbf{C}_s^a (\mathbf{C}_s^b)^{-1} \dot{\mathbf{C}}_s^b. \end{aligned} \tag{44}$$

The term  $\mathbf{D}_{ir}^{wi}$  is linear with respect to the second time-derivative of the irregularities. This term has little influence because the relatively high-wave length irregularities that are considered in rigid-body railway dynamics vary smoothly. In addition, it is a term that in practice is difficult to know accurately. Therefore, this term will be neglected in the following.

Considering all the developments shown in this chapter, the equations of motion of the railway vehicle of Eq. (36) can also be written in the following DAE-index 1 form:

$$\begin{bmatrix} \mathbf{M} & \mathbf{N} \\ \mathbf{B} & \mathbf{0} \end{bmatrix} \begin{bmatrix} \ddot{\mathbf{q}} \\ \lambda \end{bmatrix} = \begin{bmatrix} \mathbf{Q} + \mathbf{Q}^{tang} \\ -\mathbf{E}\dot{\mathbf{q}} - \mathbf{G}\dot{\mathbf{s}} \end{bmatrix} \tag{45}$$

where  $\mathbf{N}$ ,  $\mathbf{B}$ ,  $\mathbf{E}$  and  $\mathbf{G}$  are the result of assembling the matrices  $\mathbf{N}^{wi}$ ,  $\mathbf{B}^{wi}$ ,  $\mathbf{E}^{wi}$  and  $\mathbf{G}^{wi}$  associated with all the wheelsets in the vehicle. Vector  $\dot{\mathbf{s}}$  includes the profile parameters  $\dot{\mathbf{s}}^k$

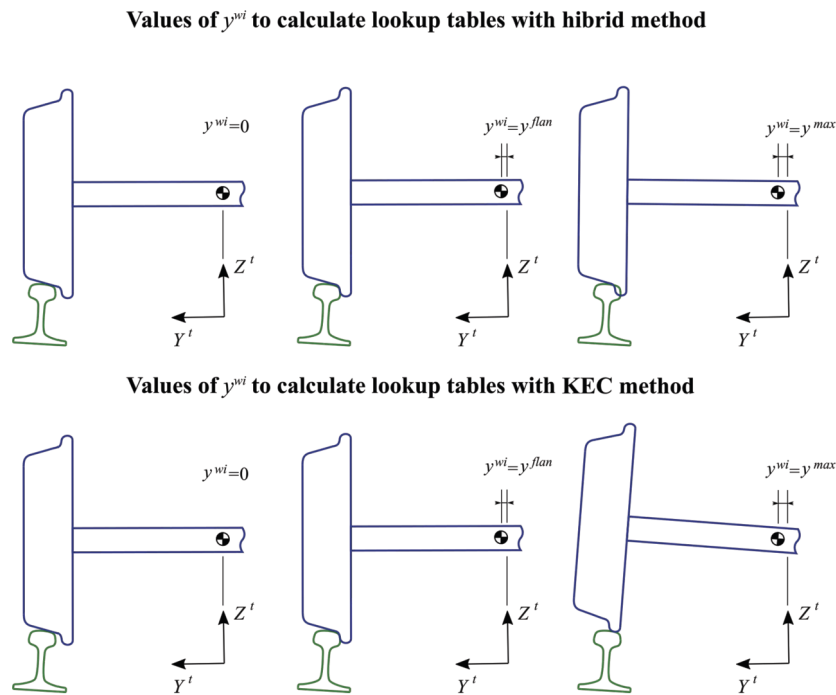


**Fig. 15** Lateral displacement of wheels in the generation of lookup tables

of all the wheelsets in the vehicle. To find the value of  $\dot{\mathbf{s}}^k$ , the first derivative of the constraint equations given in Eq. (37) has to be found each time-step. This is a linear algebraic system of 4 equations and 2 unknowns. If the coordinates fulfil the KEC equations, the resulting linear system has to be compatible and it can be solved using the pseudo-inverse.

The calculation of the generalised tangential forces  $\mathbf{Q}^{tang}$  follows the same procedure that was explained in Sect. 3.3.

### 5 Generation of lookup tables for flanging wheelsets

For the generation of contact lookup tables of wheelsets with wheel–rail profile combinations that show two-point contact, that is, simultaneous contact in the tread and the flange, the procedure differs depending on whether these tables are going to be used with a hybrid method (explained in Sect. 3) or with a KEC-method (explained in Sect. 4). Recall that the KEC-method is an online contact method that requires the real wheel–rail contact problem to be solved first to find the equivalent profiles. In this context, Fig. 15 illustrates such difference between methods.

Assume that, for the track with nominal gauge, the lateral displacement that produces two-point contact is  $y^{flan}$ . Then, the range of values of  $y^{wi}$  for which the lookup table is calculated is  $[0 \quad y^{max}]$ , where  $y^{max} > y^{flan}$ . In the subrange  $y^{wi} \in [0 \quad y^{flan}]$ , the lookup tables for both methods are equal. However, in the subrange  $y^{wi} \in [y^{flan} \quad y^{max}]$  the lookup tables for both methods differ.

In the case of lookup tables to be used with a hybrid method, the constraint contact on the tread is kept, allowing the wheel flange to penetrate the railhead. The location of the

**Table 1** Simulation parameters for the vehicle

Wheelsets	Parameters	Bogie	Parameters
Mass $m^{wh}$	1568 kg	Mass $m^b$	2982 kg
Roll inertia $I_{xx}^{wh}$	656 kg·m <sup>2</sup>	Roll inertia $I_{xx}^b$	1398.5 kg·m <sup>2</sup>
Pitch inertia $I_{yy}^{wh}$	168 kg·m <sup>2</sup>	Pitch inertia $I_{yy}^b$	2667 kg·m <sup>2</sup>
Yaw inertia $I_{zz}^{wh}$	656 kg·m <sup>2</sup>	Yaw inertia $I_{zz}^b$	2667 kg·m <sup>2</sup>

**Table 2** Primary suspension element used in the vehicle

Suspension element direction	Spring stiffness (N/m)	Damping coefficient (N·s/m)	Number of elements
Lateral	$1.5 \cdot 10^6$	$4.5 \cdot 10^4$	4 per bogie
Vertical	$3 \cdot 10^6$	$6.75 \cdot 10^4$	4 per bogie
Longitudinal	$6 \cdot 10^6$	$9 \cdot 10^4$	8 per bogie

point of maximum indentation is stored in the lookup table to be used online as the flange contact point. In the case of the KEC-method, the constraint contact is moved to the flange, allowing the wheel tread to separate the railhead [35]. That way, the KEC-method accounts for the wheel climbing that is fundamental in simulation of derailment.

## 6 Simulation results

In this section, to analyse the differences between the lookup table and the KEC-method, a numerical comparison of three different case studies is presented: (1) simulation in irregular track with a wheel–rail profile combination that does not show two-point contact, (2) simulation in irregular track with a wheel–rail profile combination that shows two-point contact and (3) a wheelset climbing and derailment scenario with a wheel–rail profile combination that shows two-point contact. The contact lookup tables for the different wheel–rail combinations are discretized for 11 different track gauge irregularities and a range of 350–400 different wheelset lateral displacements, which results in a storage size of around 25 KB for each case. Also, the *Matlab* variable-time step integrator *ode15s* with relative and absolute tolerances of  $1 \cdot 10^{-6}$  and a maximum time step of  $\Delta t = 1$  ms is used for the dynamic simulations described in the rest of the paper.

For all cases, a three-body suspended vehicle formed by two wheelsets and a bogie frame is analysed. The mass and inertia properties with respect to the wheelset and bogie frame are presented in Table 1. The primary suspension is modelled with four three-dimensional spring–damper elements per wheel depicted in Fig. 16. These elements, that connect the axlebox to the bogie frame, have stiffness and damping properties defined in lateral, vertical and longitudinal direction as shown in Table 2. In this work, axleboxes are assumed to follow the wheelset motion with the exception of the rolling motion. In other words, the body frame of the axle boxed is assumed to be parallel to the wheelset intermediate-frame. Moreover, Polach rolling contact theory [42] is used for tangential contact force computation.

Track irregularities are generated using analytical expressions of the power spectral density functions (PSD) [43]. The alignment, vertical profile, gauge variation and cross level are shown in Fig. 17.

**Fig. 16** Three-dimensional vehicle: (a) elevation; (b) end view

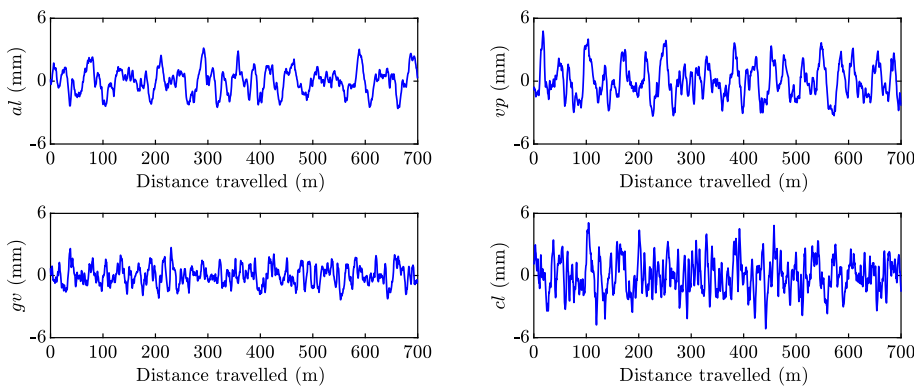
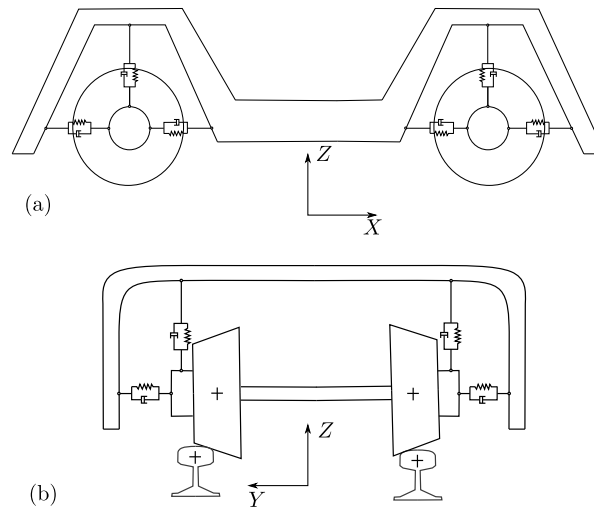


**Fig. 17** Track irregularities, *al* is alignment, *vp* is vertical profile, *gv* is gauge variation, *cl* is cross level

### 6.1 Simulation results in a track with irregularities with one-point contact wheel–rail profile combination

The proposed first case study considers a wheel–rail profile combination that does not show two-point contacts. It is simulated at a constant forward velocity of  $V = 10$  m/s, in a 700-m track with irregularities formed by the following five segments: 100-m tangent, 50-m transition, 400-m left curve of  $R = 235$  m radius segment, 50-m transition and 100-m tangent. The track geometry is shown in Fig. 18 where the different track segments limits are identified. This segment description is latter used in all simulation results figures. Wheel and rail profiles are shown in Fig. 19, which are those used by the metropolitan train at the city of Seville. The parameters for both the wheelset and the rail are given in Table 3.

The relationship of transverse curve parameters between KEC and real wheel profiles can be found in Fig. 20. It can be seen that for each value of the equivalent parameter  $s^{lk}$ , only one contact point in the real profile  $s^{lw}$  can be obtained. This corresponds to a single point wheel–rail contact scenario.

**Fig. 18** Track geometry in solid dark line. Lines perpendicular to the track geometry show the transition points of the track segments (Color figure online)

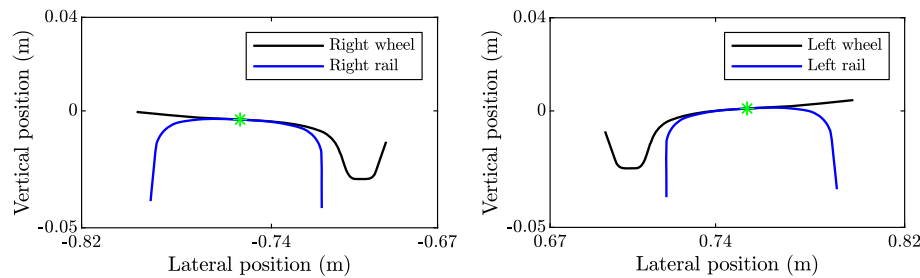
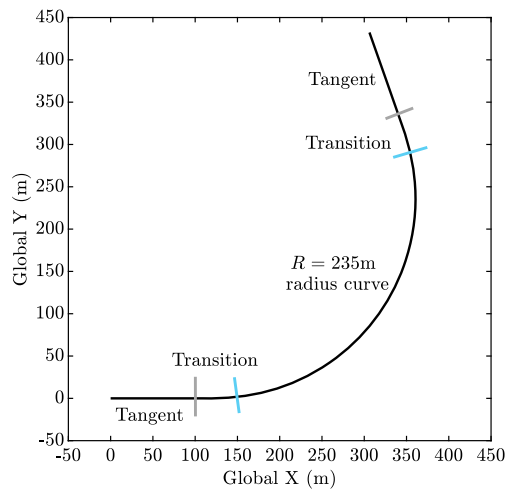


**Fig. 19** Wheel–rail profile combination which does not show two-point contacts (used by the metropolitan train of the city of Seville)

**Table 3** Simulation parameters for the wheelset which do not show two-point contact

Parameters	Model	Parameters	Model	Parameters	Model	Parameters	Model
$L_w$ (m)	0.7526	$R_0$ (m)	0.43	$L_r$ (m)	0.7526	$\beta$ (rad)	0.05

The comparison of lateral displacement and yaw angle for the wheelsets and bogie frame using lookup table and KEC-method is shown in Fig. 21. As it can be seen from the figures, the results of both approaches are almost identical. Due to the curve negotiation, the three bodies show negative values of the lateral displacement and the yaw angle. A steady curving motion is not achieved due to the track irregularities.

Figures 22 and 23 show a comparison of normal contact forces at front and rear wheelsets using both approaches. Since there is always a unique contact point per wheel–rail pair, normal contact forces of both approaches are treated as reaction forces using Eq. (23). In this context, the results from both approaches are very close to each other. When the vehicle negotiates the left curve, the right wheel for both wheelsets experiences a higher normal contact force than the left one, which has identical behaviour as in [26]. Also note that all constraints used in the paper (for both KEC- and lookup table method) are bilateral. This

**Fig. 20** Transverse curve parameters relation between KEC and real wheel profiles

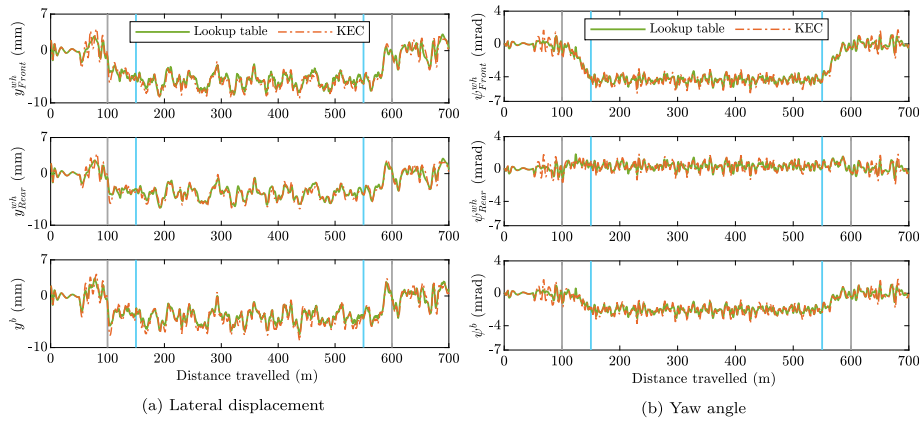
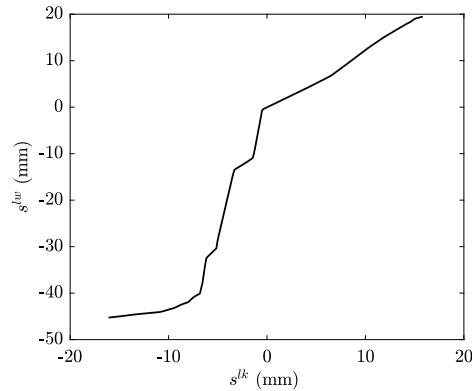


**Fig. 21** Comparison of kinematics with the profiles which do not show two-point contact using both approaches. Full vertical lines refer to the limits of track segments as shown in Fig. 18. Top figures show the motion of the front wheelset, middle figures show the motion of the rear wheelset and bottom figures show the motion of the bogie frame (Color figure online)

means that the associated normal contact force, which is calculated as a reaction force, can be negative (adhesion force). Clearly, these forces would be physically inadmissible. Therefore, simulation results are acceptable only if the calculated normal contact forces are all compressive.

### 6.2 The selection of the flange contact stiffness with two-point contact wheel–rail profile combination

The second case study is the same bogie vehicle whose wheelsets use a wheel–rail profile combination that shows two-point contacts. Wheel and rail profiles are shown in Fig. 24. The parameters for the wheelset and the rail are given in Table 4. Moreover, the vehicle is assumed to have a constant forward velocity of  $V = 10$  m/s along the same 700-m length track with irregularities shown in Fig. 18.

For this case study in which two-point wheel–rail contact scenarios occur, there is an important parameter that controls the simulations using the lookup table method and

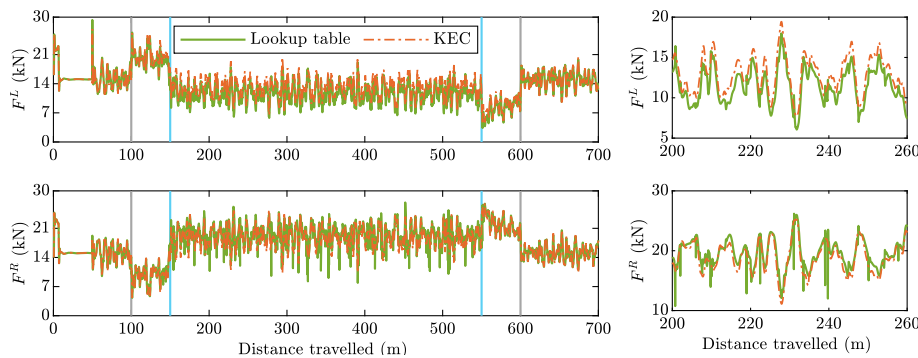


**Fig. 22** Comparison of normal contact forces at front wheelset using both approaches: (left) original figure; (right) zoom within the distance travelled from 200 to 260 m (Color figure online)

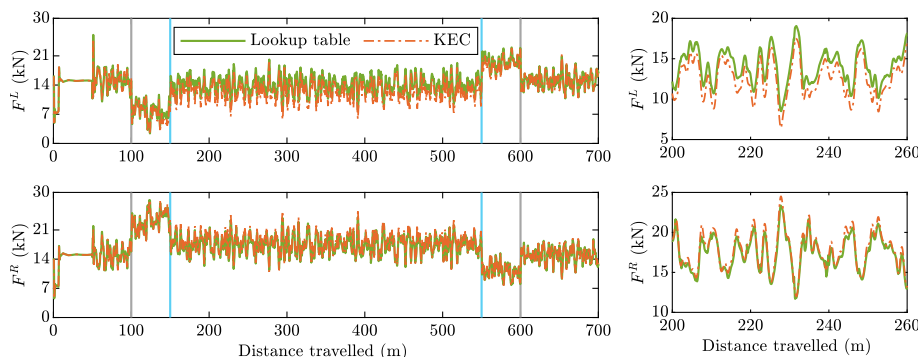


**Fig. 23** Comparison of normal contact forces at rear wheelset using both approaches: (left) original figure; (right) zoom within the distance travelled from 200 to 260 m (Color figure online)

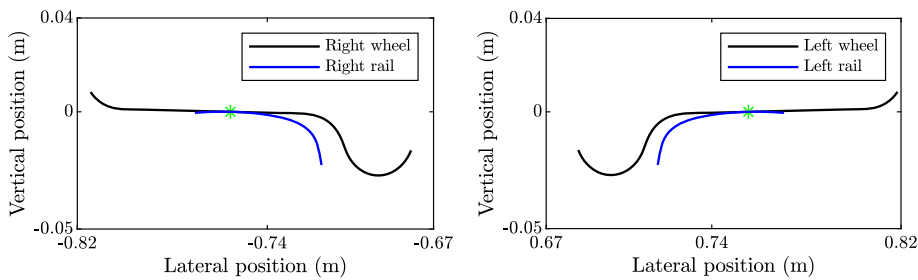


**Fig. 24** Wheel–rail profile combination which shows two point contact (S1002 wheel profile and LB-140-Area rail profile) (Color figure online)

hybrid contact. This parameter is the flange contact stiffness. According to the wheel–rail profile combination shown in Fig. 24, the Hertzian stiffness at the flange contact point can be computed from the application of the Hertz contact theory in Eq. (29) as  $K_{hertz} = 7.7075 \cdot 10^{13} \text{ N/m}^{1.5}$ , where the Poisson’s ratio is  $\nu = 0.28$  and Young’s modulus is  $E_k = 2.1 \cdot 10^{11} \text{ N/m}^2$ . However, the value of this Hertzian stiffness is actually higher

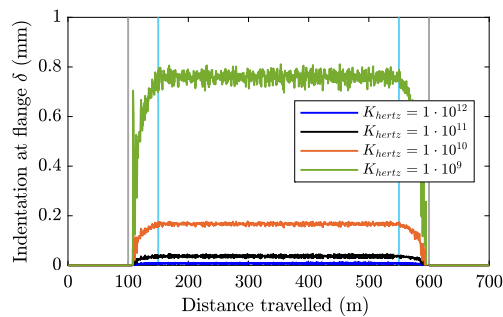
**Table 4** Parameters for the wheel–rail profile combination which can show two-point contact

Parameters	Model	Parameters	Model	Parameters	Model	Parameters	Model
$L_w$ (m)	0.7515	$R_0$ (m)	0.457	$L_r$ (m)	0.7555	$\beta$ (rad)	0

**Table 5** Computation efficiency with different flange contact stiffness and damping parameters by using lookup table approach

$K_{hertz}$ (N/m <sup>1.5</sup> )	$1 \cdot 10^{13}$	$1 \cdot 10^{12}$	$1 \cdot 10^{11}$	$1 \cdot 10^{10}$	$1 \cdot 10^9$
$C_{damp}$ (N · s/m <sup>2</sup> )	$1 \cdot 10^{11}$	$1 \cdot 10^{10}$	$1 \cdot 10^9$	$1 \cdot 10^8$	$1 \cdot 10^7$
CPU time ratio (s/1 s)	Stall	11.8	6.9	2.45	1.09
Function evaluation	Stall	153 338	81 265	20 901	11 822

**Fig. 25** Flange to rail-head indentations at front wheelsets with different flange contact stiffness when using the lookup table approach. The unit of flange contact stiffness  $K_{hertz}$  is N/m<sup>1.5</sup> (Color figure online)



than the real one because Hertz theory assumes that both bodies in contact are semi-infinite spaces. This means that the structural flexibility, which is important for the flange when the load is applied transversely, is not considered.

Since the rail and wheel profiles have fast change of curvature from tread contact to flange contact, the computed Hertzian stiffness evolves similarly. However, the surface parameters to rail/wheel at the flange contact points shows almost no difference for different lateral displacement  $y^{wh}$ . The flange contact point remains the same with two-point contact scenario and hybrid method. Thus, in this work, constant values are chosen for flange contact stiffness.

Due to the high values of contact stiffness and because flange contact is an event that appears suddenly as an impact, simulations slow down tremendously any time flange contact occurs. In these conditions, the resulting flange normal contact forces are so high that they can be considered as physically inadmissible.

In this context, Table 5 shows a comparison of the computational efficiency of the lookup table method with different flange contact stiffness. Along the different stiffness used for the flange contact, the one that is close to  $7.075 \cdot 10^{13}$  N/m<sup>1.5</sup> leads the integrators to stall during the simulation. If the selected contact stiffness is low, simulations are relatively smooth, even with multiple flange contacts. For this reason, the dynamicist may be tempted to use a low value of the stiffness just to get any simulation results, or to get them in a reasonable period of time, such as  $K_{hertz} = 1 \cdot 10^9$  N/m<sup>1.5</sup>. However, the results may show flange to rail-head indentations so large that they can be considered as physically inadmissible as shown in Fig. 25.

As a conclusion, on the one hand, the selection of the contact stiffness is fundamental in the simulation of wheel flange contact with a hybrid method and, on the other hand, this selection is somehow arbitrary when not much information is known about the local contact

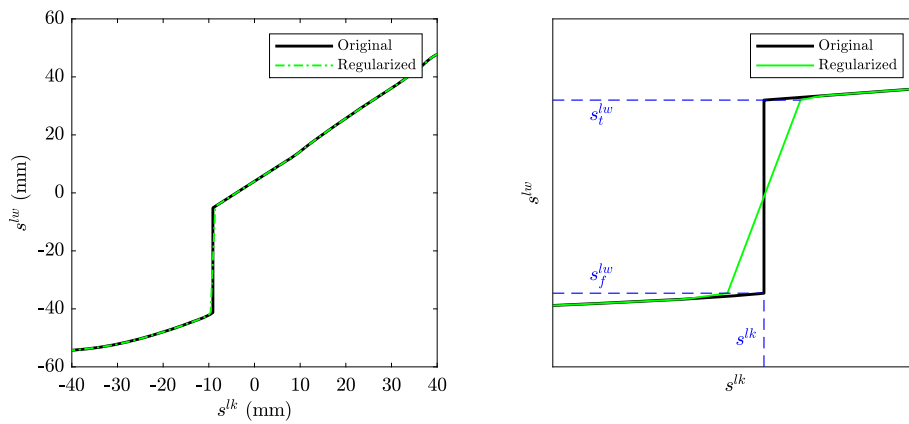


**Fig. 26** Regularisation of the transverse curve parameter relation for the left equivalent and real wheels when KEC-method is used (Color figure online)

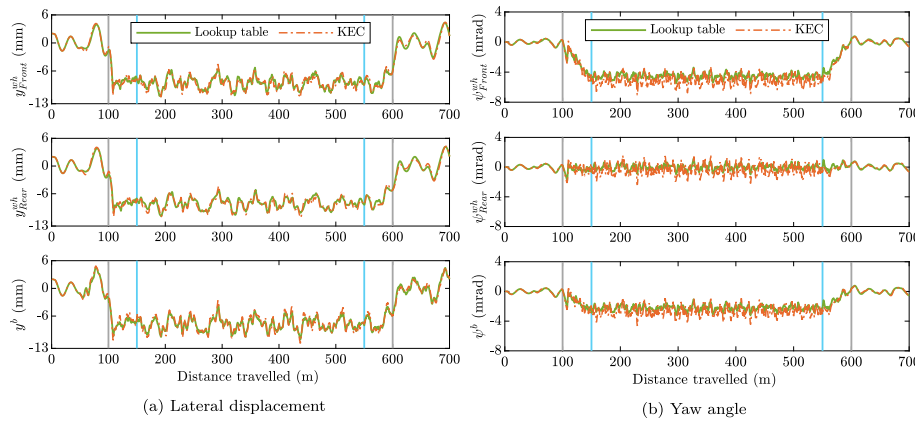
process and the wheel structural deformation. In order to improve computation efficiency and obtain physically admissible indentations of the vehicle motion, the Hertzian parameters for the flange contact when using the lookup table approach are chosen as constant values of  $K_{hertz} = 1 \cdot 10^{10} \text{ N/m}^{1.5}$  and  $C_{damp} = 1 \cdot 10^8 \text{ N} \cdot \text{s/m}^2$ , in the rest of the work.

### 6.3 Simulation results in a track with irregularities with two-point contact wheel–rail profile combination

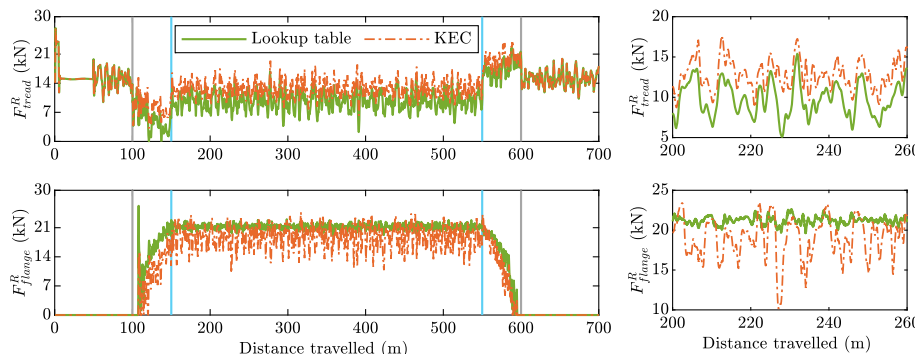
Due to the cumbersome effort to choose flange contact stiffness for the lookup table approach, it is preferable to use a method that treats equally the tread and the flange contacts, as the KEC-method does. The use of the KEC-method results in smooth simulations even with multiple flange contacts. More importantly, the KEC-method is able to simulate wheel climbing. The KEC-method fulfils these conditions. In this and the following sections, the KEC method is compared to the lookup table approach with the two-point contact problem and the wheel–rail profile combination shown in Fig. 24.

Figure 26 plots the location of the contact points in the real profile as a function of the location of the contact point in the KEC profile. It can be seen that for a certain value of the equivalent parameter  $s^{lk}$  there are two simultaneous contact points in the real profile  $s^{lw}$ . This corresponds to a two-point wheel–rail contact scenario where one contact point is located at the tread  $s_t^{lw}$ , and another one is located at the flange  $s_f^{lw}$ . Based on the parameters given in [35] to efficiently use the KEC-method with the two-point contact scenario, this relation between the equivalent and real wheel profiles is regularised as a dashed green line in Fig. 26. This allows a continuous contact point evolution from tread to flange avoiding the discontinuities associated with the contact constraints. However, Fig. 26 is not completely used for the lookup table approach, since only tread contact is considered. Instead, a compliant lateral force model is considered to account for wheel penetration at the flange, as shown in Sect. 5.

The vehicle is assumed to have a constant forward velocity of  $V = 10 \text{ m/s}$  along the same 700-m length track with irregularities shown in Fig. 18. Due to these rail irregularities, a high frequency content can be observed in the following figures. The lateral displacement and the



**Fig. 27** Comparison of kinematics using profiles that show two-point contacts: (left) lateral displacement; (right) yaw angle (Color figure online)



**Fig. 28** Comparison of normal contact forces at front wheelset with two-point contacts: (left) original figure; (right) zoom within the distance travelled from 200 to 260 m (Color figure online)

yaw angle of both wheelsets are compared in Fig. 27. The resulting lateral displacements are quite similar using both approaches. However, when the vehicle enters into the 235 m radius curve, flange contacts occurs. The lateral displacement  $y^{wh}$  enters into the subrange  $y^{wh} \in [y^{flan} \quad y^{max}]$ , in which the kinematic of yaw angle for both methods differs (see Fig. 15 in Sect. 5). However, as it can be seen in Fig. 27, the lateral displacement of the vehicle bodies is very similar in this particular problem. Slight differences can be observed in the yaw angles shown in Fig. 27.

Figures 28 and 29 show a comparison of the normal contact force at the right wheel of front and rear wheelset using both approaches. The normal contact forces at the right tread and flange differ when the wheelset is negotiating the curve. That is due to the two different contact approaches (constrained in the KEC-method, elastic in the lookup table method) used in the wheel flange area.

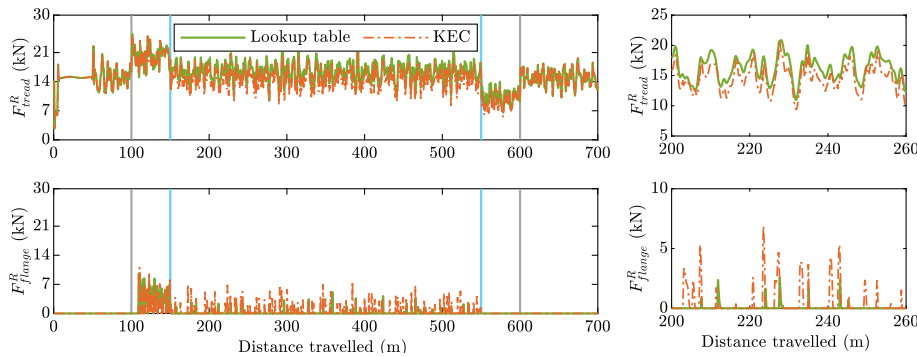


**Fig. 29** Comparison of normal contact forces at rear wheelset with two-point contacts: (left) original figure; (right) zoom within the distance travelled from 200 to 260 m (Color figure online)

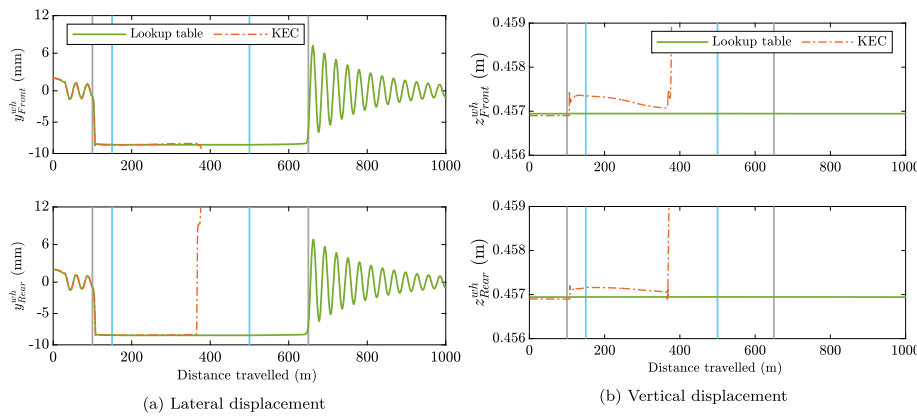


**Fig. 30** Comparison of kinematics at wheel-climbing scenario using profiles that show two-point contacts: (left) lateral displacement; (right) vertical displacement (Color figure online)

### 6.4 Wheelset climbing and derailment with two-point contact wheel–rail profile combination

Due to the large angle of attack generated by friction force, wheel climbing and derailment may occur when the vehicle is running with a high forward velocity or on a small radius curve. In this case study, the bogie vehicle is running at a constant forward velocity of  $V = 25$  m/s on a 1000-m track without irregularities, formed by the following five segments: 100-m tangent, 50-m transition, 350-m left curve of  $R = 100$  m radius segment, 150-m transition and 350-m tangent.

A comparison of the lateral and vertical displacement using both approaches is shown in Fig. 30. When using the lookup table approach, the lateral displacement reaches the steady motion due to permanent flange contact. As a result, the vertical displacement keeps constant during the simulation. However, when using the KEC-method, the wheelset vertical displacement in Fig. 30 shows that the wheelset tends to climb several times when it starts to enter into transitions at around 100 m. Due to regularised tread–flange transition used in the KEC-method, the rear flange climbs when passing through the small curve and the derailment occurs when the longitudinal coordinate is approximately 380 m.

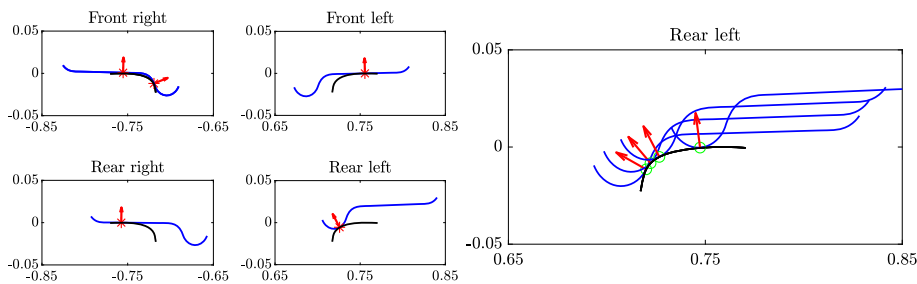


**Fig. 31** Frames of the wheelsets during wheelset climbing using KEC approach (left); Wheel/rail contact in point section with different wheelset lateral displacement during the simulation (right)

Finally, Fig. 31 shows the wheelset climbing scenario during the simulation. Accordingly, the configurations of the rear left wheel in the contact point section during the simulation is shown in the same figure with different wheelset lateral displacements. It is observed that the rear left wheel is climbing the rail with one distinct jumps in contact point. The contact point on the wheel tread which is in contact with the top of the rail is jumped to the rail corner, in which wheel flange is in contact. As the lateral displacement increases, the wheel is completely moved up to the top of the rail. This scenario agrees with the results proposed in [30].

In this example, the lookup method and the KEC-method result in totally different behaviour of the vehicle. As it has been shown, simulations based on the hybrid-lookup table method may produce results that are not on the safe side because wheel climbing cannot be such.

## 7 Conclusion

Two constraint-based formulations for the wheel–rail contact simulation in multibody dynamics are introduced and compared, namely the use of precalculated contact lookup tables and the Knife-edge Equivalent Contact method (KEC-method). Contact search simulation with lookup tables is a well-known and widely used technique. This paper describes a method that does not consider the influence of the yaw angle in the contact geometry. This approach, that is sufficiently accurate in most scenarios, is commonly improved in most simulation codes by including the wheelset yaw as an additional entry to the lookup tables. Regarding this method, the original contributions of this paper are: (1) a method for interpolating the tables in the presence of irregularities and (2) a method for the calculation of the normal contact forces that does not require the use of the Jacobian of the wheel–rail contact constraints. This method models the wheel–rail flange contact using an elastic approach to be able to simulate the two-point contact scenario. That is why this method is considered as a hybrid approach.

The KEC-method is a new wheel–rail contact approach recently developed by the authors. The KEC-method substitutes the real wheel and rail profiles with a fictitious wheel profile that contacts a spatial curve such that the relative wheel–track motion remains unchanged. This method results in very important advantages for the simulations: (1) the contact constraints are very simple and can be solved online, (2) constraint functions are continuous even in the case of two-point contact, (3) it allows a smooth transition of the contact force from the wheel-tread to the wheel-flange and (4) it is effective in the simulation of

wheel climbing. This is the only constraint-based contact method that can be used to simulate the two-point wheel rail contact. Regarding this method, the main contribution of this paper is to show that the wheel KEC profile, that is generated using an irregularity-free track section, remains valid, this is, keeps the same space of allowable motion, also in the presence of track irregularities.

Three different case studies of a bogie vehicle with different wheel–rail profile combinations in a tangent and curved track are examined. Results show that, in general, both approaches provide a similar dynamic behaviour and normal contact forces. Due to the differences in the simulation of flange contact, the wheelsets yaw angle differs at curve negotiation. However, when simulating the negotiation of a curve at relatively high velocity, the results of both methods are drastically different. Due to its ability to simulate wheel climbing, the KEC-method predicts derailment while the lookup-hybrid method predicts a permanent and stable flange contact, even in the presence of track irregularities. It can be concluded that simulations with the lookup-hybrid method may not be on the safe side and the KEC-method can be considered as superior when doing safety analysis.

**Acknowledgements** The first and third authors thank the Department of Economy, Science, Enterprise and University of the Andalusian Regional Government, in Spain, under the PAIDI 2020 program with project reference P18-RT-1772. The second author thanks for the support given by Business of Finland under the SmartTram-LUT project with reference 6292/31/2018. All this support is gratefully acknowledged.

**Conflict of interest** The authors declare that there is no conflict of interest to this work.

**Publisher's Note** Springer Nature remains neutral with regard to jurisdictional claims in published maps and institutional affiliations.

## References

1. Bruni, S., Meijaard, J., Rill, G., Schwab, A.: State-of-the-art and challenges of railway and road vehicle dynamics with multibody dynamics approaches. *Multibody Syst. Dyn.* **49**, 1–32 (2020)
2. Meymand, S.Z., Keylin, A., Ahmadian, M.: A survey of wheel–rail contact models for rail vehicles. *Veh. Syst. Dyn.* **54**(3), 386–428 (2016). <https://doi.org/10.1080/00423114.2015.1137956>
3. Shabana, A.A., Tobaa, M., Sugiyama, H., Zaazaa, K.E.: On the computer formulations of the wheel/rail contact problem. *Nonlinear Dyn.* **40**(2), 169–193 (2005). <https://doi.org/10.1007/s11071-005-5200-y>
4. Ye, Y., Sun, Y., Dongfang, S., Shi, D., Hecht, M.: Optimizing wheel profiles and suspensions for railway vehicles operating on specific lines to reduce wheel wear: a case study. *Multibody Syst. Dyn.* **51**, 91–122 (2021)
5. Antunes, P., Magalhães, H., Ambrosio, J., Pombo, J., Costa, J.: A co-simulation approach to the wheel–rail contact with flexible railway track. *Multibody Syst. Dyn.* **45**(2), 245–272 (2019)
6. Tu, T.W.: Dynamic modelling of a railway wheelset based on Kane's method. *Int. J. Heavy Veh. Syst.* **27**(1–2), 202–226 (2020)
7. Shabana, A.A., Zaazaa, K.E., Escalona, J.L., Sany, J.R.: Development of elastic force model for wheel/rail contact problems. *J. Sound Vib.* **269**(1–2), 295–325 (2004). [https://doi.org/10.1016/S0022-460X\(03\)00074-9](https://doi.org/10.1016/S0022-460X(03)00074-9)
8. Machado, M., Moreira, P., Flores, P., Lankarani, H.M.: Compliant contact force models in multibody dynamics: evolution of the Hertz contact theory. *Mech. Mach. Theory* **53**, 99–121 (2012)
9. Flores, P., Lankarani, H.M.: Contact Force Models for Multibody Dynamics, vol. 226. Springer, Berlin (2016)
10. Shabana, A.A., Sany, J.R.: An augmented formulation for mechanical systems with non-generalized coordinates: application to rigid body contact problems. *Nonlinear Dyn.* **24**(2), 183–204 (2001). <https://doi.org/10.1023/A:1008362309558>
11. Sugiyama, H., Suda, Y.: On the contact search algorithms for wheel/rail contact problems. *J. Comput. Nonlinear Dyn.* **4**(4), 041001 (2009)
12. Marques, F., Magalhães, H., Pombo, J., Ambrósio, J., Flores, P.: A three-dimensional approach for contact detection between realistic wheel and rail surfaces for improved railway dynamic analysis. *Mech. Mach. Theory* **149**, 103825 (2020)

13. Magalhães, H., Marques, F., Liu, B., Antunes, P., Pombo, J., Flores, P., Ambrósio, J., Piotrowski, J., Bruni, S.: Implementation of a non-Hertzian contact model for railway dynamic application. *Multibody Syst. Dyn.* **48**(1), 41–78 (2020)
14. Sun, Y., Zhai, W., Guo, Y.: A robust non-Hertzian contact method for wheel–rail normal contact analysis. *Veh. Syst. Dyn.* **56**(12), 1899–1921 (2018)
15. Piotrowski, J., Kik, W.: A simplified model of wheel/rail contact mechanics for non-Hertzian problems and its application in rail vehicle dynamic simulations. *Veh. Syst. Dyn.* **46**(1–2), 27–48 (2008)
16. Sun, Y., Zhai, W., Ye, Y., Zhu, L., Guo, Y.: A simplified model for solving wheel-rail non-Hertzian normal contact problem under the influence of yaw angle. *Int. J. Mech. Sci.* **174**, 105554 (2020)
17. Pombo, J., Ambrósio, J., Silva, M.: A new wheel–rail contact model for railway dynamics. *Veh. Syst. Dyn.* **45**(2), 165–189 (2007). <https://doi.org/10.1080/00423110600996017>
18. Pombo, J., Ambrósio, J.: Application of a wheel–rail contact model to railway dynamics in small radius curved tracks. *Multibody Syst. Dyn.* **19**, 91–114 (2008). <https://doi.org/10.1007/s11044-007-9094-y>
19. Pombo, J., Ambrósio, J.: An alternative method to include track irregularities in railway vehicle dynamic analyses. *Nonlinear Dyn.* **68**, 161–176 (2012). <https://doi.org/10.1007/s11071-011-0212-2>
20. O’Shea, J.J., Shabana, A.A.: Analytical and numerical investigation of wheel climb at large angle of attack. *Nonlinear Dyn.* **83**, 555–577 (2016). <https://doi.org/10.1007/s11071-015-2347-z>
21. O’Shea, J.J., Shabana, A.A.: Further investigation of wheel climb initiation: three-point contact. *Proc. Inst. Mech. Eng., Proc., Part K, J. Multi-Body Dyn.* **231**(1), 121–132 (2017)
22. Malvezzi, M., Meli, E., Falomi, S., Rindi, A.: Determination of wheel–rail contact points with semianalytic methods. *Multibody Syst. Dyn.* **20**(4), 327–358 (2008). <https://doi.org/10.1007/s11044-008-9123-5>
23. Falomi, S., Malvezzi, M., Meli, E.: Multibody modeling of railway vehicles: innovative algorithms for the detection of wheel–rail contact points. *Wear* **271**(1–2), 453–461 (2011). <https://doi.org/10.1016/j.wear.2010.10.039>
24. Baeza, L., Thompson, D.J., Squicciarini, G., Denia, F.D.: Method for obtaining the wheel–rail contact location and its application to the normal problem calculation through ‘CONTACT’. *Veh. Syst. Dyn.* **56**(11), 1734–1746 (2018). <https://doi.org/10.1080/00423114.2018.1439178>
25. Muñoz, S., Aceituno, J.F., Urda, P., Escalona, J.L.: Multibody model of railway vehicles with weakly coupled vertical and lateral dynamics. *Mech. Syst. Signal Process.* **115**, 570–592 (2019). <https://doi.org/10.1016/j.ymsp.2018.06.019>
26. Escalona, J.L., Aceituno, J.F., Urda, P., Balling, O.: Railway multibody simulation with the knife-edge-equivalent wheel–rail constraint equations. *Multibody Syst. Dyn.* **48**, 373–402 (2020). <https://doi.org/10.1007/s11044-019-09708-x>
27. Escalona, J.L., Aceituno, J.F.: Multibody simulation of railway vehicles with contact lookup tables. *Int. J. Mech. Sci.* **155**, 571–582 (2019). <https://doi.org/10.1016/j.ijmecsci.2018.01.020>
28. Bozzone, M., Pennestrì, E., Salvini, P.: A lookup table-based method for wheel–rail contact analysis. *Proc. Inst. Mech. Eng., Proc., Part K, J. Multi-Body Dyn.* **225**(2), 127–138 (2011)
29. Sugiyama, H., Araki, K., Suda, Y.: On-line and off-line wheel/rail contact algorithm in the analysis of multibody railroad vehicle systems. *J. Mech. Sci. Technol.* **23**, 991–996 (2009). <https://doi.org/10.1007/s12206-009-0327-2>
30. Sugiyama, H., Sekiguchi, T., Matsumura, R., Yamashita, S., Suda, Y.: Wheel/rail contact dynamics in turnout negotiations with combined nodal and non-conformal contact approach. *Multibody Syst. Dyn.* **27**, 55–74 (2012). <https://doi.org/10.1007/s11044-011-9252-0>
31. Piotrowski, J., Liu, B., Bruni, S.: The Kalker book of tables for non-Hertzian contact of wheel and rail. *Veh. Syst. Dyn.* **55**(6), 875–901 (2017)
32. Marques, F., Magalhães, H., Liu, B., Pombo, J., Flores, P., Ambrósio, J., Piotrowski, J., Bruni, S.: On the generation of enhanced lookup tables for wheel–rail contact models. *Wear* **434–435**, 202993 (2019). <https://doi.org/10.1016/j.wear.2019.202993>
33. Piotrowski, J., Bruni, S., Liu, B., Gialleonardo, E.D.: A fast method for determination of creep forces in non-Hertzian contact of wheel and rail base on a book of tables. *Multibody Syst. Dyn.* **45**, 169–184 (2019). <https://doi.org/10.1007/s11044-018-09635-3>
34. Santamaría, J., Vadillo, E.G., Gómez, J.: A comprehensive method for the elastic calculation of the two-point wheel–rail contact. *Veh. Syst. Dyn.* **44**(sup1), 240–250 (2006). <https://doi.org/10.1080/00423110600870337>
35. Aceituno, J.F., Urda, P., Briaies, E., Escalona, J.L.: Analysis of the two-point wheel–rail contact scenario using the knife-edge-equivalent contact constraint method. *Mech. Mach. Theory* **148**, 103803 (2020). <https://doi.org/10.1016/j.mechmachtheory.2020.103803>
36. Kalker, J.: *Three Dimensional Elastic Bodies in Rolling Contact*. Kluwer Academic, Dordrecht (1990)
37. Polach, O.: Creep forces in simulations of traction vehicles running on adhesion limit. *Wear* **258**(7–8), 992–1000 (2005). <https://doi.org/10.1016/j.wear.2004.03.046>

38. Hunt, K., Crossley, E.: Coefficient of restitution interpreted as damping in vibroimpact. *J. Appl. Mech.* **7**, 440–445 (1975)
39. Shabana, A.A., Zaazaa, K.E., Sugiyama, H.: *Railroad Vehicle Dynamics: A Computational Approach*. CRC Press, Boca Raton (2007)
40. Goldsmith, W.: *Impact—the Theory and Physical Behaviour of Colliding Solids*. Edward Arnold, London (1960)
41. Ascher, U.M., Petzold, L.R.: *Computer Methods for Ordinary Differential Equations and Differential-Algebraic Equations*, vol. 61. SIAM, Philadelphia (1998)
42. Polach, O.: A fast wheel-rail forces calculation computer code. *Veh. Syst. Dyn.* **33**(sup1), 728–739 (1999). <https://doi.org/10.1080/00423114.1999.12063125>
43. Claus, H., Schiehlen, W.: Modeling and simulation of railway bogie structural vibrations. *Veh. Syst. Dyn.* **29**, 538–552 (1998). <https://doi.org/10.1080/00423119808969585>



## ACTA UNIVERSITATIS LAPPEENRANTAENSIS

938. METSOLA, JAAKKO. Good for wealth or bad for health? Socioemotional wealth in the internationalisation process of family SMEs from a network perspective. 2020. Diss.
939. VELT, HANNES. Entrepreneurial ecosystems and born global start-ups. 2020. Diss.
940. JI, HAIBIAO. Study of key techniques in the vacuum vessel assembly for the future fusion reactor. 2020. Diss.
941. KAZARNIKOV, ALEXEY. Statistical parameter identification of reaction-diffusion systems by Turing patterns. 2020. Diss.
942. SORMUNEN, PETRI. Ecodesign of construction and demolition waste-derived thermoplastic composites. 2020. Diss.
943. MANKONEN, ALEKSI. Fluidized bed combustion and humidified gas turbines as thermal energy conversion processes of the future. 2020. Diss.
944. KIANI OSHTORJANI, MEHRAN. Real-time efficient computational approaches for hydraulic components and particulate energy systems. 2020. Diss.
945. PEKKANEN, TIIA-LOTTA. What constrains the sustainability of our day-to-day consumption? A multi-epistemological inquiry into culture and institutions. 2021. Diss.
946. NASIRI, MINA. Performance management in digital transformation: a sustainability performance approach. 2021. Diss.
947. BRESOLIN, BIANCA MARIA. Synthesis and performance of metal halide perovskites as new visible light photocatalysts. 2021. Diss.
948. PÖYHÖNEN, SANTERI. Variable-speed-drive-based monitoring and diagnostic methods for pump, compressor, and fan systems. 2021. Diss.
949. ZENG, HUABIN. Continuous electrochemical activation of peroxydisulfate mediated by single-electron shuttle. 2021. Diss.
950. SPRINGER, SEBASTIAN. Bayesian inference by informative Gaussian features of the data. 2021. Diss.
951. SOBOLEVA, EKATERINA. Microscopy investigation of the surface of some modern magnetic materials. 2021. Diss.
952. MOHAMMADI ASL, REZA. Improved state observers and robust controllers for non-linear systems with special emphasis on robotic manipulators and electro-hydraulic servo systems. 2021. Diss.
953. VIANNA NETO, MÁRCIO RIBEIRO. Synthesis and optimization of Kraft process evaporator plants. 2021. Diss.
954. MUJKIC, ZLATAN. Sustainable development and optimization of supply chains. 2021. Diss.
955. LYYTIKÄINEN, JOHANNA. Interaction and barrier properties of nanocellulose and hydrophobically modified ethyl(hydroxyethyl)cellulose films and coatings. 2021. Diss.
956. NGUYEN, HOANG SI HUY. Model based design of reactor-separator processes for the production of oligosaccharides with a controlled degree of polymerization. 2021. Diss.

957. IMMONEN, HEIKKI. Application of object-process methodology in the study of entrepreneurship programs in higher education. 2021. Diss.
958. KÄRKKÄINEN, HANNU. Analysis of theory and methodology used in determination of electric motor drive system losses and efficiency. 2021. Diss.
959. KIM, HEESOO. Effects of unbalanced magnetic pull on rotordynamics of electric machines. 2021. Diss.
960. MALYSHEVA, JULIA. Faster than real-time simulation of fluid power-driven mechatronic machines. 2021. Diss.
961. SIEVINEN, HANNA. Role of the board of directors in the strategic renewal of later-generation family firms. 2021. Diss.
962. MENDOZA MARTINEZ, CLARA. Assessment of agro-forest and industrial residues potential as an alternative energy source. 2021. Diss.
963. OYEWO, AYOBAMI SOLOMON. Transition towards decarbonised power systems for sub-Saharan Africa by 2050. 2021. Diss.
964. LAHIKAINEN, KATJA. The emergence of a university-based entrepreneurship ecosystem. 2021. Diss.
965. ZHANG, TAO. Intelligent algorithms of a redundant robot system in a future fusion reactor. 2021. Diss.
966. YANCHUKOVICH, ALEXEI. Screening the critical locations of a fatigue-loaded welded structure using the energy-based approach. 2021. Diss.
967. PETROW, HENRI. Simulation and characterization of a front-end ASIC for gaseous muon detectors. 2021. Diss.
968. DONOGHUE, ILKKA. The role of Smart Connected Product-Service Systems in creating sustainable business ecosystems. 2021. Diss.
969. PIKKARAINEN, ARI. Development of learning methodology of additive manufacturing for mechanical engineering students in higher education. 2021. Diss.
970. HOFFER GARCÉS, ALVARO ERNESTO. Submersible permanent-magnet synchronous machine with a stainless core and unequal teeth widths. 2021. Diss.
971. PENTTILÄ, SAKARI. Utilizing an artificial neural network to feedback-control gas metal arc welding process parameters. 2021. Diss.
972. KESSE, MARTIN APPIAH. Artificial intelligence : a modern approach to increasing productivity and improving weld quality in TIG welding. 2021. Diss.
973. MUSONA, JACKSON. Sustainable entrepreneurial processes in bottom-of-the-pyramid settings. 2021. Diss.
974. NYAMEKYE, PATRICIA. Life cycle cost-driven design for additive manufacturing: the frontier to sustainable manufacturing in laser-based powder bed fusion. 2021. Diss.
975. SALWIN, MARIUSZ. Design of Product-Service Systems in printing industry. 2021. Diss.





ISBN 978-952-335-702-0  
ISBN 978-952-335-703-7 (PDF)  
ISSN-L 1456-4491  
ISSN 1456-4491  
Lappeenranta 2021